UNIVERSITÀ DEGLI STUDI DI PALERMO

Dottorato in Scienze Fisiche
Dipartimento di Fisica e Chimica
Settore Scientifico Disciplinare FIS/05

Timing and Spectral properties of Low Mass X-ray Binary Systems hosting Neutron Stars

IL DOTTORE

Angelo F. Gambino

IL COORDINATORE

Prof. Gioacchino Massimo Palma

TUTOR

Prof. Rosario Iaria

CO TUTOR

Prof.ssa Tiziana Di Salvo

CICLO XXX
ANNO CONSEGUIMENTO TITOLO 2017/2018

To my father and my mother.

«Sta da mezzora sulla spiaggia buia, seduto su uno sdraio, contorcendosi verso sud o verso nord, ogni tanto accendendo la lampadina e avvicinando al naso le carte che tiene dispiegate sui ginocchi; poi a collo riverso ricomincia l'esplorazione partendo dalla Stella Polare. Delle ombre silenziose si stanno muovendo sulla sabbia; una coppia di innamorati si stacca dalla duna, un pescatore notturno, un doganiere, un barcaiolo. Il signor Palomar sente un sussurro. Si guarda intorno: a pochi passi da lui si è formata una piccola folla che sta sorvegliando le sue mosse come le convulsioni di un demente.»

Palomar
Italo Calvino

Abstract

The topic of this thesis is the timing study of binary systems called Low Mass X-ray binaries (LMXB). These systems consist of a compact object that could be a neutron star (NS) or a black hole (BH) and of a companion star with a mass lower than 1 $M_{\odot}$. As a consequence of the angular momentum loss from the system, the orbital separation could shrink. Consequently, the radius of the Roche lobe of the companion star could decrease until it touches the stellar atmosphere. Then, once the companion star filled its own Roche lobe, part of its mass could be transferred onto the NS surface, forming an accretion disk. Owing to the energetic losses due to the accretion process, these systems emit in the X-rays and the light curves of the source in this band is considerably important to obtain information about the physical characteristic of the celestial objects of the system and about the orbital parameters. Some of the source show a time-localised periodic decrease of the count-rate in the X-rays that is caused by the partial obscuration of the central emitting source by a bulge of opaque and/or partially ionised material that forms at the disk rim, where the accretion flow from the companion star hits the accretion disk. This feature is called dip and is present in some LMXB systems that have an inclination angle between 60°and 80°. A similar time-localised decrease of the count rate could manifest in LMXB systems that have an inclination angle between 75°and 90°. The cause of this phenomenon is actually the eclipse of the central emitting region by the disk of the companion star. In both the cases these features occur with the same orbital frequency of the system and then, they represent useful markers to extrapolate the orbital parameters of the system.
These parameters are fundamental in order to extrapolate information about the physical scenarios in which the mass transfer between the companion star and the compact object occur, and consequently to locate these systems in a well defined evolutionary scenario, that is predicted by the evolutionary theories for binary systems.
The study of the distribution of the arrival times of the dips allows to obtain an estimation of the orbital period of the system. In particular, the orbital ephemerides of these sources allow to obtain a distribution of the delays of the dip arrival times with respect to the adopted ephemerides, that in principle should be used to obtain corrections to the existing ephemerides, that allow to further constrain the orbital parameters.

In this thesis it is proposed a study of the timing properties of a sample of LMXB systems, that aims to extrapolate the orbital parameters of these system in order to understand which is the evolutive scenario in which they can be located.
The LMXB systems are introduced in chapter 1, where a particular importance will be given to the physics of the accretion. The theory of secular evolution for the binary systems will be introduced and obtained in chapter 2. This theory will be used in the next chapters to well locate the studied systems in a well defined evolutive scenario. In chapter 3 I introduce the most relevant physical processes that represent the cause of the observed spectra for these source. Finally, in the second part of the thesis I will report the results of the timing analysis performed

on a sample of LMXB systems.

The sources 4U 1323-619 and 4U 1254-690 are presented in chapter 4 and chapter 5 respectively. The analysis of the delays of the dips' arrival times allowed to obtain the orbital ephemerides and to increase the accuracy on the orbital period by one order of magnitude for both the sources. Furthermore, this analysis has been fundamental to evaluate a constrain on the orbital period derivative for these sources for the first time. From a comparative analysis performed between the observational data and the theory of secular evolution for binary systems we rescaled the previous estimations of the distances to the source, finding out that in both cases the mass accretion from the companion star onto the NS is conservative (that is no mass is lost from the system).

The system XB 1916-053, is introduced in chapter 6. Here the analysis of the distribution of the delays of the dip arrival times highlighted the evidence of a modulation that could be explained invoking the presence of a third body that orbits around the binary system. We find that the observational data are in agreement with the same level of statistical confidence both considering a conservative mass transfer scenario and a highly non conservative scenario in which about the 92% of the mass of the companion star is lost from the system. Then, the physical properties of the third body considerably differs according to the specific physical scenario that is adopted. In the case of a conservative mass transfer, we predict that the third body has a mass between 0.10 and 0.14 $M_\odot$, an orbital period of about 51 years and an eccentricity of the orbit of about 0.28. In the opposite case, we predict that the third body has a mass of 0.055 $M_\odot$ and an orbital period of about 26 years.

A spectral study of XB 1916-053 is also presented in chapter 7. In this work, we analyse both the spectra of the persistent emission and those of the dip. We find that the continuum contribution to the persistent spectrum can be described adopting a model that takes into account the comptonization of photons emitted by the neutron star surface, plus a multi-disk blackbody component that models the emission of the accretion disk. We find the system in a soft spectral state in all the observations we analysed. We confirm the presence of the Kα absorption lines of Fe XXV and Fe XXVI already reported in literature and in addition we detect the Kβ absorption lines of the same ions and the K absorption edge of O VIII.
On the other hand, we find that the dip spectrum can be described a gradual covering of the persistent spectrum by a cold and partially ionized bulk of matter in which the morphology continually changes in considerably short time scales of the order of some orbital periods.

We furthermore report in chapter 8 the timing analysis performed on the transient source MXB 1659-298. We find that the distribution of the delays of the dip arrival times with respect to the ephemeris in literature allow evaluate an orbital period derivative that could be explained only with a conspicuous loss of matter from the system. In addition these delays show a modulation that could be explained or invoking a coupling between the orbital motion and the shape of the companon star that should oblate due to an intense torque generated by an intense magnetic activity in the companion star, or equivalently with the presence of a third body orbiting around the binary system whose mass is dependent on the assumptions we make on the co-planarity of the orbit. We predict a mass of 22 M_J (Giovian masses) if we assume the co-planarity between the orbit of the third body and that of the binary system, or a lower limit of 21 M_J in the case of non co-planar orbits. If confirmed, the presence of a super-Jovian planet around a LMXB system should be the first ever detected.

Finally, in chapter 9 we report some preliminary results obtained from the analysis of a sample of Gamma-ray pulsars performed with the Fermi mission in the energy range between 20 MeV and 300 GeV. The work has been conducted with the collaboration of the high energy

astrophysics group of the Institut de Ciencies de l'Espai (ICE) of Barcelona (Spain) and consists of a temporal and phase-resolved spectral analysis aimed to detect (if present) a hard spectral component that extends beyond the cut-off energy exhibited in the catalogued spectra of these pulsars. The detection of this further component should be an indication of the presence of a pulsar wind nebula around these compact object that, interacting with the pulsar wind, could emit in the gamma rays, then contributing with a high energy tail to the observed spectrum of the source. From the analysis of the conveniently selected candidates pulsars we found a weak detection of a hard spectral component for the source PSR J0633+1746, even known with the name of Geminga. However, the work is still in process and we are currently investigating on the actual confirmation for this detection.

TABLE OF CONTENTS

CHAPTER 1

ACCRETION PHYSICS

1.1 Efficiency of Accretion

The mass transfer is the mechanism by explain the X-rays emission in systems containing compact objects. In a scenario in which the matter placed at large distance falling down onto the compact object, the variation of the gravitational energy potential of a mass m considered at a infinite distance is $\Delta E_g = GMm/R_*$, where M is the mass of the compact object, G is the gravitational constant and R_* is the radius of the compact star. Assuming that all the potential energy is converted in radiation, the luminosity associated to the accretion is given by:

$$L_{acc} = \frac{GM\dot{m}}{R_*} = \eta \dot{m} c^2, \tag{1.1}$$

where the parameter η allows to write the accretion luminosity in terms of rest energy of the accreted mass and is defined as $\eta = GM/(R_* c^2)$. This parameter represents the *efficiency of accretion* in terms of radiated luminosity and is strictly linked to the measure of the compactness of the system through the ratio between the mass of the compact object and its radius. This means that we expect a larger efficiency for more compact objects.

As an example, for a neutron star with a mass of 1.4 $M_\odot$ and $R_{NS} = 10^6$ cm, the accretion efficiency is of about $\eta \sim 0.2$, while for a white dwarf with a mass of 1 $M_\odot$ and a radius of $R_{WD} = 5 \times 10^8$ cm the accretion efficiency is $\eta \sim 3 \times 10^{-4}$.

On the other hands, black holes (hereafter BH), have not a solid surfaces and the so called *event horizon* delimits a region from which no matter or radiation can escape owing to the gravitational attraction. For a non-rotating BH this radius corresponds to the Schwarzschild radius defined as $R_S = 2GM/c^2$.

Assuming that the black hole is surrounded by an accretion disk, we should consider the last

stable orbit (LSO) of the accretion disk as radius of the star. The LSO is the smallest orbit around the central object for which a mass particle can persist in a steady orbital motion. This means that for smaller orbits the mass has to necessarily fall down into the BH, then accreting its mass. The LSO for a Schwarzschild BH is equal to $R_{LSO} = 3R_S$, and then the efficiency of accretion is $\eta \sim 0.12$.

1.2 Mass Accretion and Roche Potential

To understand how the mass moves from the companion star to the compact object we need to consider the total effective potential Φ felt by a test particle located in the binary system. This can be written as the sum of the gravitational potential associated with the two masses of the system, plus a term that origins from the centrifugal force. Here, I will assume that the stars are represented by point-like particles that have an orbital separation a follow circular orbits. This is not an strong assumption, owing to the fact that actually the orbits of such systems in which we have strong gravitational fields and relatively small orbital separations become circular in short time scales. In addition, to simplify the mathematical formulation, I will reference all the orbital parameters with respect to a Cartesian reference frame whose origin corresponds to the position of the mass M_1 and that rotates around the center of mass of the binary system with an angular speed Ω. With this assumption, the total effective potential of the binary system can be written as:

$$\Phi(x,y,z) = -\frac{GM_1}{R_1} - \frac{GM_2}{R_2} - \frac{1}{2}\Omega^2 R_3^2 \tag{1.2}$$

where $R_1 = \sqrt{x^2+y^2+z^2}$ and $R_2 = \sqrt{(x-a)^2+y^2+z^2}$ are the distances of M_1 and M_2 respectively from the origin of the reference frame, and R_3 is the distance of the rotation axis of the binary system with respect to the origin of the reference frame.
Using the the third Kepler law, we obtain that the orbital frequency of the period is related to the orbital separation of the two stars of the system as $\Omega = \sqrt{2GM/a^3}$, where M is the total mass of the system, that is $M = M_1 + M_2$. On the basis of all these considerations, a section of all the equipotential surfaces is shown in Figure 1.1. The unique surfaces that envelope the masses and are in contact through a point located along the direction that connects the positions of the two masses and between them are called Roche Lobes. The point that connects the two Roche lobes is called *Inner Lagrangian point* L_1 and is an unstable equilibrium point, in which the total net force felt by a test particle is null. In addition to the Inner Lagrangian point, there are other four points of equilibrium in the system that are reported in Figure 1.1.
The inner Lagrangian point plays a crucial role for the mass transfer mechanism. Indeed, when the donor star fills its own Roche lobe, the pressure gradient pushes the matter of the star envelope through L_1, then transferring material into the Roche lobe of the compact object. This mechanism is called *Roche Lobe Overflow (RLO)*.

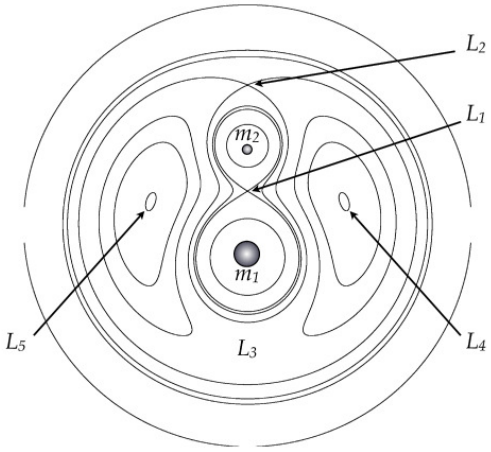

FIGURE 1.1. 2-dimensional representation of a binary system equipotential surfaces and of the Roche Lobe. The Equipotential surfaces. The five Lagrangian points are also reported.

For the particular binary systems that are studied in this thesis, the RLO can be caused by the fact that the system should actually experience a loss of angular momentum and a consequent shrinking of the orbital separation a (an explanation of the mechanisms that cause angular momentum loss from the system will be presented in chapter 2). The radius of the Roche lobe of a star is linearly linked to the orbital separation of the system through the formula Paczyński (1971):

$$R_{L2} = 0.46224\, a \left(\frac{m_2}{m_1 + m_2}\right)^{1/3}, \tag{1.3}$$

where m_1 and m_2 are the NS and companion star masses in units of solar masses and a is orbital separation of the binary system.
This means that when the orbital separation decreases the radius of the Roche lobe decreases at the same time until touching or or even becoming smaller than the radius of the secondary star itself. In this way the RLO regime could take place.

Once the secondary star has filled its Roche lobe, the matter can spill inside the Roche lobe of the compact object via the inner Lagrangian point. In the majority of the cases, L_1 does not corresponds with the center of mass of the binary system and then the matter falling into the compact object has an angular momentum. This causes that the material falls following a spiral path, and forms a disc while it is accreted owing to a redistribution of the angular momentum between the particles of the disc: the innermost particles that fall onto the surface of the NS transfer angular momentum to the outer particles. In this way we have a spread of the disc: a small amount of matter will carry all the angular moment outwards, while the rest of the mass,

losing angular momentum, falls onto the compact star (Papaloizou and Pringle, 1977; Lin and Papaloizou, 1979).

1.3 The Eddington limiting luminosity

The X-ray luminosity is a direct consequence of the accretion of material coming from the companion star onto the compact object. This luminosity, however, can not increase indefinitely. If the luminosity reaches sufficiently high levels, in fact, the radiation pressure opposes a force to the accreting matter that causes the inhibition of the accretion, with a consequent turning off of the observable radiation.
This limiting luminosity is called *Eddington luminosity* and represents an upper limit to the luminosity that a binary system can have in a steady state. This limit to the luminosity can be easily evaluated assuming that the accretion takes place in a steady state and with a spherical geometry. In addition, it is assumed that the accreting matter is mainly formed by hydrogen and that is fully ionised. Under this hypothesis the radiation pressure is provided mainly to the electrons through the Thomson scattering (the scattering cross-section for protons is a factor $(m_e/m_p)^2$ smaller). In addition, we also suppose that the net force acting on a electron-proton pair at a distance r from the source is null.
If we consider the balance of the acting forces onto a test particle, on the one hand we have the gravitational force that pushes the particles inward: $F_g = G m_p m_e / r^2 \approx G m_p / r^2$, where m_p and m_e are the masses of the proton and electron, respectively.
On the other hands, we must consider the outward radial force provided by the radiation to each electron. This force is given by the rate at which the electron absorbs momentum from the outcoming radiation. Then, if u is the radiant energy flux we have that $F_{rad} = \sigma_T \, u/c$. If the luminosity of the source is L, then by spherical symmetry we have that $u = L/4\pi r^2$.

Balancing the two forces we obtain:

$$\left(G M m_p - \frac{L \, \sigma_T}{4\pi \, c} \right) \frac{1}{r^2} = 0$$

and then the Eddington luminosity is:

$$L_E = \frac{4\pi G M m_p c}{\sigma_T}$$

This relation can be expressed in terms of the Schwarzschild radius R_S as :

$$L_E = \frac{2\pi R_S m_p c^3}{\sigma_T} = 1.3 \times 10^{38} \frac{M}{M_\odot} \text{ erg/s} \tag{1.4}$$

This is the limiting luminosity that every binary system should not exceed under the assumptions we made. However, some sources have been observed in the so called super Eddington

regime. This is because it is possible to exceed the Eddington limit by adopting different geometries of the accretion.
Assuming to have a NS accreting matter at the Eddington limit, we can evaluate its blackbody temperature in order to understand in which energy band the system emits.
The blackbody temperature can be found as:

$$T = \left(\frac{L_E}{4\pi R_{NS}^2 \sigma} \right)^{1/4} \simeq 2 \text{ keV} \tag{1.5}$$

where σ is the Stefan-Boltzmann constant and R_{NS} is the neutron star radius, whose typical value is of 10^6 cm. This temperature is actually a lower limit to the temperature of the system, owing to the fact that blackbody is the most efficient emission mechanism. This result suggests that binary systems containing compact objects will emit most of the energy in the X-ray range.

1.4 Effects of the Magnetic field of a NS on the accretion

Neutron Stars can have considerably strong magnetic fields **B** that can range between 10^8 and 10^{12} Gauss. For this reason, the plasma accreted onto the compact object interacts with the magnetic field of the neutron star and the effects of the magnetic induction could be considerably strong due to the high conductivity of the plasma. The main effect of this interaction is the *flux freezing* phenomenon, that produces important effects on the accretion dynamics of the system. The plasma is forced to move along the magnetic field lines as long as the magnetic energy density ϵ_B is greater that the energy density of the accreting plasma $\epsilon_{\dot{M}}$ at a certain distance from the NS. The limit case in which $\epsilon_{\dot{M}} \sim \epsilon_B$ is important in order to find out the limiting area in which the plasma is dominated by the magnetic field.
On the one hand,

$$\epsilon_B \sim \frac{B^2}{8\pi} \tag{1.6}$$

On the other hands, the energy density of the accreting matter is

$$\epsilon_{\dot{M}} = \frac{1}{2} \rho v_{ff}^2, \tag{1.7}$$

where v_{ff} is the free fall velocity of the matter, that is linked to the Keplerian velocity $v_K^2 = GM_1/R$ through the relation $v_{ff}^2 = 2v_K^2$. Imposing the continuity equation $\dot{M} = 4\pi R^2 \rho v_{ff}$ for an axis-symmetric geometry and taking into account that the magnetic momentum of a dipole is $\mu = BR^3$, imposing the equality between ϵ_B and $\epsilon_{\dot{M}}$, we find the value of the Alfvén radius:

$$R_A = 1 \times 10^6 \left(\frac{\mu}{10^{26} \, Gauss \, cm^3} \right)^{4/7} \left(\frac{\dot{M}}{\dot{M}_{Edd}} \right)^{-2/7} \left(\frac{M}{M_\odot} \right)^{-1/7} \text{ cm} \tag{1.8}$$

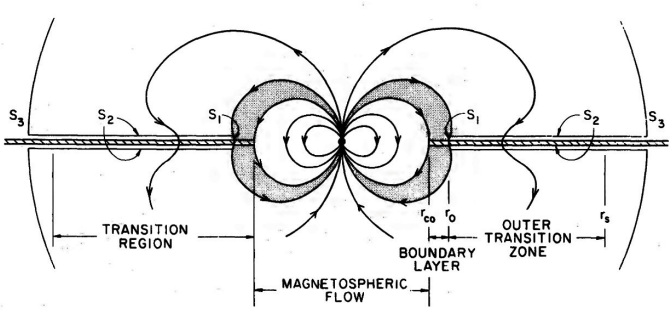

FIGURE 1.2. Innermost part of the accretion disc truncated by the interaction with the magnetic field of the NS. Credit: Ghosh and Lamb (1979).

The *Magnetospheric radius* R_m, that defines the area inside of which the plasma is dominated by the magnetic field, is equal to $R_m = b \times R_A$. The factor b is in the range 0.1 - 0.5 (see e.g. Ghosh and Lamb, 1979; Burderi et al., 1998, 2000) and depends on the details of the accretion processes, taking into account that the shape of the magnetosphere could be significantly distorted by the accretion disk.

On the basis of what has been explained, we can imagine the accretion disk of the compact object divided in two parts:

- the region between the accretion disk rim and R_m, in which the motion of the plasma follows Keplerian orbits
- the region between R_m and the NS surface, where the accreting plasma is funnelled into the magnetic field lines and moves towards the magnetic polar caps of the NS.

If the magnetic axis of the NS does not coincide with its rotation axis, and the magnetic axis points toward the direction of observation, we could observe X-ray periodical modulations of the light curves with a periodicity equal to the period of rotation of the neutron star. These features are called X-ray pulsations and the NSs showing this property are called *X-ray pulsars*.
A NS having a magnetic field of $B \sim 10^8$ Gauss and an accretion rate close to the Eddington limit, for eq. 1.8 has a magnetospheric radius of $R_m \sim 10^6$ cm $\sim R_{NS}$. This means that for these kind of systems (that will be introduced in the next section and that are known as Low Mass X-ray Binary systems or LMXB) the plasma of the accretion disc in theory should be uniformly accreted up to the surface of the neutron star.
Then, in these kind of systems the plasma forming the accretion disk follows Keplerian orbits in principle up to the surface of the NS and as a consequence of this for these systems it is not expected any evidence of X-ray pulsations.
The X-ray pulsations were not detected in LMXB systems before 1989, when the system SAXJ 1808-3658 was discovered and X-ray pulsations with a period of $P \sim 2.49$ ms were detected Wijnands and van der Klis (1998).

1.5 X-ray Binary Systems

Before the X-ray observations of the sky opened a new observational window to study the celestial phenomena, the astronomers were not used to observe transient events on considerably short time scales in the optical band. This perspective radically changed when the firsts satellites provided the firsts data in the X-rays band of many sources. The observations revealed a completely different appearance of the sky with an extended range of phenomena that occur also in time scales of few seconds. Simultaneously, the discovery of the radio pulsars gave the first evidences of the existence of these compact objects only theorized until that moment (Hewish et al., 1968), that has been recently confirmed with the detection of the gravitational wave GW170817 performed by the LIGO-Virgo collaboration with a significant candidate event consistent with the merging of two neutron stars (see Abbott et al., 2017a,b; Troja et al., 2017).
Today, we know that half of the stars in the Galaxy are binary systems in which one of the components is a compact stellar object. The secondary star is usually a star whose mass should range from fractions of the mass of the Sun (1 $M_\odot$) until several Solar masses. The components of the binary systems, could be close enough to influence their evolution between each other through a gravitational interaction and a consequent mass transfer from the donor star to the compact object. The X-ray binary systems are generally classified in two main classes: the Low Mass X-ray Binary systems (hereafter LMXB) and the High Mass X-ray Binary systems (hereafter HMXB). In the LMXBs the donor star is generally a late-type cold star with masses $< 1\ M_\odot$, whilst for the HMXB the donor star is generally a massive and luminous OB star (Verbunt, 1993).
A more specific classification has been done by Bradt and McClintock (1983) and it is based on the ratio between the X and optical luminosity:

$$\frac{L_X(2-10keV)}{L_{opt}(3000-7000\text{Å})}.$$

According to this classification, if this ratio is ≤ 10 the binary system is an HMXB system, whilst it a LMXB system if the ratio is $\gg 10$.
This classification based on the luminosity is also in agreement with a classification in terms of masses of the donor star. Actually, an early type massive star shows an optical luminosity that is dominant with respect to the X-ray luminosity. On the other hands, a low mass donor star contributes on the observed optical radiation only with the accretion disc and for this reason the X-ray emission is dominant.

Generally speaking the LMXBs are old objects, and when the compact object is a neutron star (hereafter NS) the magnetic field associated to this object is relatively weak ($10^8 - 10^9$; Frank et al., 1992). In these systems, the emission in the X-rays is essentially produced by the transfer of mass from the companion star onto the compact object through the process of the Roche Lobe overflow.

On the other hand, the HMXBs are younger objects (the life time of a OB star is of about 10^7 years) in which the NS have strong magnetic fields ($\sim 10^{12}$ G) and in which the mass transfer onto the neutron star is driven almost exclusively by the strong wind generated from the companion star itself.
The LMXB systems are the subjects of study of this thesis and will be presented more in particular In the following.

1.5.1 Low Mass X-ray Binary Systems

Low Mass X-ray binary systems are old objects ($> 10^9$ years) that show several observational features. The estimation of the age is also confirmed by the fact that some LMXBs are located inside globular clusters, that are between the oldest object in the Galaxy, and in which the formation of a binary system for gravitational capture is considerably fostered owing to the high concentration of stars. However, a big part of LMXBs is located along the galactic plane.
The donor star is usually a late-type main sequence star or a white dwarf whose stellar wind is considerably negligible with respect to the case of that of HMXBs. For this reason, a mandatory request for transferring mass from the donor star onto the compact object via RLO is that the system has to be enough compact. The optical luminosity of the companion star is generally lower than the optical luminosity of the accretion disc. The latter is generated by the reprocessed X-ray radiation that interacts with the matter forming the disc. The neutron stars hosted in these objects have magnetic fields ($\sim 10^8$ G) that are weaker with respect to those of HMXBs. This means that the accretion discs are truncated at lower distances from the neutron star, where the net flux is considerably higher. As a consequence of this, part of the matter forming the innermost disc is photoionized by the incoming radiation and a corona of hot electrons forms. The orbital periods of LMXBs until now detected can vary from 11 min up to 17 days. Many of these periods have been evaluated by taking the advantage of specific periodic phenomenology occurring in some of these systems: dips and eclipses. The periodic dips are localized decrements of the count-rate due to the partial coverage of the main central X-ray source by a cold but partially ionized bulge of matter that forms in the point in which the accretion stream coming from the companion star impact onto the outer rim of the accretion disc. As a consequence of the photoelectric absorption of the radiation by the bulge, we observe an increase in the low energy absorption and then a net hardening of the spectrum. The bulge rotates with the same orbital frequency of the binary system and for this reason the evaluation of the periodicity at which the dips occur corresponds to the real orbital period of the system. This implies that the bulge of opaque matter should be located at a fixed position in the overall geometry of the binary system. This condition is actually verified and could be explained considering how the circularization radius R_{circ} of the system evolves with respect to the orbital separation a of the system. R_{circ} is defined as the orbit in the accretion disk that has the lowest energy (is circular) and the same angular momentum of the plasma passing through the inner Lagrangian point L_1. The functional

form of R_{circ} is reported in Frank et al. (1992) and is:

$$R_{circ} = a\ (1+q)[0.5 - 0.227\ log(q)]^4,$$

where $q = M_2/M_1$ and a is the orbital separation of the system.
Assuming q as a constant quantity, then $\dot{R}_{circ} = \dot{a} \sim \dot{P_{orb}}$, where P_{orb} is the orbital period of the system. Then, the fact that the time derivative of the circularization radius scales as the orbital period derivative explains how the position of the bulge of matter located into the accretion disk rim can be considered fixed with respect to the geometry of the system. On the other hand, the size of the bulge could be different depending on the rate at which the matter is accreted from the companion star to the compact object. This could affect the shape of the observed dips and consequently also the estimation of the dip arrival times. However, in the case in which the studied sources show an approximately constant count-rate (as it occurs for the sources studied in this thesis) this issue can be neglected.

On the other hand, the eclipses are a direct consequence of the occultation of the central X-ray source by the companion star. However, this latter phenomenon is quite rare for LMXB, and when present, photons of all energies are shielded even if the central source is often only partially blocked. This is a cause of the modest size of the companion stars in LMXBs and due to the apparent extension of the X-ray source caused by the scattering of the X-rays in the ADC. On the basis of the arguments above reported, it is clear that there's a relation between the inclination angle i of the binary system (i.e. the angle between the perpendicular direction to the orbital plane and the direction of observation) and the observability of these phenomena. Actually, dips can be observed for inclination angles between 60°and 80°. On the other hands, eclipses generally occur for inclination angles between 75°and 80°Frank et al. (1987) (Figure 1.3). A feature that some of the LMXB systems could show is the occurrence of thermonuclear flashes due to the ignition of the H-rich material falling down onto the NS surface. These features are called *type I X-ray bursts* and have a recurrence that is strictly linked to the rate at which the matter is transferred onto the NS surface. Actually, the matter is collected onto the surface of the neutron star until when the strong pressure exerted on it due to the strong gravity reaches the ignition temperature of the specific chemical component. The type I X-ray bursts appear as sudden increases of the count-rate that reaches a peak. After this peak the count-rate exponentially decreases until when the persistent count-rate level is reached. Actually, during the decrease the neutron star surface is undergoing a cooling that corresponds to a softening of the burst spectrum Lewin et al. (1995). The bursts can be sporadic as well as periodic. The occurrence times vary between minutes to days. Only one source called *Rapid Burster* so far has shown the evidence of type I and type II bursts occurring in times of seconds (Lewin et al., 1976a). Type II bursts are peculiar bursts occurring in a rapid succession and due to a spasmodic increase of the accretion rate Lewin et al. (1995).

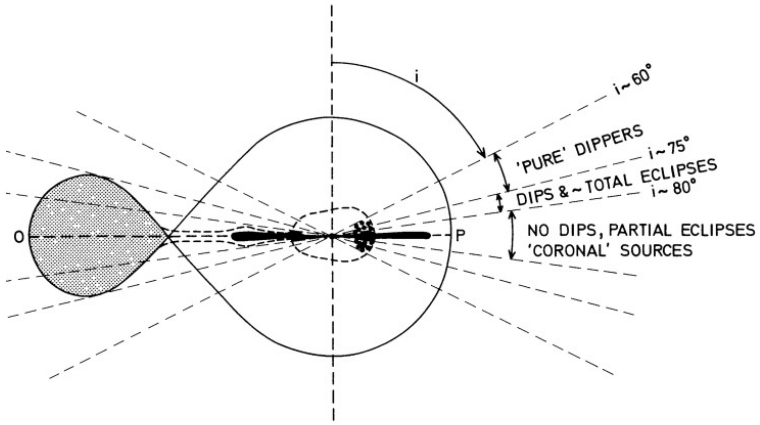

FIGURE 1.3. Ranges of inclinations corresponding to the types of modulations called dips and eclipses Frank et al. (1987).

Formation of LMXBs The LMXB systems can form essentially in two ways: the progenitor stars could be gravitationally bounded since the beginning or a star could be tidally captured by a compact object (see e.g. Fabian et al., 1975; Michaely and Perets, 2016).

In the first case, according to the evolutionary scenario depicted in Tauris and van den Heuvel (2006) and sketched in Figure 1.4, the progenitor stars forming the LMXB systems are detached massive OB stars in main sequence. This evolutive scenario can be applied to close binary systems and will be reported in its fundamental steps below.

- The most massive of the two stars (hereafter named "star 1") evolves more rapidly than the companion star ("star 2") and burns hydrogen in its core, producing helium. The process develops in a nuclear time scale (the most important time scales of the physical processes will be derived and explained in the next chapter).

- Once the star 1 has burnt the hydrogen, an helium core has formed in its interior. The star leaves the main sequence and starts to expand until it approaches its own Roche lobe. Then, a mass accretion via RLO starts and the mass is accreted onto the companion star 2 that has a lower mass and that is in main sequence. This step has a duration that is dictated by the thermal time scale of the donor star.

- At this stage it could happen that star 2 is engulfed by the extended envelope of its companion that removes angular momentum from the orbital motion. As a consequence of this the star 2 starts to spiral-in and the angular momentum losses are reprocessed into energy that

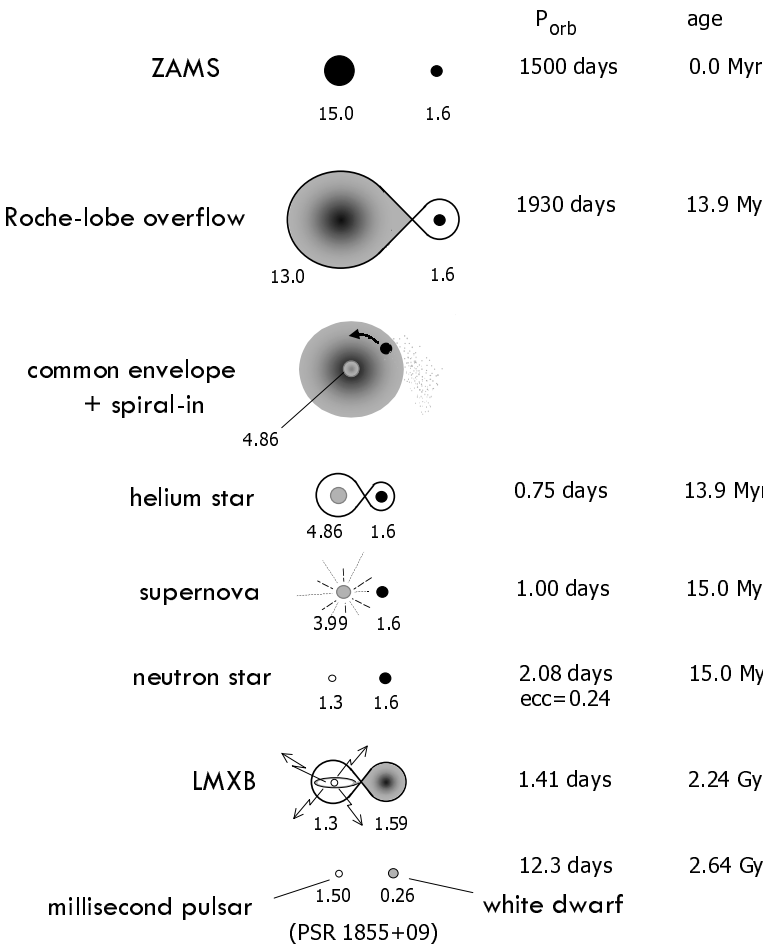

FIGURE 1.4. Evolution a binary system that explains the formation of LMXB systems Tauris and van den Heuvel (2006). Parameters governing the specific orbital angular momentum of ejected matter, the common envelope and spiral-in phase, the asymmetric supernova explosion and the stellar evolution of the naked helium star all have a large impact on the exact evolution. Parameters are given for a scenario leading to the formation of the observed binary millisecond pulsar PSR 1855+09. The stellar masses given are in solar units.

is released into the envelope. This process continues until when the envelope has stored enough energy to be ejected from the system. At the end of this step, only the helium core of the star 1 remains together with the star 2.

- The next step consider the formation of a NS. There are two possible scenarios for the formation of this compact object. The first scenario considers that the helium core of star 1, after the common envelope stage, explodes as a supernova. The supernova explosion is the critic point that decides if the binary system is going to survive or not. In this case, the system could remain bounded after the explosion owing to the fact that a sufficient amount

of matter has been lost from the system when the common envelope has been ejected, and if a properly oriented kick has been applied to the new born NS (Kalogera and Webbink, 1998).
Another scenario has been advanced by Whelan and Iben (1973) and considers that the helium star could evolve into a massive white dwarf avoiding the supernova explosion. A mass transfer could occur from star 2 to the white dwarf in case the star 2 evolving fills up its Roche lobe, or if some angular momentum losses occur into the system. As a consequence of the mass transfer the white dwarf should exceed the Chandrasekhar mass limit, then imploding with little mass losses and forming a NS.

- Then low mass star 2 evolving should fill up is Roche lobe and can transfer part of its matter onto the NS surface, then forming a LMXB system.

Anothe possible scenario for the formation of LMXB systems, instead, sees the system forming from the capture of a star by the gravitational field of the compact object.
This compact object forms as the result of a supernova explosion underwent from a massive star evolved until its final stage of life. As a consequence of the strong gravitational field generated by the compact object, a second star could be attracted and bounded to the first, forming a binary system. This scenario is more easily feasible when the compact object is located in a crowded area of space in which other stars accumulates. This is the case of the globular clusters. However, the majority of the known binary systems seem to be formed already bounded from the beginning Verbunt (1993).

CHAPTER 2

THEORY OF SECULAR EVOLUTION FOR BINARY SYSTEMS

Now we know that the X-ray binary systems bright thanks to the mass transfer, that starts owing to the normal evolution of the companion star itself. The angular momentum balance into the system, that can also include possible losses, dictates the behaviour of the system in to the future and the so called *Theory of secular evolution* predicts how the binary system will evolve on the basis of physical observables.
To facilitate the discussion on the evolutionary scenarios of X-ray binaries, before addressing the steps that will lead us to obtain the theory of secular evolution, we first describe some of the fundamental ingredients that will be useful in the subsequent discussion, i.e. the relevant time scales of the most important processed that generally occur in the binary systems.

2.1 Time Scales

In the following subsections I will obtain the expressions for the nuclear, thermal and dynamic time scales. In the next chapters it will be shown how these times, and in particular a comparison between them, is fundamental in order to understand how a binary system evolves when the dynamic response of the donor star to the mass transfer is taken into account.

2.1.1 Nuclear time scale

The proton–proton chain reaction (p-p chain), is the dominant energy source in stars with masses up to about the mass of the Sun and it is efficient during the permanence of the star in the main sequence. The nuclear time scale is the time that a star takes to move a significant distance to the right of the initial main sequence in the HR diagram, owing to the general expansion of the outer

layers associated with the increasing composition inhomogeneity caused by the transmutation of hydrogen to helium (Morton, 1960).
More in particular, this time scale can be thought as the ratio between the energy produced by nuclear reactions in the p-p chain, and the dissipation of the produced energy, i.e:

$$\tau_n = \frac{E_{ntot}}{L}, \tag{2.1}$$

where $Entot$ is the energy produced by the nuclear reactions and L is the luminosity.
The energy produced in the transformation of one atom of hydrogen into one atom of helium is $0.007mc^2$ (Bradt, 2014), then we can assume that

$$E_{ntot} = 0.007\, mc^2\, n_p, \tag{2.2}$$

where n_p is the number of protons. On the other hands, stars move off the main sequence when the central 10% of their mass has been converted into helium (Longair, 2011). For this reason, we can estimate

$$n_p m_p = 0.1\, M_{tot} \Longrightarrow n_p = 0.1\, \frac{M_{tot}}{m_p}, \tag{2.3}$$

where $m_p = 1.66 \times 10^{-24}\, g$ is the mass of the proton.
Using Equation 2.3 in Equation 2.2, we can re-arrange Equation 2.1 with few algebraic steps, obtaining the expression of the nuclear time scale:

$$\tau_{nucl} \sim 10^{10}\, \frac{M}{M_\odot} \frac{L_{sun}}{L} \text{ years} \tag{2.4}$$

This relation shows that the estimated life for the sun in main sequence is of 10^{10} years. For example, if the mass is 30 $M_\odot$ one obtains $\tau_{nucl} \sim 2 \times 10^6$ years. The reason for the shorter time scale is that the stellar luminosity strongly increases for higher masses.

2.1.2 Thermal time scale

If a star deviates from thermal equilibrium, it will secularly expand or contract until the equilibrium is established. The typical time to reach equilibrium is called *thermal or Kelvin Helmholtz time scale* and it is defined as the ratio between the thermal energy of the star and the luminosity, i.e.

$$\tau_{KH} = \frac{E_{th}}{L}, \tag{2.5}$$

It is easily evaluated if we think that the mean thermal energy is generated by the mean kinetic motion of the particle forming the plasma: $< E_{th} > \simeq < E_K >$, where $< E_{th} >$ is the mean thermal energy and $< E_K >$ is the kinetic energy of the particles. For the *Virial theorem* $< E_K > = \frac{1}{2} < E_p >$, where $< E_p >$ is the potential energy of the star. Then, we have:

$$< E_{th} > \simeq \frac{1}{2} < E_p >, \tag{2.6}$$

where the potential energy of the star can be calculated as:

$$< E_p > = \int_0^R \frac{GM}{r}\, dm, \tag{2.7}$$

where R is the radius of the star, M is its mass and $dm = (4\pi r^2 dr)\rho$, where r is a radial coordinate over which we have to integrate. With some algebraic steps, Equation 2.5 returns the expression for the Kelvin Helmholtz time scale:

$$\tau_{KH} = 2.5 \times 10^7 \left(\frac{M}{M_\odot}\right)^2 \left(\frac{L}{L_\odot}\right)^{-1} \left(\frac{R}{R_\odot}\right)^{-1} \text{ years} \tag{2.8}$$

Substituting the solar values in this equation, we realize that for the Sun $\tau_{KH} \sim 10^8$ years. In other words, if the nuclear energy source were to turn off today, it would take about 10^8 years for the Sun to restore the perturbed hydrostatic equilibrium.
This time scale is by a factor of 100 smaller that the nuclear time scale.

2.1.3 Dynamic time scale

The dynamical time scale τ_{dyn} is the time for a star to collapse inward under the influence of gravity with no opposing forces such as pressure.
If we assume a spherical star in which an element of matter of mass m is free to move with an azimuthal velocity v_ϕ around the surface of the star, we have that:

$$\tau_{dyn} = \frac{2\pi R}{v_\phi}, \tag{2.9}$$

where R is the star radius. The gravitational force acting on the mass m is the centripetal force:

$$\frac{m\, v_\phi^2}{R} = \frac{GMm}{R^2} \Rightarrow v_\phi = \sqrt{\frac{GM}{R}} \tag{2.10}$$

Substituting Equation 2.10 into Equation 2.9, we find the expression of the dynamical time scale, i.e.:

$$\tau_{dyn} = 0.07 \left(\frac{M_\odot}{M}\right)^{1/2} \left(\frac{R}{R_\odot}\right)^{3/2} \text{ days} \tag{2.11}$$

If we substitute the solar values in this relation, we find that $\tau_{dyn} \sim 0.04$ days, i.e. approximately 1 hour. Actually, this time is much more shorter than the thermal time, meaning that in the case of mass loss the Sun reaches the hydrostatic equilibrium before of approaching the thermal equilibrium.

2.2 The total angular momentum of a binary system

Before any speculation about the evolutive aspect of the binary systems it is essential to obtain the expression of the total angular momentum.
This can be written as:

$$J_b = \left(M_1 r_1^2 + M_2 r_2^2\right) \omega, \tag{2.12}$$

where M_1 and M_2 are the mass of the neutron star and of the companion star respectively, r_i is the distance of each mass from the center of mass of the binary system, and ω is the angular velocity of the two bodies.
To be more precise, we should add to these two terms also the angular momenta contributions due to the rotation of each mass around its own rotational axis. However these terms are absolutely negligible for the reasons I am going to present.
In a generic binary system the companion star undergoes the effect of the tidal force due to the gravitational field of the compact object. This force is proportional to a^{-3} and for this reason the more compact is the system the more important is this effect. In a relatively short period the orbital motion of the star is synchronized and the rotational period ends to be equal to the orbital period of the system. The, the contribution due to the angular momentum of spin for the secondary star is negligible.
On the other hands, the angular momentum for a spinning NS of mass M_1 is equal to $J_{NS} = M_1 R_1^2 \omega_{NS}$, where R_1 is the star radius whose typical value is $10^6\ cm$ and ω_{NS} is the angular velocity of the NS rotating around its axis: we can assume a typical value of 400 Hz. With these values, we obtain an angular momentum for the spin of about $3 \times 10^{48}\ g\ cm^2\ s^{-1}$.
Using the third Kepler law and taking into account that $r_1 = a\ \dfrac{M_2}{M_1 + M_2}$ and $r_2 = a\ \dfrac{M_1}{M_1 + M_2}$, we can write Equation 2.12 as:

$$J_{ORB} = M_1 M_2 \sqrt{\frac{Ga}{M_1 + M_2}}, \tag{2.13}$$

This is the total angular momentum of the binary system as a function of the orbital parameters. For a NS of mass $M_1 = 1.4\ M_\odot$ and $M_2 = M_\odot$, and assuming an orbital period of 1 hour, we evaluate an angular momentum $J_b \sim 4.7 \times 10^{51}\ g\ cm^2\ s^{-1}$, that is actually of three order of magnitudes higher.

2.3 Conservative Mass Transfer

In the case in which the mass is transferred onto the neutron star surface without losses out of the system, we speak of conservative mass transfer. In this case we can well establish that $M_1 + M_2 = cost$, that is equal to the condition:

$$\dot{M}_1 = -\dot{M}_2 \tag{2.14}$$

In order to find out a relation that describes how the system evolves as a function of the physical properties of the two stars, we can take into account the total orbital angular momentum of the system (Equation 2.13) applying a logarithmic differentiation (see Appendix A).
We obtain:

$$\frac{\dot{J}_b}{J_b} = \frac{\dot{M}_1}{M_1} + \frac{\dot{M}_2}{M_2} + \frac{1}{2}\frac{\dot{a}}{a} - \frac{1}{2}\frac{\dot{M}_1 + \dot{M}_2}{M_1 + M_2} \tag{2.15}$$

If we apply the condition of mass conservation (Equation 2.14) to Equation 2.15, and we re-arrange the obtained equation, at the end we have one relation that relates the time derivative of the orbital separation of the system with the masses of the stars:

$$\frac{\dot{a}}{a} = -2\left(\frac{M_1 - M_2}{M_1 + M_2}\right)\frac{\dot{M}_2}{M_2} \tag{2.16}$$

In this equation $\dot{M}_2$ is negative, being the mass of the companion star that is transferred onto the NS. For this reason the sign of the time derivative of the orbital separation is strongly dependent on the quantity $M_1 - M_2$.
Thus,

- if $M_1 > M_2 \Longrightarrow \dot{a} > 0$
- if $M_1 < M_2 \Longrightarrow \dot{a} < 0$

This actually means that if the donor star is more massive than the NS, assuming a conservative mass transfer we should expect that the binary system shrinks. On the other hands, the system should broaden.
In the majority of the circumstances, however, we deals with LMXBs having donor stars with smaller masses with respect to that of the NS, and emitting a persistent radiation in the X-ray band. Then, according to this result, we should expect that the system broadens, and as a consequence the mass transfer should stop due to the enlargement of the Roche Lobe radius that is proportional to the orbital separation (see Equation 1.3).
In order to explain the emission that we observe, as a result of the RLO, then we have to realize the presence of channels of angular momentum losses, that will be shown in the next section, where a detailed evalaution of the theory of secular evolution for binary systems will be obtained.

2.4 Non-conservative Mass Transfer

The total angular momentum of a binary system consists of the contributions of three channels of angular momentum: the angular momentum due to the rotation of the companion star around its axis, the same contribution due to the companion star and finally the orbital angular momentum of the system itself. Then,

$$J_{TOT} = J_{NS} + J_{COMP} + J_{ORB} = J_{ORB}\left\{1 + \frac{J_{NS}}{J_{ORB}} + \frac{J_{COMP}}{J_{ORB}}\right\} \tag{2.17}$$

On the one hand, we can write the companion star angular momentum J_{COMP} as:

$$J_{COMP} = I_{COMP}\,\omega_{COMP} = \frac{2}{5}\chi M_2 R_2^2 \omega \tag{2.18}$$

Assuming that the donor star has filled its own Roche lobe and transfers part of its mass onto the NS surface as a cause of the observable X-ray emission, we can impose that the radius of the star is equal to the radius of its Roche Lobe $R_2 = R_{L2}$, where the radius R_{L2} of the Roche Lobe is given by Equation 1.3 (Paczyński, 1971).
Then,

$$J_{COMP} = 4.6 \times 10^{50}\,\chi\, m_1^{5/3} q^{5/3} P_{2h}^{1/3}, \tag{2.19}$$

where χ is an adimensional factor that takes into account the fact that the momentum of inertia of the companion star actually slightly deviates from that of a spheric star, due to the fact that the Roche lobe is not perfectly spherical. Thus, using the expression of the total orbital angular momentum J_{ORB} of the binary system (Equation 2.13), we obtain:

$$\begin{aligned} \frac{J_{COMP}}{J_{ORB}} &= \frac{4.6 \times 10^{50}\,\chi\, m_1^{5/3} q^{5/3} P_{2h}^{1/3}}{55 \times 10^{51} m_1^{5/3} \dfrac{q}{(1+q)^{1/3}} P_{2h}^{1/3}} = \\ &= 8.4 \times 10^{-2} \chi q^{2/3} (1+q)^{1/3}, \end{aligned} \tag{2.20}$$

where $q = M_2/M_1$.

On the other hand, the contribution J_{NS} to the angular momentum of the system is given by:

$$\begin{aligned} J_{NS} &= I_{NS}\,\omega_{NS} = \\ &= 2\pi\, I_{NS} P_{NSpin}^{-1} = \\ &= 2\pi\, 10^{45}\, I_{45}\, P_{-3}^{-1}\, 10^3 = \\ &= 6.28 \times 10^{48}\, I_{45}\, P_{-3}^{-1} \end{aligned} \tag{2.21}$$

In this relation I_{45} is the moment of inertia of the NS in units of 10^{45} and P_{-3} is the spin period of the NS in units of 10^{-3}.
For this reason, as done before, we calculate:

$$\begin{aligned} \frac{J_{NS}}{J_{ORB}} &= \frac{6.28 \times 10^{48}\, I_{45}\, P_{-3}^{-1}}{55 \times 10^{51} m_1^{5/3} \dfrac{q}{(1+q)^{1/3}} P_{2h}^{1/3}} = \\ &= 1.1 \times 10^{-3}\, I_{45} P_{-3}^{-1} m_1^{-5/3} q^{-1} (1+q)^{1/3} P_{2h}^{-1/3} \end{aligned} \tag{2.22}$$

Substituting Equation 2.20 and 2.22 into Equation 2.17 we have that:

$$
\begin{aligned}
&J_{TOT} = \mu J_{ORB} \\
&\quad \text{where} \\
&\mu = 1.1 \times 10^{-3}\, I_{45} P_{-3}^{-1} m_1^{-5/3} q^{-1} (1+q)^{1/3} P_{2h}^{-1/3} + \\
&\quad + 8.4 \times 10^{-2} \chi q^{2/3} (1+q)^{1/3}
\end{aligned} \tag{2.23}
$$

If we differentiate logarithmically the Equation 2.23, we obtain

$$
\frac{\Delta J_{TOT}}{J_{TOT}} = \frac{\Delta J_{ORB}}{J_{ORB}} + \frac{\Delta \mu}{\mu} \tag{2.24}
$$

Differentiating logarithmically the relation for J_{ORB} in 2.13 we have:

$$
\frac{\Delta J_{ORB}}{J_{ORB}} = -\frac{1}{3}\frac{\Delta \Omega}{\Omega} - \frac{1}{3}\frac{\Delta (M_1+M_2)}{M_1+M_2} + \frac{\Delta M_1}{M_1} + \frac{\Delta M_2}{M_2} \tag{2.25}
$$

and thus,

$$
\frac{\Delta J_{TOT}}{J_{TOT}} = -\frac{1}{3}\frac{\Delta (M_1+M_2)}{M_1+M_2} + \frac{\Delta M_1}{M_1} + \frac{\Delta M_2}{M_2} + \frac{\Delta \mu}{\mu} \tag{2.26}
$$

This time, we want to assume a more realistic scenario for the analysis of the evolution of the binary system with respect to the conservative case seen in section 2.3. For this reason we assume now that a fraction of matter β is accreted onto the NS surface, while the remaining fraction $(1-\beta)$ is lost from the system. This can be written with the following relation:

$$
\dot{M}_1 = -\beta \dot{M}_2 \tag{2.27}
$$

Here we should notice that the term $\dot{M}_2$ is intrinsically negative due to the fact that the donor star is loosing part of its mass.
On the basis of Equation 2.27 we can write that

$$
\begin{aligned}
\Delta (M_1+M_2) &= \left(\dot{M}_1 + \dot{M}_2\right)\Delta t = \\
&= -\beta \dot{M}_2 \Delta t + \dot{M}_2 \Delta t = \dot{M}_2 (1-\beta)\Delta t
\end{aligned} \tag{2.28}
$$

Taking into account that we can write $M_1 + M_2 = M_2\left(\frac{1+q}{q}\right)$, we have that:

$$
\frac{\Delta (M_1+M_2)}{M_1+M_2} = \dot{M}_2 (1-\beta)\Delta t \frac{1}{M_2}\frac{q}{1+q} \tag{2.29}
$$

Furthermore, we can also write:

$$
\begin{aligned}
\frac{\Delta M_1}{M_1} = \frac{\Delta M_1}{M_2}\frac{M_2}{M_1} = q\frac{\dot{M}_1}{M_2}\Delta t = \\
= -\beta q \frac{\dot{M}_2}{M_2}\Delta t
\end{aligned} \tag{2.30}
$$

and

$$\frac{\Delta M_2}{M_2} = \frac{\dot{M}_2}{M_2}\Delta t \tag{2.31}$$

With these relations in our hands, we can substitute Equation 2.29, 2.30 and 2.31 into Equation 2.26, thus obtaining after some algebraic steps that:

$$\frac{\Delta J_{TOT}}{J_{TOT}} = -\frac{1}{3}\frac{\Delta\Omega}{\Omega} + \left[1 - \beta q - \frac{1}{3}(1-\beta)\frac{q}{(1+q)}\right]\frac{\dot{M}_2}{M_2}\Delta t + \frac{\Delta\mu}{\mu} \tag{2.32}$$

Generally, the angular momentum of a binary system is not preserved and some specific phenomena could contribute to the loss of angular momentum from the binary system. These phenomena are the mass loss (ML) from the system occurring during the accretion of matter from the donor star to the NS, the emission of gravitational waves (GR) and the magnetic braking (MB) of the companion star due to the coupling of the stellar wind with the magnetic field lines of the star itself.
Then we can write that

$$\frac{\Delta J_{TOT}}{J_{TOT}} = \frac{1}{J_{TOT}}(\Delta J_{ML} + \Delta J_{GR} + \Delta J_{MB}) = \frac{1}{\mu}\frac{(\Delta J_{ML} + \Delta J_{GR} + \Delta J_{MB})}{J_{ORB}} \tag{2.33}$$

where we applied the relation $J_{TOT} = \mu J_{ORB}$ found in Equation 2.23.
Substituting Equation 2.32 into Equation 2.33, then we have:

$$-\frac{1}{3}\frac{\dot{\Omega}}{\Omega}\Delta t + \left[1 - \beta q - \frac{1}{3}(1-\beta)\frac{q}{(1+q)}\right]\frac{\dot{M}_2}{M_2}\Delta t + \frac{\Delta\mu}{\mu} = \frac{1}{\mu}\left[\frac{\Delta J_{ML}}{J_{ORB}} + \frac{\Delta J_{GR}}{J_{ORB}} + \frac{\Delta J_{MB}}{J_{ORB}}\right] \tag{2.34}$$

Now we have to evaluate and parameterize each contribution to the angular momentum loss from the system. The meaning and the evaluation of each term will be described in the subsequent subsections.

Mass Loss One of the possible channels of angular momentum loss as anticipated before could be the possible loss of matter from the system. It is not unusual, indeed, that part of the mass from the donor is expelled out of the system instead of being accreted onto the NS (see e.g. Burderi et al., 2010; Marino et al., 2017, to name but a few).
We can describe the mass expelled from the system as

$$M_{lj} = \dot{M}_2\Delta t(1-\beta) \tag{2.35}$$

The variation of the angular momentum of the system can be written as:

$$\Delta J_{ML} = M_{lj} l_{lj} = \dot{M}_2 \Delta t (1-\beta) l_{lj}, \tag{2.36}$$

where l_j is the angular momentum per unity of mass lost from the system.
If we assume that the mass leaves the system from the position of the inner Lagrangian point, the specific angular momentum of the mass leaving the system can be written as

$$l_{RL2} = d^2 \Omega, \tag{2.37}$$

where d is the distance of the inner Lagrangian point with respect to the position x_{CM} of the center of mass of the binary system. If we consider a Cartesian reference frame in which the NS occupies the origin and the donor star is at a distance a from the NS, then we can evaluate the value of d as:

$$\begin{aligned} d =& a - x_{CM} = \\ &= a - R_{L2} - x_{CM} = \\ &= a - R_{L2} - a\frac{M_2}{M_1+M_2} = \\ &= a - 0.46224\, a \left(\frac{q}{1+q}\right)^{1/3} - a\frac{M_2}{M_1+M_2} = \\ d =& a\left[1 - \frac{q}{1+q} - 0.46224\left(\frac{q}{1+q}\right)^{1/3}\right] \end{aligned} \tag{2.38}$$

where we expressed the position of the center of mass x_{CM} as a function of the orbital separation and of the masses in the system, i.e.

$$x_{CM} = a\frac{M_2}{M_1+M_2} \tag{2.39}$$

Substituting Equation 2.38 into Equation 2.37 we obtain that

$$l_{RL2} = d^2\Omega = a^2\left[1 - \frac{q}{1+q} - 0.46\left(\frac{q}{1+q}\right)^{1/3}\right]^2 \Omega$$

For the III Kepler law $a^3 = \dfrac{G(M_1+M_2)}{\Omega^2}$, then:

$$l_{RL2} = (GM_1)^{2/3}\Omega^{-1/3}\left[\frac{1}{(1+q)^{2/3}} - 0.46 q^{1/3}\right]^2 \tag{2.40}$$

Remembering the value of the mass M_{lj} expelled from the system (see Equation 2.35) and assuming that the value of the specific angular momentum l_{lj} of the mass expelled is proportional to a constant parameter, i.e.

$$l_{lj} = \alpha l_{RL2} \qquad \text{where } \alpha = \left(\frac{d}{a - x_{CM}}\right)^2 \tag{2.41}$$

then, the variation of the angular momentum of the system in Equation 2.36 can be written as:

$$\Delta J_{ML} = M_{lj} l_{lj} = \\ = \dot{M}_2 \Delta t (1-\beta) \times \alpha (G M_1)^{2/3} \Omega^{-1/3} \left[\frac{1}{(1+q)^{2/3}} - 0.46 q^{1/3}\right]^2 = \tag{2.42}$$

Taking into account the value of J_{ORB} in Equation 2.13, after some simple algebraic rearrangements we obtain the contribution of the mass loss to the angular momentum loss from the system, that is:

$$\frac{\Delta J_{ML}}{J_{ORB}} = \alpha (1-\beta) \left[\frac{1}{(1+q)^{1/2}} - 0.46 q^{1/3} (1+q)^{1/6}\right]^2 \frac{\dot{M}_2}{M_2} \Delta t \tag{2.43}$$

Gravitational Radiation Similarly to an accelerated electric charge that generates electromagnetic waves, an accelerated mass generates gravitational waves. These waves transport angular momentum and consequently they represent one possible source of angular momentum loss from the binary system.
The expression of Landau and Lifshitz (1975) for the angular momentum loss due to gravitational radiation is:

$$\frac{\Delta J_{GR}}{J_{ORB}} = -\frac{32}{5} \frac{G^3}{c^5} M_1 M_2 \frac{(M_1 + M_2)}{a^4} \Delta t \tag{2.44}$$

From this relation it is evident that this contribution is strongly dependent on the compactness of the system. Given the masses of the two stars, the shorter is the orbital separation, the bigger is the loss of angular momentum due to the generation of gravitational waves.
Using the third Kepler law we can express the orbital separation a as a function of the masses and of the orbital rotation frequency Ω, then obtaining the final expression of the gravitational radiation contribution to the angular momentum loss from the system, that is:

$$\frac{\Delta J_{GR}}{J_{ORB}} = -\frac{32}{5} (G\, M_1)^{5/3} \frac{1}{c^5} \frac{q}{(1+q)^{1/3}} \Omega^{8/3} \Delta t \tag{2.45}$$

Magnetic Braking It can occur that part of the mass of the donor star is lost from the system instead of accreting onto the neutron star surface. This plasma interacts with the magnetic field of the companion star and freezes the magnetic lines on it. This causes a braking of the companion star and a consequent transfer of the angular momentum from the star to the plasma that leaves the system.
Verbunt and Zwaan (1981) find that for G-stars in main sequence the equatorial velocity v_e can be expressed as

$$v_e = \omega_2 R_2 \simeq f \times 10^{14}\, t^{-2} \text{ cm/s}, \tag{2.46}$$

where ω_2 is the orbital frequency of the star, R_2 is its radius and f is an a-dimensional parameter that can assume two different values:

$$f = \begin{cases} 0.73 & \text{(Skumanich, 1972)} \\ 1.78 & \text{(Smith et al., 1979)} \end{cases} \tag{2.47}$$

The angular momentum of the secondary star of mass M_2 is:

$$J_2 = k^2\, M_2 R_2^2 \omega_2, \tag{2.48}$$

where for cool stars in Main sequence $k^2 \simeq 0.1$ (Verbunt and Zwaan, 1981). Then, combining Equation 2.46 with Equation 2.48, we have that:

$$J_2 = k^2\, M_2 R_2^2 \left[\frac{f}{R_2} \times 10^{14}\, t^{-1/2} \right]. \tag{2.49}$$

Differentiating this relation and taking into account Equation 2.46 we have:

$$\dot{J}_{2_{MB}} = -\frac{1}{2 \times 10^{28}} k^2\, M_2 R_2^4 f^{-2}\, \omega_2^3. \tag{2.50}$$

Taking into account that the total orbital angular momentum of a binary system is equal to

$$J_{ORB} = M_1 M_2 \left(\frac{G^2}{\Omega (M_1 + M_2)} \right)^{1/3}, \tag{2.51}$$

after a bit of simple algebraic steps we can write Equation 2.50 as:

$$\frac{\dot{J_{MB}}}{J_{ORB}} = -\frac{k^2}{2\, f^2 \times 10^{28}} \frac{R_2^4}{(G\, M_1)^{2/3}} (1+q)^{1/3} \omega_2^3 \Omega^{1/3}, \tag{2.52}$$

where the gravitational constant $G = 6.67 \times 10^{-8}\, g^{-1}\, cm^3\, s^{-2}$, Ω is the orbital frequency of the binary system and M_1 is the mass of the compact object and $q = M_2/M_1$.
Here, we realistically assume that the binary system is tidally locked, this meaning that the orbital frequency of the binary system Ω is equal to the frequency ω_2 at which the donor star spins around its rotation axis. In addition, we apply the RLO regime condition, owing to the fact that detecting the binary system in the X-rays actually means that the secondary star has filled its own Roche Lobe and transfers mass to the compact object. For this reason $R_2 = R_{L2}$, where

$$R_{L2} = 0.46224\, a \left(\frac{m_2}{m_1 + m_2}\right)^{1/3}, \tag{2.53}$$

where m_1 and m_2 are the NS and companion star masses in units of solar masses and a is orbital separation of the binary system.
The orbital separation of the system can be written with respect to the orbital frequency of the binary system through the third Kepler law:

$$a = \left[\frac{G(M_1 + M_2)}{\Omega^2}\right]^{1/3} \tag{2.54}$$

Applying these conditions in Equation 2.52, we obtain the magnetic braking contribution to the angular momentum loss from the binary system, that is :

$$\frac{\Delta J_{MB}}{J_{ORB}} = -2.24 \times 10^{-30} \left(\frac{k}{f}\right)^2 q^{4/3} (1+q)^{1/3} (GM_1\Omega)^{2/3}\, \Delta t \tag{2.55}$$

Once that every contribution to angular momentum loss from the system has been evaluated, we can reconsider Equation 2.34. However, before we have to take into account that in the expression of μ of Equation 2.23 the second and third terms are usually negligible, and for this reason we can consider that $\mu \sim 1$ and then $\Delta\mu = 0$. On the basis of this, and on the basis of the results found in the previous paragraphs, we have that Equation 2.34 can be written as:

$$\begin{aligned} &-\frac{1}{3}\frac{\dot{\Omega}}{\Omega} + \left[1 - \beta q - \frac{1}{3}(1-\beta)\frac{q}{(1+q)}\right]\frac{\dot{M}_2}{M_2} = \\ &= \alpha(1-\beta)\left[\frac{1}{(1+q)^{1/2}} - 0.46 q^{1/3}(1+q)^{1/6}\right]^2 \frac{\dot{M}_2}{M_2} + \\ &-\frac{32}{5}\frac{q}{(1+q)^{1/3}}\frac{1}{c^5}(GM_1)^{5/3}\Omega^{8/3} - 2.24 \times 10^{30}\left(\frac{k}{f}\right)^2 (GM_1)^{2/3}\Omega^{2/3} q^{4/3}(1+q)^{1/3} \end{aligned} \tag{2.56}$$

Rearranging conveniently this relation we obtain that:

$$\frac{\dot{\Omega}}{\Omega} = 3\left\{g(\alpha,\beta,q)\frac{\dot{M}_2}{M_2} + 3.6 \times 10^{-17} m_1^{5/3} P_{2h}^{-8/3} \frac{q}{1+q}^{1/3}\left[1 + 8.4 k_{0.1}^2 f^{-2} m_1^{-1} P_{2h}^2 q^{1/3}(1+q)^{2/3}\right]\right\} \tag{2.57}$$

where

$$g(\alpha,\beta,q)=1-\beta q-\frac{(1-\beta)}{3}\frac{q}{(1+q)}-\alpha(1-\beta)\left[\frac{1}{(1+q)^{1/2}}-0.46q^{1/3}(1+q)^{1/6}\right]^2$$

Here the mass accretion rate $\dot{M}_2$ is in units of s^{-1}. In order to have this quantity in units of solar masses per year we should consider that

$$\frac{\dot{M}_2}{M_2}=\frac{\dot{m}_{-8}}{m_2}\times\frac{10^{-8}}{3.15\times10^7}=3.2\times10^{-16}\frac{\dot{m}_{-8}}{m_2}, \tag{2.58}$$

where $\dot{m}_{-8}$ is the mass accretion rate in units of 10^{-8} $M_\odot yr^{-1}$.
In this way, we can re-write Equation 2.57 as

$$\begin{aligned}\frac{\dot{\Omega}}{\Omega}=&3\left\{g(\alpha,\beta,q)3.17\times10^{-16}\frac{\dot{m_{-8}}}{m_2}+\right.\\&\left.+6.4\times10^{-17}m_1^{5/3}P_{2h}^{-8/3}\frac{q}{(1+q)^{1/3}}\left[1+8.4k_{0.1}^2f^{-2}m_1^{-1}P_{2h}^2q^{1/3}(1+q)^{2/3}\right]\right\}\end{aligned} \tag{2.59}$$

On the other hands, we can write the following relation:

$$\frac{\dot{\Omega}}{\Omega}=-\frac{\dot{P_{ORB}}}{P_{ORB}}=-\frac{10^{-12}}{7200}\frac{\dot{P_{-12}}}{P_{2h}}=-1.39\times10^{-16}\frac{\dot{P_{-12}}}{P_{2h}} \tag{2.60}$$

that substituted into Equation 2.59 gives a final relation that links the orbital period derivative of the system with the mass accretion rate, the orbital period and the masses of the stars that make up the system, that is:

$$\begin{aligned}\frac{\dot{P_{-12}}}{P_{2h}}=&6.8\left\{g(\alpha,\beta,q)q^{-1}m_1^{-1}(-\dot{m_{-8}})+\right.\\&\left.-0.2m_1^{5/3}P_{2h}^{-8/3}\frac{q}{(1+q)^{1/3}}\left[1+8.4k_{0.1}^2f^{-2}m_1^{-1}P_{2h}^2q^{1/3}(1+q)^{2/3}\right]\right\}\end{aligned} \tag{2.61}$$

2.5 Dynamical Evolution

So far, no information about the dynamical response of the companion star has been inserted in the exposition of the theory of the secular evolution. Assuming that the companion star fills its own Roche lobe, we can assume in first approximation that $R_2=R_{L2}$, that is:

$$\dot{R}_2=\dot{R}_{L2} \tag{2.62}$$

Taking into account the relation of Paczyński (1971) for the radius R_{L2} of the Roche Lobe (see Equation 2.54) and performing a logarithmic differentiation, using the third Kepler law we have:

$$\frac{\dot{R_{L2}}}{R_{L2}} = \frac{1}{3}\frac{\dot{M_2}}{M_2} - \frac{2}{3}\frac{\dot{\Omega}}{\Omega} \tag{2.63}$$

Assuming that the companion star is in main sequence, we can assume that the mass-radius relation assumes the general functional form

$$R_2 \propto M_2^n, \tag{2.64}$$

where n is a empirical power that depends on the internal structure of the companion star (see Neece, 1984, for more details).
If we perform a logarithmic derivative on Equation 2.64, we obtain the following relation

$$\frac{\dot{R}_2}{R_2} = n\,\frac{\dot{M}_2}{M_2} \tag{2.65}$$

Substituting the Equation 2.62 and 2.63 we obtain

$$n\,\frac{\dot{M}_2}{M_2} = \frac{1}{3}\frac{\dot{M}_2}{M_2} - \frac{2}{3}\frac{\dot{\Omega}}{\Omega}$$

and then

$$-\frac{\dot{\Omega}}{\Omega} = \left(\frac{3n-1}{2}\right)\frac{\dot{M}_2}{M_2} \tag{2.66}$$

but

$$\frac{\dot{\Omega}}{\Omega} = -\frac{\dot{P}}{P}$$

thus Equation 2.66 becomes:

$$\frac{\dot{P_{ORB}}}{P_{ORB}} = \left(\frac{3n-1}{2}\right)\frac{\dot{M}_2}{M_2} \tag{2.67}$$

In addition, we can take into account Equation 2.60 and 2.58 to obtain

$$\frac{\dot{P_{12}}}{P_{2h}} = 2.28\left(\frac{1-3n}{2}\right)\left(-\frac{\dot{m}_{-8}}{m_2}\right) \tag{2.68}$$

Expressing this equation as a function of m_1, that is the mass of the compact object in units of solar masses, we have:

$$q^{-1}m_1^{-1}(-\dot{m}_{-8}) = 0.44\left(\frac{1-3n}{2}\right)^{-1}\frac{\dot{P_{12}}}{P_{2h}} \tag{2.69}$$

This expression should be substituted in the final relation we found for the non-dynamical theory of secular evolution, that is Equation 2.61. With this substitution we obtain:

$$2.28\left(\frac{1-3n}{2}\right)q^{-1}m_1^{-1}(-\dot{m}_{-8}) = 6.8\left\{g(\alpha,\beta,q)q^{-1}m_1^{-1}(-\dot{m}_{-8})+ \right. \\ \left. -0.2m_1^{5/3}P_{2h}^{-8/3}\frac{q}{(1+q)^{1/3}}\left[1+8.4k_{0.1}^2 f^{-2}m_1^{-1}P_{2h}^2 q^{1/3}(1+q)^{2/3}\right]\right\} \tag{2.70}$$

rearranging this equation, after some simple algebraic steps we obtain the fundamental equation that describe how a binary system evolves taking into account the dynamical response of the companion star to the mass transfer, that is:

$$\frac{\dot{P}_{-12}}{P_{2h}} = \left[\frac{1/3-n}{2g(\alpha,\beta,q)-1/3+n}\right]1.37\,q(1+q)^{-1/3}m_1^{5/3}P_{2h}^{-8/3}\times \\ \times\left[1+8.4k_{0.1}^2 f^{-2}m_1^{-1}P_{2h}^2 q^{1/3}(1+q)^{2/3}\right] \tag{2.71}$$

where, as seen in the previous section,

$$g(\alpha,\beta,q) = 1-\beta q-\frac{(1-\beta)}{3}\frac{q}{(1+q)}-\alpha(1-\beta)\left[\frac{1}{(1+q)^{1/2}}-0.46q^{1/3}(1+q)^{1/6}\right]^2$$

This value of $g(\alpha,\beta,q)$ has been obtained assuming that the mass transferred from the donor star to the compact object is lost from the inner Lagrangian point.
In the case in which the mass is lost from the position of the companion star, on the other hand, the Equation 2.43 that describes the contribution of the angular momentum loss due to the mass lost from the system has the form

$$\frac{\Delta J_{ML}}{J_{ORB}} = \alpha(1-\beta)(1+q)^{-1/2}\frac{\dot{M}_2}{M_2}\Delta t \tag{2.72}$$

that, performing the same procedure shown so far gives the following value of $g(\alpha,\beta,q)$:

$$g(\alpha,\beta,q) = 1-\beta q-\frac{(1-\beta)}{3}\frac{q}{(1+q)}-\alpha(1-\beta)\frac{1}{(1+q)} = 1-\beta q-\frac{1-\beta}{1+q}\left[\frac{1}{3}q+\alpha\right]$$

Here it is importatn to notice that all these results have been obtained assuming the condition of the RLO regime and the generic mass-radius relation for main sequence stars $R_2 \propto M_2^n$.

Mass accretion time-scale On the basis of all these considerations, a mass accretion time-scale can be defined and added to the time scales previously reported in section 2.1. It is defined as the typical time that the secondary star spends to transfer its mass onto the compact object. It is defined as:

$$\tau_{\dot{M}_2} = \frac{M_2}{\dot{M}_2} \tag{2.73}$$

where applying Equation 2.67 we obtain:

$$\tau_{\dot{M}_2} = \frac{M_2}{\dot{M}_2} = \frac{3n-1}{2}\frac{P_{ORB}}{\dot{P}_{ORB}}. \tag{2.74}$$

Here, the sign has been changed owing to the fact that $\dot{m}_2$ is intrinsically negative, owing to the mass transfer. In addition, applying Equation 2.58 and 2.60 to this relation we obtain:

$$\tau_{\dot{M}_2} = \frac{1}{3.17}\frac{m_2}{\dot{m}_{-8}} = \frac{1-3n}{2}\frac{1}{1.39}\frac{P_{2h}}{\dot{P}_{-12}} \tag{2.75}$$

thus,

$$\tau_{\dot{M}_2} = \frac{M_2}{\dot{M}_2} = 1.1\times 10^8\,(1-3n)\frac{P_{2h}}{\dot{P}_{-12}} \tag{2.76}$$

CHAPTER 3

PHYSICS OF BINARY SYSTEMS

In Chapter 1 it has been spoken about the presence of an accretion disk and of a corona of hot electrons surrounding the central object and part of the accretion disk in LMXB systems. The presence of these features in the LMXB systems are the main cause of the spectral components that explain the observed spectra of these systems in the X-rays. In this chapter I will report a discussion on the main theories that explain the morphology and the observed spectra of the accretion disk and of the corona. Subsequently, will be discussed the main mechanisms of interaction between the radiation and matter that contribute to generate the spectra of these sources.

3.1 The main component of a LMXB system

Usually, a broad band X-ray spectrum of a binary system is characterised by the presence of a soft black body component at low energies and by one hard component at high energies. This last component is generated by the interaction of the soft photons coming from the accretion disk with the electron cloud that forms the corona. As a result of the Compton scattering of the photons with the hotter electrons of the corona the photons energy is shifted at higher energies and this leads to the generation of an hard spectral component. This component is usually fitted with a power law with a high energy cut off, when the source is in the so called "hard state", or alternatively with a blackbody law, when it is in the so called "soft state". In addition to these spectral components, some spectra can also present the contribution of a reflection component, generated by the interaction between a part of the comptonized photons and the colder material of the accretion disk. All the mentioned spectral component are reported in Figure 3.1 as an example.

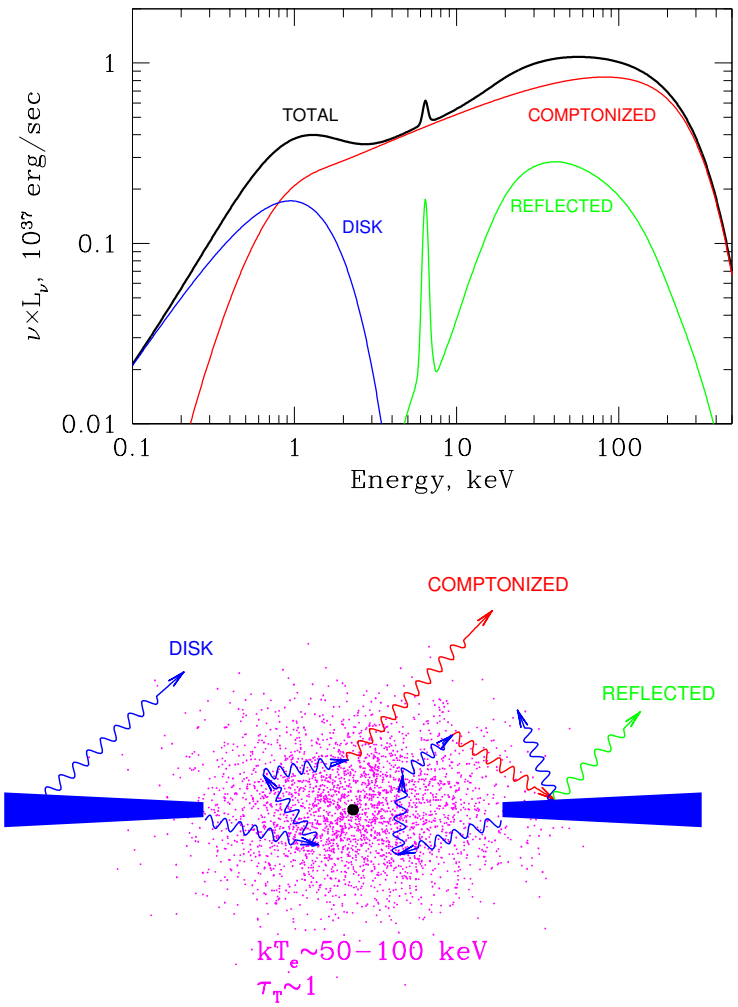

FIGURE 3.1. The three main components of the X-ray emission from an accreting black hole (top) and a plausible geometry of the accretion flow in the hard spectral state (bottom) (Gilfanov, 2010).

3.1.1 The Accretion disk

Many solutions of the accretion flow in the accretion disk around compact objects in binary systems exist. The main difference between the existing models is the efficiency of the radiative processes.

Standard Model of Accretion disks The most accepted model describing the accretion disk of compact sources is the so called *Standard Model of Accretion disks* developed by Pringle and Rees (1972) and Shakura (1973). This model belongs to the family of the efficient radiative models

and assumes a disk geometrically thin but optically thick in which we can assume that $H << r$, where H is the thickness of the disk and r is its radius. The accretion disk is assumed to emit as a blackbody source. This is owing to the fact that the friction forces due to the viscosity of the plasma of the disk produce heat that is locally radiated. However, the plasma is optically thick and as a consequence of this it is cooled efficiently and its temperature approaches that of a blackbody.

The viscosity of the plasma, is also important to describe the structure of the accretion disk and has an important role to understand how the angular momentum is transferred in it. The quantity that describes how much a plasma is turbulent is the Reynolds number R, defined as $R \sim \frac{L^2}{\nu T} \sim \frac{V L}{T}$, where L, V and T are the typical dimensions of the length, velocity and time for the accretion flow and ν is the kinematic velocity. If $R < 1$ we consider a plasma non turbulent. Otherwise, if $R > 10^3$ the plasma is considered turbulent (see e.g. Landau and Lifshitz, 1975; Feynman, 1965). If we take into account the case of an accretion disk around a neutron star, $R \sim 10^{12}$ (Longair, 2011). Then, the generation of turbulence within the disc results in a turbulent viscosity and the transport of momentum is associated with the motion of turbulent eddies in the plasma. But we should also take into account that there is also a magnetic field in the disc and this provides a further means of transporting momentum on a large scale.

Shakura (1973) introduced the following prescription for the turbulent viscosity, $\nu = \alpha\, v_s H$, where v_s is the speed of sound in the disc and H is its scale height. The turbulent eddies must have dimension less than the scale height of the disc and the turn-over velocities must be less than the speed of sound. The advantage of this formalism is that analytic solutions can be found for the structure of thin accretion discs in terms of the single parameter α – these solutions are often referred to as α-discs.

In order to understand how the disk emits, we have to consider that the disc is optically thick to radiation and that there are sufficient scatterings to ensure that the emission can be approximated as blackbody radiation at each point in the disc. Here, we will consider that the disk radiates from both the the upper and lower surface and that the heat is dissipated between r and $r + \Delta r$. The total luminosity of a thick accretion disk formed due to the accretion around a NS and with no mass losses from the system can be written in first approximation as $L = \frac{G\dot{m}M_1}{r}$. The black-body emission from the surfaces of the accretion disk is $L = 2\sigma T^4 \times 2\pi r \Delta r$, where σ is the Stefan-Boltzmann constant. Then, with these considerations one can find that

$$\sigma T^4 = \frac{G\dot{m}M_1}{4\pi r^3} \Longrightarrow T = \left(\frac{G\dot{m}M_1}{4\pi r^3 \sigma}\right)^{1/4}, \tag{3.1}$$

where M_1 is the mass of the accreting object, r the radial distance from the center and $\dot{m} = 2\pi r v_r \Sigma$ is the mass transfer rate through the optically thick disk of surface density Σ, at velocity v_r (Frank et al., 1992). Equation 3.1 shows that the temperature of the disk increases towards the centre as $T \propto r^{-3/4}$. The total intensity of the disk is

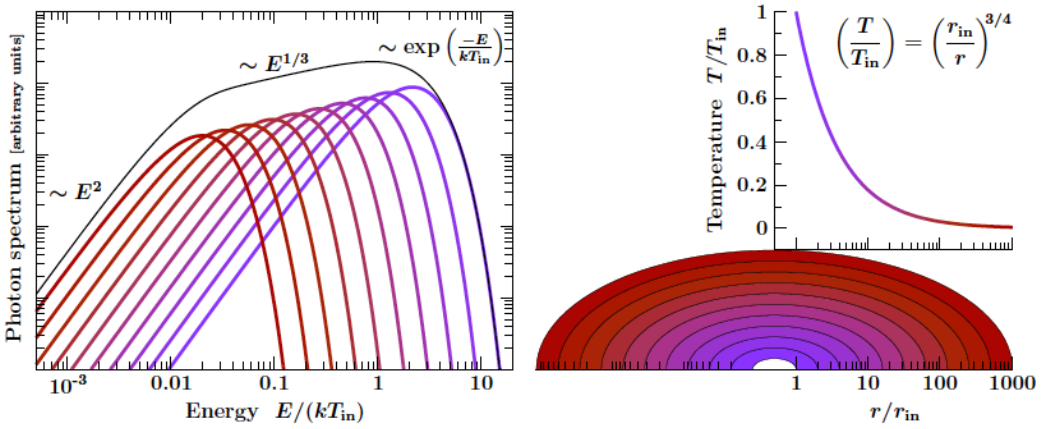

FIGURE 3.2. Spectrum resulting from the superposition of black-body components originating from individual rings in the optically-thick accretion disk (Hanke, 2011).

$$I(\nu) = \int 2\pi r\, B(\nu, T)\, dr, \tag{3.2}$$

where the function $B(\nu, T)$ is the Plank distribution that is

$$B(\nu, T) = \frac{2h\nu^3}{c^2} \frac{1}{(e^{h\nu/K_B T} - 1)}, \tag{3.3}$$

where ν is the frequency of the photons, c is the speed of light in the vacuum, h is Plank constant, K_B is the Boltzmann constant and T is the temperature of the blackbody.
Solving the integral, we notice that the spectrum of the thick accretion disk has the form $I(\nu) \propto r^{1/3}$ (Frank et al., 1992).
In addition we can consider the following limit cases:

- $h\nu << K_B T \Longrightarrow B(\nu, T) \sim \frac{2\nu^2 K_B T}{c^2}$ (Rayleigh-Jeans approximation)
- $h\nu >> K_B T \Longrightarrow B(\nu, T) \sim \frac{2h\nu^3}{c^2} e^{-h\nu/K_B T}$ (Wien approximation)

The typical spectral component due to the accretion disk contribution, is a blackbody which peaks at about 1 keV if we assume a typical temperature of $T = 10^7\, K$ for the disk. Alternatively, the emission could also be fitted by a multi-color blackbody which approximates the black body emission at each radius of the disk (see Figure 3.2).

Accretion disk dominated by advection The Standard model of accretion disk, cannot explain all the observed spectral energy distributions (SED), and in particular some cases in

which the sources show low accretion (Esin et al., 1996). The advection dominated accretion flow (ADAF) model (Ichimaru, 1977) consists in a disk whose innermost part is optically thin. As a consequence of this, in the region of the disk closer to the compact object, the accretion flow is replaced by a hot flow of plasma that forms a sort of corona. At the origin of this component there is the impossibility of the flow to be cooled efficiently by the radiative processes. In this way, the viscous energy collects gradually under the form of thermal energy that is advected radially towards the compact object (Narayan, 1996). In the case of a NS, this energy is transferred onto the surface and from there it is radiated away.
The regimes in which we can expect ADAF are essentially two. In the first case, the mass accretion rate $\dot{M}$ and the optical depth τ are high. In this case the radiation is trapped into the plasma (Abramowicz et al., 1998).
In the second case, $\dot{M}$ is low and the plasma is optically thin ($\tau < 1$) (Narayan and Yi, 1994; Abramowicz et al., 1995). In addition, the plasma could be strongly magnetized and as a consequence of this, the magnetic field could play an important role into the structure of the hot flow (Balbus and Hawley, 1998; Shadmehri and Khajenabi, 2005; Abbassi et al., 2008).

3.1.2 The Corona

The corona is composed of hot and energetic electrons, being the plasma at considerably high temperatures ($T > 10^9\,K$) in proximity of the central object. Indeed, on the contrary of the ADAF case in which the inner accretion disk is replaced by the corona of electrons, here the corona surrounds the compact object and can also envelope part of the inner accretion disk.
Between the models that describe the formation of an hot corona around LMXBs, the most accreditable are two. The first model describes the corona as a result of an evaporation process of hot matter from the disk surface (Shakura and Sunyaev, 1973). On the other hands, in another model is contemplated the possibility that the accretion disk could transfer part of its energy to an external thin layer of its atmosphere, then forming the corona (Liang and Price, 1977). Additionally, the magnetic field anchored on the accretion disk could generate an additional source of energy via the process of the magnetic reconnection of the magnetic loop in which part of the plasma of the accretion disk is confined, exactly as observed in the Solar Corona (Galeev et al., 1979; Golub and Pasachoff, 2009; Reale, 2010).

Accretion disk corona The simplest model that reproduce the spectra of some X-ray binary systems is the model of the Accretion Disk Corona. According to this model, the accretion disk extends close to the compact object, and a hot gas of electrons surrounds the disk with a plane-parallel symmetry.

Truncated Disk Model In this model the thick accretion disk is replaced by an inner ADAF, and for this reason the corona is a continuation of the accretion disk. The main feature of this model is that it takes into account the spectral state of the source as will be shown in the next chapters. Indeed, on the basis of the value of the accretion rate $\dot{M}$, we can distinguish between two cases. In the first case, $\dot{M}$ is low and then the ADAF is radiatively inefficient: this results in an accretion disk truncated at higher distances from the compact object. On the other hands, if $\dot{M}$ is high, the ADAF becomes radiatively efficient and the system increases its luminosity. In this case the ADAF shrinks and the inner part of the accretion disk approaches the NS surface.

3.2 Physical processes in the Corona and Accretion disk

Generally speaking, the main processes that intervene in the interaction between the the photons and matter are the photoelectric absorption, the Compton scattering and the electron-positron pair production. These processes are in competition between each other and the cooling efficiency is the main factor that decides the prevalence of one among the others. However, the cooling efficiency depends on the probability of interaction and then, it is strictly linked to the cross section of the process.
In this chapter, I report the main mechanisms that are involved in the production of the components that describe the spectra of LMXB system.

3.2.1 Compton Scattering and Comptonization

If we look at the broad band spectra of many LMXB systems, we can notice the presence of an hard component that usually follows a power law trend with an high energy cut off. The physical process that is responsible for this component is the interaction between the photons generated into the central part of the binary systems with the hot corona of electrons that surrounds this area. The Compton scattering between photons and electrons is the cause of this spectral component at high energies. In particular we will see that the contribution of many orders of scattering describes the observed spectral shape. For this reason it is fundamental to understand which are the processes at the basis of the observed spectral features. Now, I am going to describe the formal theory of the Compton scattering.

Direct Compton Scattering In this process in the interaction are involved photons and electrons. If we have photons with an energy $h\nu \ll m_e c^2$ the so called Thomson scattering occurs. The scattering is elastic and well describable by the classical physics. In this case the photon is scattered in a random direction after the interaction with the electron, without loosing energy.
If $h\nu \geq m_e c^2$, instead, the interaction is not elastic anymore and quantum effects contribute to modify the scattering for example making the cross section of the interaction strongly dependent

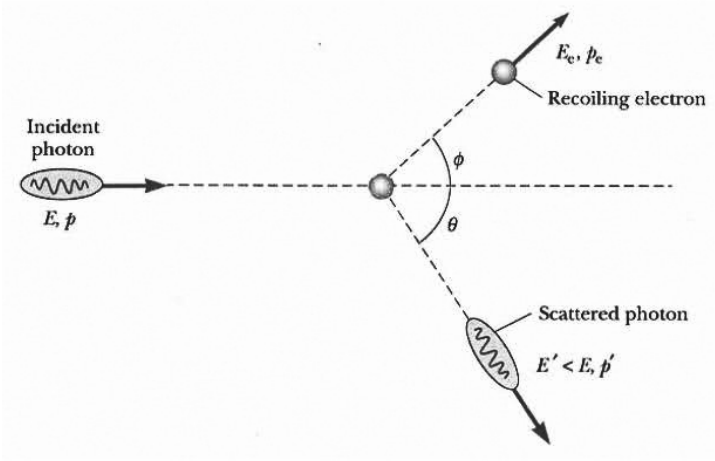

FIGURE 3.3. Schematic representation of the Scattering Compton process.

from the scattering angle θ (regime of Klein-Nishina).
In order to obtain the relation that relates the final energy of the photon to the scattering angle and to its initial energy, we have to imagine a single interaction between a photon of energy $h\nu$ and initial momentum $h\nu/c$ and an electron initially not in motion, having a rest energy of $m_e c^2$. The product of the interaction will be a photon having an energy $h\nu' \neq h\nu$ and a momentum $h\nu'/c$. In addition, the electron will be in motion with a recoil energy of γmc^2 and a momentum $p_e = \gamma\beta m_e c = \gamma m_e c$. Here β is defined as $\beta = v/c$, where v is the recoil speed and γ is the Lorentz factor that is equal to $\gamma = (1-\beta^2)^{-1/2}$. In Figure 3.3 a schematic representation of the process is reported.
If we take into account the relations of the conservation of energy and momentum for the electron and photon respectively in the process, treating these as particles we have the following set of equations:

$$h\nu + m_e c^2 = h\nu' + \gamma m_e c^2 \tag{3.4}$$

$$\frac{h\nu}{c} = \frac{h\nu'}{c}\, cos(\theta) + \gamma\beta m_e c\, cos(\phi) \tag{3.5}$$

$$0 = \frac{h\nu'}{c}\, sin(\theta) + \gamma\beta m_e c\, sin(\phi) \tag{3.6}$$

In these equations the initial values of the energy and momenta are in the left, whilst the final ones are on the right. Here ϕ is the electron scattering angle.
Combining the equations above it is possible to obtain the relation

$$h\nu' = \frac{h\nu}{1 + \frac{h\nu}{m_e c^2}(1 - cos(\theta))}. \tag{3.7}$$

From this relation it is clear that when the energy of the photon $h\nu$ starts to become of the same order of the rest energy of the electron $m_e c^2$, then after the interaction the photon undergoes a change of energy, that depends on the scattering angle θ. In particular, the case $h\nu << m_e c^2$ contemplates the Thomson scattering limit, where the photon does not substantially change its energy after the interaction. According to the angle dependence of Equation 3.7, the decrease in energy is larger when the photon is back scattered ($\theta \sim \pi$). On the other hands, for $h\nu >> m_e c^2$ a back scattered photon has an energy $m_e c^2/2$ independently by its initial energy. In terms of wavelengths, Equation 3.7 can be written as

$$\lambda' - \lambda = \frac{h}{m_e c^2}(1 - cos(\theta)), \tag{3.8}$$

where the quantity $h/m_e c^2 = 2.426 \times 10^{-12}\ m$ is the Compton wavelength λ_C. Here it is possible to notice that the fractional wavelength shift is high when the incoming photon energy is so high to be of the same order of λ_C. For longer wavelengths (i.e for $h\nu << m_e c^2$) the scattering is almost elastic.
The probability that a photon is scattered through a given solid angle $d\omega$ is not constant, and then the Compton scattering is not isotropic. As a matter of fact, the probability of scattering is higher when the photon interacts with the electron wit $\theta = 0$. In particular, the differential cross section for the Compton scattering is the Klein-Nishina formula (Klein and Nishina, 1929):

$$\frac{d\sigma_{KN}}{d\Omega} = \frac{3}{16\pi}\sigma_T \left(\frac{\nu'}{\nu}\right)^2 \left(\frac{\nu}{\nu'} + \frac{\nu'}{\nu} - sin(\theta)^2\right), \tag{3.9}$$

where

$$\sigma_T = \frac{8}{3}\pi r_0^2 = \frac{8}{3}\pi \left(\frac{e^2}{m_e c^2}\right)^2 = 6.652 \times 10^{-25}\ \text{cm}^2 \tag{3.10}$$

is the classical Thomson cross section and $r_0 = \frac{e^2}{m_e c^2} = 2.82 \times 10^{-13}$ cm is the classical electron radius.
The fact that in Equation 3.10 we see that the Thomson cross section is proportional to m_e^{-1} is important to understand why the electrons are the favourite particles for the Compton scattering. Indeed, σ_T is higher for the electrons owing to the fact that their mass is a factor $(m_e/m_p) \sim 10^{-7}$ smaller than the mass of the protons.

From Equation 3.9 it is possible to derive the formula of the total cross section for the Compton scattering integrating over all the directions. We obtain (Rybicki and Lightman, 1979):

$$\sigma_{KN} = \frac{3}{4}\sigma_T \left[\frac{1+x}{x^3} \left(\frac{2x(1+x)}{1+2x} - ln(1+2x) \right) + \frac{1}{2x} ln(1+2x) - \frac{1+3x}{(1+2x)^2} \right], \tag{3.11}$$

where $x = h\nu/(m_e c^2)$.
From this equation it is possible to derive the classical and relativistic limits:

$$\sigma_{KN} = \sigma_T \left(1 - 2x + \frac{26x^2}{5} + ... \right) \quad \text{for } x << 1 \tag{3.12}$$

$$\sigma_{KN} = \frac{3}{8}\sigma_T \left(ln(2x) + \frac{1}{2}. \right) \quad \text{for } x >> 1 \tag{3.13}$$

From Equation 3.13 it is possible to notice how the Compton scattering becomes less efficient for high photon energies, due to the fact that the cross section is reduced. On the other hands, for low photon energies, the Klein-Nishina formula reduces to the Thomson cross section.

Inverse Compton Scattering In a more realistic scenario, the electrons are not at rest being continually irradiated by the emission coming from the innermost and hotter part of the system. As a consequence of this, the previous regime represents only a part of the dissertation about Compton scattering. In the scenario just mentioned, indeed, the electron could also transfer part of its energy to the colliding photon. To distinguish this process to the previous one we call this process *Inverse Compton Scattering*. The energy of the scattered photon can be easily obtained setting the frame in which the electron is at rest as a reference frame. In this way, the collision is seen in the rest frame and we can use Equation 3.7. Applying the Lorentz transformations to obtain relations in the observer frame, we can evaluate the energy of the scattered photon. If the energy of the incoming photon is smaller than $m_e c^2$ the Thomson regime is considered, whilst in the opposite case the Klein-Nishina regime is applied. However, in both the regimes the photons gain energy from the electrons after the collision.
If we assume an isotropic distribution of photons, the power emitted by an electron during the process of the Compton scattering is (Rybicki and Lightman, 1979):

$$P_{Comp} = \frac{4}{3}\sigma_T c U_{rad} \gamma^2 \beta^2, \tag{3.14}$$

where γ is the Lorentz factor, $\beta = v/c$ and U_{rad} is the energy density of the radiation of the photon field before the scattering.
The relative gain of energy of the photon during the process is:

$$\frac{\Delta E}{E} = \frac{P_{Comp}}{\sigma_T c U_{rad}} = \frac{4}{3}\gamma^2\beta^2 \tag{3.15}$$

From the last relation it is possible to notice that after the Compton scattering the photon energy is increased by a factor of γ^2. This is the reason because the inverse Compton scattering is very important to create high energy photons.

Thermal Comptonization A distribution of photons that transit through a cloud of hot electrons undergoes inverse Compton scattering. If the electrons are more energetic of the incoming photons and the optical depth is sufficiently high, these transfer part of their energy to the photons with the collisions, then increasing the final energy of the photons. If the plasma is thin enough, processes like the bremsstrahlung do not dominate, then the Compton processes dominate the observed spectra of the X-ray sources, and the spectrum is said Comptonized.

From Equation 3.7, for non-relativistic electrons and photons with energy $h\nu << m_e c^2$ we can see that the relative change of energy of the photons is

$$\frac{\Delta E}{E} = \frac{h\nu}{m_e c^2}(1 - cos(\theta)) \tag{3.16}$$

If we adopt the reference frame of the electron at rest, the scattering is Thomson, that is symmetric around the incident direction of the photons. The average energy increase of the electrons per direct Compton scattering is then

$$\frac{\Delta E}{E} = \frac{h\nu}{m_e c^2} \quad \text{for } h\nu << m_e c^2 \tag{3.17}$$

On the other hands, if the energy is transferred from the electrons to the photons, the average energy increase of the photons per inverse Compton scattering is

$$\frac{\Delta E}{E} = \frac{4}{3}\beta^2 \quad \text{for } h\nu >> m_e c^2 \tag{3.18}$$

In a realistic scenario, however, the photons that pass through a cloud of electrons do not undergo a unique scattering process, but depending on the optical depth τ of the cloud they could be scattered several times. When the process of multiple scattering is due to a thermal or quasi-thermal[1] distribution of electrons, then we refer to this process as *Thermal Comptonization*. These electrons have a thermal distribution of the velocity at temperature T_e, that is

[1] A quasi-thermal distribution of electrons is a distribution that shows a clear peak, but that is not purely Maxellian.

$$\frac{3}{2}K_B T_e = \frac{1}{2}m_e v^2, \tag{3.19}$$

where v is the typical velocity of the electrons. Then we have:

$$\frac{\Delta E}{E} = \frac{4K_B T_e}{m_e c^2} \quad \text{for } h\nu << m_e c^2 \tag{3.20}$$

The equation that describes the average energy change of a photon per collision, for both the high and low frequecies is

$$\frac{\Delta E}{E} = \frac{4K_B T_e - h\nu}{m_e c^2} \tag{3.21}$$

From this equation we see that for $4K_B T_e = h\nu$ there is no transfer of energy between the electron and the photon and this is the case that is called *Compton Saturation*. Instead, the Inverse Compton Scattering is contemplated for $h\nu < 4K_B T_e$, that is the case in which the electron transfer energy to the photon. Finally, the case in which the photon transfer energy to the electron (Direct Compton) is included by assuming $h\nu > 4K_B T_e$.
In the final shape of the observed spectrum, however, the optical depth of the cloud that has to be crossed by the photons is considerably important, owing to the fact that it dictates the number of scattering processes between photons and electrons. The optical depth of the gas of electrons is defined as

$$\tau = n_e \sigma_T R, \tag{3.22}$$

where n_e is the density of electrons, and R is the typical dimension of the cloud. The probability for a photon to cross the cloud without interacting with any electron is equal to $e^{-\tau}$. If we assume that inside the cloud the photon is continually scattered following a random walk, then for $\tau > 1$ the mean free path is equal to $d = R/\tau$ and the photon will experience on average τ^2 interactions before leaving the cloud of electrons. On the other hands, if $\tau < 1$, on average the photon does not interacts with any electron.
The importance of the Compton scattering, in some sense, is related to the quantity of energy gained by the photon. Then, we define the fundamental parameter y which measures the importance of the inverse Compton scattering as the product of the energy gained by the photon in one interaction and the mean number of interactions. According to this, the theory of Brownian motion gives an estimate of this number, that is equal to $\max(\tau, \tau^2)$, depending if the cloud of electron is optically thin ($\tau < 1$) or optically thick ($\tau > 1$), respectively.
If $y > 1$, the Comptonization process is important due to the fact that the Comptonization spectrum dominates on the seed photons spectrum. On the other hands, if $y << 1$ the spectrum of the

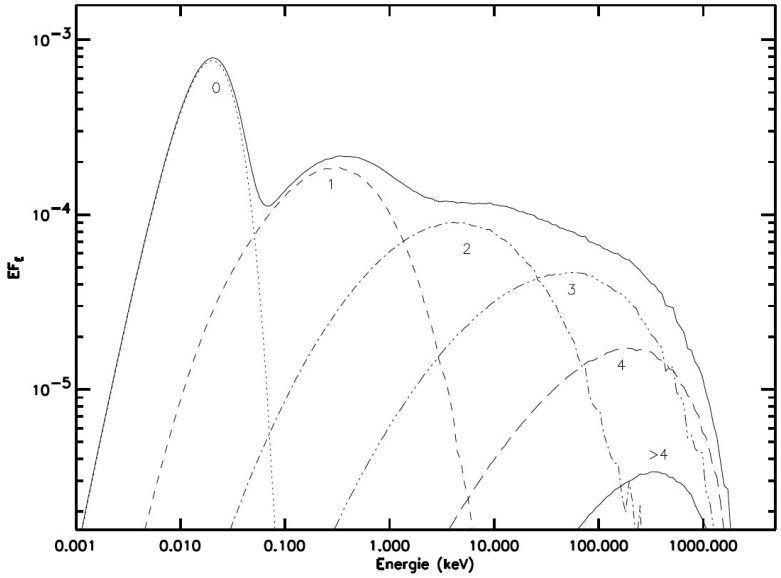

FIGURE 3.4. Comptonization spectrum arising from seed photons having a blackbody temperature $kT_{bb} = 5eV$ in an homogeneous plasma sphere having a temperature $kT_e = 300keV$ and optical depth $\tau = 0.1$. The Compton orders are also represented (Malzac, 1999).

seed photons is not considerably altered (Ghisellini, 2013).

The spectrum of the seed photons coming from the accretion disk, then, is considerably modified by the hot corona surrounding the central object. The entity of the modification is dictated essentially by the electron temperature and by the optical depth of the corona. This last parameter influences the number of scattering processes undergone by the photons and as a consequence of the multiple scattering, the resulting spectrum has a power law trend with a high energy cut off at an energy of $3K_BT_e$ if the source is in the soft state, or of K_BT_e if the source is in the hard state. The spectrum becomes harder (i.e the the spectral index of the power law decreases $\Gamma < 2$) when the electron temperature and optical depth of the corona increases. Furthermore, if the optical depth of the corona is sufficiently high, the photons have the time to thermalize with the gas of electrons and a bump forms in the source spectrum at high energies (*Compton Saturation*, see Figure 3.4) .

3.2.2 Photoelectric absorption

The interstellar medium (ISM) consists of dust and and gas that form a large fraction of material in the Galaxy. This gas is composed by atoms and small molecules, mostly hydrogen and helium, with less than a percent other elements that have a certain abundance. The photons of a celestial source interact with the ISM that is located between the observer and the source with a certain

probability that is higher for low energy photons ($E < 1-10\,keV$) how it will be explained later. If a photon of energy $h\nu$ transfers the totality of its energy to an atom and it has an energy greater than the X-ray atomic energy level E_I the photon is absorbed and an electron is ejected with a certain kinetic energy given by

$$E_e = h\nu - E_{nlj}, \tag{3.23}$$

where E_{nlj} is the the binding energy of the electron for the specific energetic level. The most energetic is the incident photon, the larger is the probability to eject electrons that are bound to the nucleus. However, the probability of absorption for a given atom is strongly dependent from the energy of the incoming photon, due to the fact that the photoelectric cross section has a functional trend that decreases as ν^{-3}. This means that low energy X-rays are more absorbed than radiation at higher frequencies.
On the other hands, the cross section is strongly dependent by atomic number Z of the chemical elements present in the ISM. This means that nevertheless atoms heavier that H and He are less abundant, however they contribute to the total cross section significantly.
All these piece of information are contained in the actual functional form of the photoelectric cross section (Heitler, 1954), that is

$$\sigma_K = 4\sqrt{2}\sigma_T \alpha^4 Z^5 \left(\frac{m_e c^2}{h\nu}\right)^{7/2} \tag{3.24}$$

where $\alpha = e^2/4\pi\epsilon_0\hbar c$ is the fine structure constant and σ_T is the Thomson cross section. Equation 3.24 is the analytic solution for the photoelectric absorption that counts for photons with energy $h\nu >> E_I$ and $h\nu << m_e c^2$. The effective total photoelectric cross section is obtained by summing the contributions of all the chemical elements and weighting each cross section for the relative abundance:

$$\sigma_e(E) = \frac{1}{n_H}\sum_i n_i \sigma_i(E) \tag{3.25}$$

3.2.3 The reflection component

The radiation emitted from the central object, as seen in the previous sections, undergoes Inverse Compton scattering by the hot electron cloud located around the compact object. The resulting radiation is shifted at higher energies and it is free to be radiated into the interstellar space. A fraction of this radiation however, owing to the uniform emission of the corona, can interact with the innermost part of the accretion disk that is however colder (see Figure 3.1). This process reasons behind the formation of a supplementary spectral component called reflection component, whose continuum emission is due to direct Compton scattering between the hot photons coming

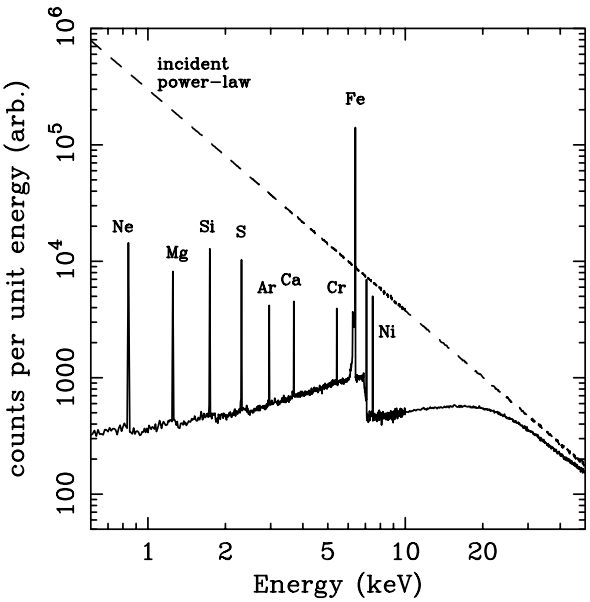

FIGURE 3.5. X-ray reflection obtained from a Monte Carlo simulation from an illuminated slab. Dashed line shows the incident continuum and solid line shows the reflected spectrum integrated over all angles (Reynolds, 1999).

from the corona and the colder matter of the accretion disk. One of the most evident features, when present, is the Kα Fe emission line at 6.4-7 keV, whose analysis is considerably important to study and understand the nature of the accretion flow in proximity of the central compact object, where non negligible relativistic effects occur (Fabian et al., 1989). Other important features in the reflection spectra are the presence of emission lines at lower energies with respect to the energy of the Fe Kα emission line and the Fe absorption edges. In addition a Compton hump is visible at about 30 keV (see Figure 3.5 as example).

Fe emission line The Fe Kα emission line is actually the most important emission feature present in the reflection spectrum. As a consequence of the irradiation of the innermost part of the accretion disk by the hot comptonized X-ray photons from the corona, the iron atoms and/or ions could absorb a photon, loosing one electron from the innermost K atomic shell. After this loss the ion becomes highly unstable and the minimum energy configuration can be reached in two ways. The first phenomenon that could occur is the radiative process of the fluorescence that generates a Kα emission line as a consequence of the replacement of the vacancy by a less bounded electron. In this case the emitted photon has an energy that is equal to the energy gap between the initial and the final state of the electron. The other possible phenomenon is the Auger effect that is a non radiative transfer of energy to an electron as a consequence of the transition of an electron to the ground state to fill the vacancy. The generation of an emission line is decided by the competition between these two effects. The decisive factor is the fluorescence

yield ϖ for the specific ion and transition, that is strongly dependent on the atomic number Z of the ion as

$$\varpi_K = \frac{Z^4}{a_K + Z^4}, \tag{3.26}$$

where $a_K = 1.12 \times 10^6$. According to this parameter, it is clear that the probability of having fluorescent transitions is higher for heavier ions, and among the others especially for the Fe ions, whose fluorescence yield percentage is for the Kα transition $\varpi \sim 34\%$ (Kaastra and Mewe, 1993). In addition to the high fluorescence yield, the iron ions are considerably abundant in the majority of the LMXB systems and all these factors foster the the presence of a strong Fe Kα emission line into the reflection spectra of many systems at 6.4 keV.
Depending on the ionization state of the plasma into the accretion disk it is possible to find out the evidence of highly ionized iron as the He-like Fe XXV and H-like Fe XXVI ions at 6.67 - 6.70 keV and 6.95-6.97 keV, respectively. While the He-like ions are usually generated partly by the recombination of oh H-like ions and partly by the fluorescence process after the ionization of a Li-like ions, in the case of H-like ions the only possible mechanism that contributes to the formation of the ion is the recombination.
LMXB spectra showing a reflection component could also show a broadened Fe Kα emission line. This line is intrinsically narrow and the reason of the broadening has to be searched in the fact that the line is probably produced in the innermost part of the accretion disk where the matter moves at relativistic velocities (Cackett et al., 2008a; D'Aì et al., 2009; Di Salvo et al., 2005, 2009; Iaria et al., 2009; Matranga et al., 2017). On the one hand, the line is split in two peaks due to the classical Doppler shift undergone by the matter of the accretion disk that follows Keplerian orbits (see Figure 3.6). Each radius of the disk contributes to generate a Doppler shifted peak. On the other hands, an increase of the blue-shifted peak and a decrease of the red-shifted peak is due to the Doppler boosting, that is an effect predicted by the theory of Special Relativity. In addition to these effects, the gravitation redshift moves the peaks at lower energies. Other parameters as the inclination angle with respect to the line of sight, the inner and outer radii of the accretion disk and the line emissivity have a direct influence on the line shape. In particular, the line emissivity depends on the radial coordinate of the accretion disk and on the ionization state of the matter into the accretion disk. While the line emissivity has a functional form that is purely empirical and is equal to r^q (where q is an adimensional index), the ionization state of the plasma is described by the ionization parameter $\xi(r)$ that is equal to

$$\xi(r) = \frac{4\pi F_X(r)}{n_e}, \tag{3.27}$$

where $F_X(r)$ is the X-ray flux arriving in the disk at the radial distance r per units of area and n_e is the density of electrons.

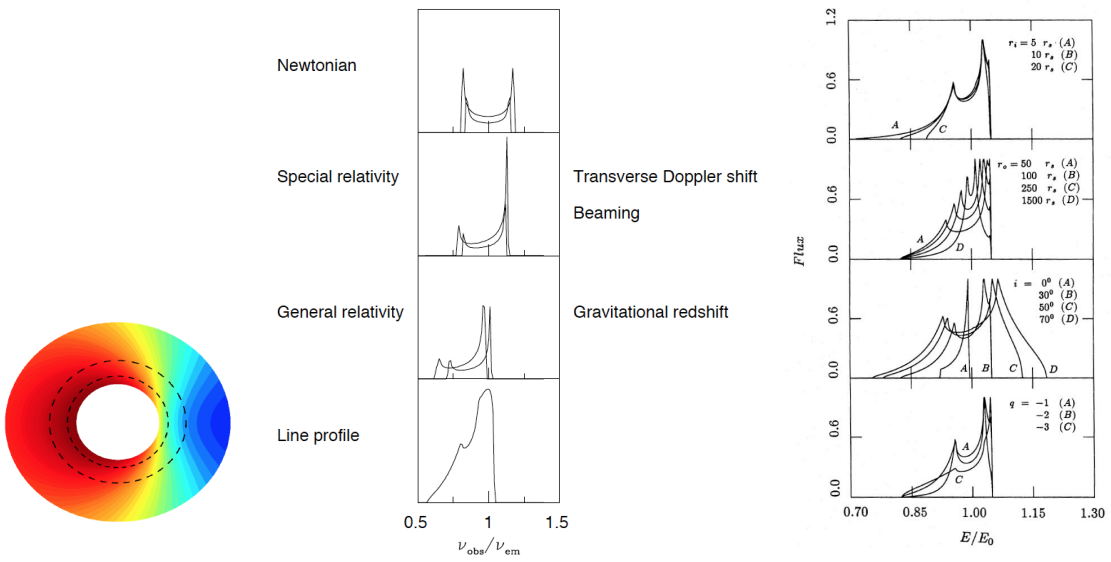

FIGURE 3.6. Left: the profile of the broad iron line is caused by the contribution of Doppler and transverse Doppler shifts, relativistic beaming, and the gravitational redshift. The upper panel shows the symmetric double-peaked profile from two narrow annuli on a non-relativistic disk. In the second panel is reported the effect of the Doppler boosting, whilst in the third panel the gravitational redshift has been included (Fabian et al., 2000). Right: Dependency of the emission line shape with respect to the inner and outer radius of the accretion disk (first and second panels from the top respectively), to inclination angle i (third panel) and witu respect to the line emissivity r^q of the plasma (bottom panel) (Fabian et al., 1989).

Depending on the ionization state of the plasma of the accretion disk and on the fluorescence yield, it is possible to find out other emission lines in the reflection spectrum. The nature of these lines is probably similar to that of the iron line: they are likely generated in the innermost part of the accretion disk, where the Comptonized photons coming from the corona excite the ions present into the disk.

The Compton Hump The Compton hump is a feature of the reflection spectra that is generally located at about 30 keV. It is the effect of two simultaneous processes: the absorption of low energy photons due to the ISM located between the source and the observer, and direct Compton scattering that affects photons having energies $> 15\,keV$, just shifting the energy of the photons to lower energies.

Absorption Edges The probability of absorbing a photon having an energy $h\nu$ considerably increases when $h\nu$ is equal to the ionization energy of an absorbing chemical element. This increase of the probability translates into an increase of the absorption cross section for that element and consequently in an absorption edge. The importance of these features is linked to

the chemical abundances of the interested medium. For this reason the Fe K edge at 7.1 keV can be detected in spectra of many X-ray binaries.

3.3 The Spectral States of a LMXB system

The X-ray source are highly dynamical and could also show fast spectral changes in strict correlation with how the accretion rate evolves. Being the accretion rate the cause of many timing properties of LMXB systems, these timing properties could be also detected during particular states of the source, as the fast quasi-periodic oscillations (QPOs) are. Three different spectral states have been defined for the X-ray sources depending on the particular nature of the spectral emission and on the accretion rate from the secondary star to the compact object.
In the *High-soft* state the emission from the accretion disk dominates the spectrum of the LMXB systems. This emission usually follows a blackbody distribution, or a multicolor-disk blackbody. The *Low-hard* spectral state, instead, is characterized by the dominant emission of the corona during the periods of low luminosity of the source.
However, few information is known about the mechanism that causes the shift in spectral state for the X-ray sources and the existing theories are continually under investigation.
In the following part of this section I am going to describe more in detail each spectral state.

3.3.1 The Soft State

One X-ray source in the soft state is characterized by the accretion disk radiation dominating the broad band spectrum. The disk emission actually follows a blackbody or equally a multicolor-disk blackbody distribution, owing to the nature of the cold plasma that is optically thick. For this reason the source has its maximum emission in the soft X-rays band and the typical photon temperature peaks around 1 keV. In the soft regime usually the accretion disk is truncated considerably close to the compact object and the accretion rate is high (see Figure 3.7). As a consequence of this, this state is important to probe the effects of very strong gravitational fields and the consequent relativistic effects that occur in the innermost orbits of the accretion disk. However, a small fraction of photons coming from the central object undergoes inverse Compton scattering by the cloud of electrons surrounding the compact object and for this reason a small steep tail is observable in the spectra of LMXB systems in the soft state. In particular the distribution of photons of the power-law tail follows the functional form $N(E) = E^{-\Gamma}$, where E is the energy and Γ is the power-law index whose typical values for the soft state is of about $\Gamma \sim$ 2-3.

3.3.2 The Hard State

When the hard power-law component dominates the spectral emission of the X-ray source, the spectral state of the source is said *Hard state*. The majority of the flux, indeed, comes from the

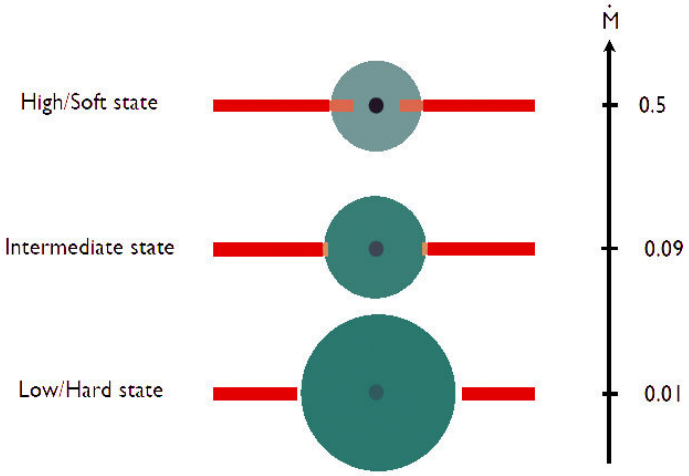

FIGURE 3.7. The geometry of the accretion disk (red line) and the corona (green circle) for the different spectral states. The variability of the mass accretion rate $\dot{M}$ is also shown for these states.

contribution of the photons that have been scattered through inverse Compton by the cloud of hot electrons surrounding the compact object. The power-law has a typical inclination of $\Gamma \sim 1.5\text{-}1.9$ and a high energy cut off is detectable. From a geometrical point of view, the theory predicts that in the hard state the accretion disk is truncated far away from the compact object (Done et al., 2007) (see Figure 3.7) probably owing to the evaporation of the innermost part of the accretion disk, but this issue is actually subject matter of the research, so far (Meyer et al., 2000; Mayer and Pringle, 2007). Being the accretion disc truncated at higher distances from the accretor compact object, the accretion disk has a lower temperature with respect to the case of the soft state. This implies two effects. On the one hand the photons of the accretion disk can not cool efficiently the corona that as a consequence dominates over the whole spectral components. On the other hand, the lower temperature of the accretion disk influences the strong evidence of emission lines in the reflection spectrum, owing to the fact that the plasma of the accretion disk is not so ionized to generate strong emission lines.

3.3.3 Spectral transitions for LMXB systems

According to Hasinger and van der Klis (1989), LMXB systems can be classified in two categories: the atoll source and the X sources. The origin of the names of these two categories is based on the spectral evolutionary track that these sources follow in the color-color diagram, that is a plot of the soft color of a source (that is the ratio of the count rates in the lowest energy bands) as a function of the hard color (the ratio of the count rates in the highest energy bands).
The main differences between the two classes concern the luminosity and the magnetic field. The

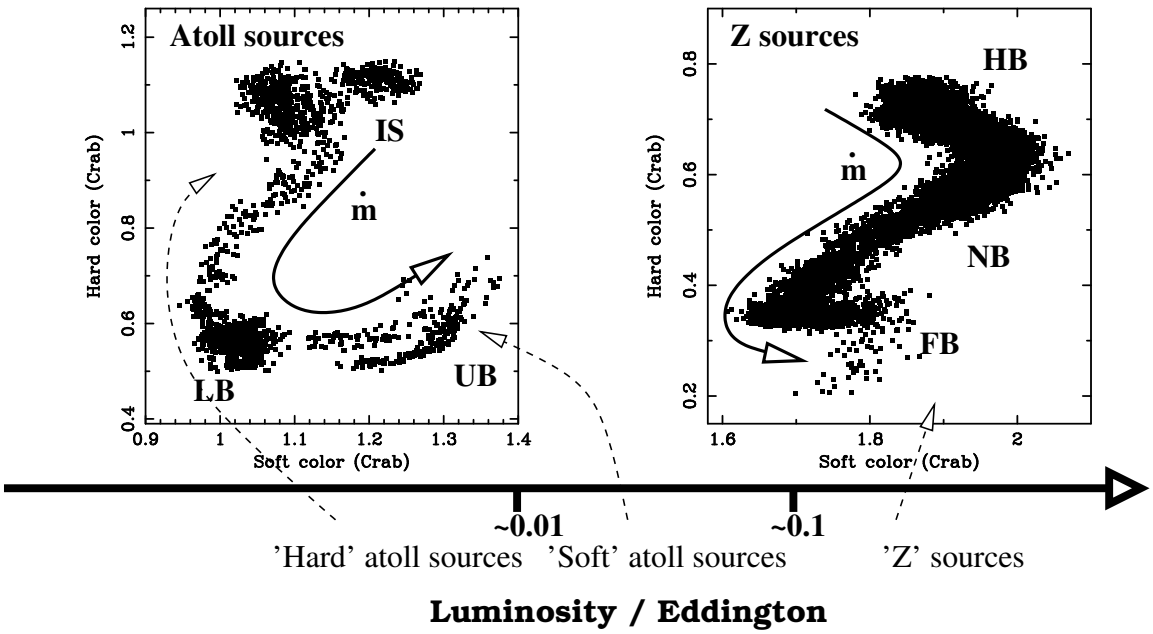

FIGURE 3.8. Color-color diagram for the atoll and Z sources. The variability of the mass accretion rate $\dot{M}$ and of the luminosity in units of Eddington luminosity is also reported (Migliari and Fender, 2006).

atoll sources have a lower accretion rate and a consequent typical luminosity that is $< 0.1\, L_{Edd}$. The Z sources, on the contrary, have higher accretion rates that translates in luminosities $> 0.5\, L_{Edd}$ and in magnetic fields $\geq 10^9\, G$ (Gierliński and Done, 2002).

The evolutionary track of the atoll sources has two main spectral states, called *hard island* and *banana state* (See Figure 3.8). The accretion rate increases going from the *Island state* (IS) to the *Upper banana state* (UB) passing from the *Lower banana state* (LB).

For the Z source, instead, the mass accretion rate increases passing from the *Horizontal branch* (HB) to the *Flaring branch* (FB), passing through the *Normal branch* (NB).

Then, we can surely assess that the spectral state of these sources is essentially decided by the mass accretion rate $\dot{M}$, that strongly influences the luminosity of the sources but also their timing properties.

CHAPTER 4

NEW ORBITAL EPHEMERIDES FOR THE DIPPING SOURCE 4U 1323-619: CONSTRAINING THE DISTANCE TO THE SOURCE

Gambino A. F., Iaria R., Di Salvo T., Del Santo M., Burderi L., Matranga M., Pintore F., Riggio A., Sanna A. (2016)
Published in Astronomy & Astrophysics,
Volume **589**, id.A34, 9 pp

4.1 Abstract

Context: 4U 1323-619 is a low mass X-ray binary system that shows type I X-ray bursts and dips. The most accurate estimation of the orbital period is 2.941923(36) hrs and a distance from the source that is lower than 11 kpc has been proposed.
Aims: We aim to obtain the orbital ephemeris, the orbital period of the system, as well as its derivative to compare the observed luminosity with that predicted by the theory of secular evolution.
Methods: We took the advantage of about 26 years of X-ray data and grouped the selected observations when close in time. We folded the light curves and used the timing technique, obtaining 12 dip arrival times. We fit the delays of the dip arrival times both with a linear and a quadratic function.
Results: We locate 4U 1323-619 within a circular area centred at RA (J2000)= 201.6543°and DEC (J2000)= -62.1358°with an associated error of 0.0002°, and confirm the detection of the IR counterpart already discussed in literature. We estimate an orbital period of P=2.9419156(6) hrs compatible with the estimations that are present in the literature, but with an accuracy ten times higher. We also obtain a constraint on the orbital period derivative for the first time,

estimating $\dot{P} = (8 \pm 13) \times 10^{-12}$ s/s. Assuming that the companion star is in thermal equilibrium in the lower main sequence, and is a neutron star of 1.4 $M_\odot$, we infer a mass of 0.28±0.03 $M_\odot$ for the companion star. Assuming a distance of 10 kpc, we obtained a luminosity of $(4.3 \pm 0.5) \times 10^{36}$ erg s^{-1}, which is not in agreement with what is predicted by the theory of secular evolution. Using a 3D extinction map of the K_s radiation in our Galaxy, we obtain a distance of $4.2^{+0.8}_{-0.7}$ kpc at 68% confidence level. This distance implies a luminosity estimation of $(0.8 \pm 0.3) \times 10^{36}$ erg s^{-1}, which is consistent with the adopted scenario in which the companion star is in thermal equilibrium.

4.2 Introduction

4U 1323-619 is a low mass X-rays binary system (LMXB) that was discovered by Forman et al. (1978) and identified as persistent by Warwick et al. (1981). Periodic dips and type I bursts were discovered in the European X-ray Observatory Satellite (*EXOSAT*) light curves (van der Klis et al., 1985; Parmar et al., 1989). The matter transferred from the companion star, impacting onto the outer accretion disc, forms a bulge of cold (and/or partially ionised) matter that photoelectrically absorbs part of the X-ray emission, which comes from the inner region of the system. The shape of a dip is generally irregular and varies from one cycle to another. However, the periodic occurrence of the dips in the light curve is strictly connected to the orbital motion of the binary system and the study of their periodicity can give information on the orbital period of the system. From *EXOSAT* and *BeppoSAX* lightcurves, Parmar et al. (1989) and Bałucińska-Church et al. (1999) inferred an orbital period of 2.932(5) hrs and 2.94(2) hrs, respectively. Levine et al. (2011), studying the RossiXTE/ASM 1.5-12 keV light curve from 1996 to 2011, find an orbital period of 2.941923(36) hrs. Although the light curves of 4U 1323-619 show dips, they do not show eclipses, which implies that the source has an inclination angle i between 60°and 80°(Frank et al., 1987). Zolotukhin et al. (2010), using a *Chandra* observation performed in continuous clocking mode, obtain the X-ray position of the source that, however, suffers from the indetermination in one direction because of the *Chandra* observational mode. The same authors also estimate the X-ray position of the source with an associated error of 3" using data of the X-ray Multi Mirror (*XMM-Newton*) mission. Zolotukhin et al. (2010), analysing the 2MASS catalogue, identify two possible infrared counterparts of 4U 1323-619 that are associated with the X-ray position estimated using *XMM-Newton* data. From the intersection of the positional error boxes of *Chandra* and *XMM-Newton,* they suggest that the probable infrared counterpart is a source with a magnitude of 18.12±0.20 in the K_s band.

The spectral analysis of the source shows that the equivalent column density of neutral hydrogen, N_H, is large and depends on the model used to fit the spectra and on the energy band covered. Bałucińska-Church et al. (2009) find $N_H = (3.2^{+0.1}_{-0.1}) \times 10^{22}$ cm^{-2} using *Suzaku* data, Boirin et al. (2005) infer $N_H = (3.5^{+0.1}_{-0.2}) \times 10^{22}$ cm^{-2} using *XMM-Newton* data and Parmar et al. (1989) obtained $N_H = (4.0 \pm 0.3) \times 10^{22}$ cm^{-2} using *EXOSAT* data. Smale (1995) suggested that

the large extinction to the source also explains why the optical counterpart has not been detected yet. Furthermore, Bałucińska-Church et al. (1999) suggested the possible presence of a local dust halo surrounding 4U 1323-619. The main effect of the halo is to absorb part of the source radiation owing to its optical depth, which depends on the inverse of the incoming radiation energy (Predehl and Schmitt, 1995).

The spectral analysis of 4U 1323-619 also highlights that the energy spectrum is dominated by a power-law component. Parmar et al. (1989) found a photon index Γ of the power-law component of 1.53±0.07, Boirin et al. (2005) obtain a Γ of $1.9^{+0.06}_{-0.10}$ and, adopting a cut-off power-law component, Bałucińska-Church et al. (2009) find a Γ of $1.67^{+0.10}_{-0.03}$ and an energy cut-off of 85^{+77}_{-35} keV. Galloway et al. (2008), analysing the type I X-ray bursts properties of 4U 1323-619 with data obtained with the proportional counter array (PCA) on board the *RXTE* mission, only infer an upper limit for the distance from the source because they do not find any evidence of photospheric radius expansion (PRE). The upper limit is of 11 kpc, assuming a companion star with cosmic abundances, and of 15 kpc, assuming a pure hydrogen companion star. Furthermore, the same authors show that the light curves demonstrate many double bursts where the secondary bursts are fainter and suggest that this can be explained taking into account a mixed composition of hydrogen and helium of the companion star, which causes short recurrence bursts generated by the hydrogen ignition onto the neutron star. In addition, using EXOSAT/ME data in the energy band 1.5-11 keV, Parmar et al. (1989) gave a lower limit of 10 kpc for the distance from the source on the basis of the observed properties of the bursts.

Zolotukhin et al. (2010), studying the photometric properties of 4U 1323-619 in the IR band and assuming a distance of 10 kpc, find a discrepancy of one order of magnitude between the observed value of the flux and that predicted by a model that describes the system as an accretion disk illuminated by a central spherical hot corona, which has a luminosity of 5.2×10^{36} erg s^{-1} in the 0.1-10 keV band (Boirin et al., 2005). Based on this discrepancy, they suggest a distance from the source between 4 and 5 kpc.

In this work, we find the first orbital linear and quadratic ephemerides of 4U 1323-619, using all the available X-ray pointing observations from 1985 to 2011. We find a weak constraint on the orbital period derivative. We compare the obtained results with the prediction of the secular evolution of the binary system (see e.g. King, 1988; Verbunt, 1993) and suggest that the source distance is less than 5 kpc (close to 4.2 kpc for a companion star in thermal equilibrium).

4.3 Observation and data reduction

To analyse the dips arrival times of 4U 1323-619, we used all the available X-ray archival data that include *RXTE*, *Chandra*, *XMM-Newton*, *Suzaku*, *BeppoSAX*, *EXOSAT* and *ASCA* observations.

Table 4.1: Observation log.

Point	Satellite/Instrument	Observation ID	Start time (UT)	Stop time (UT)	T_{fold} (TJD;TDB)
1	EXOSAT/ME	1401	1985 Feb 11 18:48:49	1985 Feb 13 04:39:18	6108.48892929229
2	ASCA/GIS2	42005000	1994 Aug 04 12:21:11	1994 Aug 04 20:10:47	9568.66237498892
3	RXTE/PCA	P20066-02-01-00, P20066-02-01-01, P20066-02-01-02, P20066-02-01-03, P20066-02-01-04	1997 Apr 25 22:04:48	1997 Apr 28 03:44:49	10565.04185436878
4	BeppoSAX/MECS	20102001	1997 Aug 22 17:06:09	1997 Aug 24 02:02:39	10683.398658095225
5	RXTE/PCA	P40040-01-01-000, P40040-01-01-00, P40040-01-02-000, P40040-01-02-00, P40040-01-03-000, P40040-01-03-00	1999 Jan 18 02:42:30	1999 Mar 13 09:10:46	11223.245347406
6	ASCA/GIS2	47015000	2000 Feb 02 12:16:04	2000 Feb 04 23:19:15	11577.746691772565
7	XMM/Epic-pn	0036140201	2003 Jan 29 09:03:42	2003 Jan 29 22:57:07	12668.666973091815
8	RXTE/PCA	P70050-03-01-00, P70050-03-01-01, P70050-03-01-02	2003 Sep 25 07:54:56	2003 Sep 25 23:57:20	12907.661355385295
9	RXTE/PCA	P90062-03-01-010, P90062-03-01-01, P90062-03-01-00, P90062-03-01-02	2004 Dec 30 21:46:40	2004 Dec 31 13:53:03	13370.240516395665
10	Suzaku/XIS0	401002010	2007 Jan 09 11:50:53	2007 Jan 10 21:58:37	14110.204689820065
11	RXTE/PCA	P95442-01-01-00, P95442-01-01-01, P95442-01-01-02, P96405-01-01-01, P96405-01-02-00, P96405-01-02-01, P96405-01-01-00	2010 Dec 25 08:01:54	2011 Mar 28 12:14:06	15601.92228420802
12	Chandra/HETG	13721, 14377	2011 Dec 19 01:03:11	2011 Dec 24 19:01:07	15916.91815760006

We used the *Chandra* data of the ObsIDs 13721, 14377, and 3826. Both the ObsID 13721 and ObsID 14377 data were collected in December 2011 in timed graded mode, while the data of the ObsID 3826 were taken in continuous clocking mode in September 2003. To process the *Chandra* data we used CIAO v. 4.7. The observations have been reprocessed with the `chandra_repro` routine. We used the ObsID 13721 to obtain an accurate estimation of the X-ray source position using the *Chandra* tool `tg_findzo`. The revised coordinates for 4U 1323-619 are: RA (J2000)= 201.6543°and DEC (J2000)= -62.1358°, with an associated error of 0.6", which represents the 90% confidence level *Chandra* positional accuracy[1].

We report the Chandra/HETG image of 4U 1323-619 that was obtained from the reprocessed level 2 data in Fig. 4.1. The green and black circles indicate the X-ray source position shown in this work and in Zolotukhin et al. (2010), respectively. The infrared sources, A and B, suggested by Zolotukhin et al. (2010) are indicated with crosses and have an error circle with a radius of 0.2". The B source is located inside a circular area, which has a radius of 0.2" that has been determined with the 2MASS catalogue. On the basis of our results we confirm that the source B is the infrared counterpart of 4U 1323-619 as suggested by Zolotukhin et al. (2010). Hereafter we

[1]See http://cxc.harvard.edu/cal/ASPECT/celmon/ for more details.

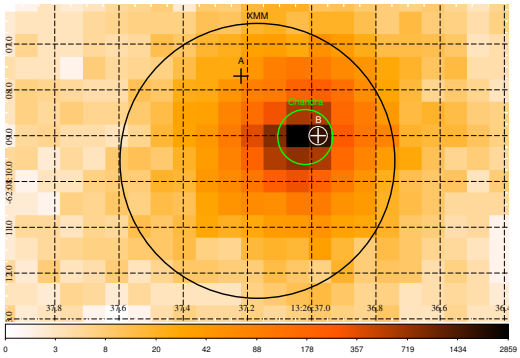

Figure 4.1: Chandra/HETG image of 4U 1323-619. The colour scale reports the number of photons. The green circle indicates the X-ray position obtained in this work, while the black circle indicates the position obtained by Zolotukhin et al. (2010) using *XMM-Newton* data. The A and B crosses are the two candidate infrared counterparts identified by Zolotukhin et al. (2010).

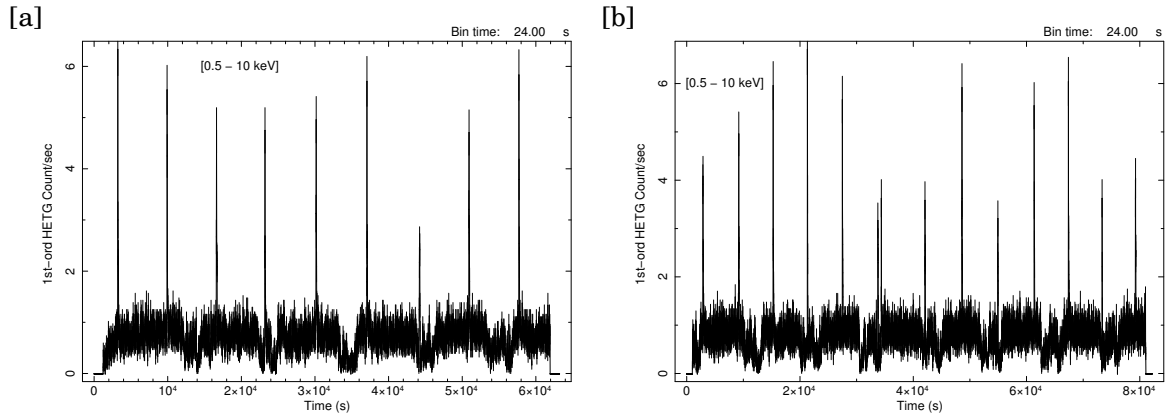

Figure 4.2: 1st order background subtracted Chandra/HETG light curves of the observations 14377 (a) and 13721 (b) in the energy range 0.5-10 keV. The light curve (a) starts on 19 December 2011 at 01:03:10 UT, while the light curve (b) starts on 23 December 2011 at 20:11:09 UT. The bin time is of 24 s.

use the new X-ray *Chandra* coordinates to apply the barycentric corrections.
We applied the barycentric corrections to the Level 2 events file using the `axbary` tool and extracted the first diffraction orders and background-subtracted HEG + MEG light curves using the `dmextract` tool. To subtract the background from the light curves, we selected a background events extraction region of 5" of radius, far away from the real source position.

The available RXTE/PCA observations span a period of about 13 years (from 1997 to 2011). We produced background-subtracted light curves, including all the energy channels and obtained the data from the HEASARC data archive. These light curves have a temporal resolution of 0.125 s and the barycentric corrections have been applied using the `faxbary` tool.
The only available observation of XMM-Newton/Epic-pn is the ObsID 0036140201 of January 2003, performed in timing mode. The data have been processed with the `epproc` tool of the

Table 4.2: Best-fit parameters obtained by fitting the dips in the folded light curves.

Point	Phase interval	Y_1 count s^{-1}	Y_2 count s^{-1}	Y_3 count s^{-1}	ϕ_1	ϕ_2	ϕ_3	ϕ_4	χ^2_{red} (d.o.f.)
1	0 - 1	4.88(4)	3.29(5)	4.94(4)	0.248(8)	0.322(8)	0.519(7)	0.604(8)	1.18(506)
2	0 - 1	1.41(2)	0.78(2)	1.51(2)	0.351(6)	0.384(5)	0.598(5)	0.621(6)	1.66(438)
3	0.6 - 1.6	19.85(5)	15.62(7)	20.32(6)	0.920(5)	1.009(4)	1.159(5)	1.301(5)	5.44(482)
4	0 - 1	0.954(8)	0.634(8)	0.961(10)	0.359(7)	0.432(6)	0.643(8)	0.744(9)	1.56(506)
5	0 - 1	21.21(5)	16.53(6)	21.06(5)	0.334(4)	0.414(4)	0.580(3)	0.651(3)	4.89(506)
6	0 - 1	1.231(12	0.724(11	1.260(12	0.294(8)	0.409(7)	0.615(7)	0.676(7)	1.50(506)
7	0.3 - 1.3	28.4(2	22 (fixed)	27.4(2)	0.632(8)	0.699(7)	0.937(7)	0.983(7)	15.65(506)
8	0.6 - 1.6	19.31 (8	14.5 (fixed)	18.96(7)	0.936(6)	1.052(5)	1.132(6)	1.246(7)	2.72(495)
9	0.9 - 1.9	17.34(13	12.83(10	17.62(12	1.224(7)	1.259(8)	1.531(6)	1.589(6)	4.94(495)
10	0.3 - 1.3	0.922(9)	0.500(9)	0.932(10)	0.629(6)	0.686(5)	0.881(8)	1.028(9)	1.65(505)
11	1 - 2	18.42(11)	13.64(11)	18.39(9)	1.278(6)	1.338(6)	1.537(8)	1.630(10	2.09(505)
12	0.27 - 1.27	0.781(7)	0.494(5)	0.813(7)	0.561(6)	0.607(5)	0.914(4)	0.956(5)	2.72(505)

Scientific Analysis System (SAS) v. 14.0.0 and the barycentric corrections have been applied with the `barycen` tool. The extraction region of the source photons has been chosen on the basis of the analysis of the histogram showing the number of photons versus the RAWX coordinate of the image. We selected a box region with a width of 21 RAWX and centred at the RAWX coordinate of the peak of the photons' distribution (RAWX=36). Thus, we extracted the light curve with the `evselect` routine, selecting events with PATTERN≤4 (single and double pixel events) and FLAG=0 (to ignore spurious events), in the energy range between 0.5 and 10 keV. We binned the resulting light curve at 1 s.

The available *Suzaku* observation of 4U 1323-619 is the ObsID 401002010 of January 2007. This has been processed with the `aepipeline` routine and the two available data formats (3X3 and 5X5) have been unified with each other. We applied the barycentric corrections to the events file with the `aebarycen` routine. We extracted the 0.2-10 keV light curve using the `xselect` tool and adopting a circular region around the brightest pixel of the source with a radius of 50". We used a bin time of 16 s.

We also used the EXOSAT/ME observation performed on February 1985. The light curve has been extracted in the energy range between 1 and 8 keV with a bin time of 10 s and the barycentric corrections have been applied with the ftool `earth2sun`.

Furthermore, we used two ASCA/GIS2 observations: the first has been taken on August 1994 and the second one on February 2000. Both observations were performed in medium bit rate mode and the light curves were extracted with a bin time of 0.5 s. We applied the barycentric corrections using the `timeconv` ftool.

Finally, the only available observation of *BeppoSAX* is of August 1997. The BeppoSAX/MECS light curve has been extracted with the `xselect` ftool in a circular region of 4' of radius, without energy filters and with a bin time of 4 s. The barycentric corrections have been applied with the ftool `earth2sun`.

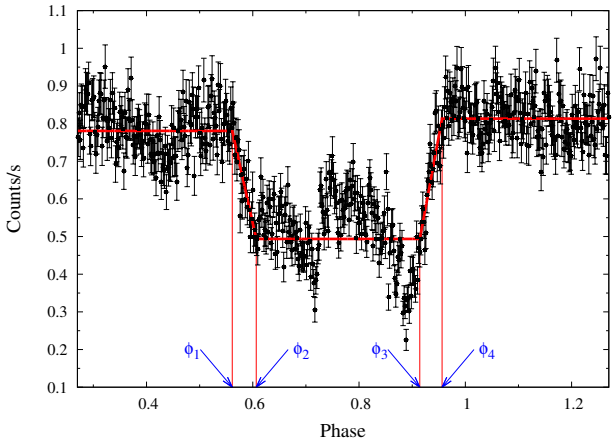

Figure 4.3: Folded light curve of the jointed Chandra observations ObsID 14377 and ObsID 13721. The red line is the step-and-ramp function that better fits the dip. The blue arrows highlight the phases of ingress (ϕ_1 and ϕ_2) and egress (ϕ_3 and ϕ_4) of the dip.

4.4 Data analysis

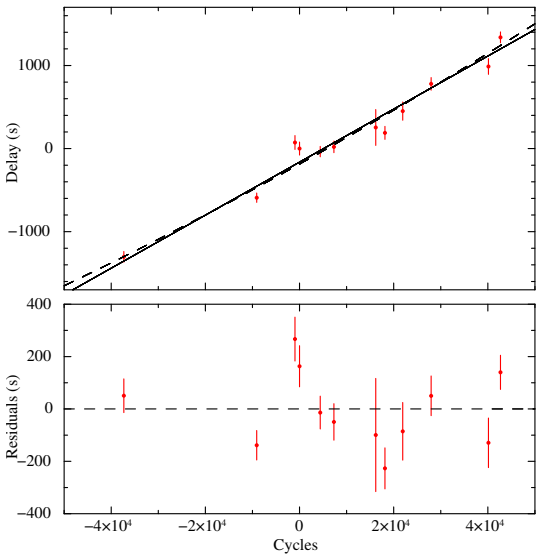

Figure 4.4: Upper panel: delays of the dip arrival times (calculated with respect to P_0 of 10590.864 s and T_0 of 10683.3987 TJD) as a function of the number of cycles. Both the linear and the quadratic models are shown as a solid and a dashed line, respectively. Lower panel: residuals associated with respect to the linear fit.

The whole analysed data-set spans a temporal range of about 26 years. All the selected observations have been grouped when close in time to obtain folded light curves to increase the statistics of the dips. We grouped the Chandra ObsIDs 13721 and 14377. The light curves of these observations are separately shown in Fig. 2a and 2b with a bin time of 24 s. The curves have been extracted from the first diffraction order of the HETG grating and the individual observations

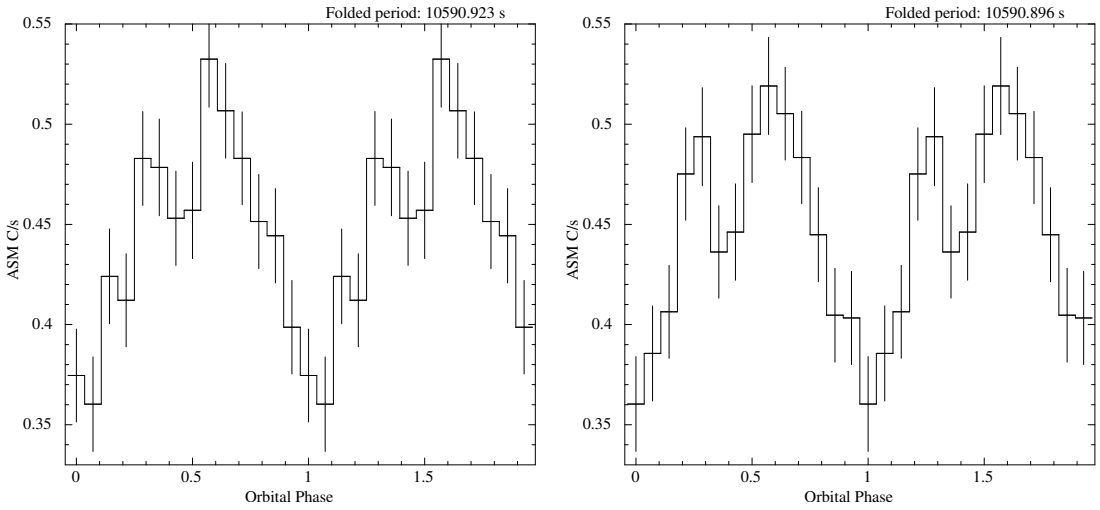

Figure 4.5: Folded RXTE/ASM light curves of 4U 1323-619 in the 2-10 keV energy band using the T_0 and orbital period suggested by Levine et al. (2011) (left panel) and the linear ephemeris shown in Eq. 4.2 (right panel). We adopted 14 phase-bins per period.

have a duration of about 62 and 80 ks, respectively. In the ObsID 14377 five dips occur, plus one more at the beginning of the observation that is only partially visible. In addition, during the observation 13 721 seven dips occur, plus one more that is partially visible at the beginning of the observation. In both observations several Type I bursts occur. The persistent emission is mainly at about 0.8 counts/s and the count-rate at the bottom of the dips is close to 0.3 counts/s.

Three RXTE/PCA observations have been ruled out from our analysis: the observation whose ObsID is P40040-01-02-01 because the dip is only partially visible in the light curve, as well as the observations whose ObsIDs are P96405-01-03-00 and P96405-01-04-00, owing to the lack of dips. We furthermore excluded four additional RXTE/PCA observations from our analysis (ObsIDs P96405-01-05-00, P96405- 01-05-01, P96405-01-05-02, and P96405-01-05-03) and one Chandra observation (ObsID 3826) owing to the fact that their folded light curves show a high count-rate variability outside the dips that does not allow us to obtain a valid fit for the dips by using the step-and-ramp function that we define below.

After this preventive selection process, we analysed 12 grouped and barycentric-corrected light curves that contain a total of 95 dips. The observations that we selected for the analysis, as well as their grouping, are shown in Tab. 4.1. Bursts were excluded from each light curve by removing the segments starting 5 s before the rise time of each burst and ending 100 s after the peak time. We verified that the shape of the dips in each light curve is quite similar from one cycle to another and folded the light curves with a reference time and a trial period (T_{fold} and P_0, respectively). To estimate the dip arrival time, we adopted the same procedure used by Iaria et al. (2015a). For each light curve T_{fold} is defined as the average value between the start and stop time of the observation. We fit the dip in each folded light curve with a step-and-ramp function that involves

seven parameters: the count-rate before (Y_1), during (Y_2) and after (Y_3) the dip, and the phases of ingress (ϕ_1 and ϕ_2) and egress (ϕ_3 and ϕ_4) of the dip. We show the step-and-ramp function fitting the folded light curve of the joint Chandra observations ObsID 14377 and ObsID 13721 in Fig. 4.3.

The phase of the dip arrival has been estimated as $\phi_{dip} = (\phi_1 + \phi_4)/2$. The corresponding dip arrival time is given by $T_{dip} = T_{fold} + \phi_{dip} P_0$.

The values of the χ^2_{red} in Tab. 4.2 are quite high. We can assume that this is a direct cause of the underestimation of the errors associated with the fitted data points. The uncertainties of all these data points can be increased by a constant factor to have a χ^2_{red} equal to 1, multiplying the uncertainties on the fitting parameters by a factor equal to the $\sqrt{\chi^2_{red}}$ of the fit. As a consequence of this, for the calculations of the uncertainty on the fitting parameters, all the uncertainties relative to the values of ϕ_{dip} have been rescaled by the factor $\sqrt{\chi^2_{red}}$, when the best-fit model gave a $\sqrt{\chi^2_{red}}$ greater than 1. Moreover, we use a trial orbital period P_0 of 10590.864 s and a reference epoch T_0 of 10683.4663 TJD to obtain the delays of the dips' arrival times with respect to the reference epoch T_0. We choose the values of P_0 and T_0 arbitrarily, which are similar to those given by Levine et al. (2011). The values of T_{fold} are shown in Table 4.1, the best-fit parameters and the χ^2_{red} obtained by fitting the dips are shown in Table 4.2. Finally, the dip arrival times, the cycle and the delays for each observation are shown in Table 4.3.

First, we fit the obtained delays as a function of cycles with a linear function, taking into account only the errors associated with the delays. The fitting function is

$$y(N) = a + bN, \tag{4.1}$$

where N is the cycle number, b is the correction to the trial orbital period (ΔP_0) in seconds, and a is the correction to the trial reference epoch (ΔT_0) in seconds. Thus, we obtain a first estimation of the corrections to the reference epoch and to the orbital period. Taking into account the error associated with the number of the cycles (Δx), we obtain a total error $\Delta_{tot} = \sqrt{(\Delta y)^2 + (b * \Delta x)^2}$, where Δy is the error associated with the dip arrival time (see Iaria et al., 2014). We repeated the fitting procedure, obtaining a $\chi^2(d.o.f.)$ of 37.81(10). For the same reason adduced before, the uncertainties of the parameters returned by the linear fit have been rescaled by the factor $\sqrt{\chi^2_{red}}$, when the best-fit model gave a $\sqrt{\chi^2_{red}}$ greater than 1. The best-fit model parameters are shown in Table 4.4. The orbital ephemeris obtained with the linear model is

$$T_{dip}(N) = \text{TJD(TDB)}\ 10683.4644(5) + \frac{10590.896(2)}{86400} N, \tag{4.2}$$

where 10683.4644(5) TJD and 10590.896(2) s are the reference epoch and orbital period, respectively. The associated errors are at 68% confidence level.

We also try to fit the delays using a quadratic function:

$$y(N) = a + bN + cN^2, \tag{4.3}$$

where a is the reference epoch correction (ΔT_0) in seconds, b is the orbital period correction (ΔP_0) in seconds, and $c = \frac{1}{2} P_0 \dot{P}$ in units of seconds. The best-fit model parameters are reported in Table 4.2. The fit returns a value of the $\chi^2(d.o.f.)$ of 36.04(9), while the F-test probability of chance improvement with respect to the previous linear fit is only of 52%. This suggests that, adopting the quadratic ephemeris, we do not improve the fit significantly. The orbital ephemeris obtained with the quadratic fit is

$$T_{dip}(N) = \text{TJD(TDB)}\, 10683.4641(7) + \frac{10590.896(2)}{86400} N + \frac{4(7) \times 10^{-8}}{86400} N^2, \tag{4.4}$$

where 10683.4641(7) TJD is the new reference epoch, 10590.896(2) s is the new orbital period and $\dot{P} = (0.8 \pm 1.3) \times 10^{-11} s/s$ is the orbital period derivative obtained by the c parameter that was returned by the fit. The associated errors are at 68% confidence level. In the upper panel of Fig. 4.4 we show the delays versus the orbital cycles and, superimposed, two best-fit models, i.e. the linear and the quadratic ephemeris. At the bottom, the residuals resulting from the linear fit are shown. The maximum discrepancy between the delays and the linear best-fit model is of about 300 s, which is about 2.8% of the orbital period.

Table 4.3: Journal of arrival times of the X-ray dips obtained from each folded light curve. The number of dips in each grouped observation is also shown.

Point	Dip time (TJD;TDB)	Cycle	Delay (s)	Number of dips
1	6108.5412(7)	-37322	-1303±64	12
2	9568.7220(7)	-9094	-592±56	2
3	10565.0554(10)	-966	73±84	8
4	10683.4663(9)	0	0 ±79	11
5	11223.3058(7)	4404	-36±63	9
6	11577.8062(8)	7296	20±70	7
7	12668.766(3)	16196	254±216	5
8	12907.6725(9)	18145	189±78	4
9	13370.2904(13)	21919	451±110	6
10	14110.3063(9)	27956	779±76	10
11	15601.9779(11)	40125	988±95	7
12	15917.0112(8)	42695	1339±65	14

Table 4.4: Best-fit values obtained from the linear and quadratic fits on the delays of the dips arrival times.

Parameter	Linear	Quadratic
a (s)	-163 ± 23	-186 ± 29
b ($\times 10^{-3}$ s)	31.9 ± 0.9	32 ± 1
c ($\times 10^{-8}$ s)	-	4 ± 7
χ^2(d.o.f)	37.81(10)	36.04(9)

To verify the goodness of the linear ephemeris shown in Eq. 4.2, we folded the RXTE/ASM light curve in the 2-10 keV energy band. This light curve covers a time interval of 15.5 years (from 5 January 1996 to 24 September 2011) and barycentric corrections have been applied using the `faxbary` tool. We show the folded light curve using the reference epoch and orbital period suggested by Levine et al. (2011) and by our linear ephemeris in the left and right panels of Fig. 4.5, respectively. We adopted 14 phase bins per period (each phase bin corresponds to ~757 s). We note that, using T_0 and P_{orb} from Eq. 4.2, the dip occurs at phase zero, while using the values from Levine et al. (2011), the dip occurs at a phase close to 0.1.

4.5 Spectral analysis

We present the spectral analysis of 4U 1323-619 performed with *INTEGRAL* data. This analysis is useful in Sect. 4.6 when extracting the unabsorbed flux of the source between 0.5 and 100 keV, to obtain an estimation of the luminosity.
We found a number of *INTEGRAL* pointings (science windows, SCW) collected on 2003 July 10–13 in the field of 4U 1323-619. To maximize the spectral response, we selected only SCWs (with a typical duration of 3 ks) with the source located within 4.5°and 3.5°from the centre of the IBIS and JEM-X FOVs, respectively. Thus, we analysed IBIS/ISGRI (Lebrun et al., 2003) data of 80 SCWs and JEM-X2 (Lund et al., 2003a) data of 51 SCWs (JEM-1 was switched-off at that time) with the standard INTEGRAL software OSA 10.1 (Courvoisier et al., 2003) We verified that, in the JEM-X2 lightcurve, no type-I bursts were present and that the source flux was almost constant, so that, an averaged spectra (3-35 keV) has been extracted in 16 channels for a total exposure time of 156 ks. Because of the faintness of the source in hard X-rays, the ISGRI spectrum has been extracted by the total (about 198 ks) mosaic image with the `mosaic_spec` tool in four energy bins, spanning from 22 keV up to 65 keV. The spectral analysis was performed using XSPEC v. 12.8.2 (Arnaud, 1996). We modelled the joint JEM-X2 and ISGRI spectrum with a thermal Comptonisation (`nthComp` in XSPEC). This spectral component takes into account the nature of the seed photons (represented by the inp_type parameter that is equal to 0 for blackbody seed photons or to 1 for disk blackbody seed photons), the temperature kT_{bb} of the seed photons, the electron temperature kT_e, an asymptotic power-law photon index Γ, the redshift, as well as a normalisation constant. The absorption that is due to the interstellar medium has been taken into account by using the `TBabs` model with the chemical abundances of Asplund et al. (2009) and the cross-sections of Verner et al. (1996). The energy domain of the spectrum, however, does not enable us to well constrain the value of N_H. As a consequence of this, we fix the column density of neutral hydrogen to the value found by Parmar et al. (1989), which is also the highest available in literature. The fit gives a χ^2_{red} of 1.07 with 11 degrees of freedom. The best-fit parameters are shown in Tab. 4.5, while the deconvolved model and the resulting residuals in unity of σ are shown in Fig. 4.6.

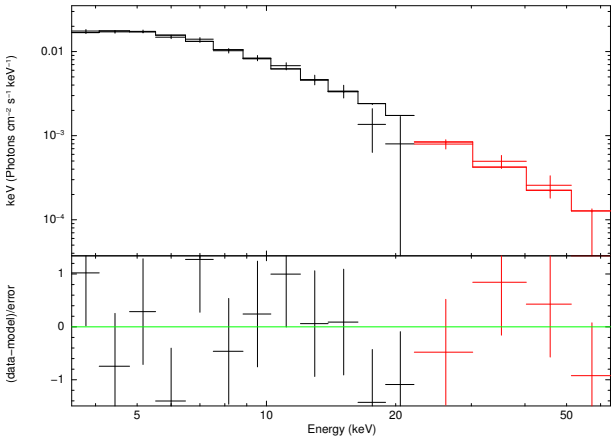

Figure 4.6: Upper panel: JEM-X (black) and ISGRI (red) spectra of 4U1323-619 in the energy range 3-65 keV. Lower panel: residuals in units of σ.

Table 4.5: Best-fit parameters of the spectral fitting on the JEM-X and ISGRI spectrum. The fitting parameters were set equal for both the JEM-X and ISGRI data-sets. The uncertainties are given at 90% confidence level.

Component	Parameter	Value
Tabs	N_H ($\times 10^{22}\ cm^{-2}$)	4 (frozen)
nthComp	Γ	$3.0^{+0.4}_{-0.5}$
nthComp	kT_e (keV)	>10
nthComp	kT_{bb} (keV)	$1.13^{+0.11}_{-0.15}$
nthComp	inp_type	0 (frozen)
nthComp	Redshift	0 (frozen)
nthComp	Norm. ($\times 10^{-3}$)	$6.9^{+1.9}_{-1.3}$
	χ^2_{red}(d.o.f.)	1.069(11)

4.6 Discussion

We estimated the orbital ephemeris of 4U 1323-619 using the whole available X-ray archival data from 1985 to 2011. We produced the linear and quadratic orbital ephemerides, finding that the value of the orbital period is 2.9419156(6) hrs. This is compatible with previous estimations (see Levine et al., 2011), but with an accuracy that is ten times higher than that proposed by Levine et al. (2011).

In a binary system the accretion of matter from the companion star onto the neutron star is the main mechanism of generation of radiation. The mass accretion rate, however, is governed by the angular momentum losses to which the binary system is subjected. The main channels of angular momentum loss are: the mass loss from the binary system as a consequence of the accretion, the generation of gravitational waves (especially in close binaries composed by massive stars), and the magnetic braking, which consists of a transfer of angular momentum from the companion star to the ionised matter that surrounds it and that interacts with its magnetic field. The redistribution of the angular momentum induced by these interactions causes a variation

of the orbital period of the binary system. As a consequence of this, an estimation of the orbital period derivative is important to understand the orbital evolution of the system.
As a first step towards the extrapolation of an evolutive scenario for 4U 1323-619, we infer the companion star mass M_2. Assuming that 4U 1323-619 is a persistent X-ray source in a Roche lobe overflow regime, as suggested by the long time monitoring of the RXTE/ASM (see Fig. 4.7), then the companion star fills its Roche lobe and, consequently, the companion star radius R_2 is equal to the Roche lobe radius R_{L2}.
The Roche lobe radius is given by the expression

$$R_{L2} = 0.46224\, a \left(\frac{m_2}{m_1 + m_2}\right)^{1/3} \tag{4.5}$$

of Paczyński (1971), where m_1 and m_2 are the NS and companion star masses in units of solar masses and a is the orbital separation of the binary system. Assuming that the companion star belongs to the lower main sequence, we adopt the relation

$$\frac{R_2}{R_\odot} = 0.877\, m_2^{0.807}, \tag{4.6}$$

valid for M-stars (Neece, 1984). Combining equations 4.5 and 4.6 with the third Kepler law, that links the orbital separation a with the value of the orbital period found with the linear ephemeris, and assuming a neutron star (NS) mass of M_1=1.4 $M_\odot$ and the orbital period obtained from our ephemeris, we find that the companion star mass is $M_2 \simeq 0.28 \pm 0.03$ $M_\odot$. Here we took into account an accuracy of 10% in the mass estimation (see Neece, 1984). Our result is compatible with 0.25 $M_\odot$, as suggested by Zolotukhin et al. (2010). Since the companion star mass is 0.28 $M_\odot$ we expect that it is fully convective and, consequently, it cannot have a magnetic field anchored to it (Nelson and Rappaport, 2003). This implies that magnetic braking as a driving mechanism of the orbital evolution is ruled out. Assuming that the unique mechanism of angular momentum loss in this binary system is due to the gravitational radiation and, considering a conservative mass transfer, we can infer the secular mass accretion rate by re-arranging Eq. 10 of Burderi et al. (2010), i.e.

$$\dot{m}_{-8} = 0.6\, \frac{1}{3q - \frac{3}{2}n - \frac{5}{2}}\, m_1^{8/3} q^2 (1+q)^{-1/3} P_{2h}^{-8/3}, \tag{4.7}$$

where $\dot{m}_{-8}$ is the mass transfer rate from the companion star in units of 10^{-8} $M_\odot$ yr^{-1}, q is the ratio of m_2 to m_1, and P_{2h} is the orbital period in units of two hours. The index n can assume the values -1/3 or 0.8 and is associated with the internal structure of the companion star. If the star is in thermal equilibrium, its index n is 0.8 (the index of the mass-radius relation we adopted in Eq. 4.6) whilst it is equal to the adiabatic index $n = -1/3$ otherwise. The values of $\dot{m}$ predicted by Eq. 4.7 are 6.4×10^{-11} $M_\odot$ yr^{-1} for n=0.8 and 1.42×10^{-10} $M_\odot$ yr^{-1} for n=-1/3.
Following the theory of secular evolution for X-ray binary systems, we can write the X-ray luminosity as

$$L = \frac{GM_1\dot{M}}{R_1} = 5.0\times10^{37}\, \frac{1}{3q - \frac{3}{2}n - \frac{5}{2}}\, m_1^{11/3} q^2 (1+q)^{-1/3} P_{2h}^{-8/3}\ erg\ s^{-1} \tag{4.8}$$

(see King, 1988), where we substitute for $\dot{M}$ the expression of Eq. 4.7, and assume an NS radius R_1 of 10 km. Since we need to compare the predicted luminosity with the bolometric observed luminosity, we extrapolate the 0.5-100 keV luminosity from all the available observations. For some observations the spectral analysis of the source was already shown in literature. Since the energy spectrum in this case is dominated by a cut-off power-law component with a cut-off energy at 85 keV (Bałucińska-Church et al., 2009), we only use this spectral component to extrapolate the unabsorbed luminosity, using the photon index and normalisation values reported in literature for each observation and fixing the cut-off energy at 85 keV. We find a flux of 3.06×10^{-10}, 3.61×10^{-10}, 3.38×10^{-10}, and 3.62×10^{-10} erg cm^2 s^{-1} for the observations taken by *Suzaku* (Bałucińska-Church et al., 2009), *EXOSAT* (Parmar et al., 1989), *BeppoSAX* (Bałucińska-Church et al., 1999), and *RXTE* (Galloway et al., 2008), respectively. On the other hand, we extract a flux of 4.7×10^{-10} erg cm^2 s^{-1} in the 0.5-100 keV energy band from the *XMM-Newton* observation, and of 3.3×10^{-10} erg cm^2 s^{-1} from the JEM-X/ISGRI observation.

If we consider the 2-10 keV RXTE/ASM light curve spanning 15.5 years of data, from 3 March 1996 (10145 TJD) to 12 September 2011 (15816 TJD), we can observe that the source maintained a roughly constant count-rate (see Fig. 4.7). Fitting the ASM light curve with a constant function, in fact, we obtain a count rate of (0.483±0.011) c s^{-1} with a $\chi^2(d.o.f.)$=5042(1388).

As a consequence of this, we estimate the mean flux for 4U 1323-619, averaging all the values of flux just obtained. The mean value of flux is of 3.6×10^{-10} erg cm^2 s^{-1}. To be more conservative, we verified that this result is not sensitive to the specific value of N_H that was previously used for the JEM-X/ISGRI fit, which is the maximum available in literature. Adopting the minimum value of N_H available in literature (3.2×10^{22} cm^{-2}; Bałucińska-Church et al., 2009), we extract a flux of 3.2×10^{-10} erg cm^2 s^{-1} for the JEM-X/ISGRI observation in the 0.5-100 keV energy band. Again, we obtain a mean value of flux of 3.6×10^{-10} erg cm^2 s^{-1} averaging all the values of flux obtained above.

Using the mean flux and adopting a distance of 10 kpc we determine a mean luminosity of $(4.3 \pm 0.4)\times10^{36}$ erg s^{-1} for 4U 1323-619. In this estimation, we took into account an arbitrary error of 10%. We observe that the luminosity predicted by Eq. 4.8 can reach a maximum value of 1.7×10^{36} erg s^{-1} for n=-1/3, and a value of 7.5×10^{35} erg s^{-1} for n=0.8. We show the mean luminosity together with that predicted by Eq. 4.8 in the upper panel of Fig. 4.8. From this comparison, we can conclude that, for a distance of 10 kpc, the observed mean luminosity is not in accordance with that predicted by the theory of the secular evolution. We note that a wrong distance value could contribute to the observed inconsistency.

For this purpose, we take into account the 3D extinction map of the radiation in the K_s band for our Galaxy (Marshall et al., 2006). This map suggests how great the extinction of the radiation is in the direction of the source ($l = 307°$, $b = 0.5°$) as a function of the distance. In Fig. 4.9 we report the extinction predicted by the model of Marshall et al. (2006) as a function of the distance from the source. We extrapolated the profile, taking into account the galactic coordinates of 4U

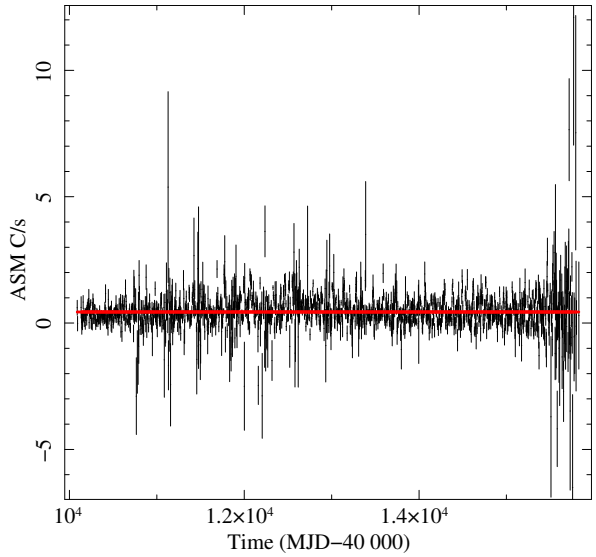

Figure 4.7: RXTE/ASM light curve in the 2-10 keV energy band. The red line represents the mean count rate maintained by 4U 1323-619 over 15.5 years. The bin time is four days.

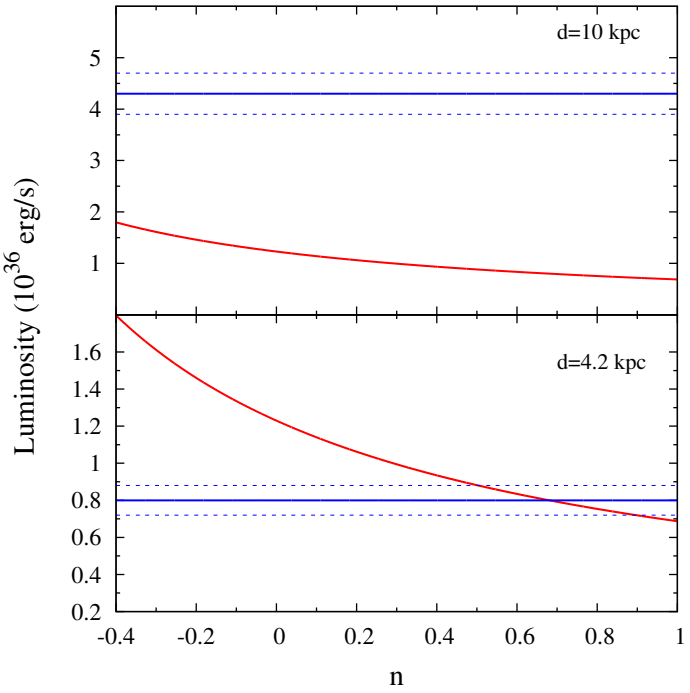

Figure 4.8: The red lines represent the luminosity as a function of the index n for a distance of 10 kpc (upper panel) and 4.2 kpc (lower panel). The blue continuous lines represent the best values of the mean luminosity, while the dashed lines represent the associated errors.

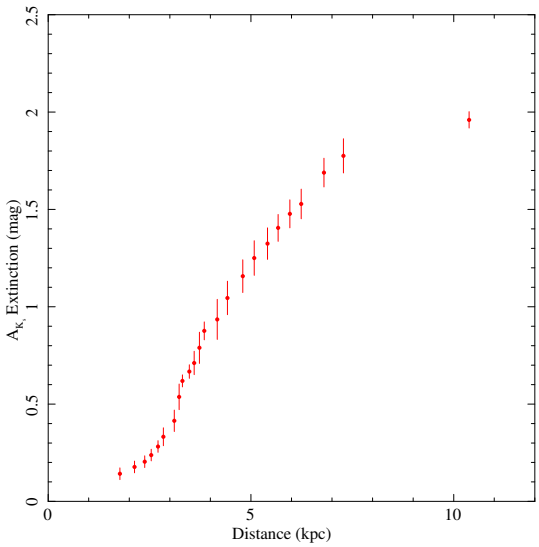

Figure 4.9: Extinction of the K_s radiation in the direction of the source ($l = 307°$, $b = 0.5°$) as a function of the distance (Marshall et al., 2006).

1323-619. We calculate the visual extinction using the Güver and Özel (2009) relation

$$N_H = (2.21 \pm 0.09) \times 10^{21} A_V, \tag{4.9}$$

where N_H is the equivalent column density of neutral hydrogen of the absorbing interstellar matter and A_V is the visual extinction of the source radiation. Using the N_H value 3.2×10^{22} cm^{-2} found by Bałucińska-Church et al. (2009), we estimate a visual extinction of A_V=14.5±0.7 mag that is compatible with the value found by Bałucińska-Church et al. (1999). The visual extinction is related to the extinction of the radiation in the K_s band through the relation

$$A_{K_S} = (0.062 \pm 0.005)\, A_V \text{ mag} \tag{4.10}$$

(Nishiyama et al., 2008), where A_{K_S} is the extinction in the K_S band. With this relation we find a value for the extinction of A_{K_S}= 0.90±0.09 mag.

We fitted the profile of the extinction of Fig. 4.9 with a quadratic function between 3 and 6 kpc, imposing a null value of the extinction for a null distance. The fit gives us a χ^2_{red} of 1.38 with 12 degrees of freedom, a linear parameter of 0.10± 0.02, and a quadratic parameter of 0.028±0.004. The uncertainties are given with a confidence level of 68%. According to the value of A_{K_S}, obtained before, we estimate a distance of $4.2^{+0.8}_{-0.7}$ kpc with a confidence level of 68%. This distance is fully in agreement with the value of distance suggested by Zolotukhin et al. (2010).

Taking into account a distance of $4.2^{+0.8}_{-0.7}$ kpc, we infer a luminosity of $(0.8 \pm 0.3) \times 10^{36}$ erg s^{-1} that is compatible with the one predicted by Eq. 4.8 for a n index close to 0.8 and thus for a thermal equilibrium state of the companion star (see Fig. 4.8).

A value of luminosity that completely matches the one predicted by Eq. 4.8 for n=0.8 is obtained for a distance to the source of d~4.17 kpc. According to the Marshall et al. (2006) model (see Fig.

4.9), an extinction of 0.88 mag competes for this value of distance in the K_s band, and thus, by Eq. 4.10 and Eq. 4.9, we infer A_v=14.2 mag and N_H ~3.1×10^{22} cm^{-2}. This value of N_H is fully in agreement with that obtained by Bałucińska-Church et al. (2009).

We also explored a non-conservative mass transfer scenario. We observe that in the case in which the mass is expelled from the position of the companion star, for an index n=0.8 and a distance from the source of 4.2 kpc, the luminosities obtained from the individual X-ray observations are compatible with the luminosity predicted by a non-conservative mass transfer theory for a value of $\beta \geq 0.8$, where β is the fraction of matter accreted onto the neutron star. This implies that the observations are in agreement with a scenario in which more than the 80% of the mass is accreted onto the neutron star. Thus, on the basis of the fact that only the 20% of mass of the companion star is lost from the system, we can confirm that the mass accretion mechanism could be rightly considered conservative.

To investigate the orbital evolution of the system, we need to compare the Kelvin-Helmholtz time-scale τ_{KH} (i.e. the characteristic time to reach the thermal equilibrium for a star) with the mass transfer time-scale $\tau_{\dot{M}}$. We calculate the Kelvin-Helmholtz time-scale adopting the relation

$$\tau_{KH} = 3.1 \times 10^7 \left(\frac{M_2}{M_\odot}\right)^2 \frac{R_\odot}{R_2} \frac{L_\odot}{L} \tag{4.11}$$

of Verbunt (1993), together with the mass-luminosity relation for a M-type star

$$\frac{L_2}{L_\odot} = 0.231 \left(\frac{M_2}{M_\odot}\right)^{2.61} \tag{4.12}$$

of Neece (1984). Moreover, we assume the Neece (1984) mass-radius relation of Eq. 4.6 for a main sequence M-type star in equilibrium. Our estimation of the Kelvin-Helmholtz time-scale is of τ_{KH}=9×10^8 yrs.

On the other hand, we extrapolate the mass transfer time-scale using the relation

$$\tau_{\dot{M}} = \frac{m_2}{\dot{m}} = \frac{G\, m_1 m_2}{L\, R_{NS}}, \tag{4.13}$$

where L is the source luminosity. To achieve this, we use the mean luminosity estimated above during the *ASM* monitoring, obtaining a mass transfer time-scale of 4.4×10^9 yrs. This value is greater than the Kelvin-Helmholtz time-scale by a factor of 4.9. This implies that the companion star is in thermal equilibrium and we can conclude that the mass-radius relation in Eq. 4.6 has been correctly used, suggesting that the proposed scenario is self-consistent.

To understand how the binary system is going to evolve, we estimate the orbital period derivative re-arranging Eq. 4 of Burderi et al. (2010):

$$\dot{m}_{-8} = 87.5\,(3n-1)^{-1} m_2 \left(\frac{\dot{P}_{-10}}{P_{2h}}\right), \tag{4.14}$$

where $\dot{P}_{-10}$ is the orbital period derivative in units of 10^{-10} s/s and P_{2h} is the orbital period of the system in units of two hours. Adopting an index n=0.8, we obtain a value of the period derivative of $\dot{P} \sim -5.4\times10^{-14}$ s/s that is compatible with the constraint on the $\dot{P}$, which is estimated

from our ephemeris, i.e. $(0.8 \pm 1.3) \times 10^{-11}$ s/s. From this result, we can infer that the orbital period is decreasing and that the system is shrinking as a consequence of the orbits being Keplerian.

4.7 Conclusions

We constrain the X-ray source position of 4U 1323-619, finding out that the source is located inside a circular area centred at RA (J2000)= 201.6543°and DEC (J2000)= -62.1358°and with a radius of 0.0002°(that is 0.6"). This result allows us to confirm the suggestion of Zolotukhin et al. (2010) that the B source in Fig. 4.1 is the IR counterpart of 4U 1323-619.
In addition, using observations from 1985 to 2011, we infer for the first time the linear and quadratic orbital ephemerides for 4U 1323-619. We estimate the orbital period of the binary system with an accuracy ten times higher than that which was proposed by Levine et al. (2011). We obtain a refined measure of the period of $P = 2.9419156(6)$ hrs, in line with previous estimates, as reported in the literature. We infer for the first time a weak constraint on the orbital period derivative of the system that is of $\dot{P} = (8 \pm 13) \times 10^{-12}$ s/s. Assuming a fully conservative mass-transfer scenario and that the companion star is an M-type main-sequence star, we estimate the mass of the companion to be of 0.28±0.03 $M_{\odot}$. This result suggests that the star is fully convective and that the magnetic braking mechanism can be ruled out as an explanation of angular momentum losses from the binary system, which is therefore driven by the mechanism of gravitational radiation.
We inferred that the companion star transfers matter onto the neutron star surface via the inner Lagrangian point in a conservative regime. According to the conservative mass-transfer scenario, and taking into account the map of the K_s radiation extinction in our Galaxy, we estimate a distance of $(4.2^{+0.8}_{-0.7})$ kpc at 68% confidence level.

CHAPTER 5

UPDATING THE ORBITAL EPHEMERIS OF THE DIPPING SOURCE XB 1254-690 AND THE DISTANCE TO THE SOURCE

Gambino A. F., Iaria R., Di Salvo T., Matranga M., Burderi L., PintoreF., Riggio A., Sanna A.

(2017)
Published in Research in Astronomy and Astrophysics,
Volume **17**, Issue 10, article id. 108

5.1 Abstract

XB 1254-690 is a dipping low mass X-ray binary system hosting a neutron star and showing type I X-ray bursts. We aim at obtaining more accurate orbital ephemeris and at constraining the orbital period derivative of the system for the first time. In addition, we want to better constrain the distance to the source in order to locate the system in a well defined evolutive scenario. We apply for the first time an orbital timing technique to XB 1254-690, using the arrival times of the dips present in the light curves that have been collected during 26 years of X-ray pointed observations performed from different space missions. We estimate the dip arrival times using a statistical method that weights the count-rate inside the dip with respect to the level of the persistent emission outside the dip. We fit the obtained delays as a function of the orbital cycles both with a linear and a quadratic function. We infer the orbital ephemeris of XB 1254-690 improving the accuracy of the orbital period with respect to previous estimates. We infer a mass of $M_2 = 0.42 \pm 0.04$ $M_\odot$ for the donor star, in agreement with the estimations already present in literature, assuming that the star is in thermal equilibrium while it transfers part of its mass via the inner Lagrangian point, and assuming a neutron star mass of 1.4 $M_\odot$. Using these assumptions, we also constrain the distance to the source, finding a value of 7.6±0.8 kpc. Finally,

we discuss the evolution of the system suggesting that it is compatible with a conservative mass transfer driven by magnetic braking.

5.2 Introduction

XB 1254-690 is a persistent low mass X-ray binary (LMXB) showing type I X-ray bursts and dips. The source coordinates have been accurately derived from Iaria et al. (2007) who, using one *Chandra* observation, located the source at RA (J2000)=194.4048°and DEC (J2000)=-69.2886°with a 90% confidence level error box of 0.6" radius. The dipping activity has been revealed during an *EXOSAT* observation in 1984 (Courvoisier et al., 1986) and consists in a periodic decrease of the count-rate. This decrease is caused by photoelectric absorption of part of the X-ray emission by the cold (and/or partially ionised) bulge of matter that forms as a consequence of the impact of the transferred plasma from the companion star onto the outer accretion disk (White and Swank, 1982). While the type I X-ray bursts testify the presence of a neutron star (NS) in the system (Mason et al., 1980), the presence of dips together with the absence of eclipses in the light curve constrain the inclination angle i of the system with respect to the line of sight to the observer between 60°and 80°(see Frank et al., 1987). The optical counterpart has been identified by Griffiths et al. (1978) with the faint V≃19 star GR Mus.
Timing analysis of the periodic dips led to the estimation of the orbital period of the system. Courvoisier et al. (1986) estimated the orbital period of the system on the basis of the recurrence time of the X-ray dips obtaining a period of 0.162(6) days. Motch et al. (1987) improved this estimate giving a period of 0.163890(9) days obtained from optical data, while Díaz Trigo et al. (2009) obtained an orbital period of 0.16388875(17) days, performing a periodogram on ASM data. In their survey of the timing properties of several LMXB systems, instead, Levine et al. (2011) assigned an orbital period of 0.1638890(4) days to XB 1254-690. Observations, however, revealed that the dipping activity is not always present and that the dips are quite different in shape from one observation to another.
Bhattacharyya (2007) reported a weak evidence of quasi periodic oscillations at about 95 Hz detected during one thermonuclear X-ray burst. Díaz Trigo et al. (2009), on the basis of the results of their spectral analysis performed on the source using *XMM-Newton* and *INTEGRAL* data, proposed the presence of a tilted accretion disk in the system. In this way they justified the disk temperature changes observed between the dip and non-dip time intervals of the XMM/INTEGRAL light curves, as well as the optical modulation observed with data collected from the optical Monitor (OM) of *XMM-Newton*. The modulation of the optical light curve was already observed by Motch et al. (1987). These authors observed that the optical light curve shows minima occurring 0.15 in phase after the X-ray dips, suggesting that the modulation is due to the varying aspect of the X-ray heated atmosphere of the donor star. They, however, did not rule out the presence of an asymmetric accretion disk that does not completely shadow

the companion star. A further confirmation of the hypothesis of a tilted accretion disk has been proposed by Cornelisse et al. (2013). They actually took advantage from the ephemeris of Díaz Trigo et al. (2009), revealing the presence of a negative superhump (i.e. a periodic photometric hump having a period shorter than the orbital period by a few percent). This supports the idea that XB 1254-690 could host a precessing accretion disk with a retrograde precession motion with a period of (6.74±0.07) days.
Cornelisse et al. (2013) proposed that the disk is tilted out of the orbital plane along its line of nodes implying that a large fraction of matter transferred from the companion star to the neutron star overflows or underflows the accretion disk instead of hitting onto the disk rim. In their opinion this could explain the presence of the absorption features observed by Iaria et al. (2007) and Boirin and Parmar (2003). They also found a marginal evidence of a possible positive superhump suggesting that the accretion disk is possibly eccentric due to effects of tidal resonance. On the basis of these results they inferred the mass ratio of the system, $q=M_2/M_1=0.33$-0.36, and constrained the mass of the neutron star, M_1, between 1.2 and 1.8 $M_\odot$.

A first estimate of the distance was advanced by Courvoisier et al. (1986). Using *EXOSAT* data, they inferred the distance to the source from two type-I bursts, assuming that the luminosity at the burst peak was the Eddington luminosity for a 1.4 $M_\odot$ neutron star. They obtained a distance of 12±2 kpc and 11±2 kpc for the two bursts, respectively. Subsequently, Motch et al. (1987) constrained the distance to the source in the range 8-15 kpc from a modeling of the optical emission. Their modeling also showed that the optical brightness of the source is well explained when assuming that the donor star is near the main sequence. in't Zand et al. (2003) reported an estimation of the distance to the source analysing data collected from *BeppoSAX* in 1999. The detection of a possible photospheric radius expansion (PRE) during one superburst precursor allowed them to estimate a distance of 13±3 kpc. A successive work by Galloway et al. (2008) allowed to infer an estimation of the distance, again on the basis of the properties of type I X-ray bursts from the source. Analysing data collected from the proportional counter array (PCA) on board the *RXTE* mission, Galloway et al. (2008) found only a marginal evidence of PRE during the observed type I X-ray bursts, and estimated a distance to the source of 15.5±1.9 kpc, in the case of a companion star with cosmic abundances, and of 20±2 kpc, in the case of a pure helium donor star, respectively.

In this work, we update the orbital ephemeris of XB 1254-690 using pointed observations collected by different space missions during a total time span of about 26 years. We constrain the orbital period derivative for the first time, and we give a revised estimate of the distance to the source. We also discuss the mass transfer in the system, suggesting that the system experiences a conservative mass transfer driven by magnetic braking of the companion star. The paper is structured as follows: in Sect. 5.3 we describe the data selection and reduction, in Sect. 5.4 we present the data analysis and the results, and in Sect. 5.5 we discuss the results.

Table 5.1: Observations used for the timing analysis

Sequential n.	Satellite/Instrument	Observation ID	Start time (UT)	Stop time (UT)	Number of dips
1	EXOSAT/ME	18332	1984 Feb 5 06:07:57	1984 Feb 5 09:08:14	1
2	EXOSAT/ME	31571	1984 Aug 7 03:10:27	1984 Aug 7 09:59:21	2
3	EXOSAT/ME	31593	1984 Aug 7 10:29:26	1984 Aug 7 14:04:14	1
4	EXOSAT/ME	49647	1985 Apr 15 04:27:23	1985 Apr 15 07:57:51	1
5	Ginga/LAC	900802113648, 900803061648	1990 Aug 02 11:37:52	1990 Aug 03 10:03:08	5
6	XMM/Epic-pn	60740101	2001 Jan 22 15:48:48	2001 Jan 22 20:02:19	1
7	RXTE/PCA	60044-01-01-02	2001 May 9 23:26:08	2001 May 10 01:37:04	1
8	RXTE/PCA	60044-01-01-03, 60044-01-01-05, 60044-01-01-08	2001 May 11 17:30:40	2001 May 12 11:46:40	3
9	XMM/Epic-pn	405510401	2007 Jan 14 01:12:04	2007 Jan 14 18:19:31	4
10	RXTE/PCA	93062-01-01-000	2008 Jan 16 05:28:00	2008 Jan 16 13:27:44	1
11	RXTE/PCA	95324-01-01-010	2009 Dec 31 03:51:12	2009 Dec 31 1 11:50:56	1
12	RXTE/PCA	95324-01-02-000, 95324-01-02-00	2010 Jan 1 01:44:48	2010 Jan 1 11:33:04	3
13	RXTE/PCA	95324-01-01-00	2009 Dec 31 21:01:52	2009 Dec 31 23:31:44	1

5.3 Observation and data reduction

To perform the data analysis of XB 1254-690 we take advantage of all the available pointed observations in X-ray archival data. However, no dip could be found in *BeppoSAX*, *ASCA*, *ROSAT*, *Swift*, and *Chandra* observations. We therefore analysed only the data collected by *EXOSAT*, *Ginga*, *RXTE* and *XMM-Newton*, which altogether span a temporal window of about 26 years (from 1984 to 2010).
EXOSAT observed XB 1254-690 eight times between 5 February 1984 and 15 April 1985. We used the background-subtracted data products of the *EXOSAT* Medium Energy experiment (ME) in the energy range between 1 and 8 keV. We binned the light curves at 6 s. In addition, we performed the barycentric corrections using the tool `earth2sun` and giving as an input the coordinates of the source found by Iaria et al. (2007). These coordinates will be used hereafter for all the subsequent analysis.

XMM-Newton observed the source five times between 22 January 2001 and 9 March 2007 with the EPIC-pn camera. The selected observations have been performed in fast timing mode. We processed the dataset with the `epproc` tool of the Scientific Analysis System (SAS) v. 14.0.0. We extracted source events only from a box centered at the RAWX coordinate of the maximum of the photons distribution (RAWX=37), and having a width of 15 RAWX. We extracted the light curves using the `evselect` tool, selecting only events with PATTERN≤4 (single and double pixel events) and FLAG=0 to ignore spurious events. The light curves have been extracted between 0.5 and 10 keV with a bin time of 0.006 s. The barycentric corrections have been applied with the `barycen` tool.

The available observations performed from RXTE/PCA are sparsely distributed in a temporal window of about 13 years (from 1997 to 2010). We used background-subtracted Standard 2 light curves covering the energy range 2-9 keV. The light curves have a bin time of 16 s and the barycentric corrections have been performed using the tool `faxbary`.

Ginga observed the binary system with the Large Area Counter experiment (LAC) on 17 July 1989 (ObsID 900802113648) and on 3 August 1990 (ObsID 900803061648). We use the background-subtracted light curves collected from the top layer of the detector covering the 2-17 keV energy band. The light curves have a bin time of 16 s and the barycentric corrections have been applied with the ftool `earth2sun`.

5.4 Data analysis

To obtain the orbital ephemeris of XB 1254-690 we need the arrival times of the dip as a function of time or of the orbital cycle. For the first time we apply a timing technique to the arrival times of the dips in order to improve the ephemeris of the source. The ephemeris obtained so far for XB 1254-690 in the X-ray band are based on periodograms performed on ASM data that have a statistic surely lower than the pointed observations we use in our analysis, which altogether span a temporal period of 26 years.
To obtain the dip arrival times we have to take into account the fact that XB 1254-690 shows dips varying in shape from one orbital cycle to another. For this reason, we cannot fit the dip with a specific function since this implies the assumption that the dip has always the same shape (see Gambino et al., 2016; Iaria et al., 2017, in preparation).
To address this issue, we take advantage from the method developed by Hu et al. (2008) to parameterize the dipping behaviour of XB 1916-053, and to systematically study its variation. The method can be applied both to dippers and eclipsing sources, and represents a powerful tool to obtain the dip arrival time for sources showing dips strongly variable in width and depth during different orbital cycles. The only constraint of this method is that the observation of at least a complete dip is required (Hu et al., 2008).
Therefore we selected all the available pointed observations in which single dips appear to be complete, collecting a total of 14 dips to analyse. In addition to these dips, the Ginga observations (ObsIDs 900802113648 and 900803061648) show 5 incomplete dips. Similarly, three RXTE observations (ObsIDs 60044-01-01-03, 60044-01-01-05 and 60044-01-01-08) show a total of three partial dips close in time, and other two incomplete dips are visible in two RXTE observations (ObsIDs 95324-01-02-000 and 95324-01-02-00). We will take into account all these incomplete dips in the second part of the data analysis. We report all the selected observations in Table 5.1. In each light curve we excluded all the type I X-ray bursts present, removing temporal intervals starting 5 s before the rise time and ending 100 s after the peak time of each burst. We implemented the method of Hu et al. (2008) on the available complete dips to find the dip arrival times. For each of these light curves we distinguished between the dip and the persistent (non-dip) states, by roughly guessing the boundaries of the dip (see Table 5.2). Then, we identified the persistent count-rate of the source by fitting the data points belonging to the persistent state

with the linear function that minimises the χ^2. Hereafter, the persistent count-rate level will be denoted by I_0. To obtain the dip arrival time in the light curve of each of the complete dips we have to average the times of each point in the dip weighting them by the difference between the corresponding count-rate and that of the predicted persistent state I_0. Then, re-arranging the relation of Hu et al. (2008) the time elapsed from the beginning of the observation at which the dip occurs is given by:

$$t_{dip} = \frac{\sum_{i=1}^{N} (I_0 - I_i)\, t_i}{\sum_{i=1}^{N} (I_0 - I_i)} \tag{5.1}$$

where i is an integer index running from the left boundary ($i = 1$) to the right boundary ($i = N$) of the dip and I_i is the value of count-rate at each time t_i included in the dip state domain. From eq. 5.1 it is evident that the choice of the dip state boundaries (i=1 and i=N) can be arbitrary. This is widely demonstrated by Hu et al. (2008) with different tests, and could be naively explained with the fact that the points lying in the persistent state beside the dip give little contribution to the sum (i.e. $I_0 - I_i \simeq 0$), and hence to the determination of the time t_{dip} at which the dip occurs.
The arrival times of the dips are then calculated as $T_{dip} = T_{start} + t_{dip}$, where T_{start} is the starting time of the specific observation (see Table 5.1). We evaluate the delays of the observed dip arrival times with respect to the arrival times predicted using the orbital period $P = 14160.01s$ of Levine et al. (2011) and an arbitrary reference epoch $T_0 = 12733.0546\, TJD$, corresponding to the arrival time of the dip observed in the XMM-Newton observation (ObsID 60740101). The arrival times, as well as the corresponding orbital cycle and the delays (O-C) are reported in Table 5.3 (First Iteration).

The error associated with the delays of the dip arrival times is determined by the standard deviation σ of the distribution of the obtained phase delays associated to each dip. The σ of the distribution is equal to 0.04 that corresponds to 544 s according to the trial orbital period we used.
Using the same technique performed in Gambino et al. (2016) and in Iaria et al. (2015a), we fit the delays with a linear function

$$y(N) = a + bN, \tag{5.2}$$

where N is the number of orbital cycles, b is the correction to the trial orbital period (ΔP_0) in seconds and a is the correction to the trial reference time (ΔT_0) in seconds. We obtain $\chi^2(d.o.f.)$= 12.94(12). The best-fit model parameters are reported in Table 5.4 (First Iteration). Applying the obtained corrections for the trial orbital period and the trial reference time we find the following linear orbital ephemeris:

$$T_{dip}(N) = \text{TJD(TDB)}\, 11931.8065(17) + \frac{14160.004(6)}{86400} N, \tag{5.3}$$

Table 5.2: Determination of the arrival times of complete dips and phases of folded dips. t_{dip} is given in seconds from the start time of the corresponding observation. ϕ_{dip} is the phase of arrival derived from the folding of close-in-time incomplete dips.

Point	Satellite/Instrument	ObsID	Time interval (s)	Phase Interval	Dip boundary (s)	Dip boundary (Phase)	t_{dip} (s)	ϕ_{dip}
1	EXOSAT/ME	18332	0 – 13038	–	5400 – 6254	–	5895.3097	–
2	EXOSAT/ME	31571	0 – 12732	–	5500 – 9350	–	7170.5962	–
3	EXOSAT/ME	31571	15168 – 29328	–	18900 – 22950	–	21302.0361	–
4	EXOSAT/ME	31593	1044 – 15204	–	6600 – 10650	–	8423.0805	–
5	EXOSAT/ME	49647	3018 – 17178	–	8548 – 10748	–	9639.4763	–
6	Ginga/LAC	900802113648, 900803061648	–	0.55 – 1.55	–	0.91 – 1.13	–	1.04
7	XMM/Epic-pn	60740101	5542 – 19702	–	11301 – 13701	–	12259.9043	–
8	RXTE/PCA	60044-01-01-02	0 – 9368	–	300 – 3500	–	1917.2109	–
9	RXTE/PCA	60044-01-01-03, 60044-01-01-05, 60044-01-01-08	–	0.47 – 1.47	–	0.83 – 1.06	–	0.95
10	XMM/Epic-pn	405510401	1277 – 15437	–	8150 – 10051	–	9143.1486	–
11	XMM/Epic-pn	405510401	15462 – 29622	–	21800 – 23100	–	22526.2440	–
12	XMM/Epic-pn	405510401	30313 – 44473	–	36401.0, 38401.0	–	37425.4854	–
13	XMM/Epic-pn	405510401	45231 – 59391	–	50801 – 52901	–	52037.2646	–
14	RXTE/PCA	93062-01-01-000	0 – 10360	–	2500 – 4000	–	3235.2159	–
15	RXTE/PCA	95324-01-01-010	19352 – 33512	–	26205 – 26705	–	26409.6572	–
16	RXTE/PCA	95324-01-02-000, 95324-01-02-00	–	0.54 – 1.54	–	0.88, 1.20	–	1.05
17	RXTE/PCA	95324-01-01-00	56 – 14216	–	6610 – 8890	–	6990.6641	–

where 11931.8065(17) TJD and 14160.004(6) s are the new reference time and orbital period, respectively. The associated errors are at 68% confidence level.

However, we expect that, due to the orbital evolution of the binary system, a quadratic term has to be included in the orbital ephemeris. At this purpose, our method easily allows to evaluate the orbital period derivative of the system taking into account the possibility that the delays follow a quadratic trend. Then, we fitted the delays with a quadratic function as

$$y(N) = a + bN + cN^2, \tag{5.4}$$

where a is the reference time correction (ΔT_0) in seconds, b is the orbital period correction (ΔP_0) in seconds and $c = \frac{1}{2} P_0 \dot{P}$ in units of seconds. The best-fit parameters are reported in Table 5.4 (First Iteration) and allow to obtain a new reference time T_0 of 11931.812(4) TJD, a new orbital period of 14159.984(15) s and the orbital period derivative $\dot{P} = (-1.3 \pm 2.0) \times 10^{-10} s/s$. Here, the associated error on the orbital period is at 68% confidence level, while the error on the orbital period derivative is at 95% confidence level.

Nevertheless, this quadratic fit gives a $\chi^2(d.o.f.)$=10.73(11) and the estimated F-test probability of chance improvement with respect to the previous linear fit is of the 82%. This suggests that adopting the quadratic ephemeris does not improve significantly the fit.

The delays as a function of the number of orbital cycles are shown in the upper panel of Fig. 5.2. Superimposed we report the best-fit linear function as a solid line. In the lower panel of the same figure we show the residuals of the delays with respect to the linear best-fit function. The maximum deviation of the points with respect to the linear model is of 794 s, that is the 6% of the orbital period. Note, however, that error we associated to the delays of the dip arrival times, while taking into account the statistical error produced by the photon counting and by the phase

jitter, also includes the contribution of the linear and quadratic terms, or even of higher orders of the time derivative of the orbital period. In order to avoid to overestimate the uncertainties on the fitting parameters, we performed again the linear and quadratic fits, assuming the *post-fit* standard deviation as error for each point. This error is determined by the distribution of the points around the best-fit parabolic trend. In this case, therefore, the χ^2 cannot be used as an estimator of the goodness of the fit, because the error is exactly equal to the distribution of the points around the best-fit function, but in this way we get a correct estimate of the uncertainty of the fit parameters. The fits returned the same parameters we found previously and that are reported in Table 5.4. This means that the uncertainty in the fit parameters is dominated in this case by the large scattering intrinsic in the data.

In order to increase the statistics on the timing technique, we can also take the advantage from the observations performed by RXTE and Ginga (sequential numbers 5, 8 and 12 in Table 5.1) that we excluded in the first part of the analysis. These pointed observations, in fact, do not show a complete dip in the light curves, but if conveniently folded when close in time, they can provide further measurements of the dip arrival times.

We folded each group of these observations using the updated ephemeris given in eq. 5.3. As already done in the first part of the analysis we distinguished the dip state from the persistent non-dip state guessing the boundaries of the dip. Then, we applied the method of Hu et al. (2008) to each folded dip profile obtaining the phases at which the dips occur. The dip boundaries as well as the phases at which the folded dips occur are reported in Table 5.2.

The dip arrival times are estimated, starting from the obtained phases, as $T_{dip} = T_0 + (N + \phi_{dip})P_0$, where T_0 and P_0 are the reference epoch and the orbital period evaluated with the updated ephemeris of eq. 5.3. With this new trial orbital period P_0 we obtain the delays of the dip arrival times with respect to T_0. To be conservative with the first part of the analysis, we associate to these delays the same error that we evaluated for the first set of delays already analysed during the first iteration. In Table 5.3 (Second Iteration) we report the dip arrival times, the orbital cycles as well as the delays for these supplementary observations.

To integrate the delays evaluated in the first part of the analysis with those evaluated just now, we rescaled the delays obtained in the first iteration with respect to the new T_0 and P_0 of the updated ephemeris in eq. 5.3. We show the whole set of delays as function of the corresponding orbital cycles in the right panel of Fig. 5.2. We fitted all the delays with respect to the linear function in eq. 5.2, obtaining a $\chi^2(d.o.f.)$= 17.47(15). We report the best-fit model parameters in Table 5.4 (Second Iteration). Applying the corrections suggested by the linear fit, we find the following new linear orbital ephemeris:

$$T_{dip}(N) = \text{TJD(TDB)}\ 11931.8069(16) + \frac{14160.004(6)}{86400}N, \tag{5.5}$$

where $11931.8069(16)TJD$ and $14160.004(6)s$ are the new corrected reference epoch and orbital period, respectively. As done before, we also tried to fit the delays with the quadratic function

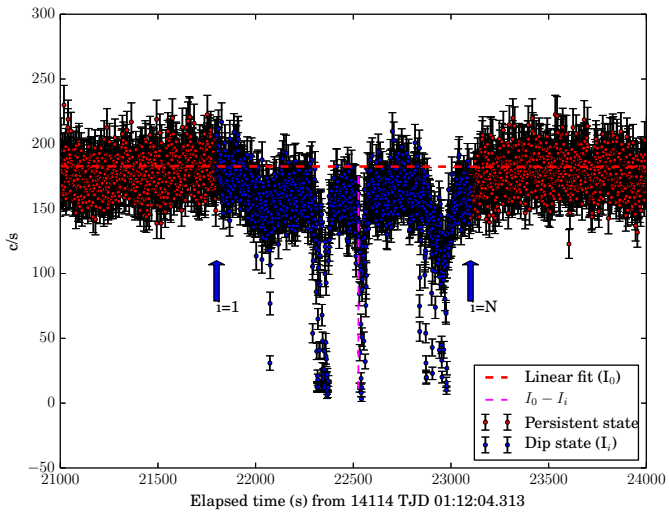

Figure 5.1: One of the dips (Point 11) analyses in this work, corresponding to an observation (ObsID 405510401) performed by the *XMM-Newton* space mission. We indicate the division between the dip state (delimited between i=1 and i=N, respectively) and the persistent state. The linear function fitting the persistent count-rate is shown as a red dashed line (I_0).

of eq. 5.4. Also in this case, the best-fit parameters are reported in Table 5.4 (Second Iteration). Applying the corrections returned by the quadratic fit to the starting ephemeris we obtain a new reference time T_0 of 11931.808(3) TJD, a new orbital period of 14160.000(11) s and the orbital period derivative $\dot{P} = (0.0 \pm 1.4) \times 10^{-10} s/s$. The associated error on the orbital period is at 68% confidence level, while the error on the orbital period derivative is at 95% confidence level.
Nevertheless, the quadratic fit gives a $\chi^2(d.o.f.)$=17.20(14) and the estimated F-test probability of chance improvement with respect to the previous linear fit is of the 63%. This suggests that adopting the quadratic ephemeris we do not improve significantly the fit.
Again, we ran the same fits using the post-fit standard deviation as error for each delay, obtaining the compatible results.
Even though the new ephemeris of eq. 5.5 does not significantly improve the ephemeris of eq. 5.3, they are extended on a data set that include all the available pointed observations in the X-ray archive. In addition, although the quadratic ephemeris does not improve the significance of the fit, it is fundamental to evaluate an upper limit on the orbital period derivative. The one reported in this paper represents also the only available constraint on the orbital period derivative present to date. This constraint will be improved when further observations of XB 1254-690 will be available.

Table 5.3: Journal of arrival times of the X-ray dips obtained from each light curve for both the iterations performed in the data analysis.

	First Iteration			**Second Iteration**		
Point	Dip time (TJD;TDB)	Cycle	Delay (s)	Dip time (TJD;TDB)	Cycle	Delay (s)
1	5735.324	-37809	202(544)	5735.324	-37809	-517(544)
2	5919.215	-36687	896(544)	5919.215	-36687	182(544)
3	5919.379	-36686	867(544)	5919.379	-36686	154(544)
4	5919.535	-36685	168(544)	5919.535	-36685	-545(544)
5	6170.297	-35155	1245(544)	6170.297	-35155	541(544)
6	–	–	–	11931.762	-23347	516(544)
7	11931.801	0	0(544)	11931.801	0	-493(544)
8	12038.999	654	1250(544)	12038.999	654	761(544)
9	–	–	–	11931.808	665	-728(544)
10	14114.156	13316	786(544)	14114.156	13316	373(544)
11	14114.311	13317	9(544)	14114.311	13317	-404(544)
12	14114.483	13318	748(544)	14114.483	13318	335(544)
13	14114.652	13319	1200(544)	14114.652	13319	787(544)
14	14481.265	15556	611(544)	14481.265	15556	211(544)
15	15196.466	19920	-306(544)	15196.466	19920	-680(544)
16	–	–	–	11931.844	19924	748(544)
17	15196.957	19923	-365(544)	15196.957	19923	-739(544)

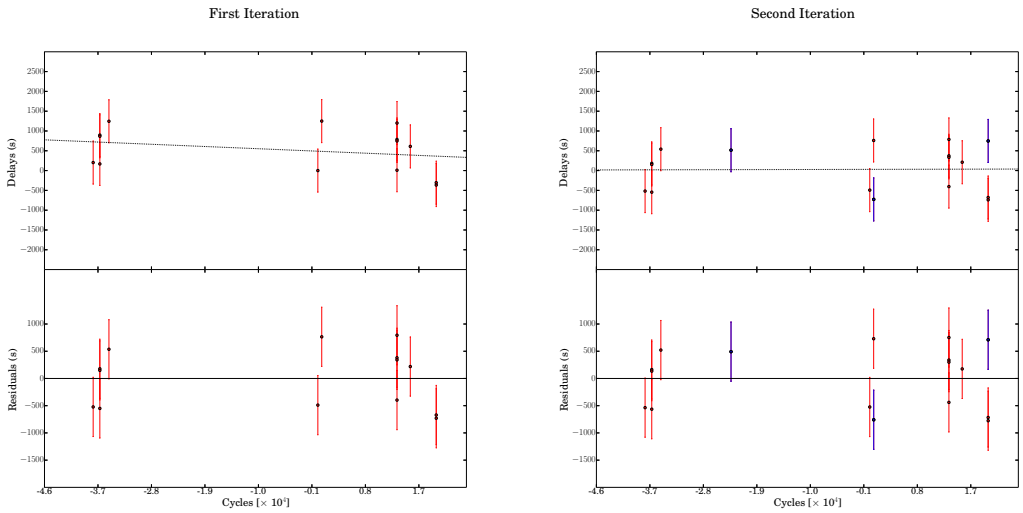

Figure 5.2: Delays as a function of the orbital cycle for the first and the second iteration. The blue points represent the supplementary points added in the second iteration. Upper panel: linear fit of the delays. Lower panel: residuals of the delays with respect to the linear best-fit function.

Table 5.4: Best-fit values obtained from the linear and quadratic fits of the delays of the dips arrival times.

	First Iteration		**Second Iteration**	
Parameter	Linear	Quadratic	Linear	Quadratic
a (s)	489 ± 154	954 ± 342	31±134	149±264
b ($\times 10^{-3}$ s)	-6 ± 6	-26±15	0±6	-5±11
c ($\times 10^{-7}$ s)	–	-9±6	–	-3±5

5.5 Discussion

We derived and improved the orbital ephemeris for XB 1254-690 taking the advantage of the whole X-ray data archive, that consists in pointed observations spanning 26 years. The direct measurement of the dip arrival times allowed to increase the accuracy of the orbital period of the system by a factor of 10 with respect to the previous estimation of Levine et al. (2011), and by a factor of 4 with respect to the value estimated by Díaz Trigo et al. (2009). Furthermore, we evaluated for the first time a constraint on the orbital period derivative of $|\dot{P}| < 1.4 \times 10^{-10}\ s/s$. This value is compatible with zero and includes both positive and negative values and for this reason should be considered an upper limit on the modulus of the orbital period derivative. However, the result represents a first evaluation of this orbital parameter so far in literature for this source and will be certainly improved including future observations when these will be available.

In the following, using the equations for the secular evolution of the source, we discuss the mass transfer for XB 1254-690 in order to get more information on the system. As a first step, we evaluate the observed mass accretion rate onto the neutron star surface.

Iaria et al. (2001), modelling the spectrum of XB 1254-690 collected by *BeppoSAX* in the wide band 0.1 - 100 keV, estimated an averaged unabsorbed flux of 1.4×10^{-9} erg cm^{-2} s^{-1}. Taking into account the value of distance of 15.5±1.9 kpc proposed by Galloway et al. (2008), and the value of flux inferred by Iaria et al. (2001), assuming a neutron star radius R_{NS} of 10 km, we can estimate the observed mass accretion rate onto the neutron star as

$$\dot{M}_{obs} = \frac{L_X R_{NS}}{G M_1} = \frac{4\pi d^2 \Phi R_{NS}}{G M_1}, \tag{5.6}$$

where L_X is the observed bolometric X-ray luminosity, M_1 is the mass of the neutron star that we assumed to be 1.4 $M_\odot$ and Φ is the flux observed by Iaria et al. (2001). We obtain an observational mass accretion rate $\dot{M}$ of $(3.4\pm0.8)\times10^{-9}$ $M_\odot$ yr^{-1}.

To understand in which evolutive scenario the system has to be located, we compare the observed mass accretion rate with that predicted by the theory of secular evolution for low mass X-ray binary systems. As mechanisms of angular momentum loss we take into account the emission of gravitational waves (gravitational radiation), as well as the magnetic braking. We do not rule out the possibility that the magnetic braking term plays a role as a mechanism of angular momentum loss, owing to the fact that the mass of the companion star, inferred assuming the condition

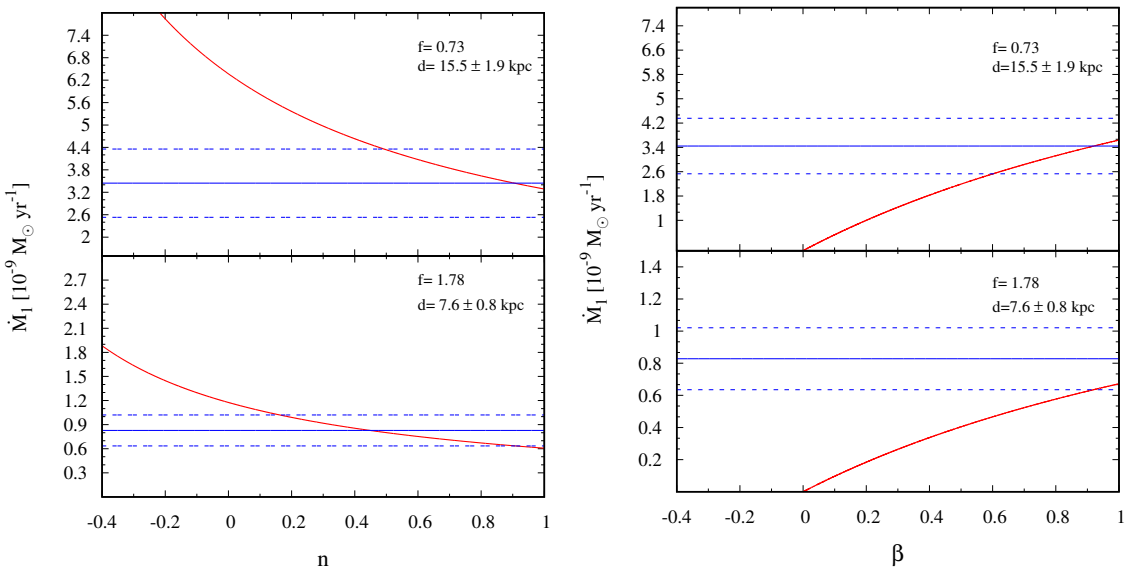

Figure 5.3: Red curves: theoretical mass accretion rate onto the neutron star surface predicted by eq. 5.7. Blue lines: best value of the mass accretion rate obtained from the observations (solid line) and relative errors (dashed lines) for d=15.5±1.9 kpc and 7.6±0.8 kpc (upper and lower panels, respectively). Left plot: mass accretion rate as a function of n adopting a conservative mass transfer scenario (β=1). Right plot: mass accretion rate as a function of β adopting an index $n = 0.8$ (donor star in thermal equilibrium).

of thermal equilibrium (see eq. 25 in Verbunt, 1993), is large enough to generate the dynamo effect resulting in a net magnetic field anchored into the companion star surface (see Nelson and Rappaport, 2003).

The mass accretion rate predicted by the theory of secular evolution, under the assumed hypothesis, is given by the relation of Burderi et al. (2010) (see also Di Salvo et al., 2008):

$$\dot{m}_{-8} = -3.5 \times 10^{-4}[1.0 + T_{MB}]\, m_1\, m_{2,0.1}^2\, m^{-1/3} P_{5h}^{-8/3} \times F(n, g(\beta, q, \alpha)), \tag{5.7}$$

where

$$F(n, g(\beta, q, \alpha)) = [n - 1/3 + 2g(\beta, q, \alpha)]^{-1}$$

and

$$g(\beta, q, \alpha) = 1 - \beta q - (1 - \beta)(\alpha + q/3)/(1 + q).$$

In these relations, $\dot{m}_{-8}$ is the secondary mass derivative (negative since the secondary star looses mass) in units of 10^{-8} $M_\odot$ yr^{-1}, m is the sum of the masses of the neutron star and of the donor star (m_1 and m_2, respectively) in units of solar masses, while $m_{2,0.1}$ is the donor star mass in units of 0.1 solar masses. In addition, $q = m_2/m_1$, β is the fraction of the mass transferred by the companion that is accreted onto the neutron star surface, α is the specific angular momentum of the mass leaving the system in units of the specific angular momentum of the companion star,

P_{5h} is the orbital period in units of five hours and n is the index of the mass-radius relation adopted in eq. 5.10. Being associated to the internal structure of the companion star, n can assume values ranging from 0.8 to -1/3. In particular, n =0.8 is the index that is associated to stars in thermal equilibrium (see Neece, 1984), meanwhile n =-1/3 is associated to stars outside the thermal equilibrium that are also fully convective (see e.g. Burderi et al., 2010). We suppose, moreover, that the mass expelled from the system (if any) is ejected from the position of the inner Lagrangian point. Then we fix $\alpha = 0.7$.
The term T_{MB} represents the contribution of angular momentum loss due to the magnetic braking. Re-arranging the expression reported by Burderi et al. (2010), this term can be expressed as:

$$T_{MB} = 8.4\, k_{0.1}^2 f^{-2} m_1^{-1} q^{1/3} (1+q)^{2/3} P_{2h}^2, \tag{5.8}$$

where f is a dimensionless parameter of order of unity: preferred values are $f = 0.73$ (Skumanich, 1972) or $f = 1.78$ (Smith et al., 1979), and $k_{0.1}$ is the radius of gyration of the star in units of 0.1 (Claret and Gimenez, 1990). Here, revealing in advance one result of the subsequent analysis, we will assume that the mass of the companion star is M_2 =0.42 $M_\odot$, which is the mass the companion star, supposed a main sequence star, should have in order to fill its Roche Lobe for the orbital period of the system, $\sim$ 3.9 h (see eq. 25 in Verbunt, 1993).
We can compare the theoretical mass accretion rate predicted by eq. 5.7 adopting a conservative mass transfer scenario (β=1) with the observed mass accretion rate in the source.
Adopting a distance to the source of d=15.5$\pm$1.9 kpc (Galloway et al., 2008), and setting the parameter f of eq. 5.8 equal to 0.73 (Skumanich, 1972), we observe an accordance between theory and observations at n$\sim$0.8 (see Fig. 5.3, left upper panel). This means that according to the theory of secular evolution of the X-ray binary systems, we expect that the companion star is in thermal equilibrium. For the same distance, we also tried the parameter f=1.78 (Smith et al., 1979) for the magnetic braking obtaining that there is accordance neither with n=0.8 nor with n=-1/3. Furthermore, we explored the case in which the magnetic braking term of eq. 5.8 does not play a role in the angular momentum losses of the binary system. In this case, however, we do not observe any accordance between the theoretical mass accretion rate and that observed by Iaria et al. (2001), owing to the fact that in this case the theoretical mass accretion rate underestimates the observed mass accretion rate for any value of n.
This value of distance, however, as well as the distance of d=13$\pm$3 kpc inferred by in't Zand et al. (2003), has been inferred by the analysis of X-ray type-I bursts, assuming that they show photospheric radius expansion (PRE), and thus, that the peak luminosity of the bursts is the Eddington luminosity for a neutron star of 1.4 $M_\odot$. However, as the same authors reported in their works, the observations they analysed have not enough statistics to be sure of a PRE, and as a consequence of this their distances could be overestimated.
On the other hand, Cornelisse et al. (2013) obtained an estimation of the range of q and of M_{NS}, totally independent from assumptions about the distance to the source. This allows us to obtain a

range of masses for the donor star of 0.46-0.50 $M_\odot$, assuming a mass of the neutron star of 1.4 $M_\odot$.

To sketch the most probable evolutive scenario, as well as to constrain the distance of XB 1254-690, we need to evaluate the companion star mass using the results of our timing analysis. At this purpose, we assume that the companion star is a main sequence star in thermal equilibrium. The self-consistency of this hypothesis will be tested in the subsequent part of the discussion. All the available X-ray data of XB 1254-690 clearly demonstrate that the source is a persistent X-ray emitter over a temporal window of about 26 years. As a consequence of this, we can properly assume that the companion star fills its Roche lobe, continuously transferring part of its mass to the neutron star. Thus, we impose that the companion star radius R_2 has to be equal to the Roche lobe radius R_{L2}, given by the expression of Paczyński (1971):

$$R_{L2} = 0.46224\, a \left(\frac{m_2}{m_1 + m_2}\right)^{1/3}, \tag{5.9}$$

where m_1 and m_2 are the NS and companion star masses in units of solar masses and a is the orbital separation of the binary system. Hereafter, we are going to assume a NS mass of 1.4 $M_\odot$ for the subsequent analysis. Our assumption that the companion star belongs to the lower main sequence brings us to adopt the mass-radius relation of Neece (1984) for M-stars:

$$\frac{R_2}{R_\odot} = 0.877\, m_2^{0.807}. \tag{5.10}$$

Using eq. 5.9 and eq. 5.10 along with the third Kepler law, that links the orbital separation a with the value of the orbital period found with the linear ephemeris, we obtain a mass of 0.42±0.04 $M_\odot$ for the donor star. Here we took into account an accuracy of 10% in the mass estimation (see Neece, 1984).

Our estimation of the donor star mass of 0.42±0.04 $M_\odot$ is in accordance with the values of Cornelisse et al. (2013) and as a consequence of this, we guess that the donor is probably a main sequence star in thermal equilibrium. With this assumption, we can estimate the maximum distance that the system can have, assuming that the Kelvin-Helmholtz time-scale τ_{KH} (i.e. the characteristic time that a star spends to reach the thermal equilibrium) is equal to the mass transfer time-scale $\tau_{\dot{M}}$.

The Kelvin-Helmholtz time-scale is given by the relation

$$\tau_{KH} = 3.1 \times 10^7 \left(\frac{M_2}{M_\odot}\right)^2 \frac{R_\odot}{R_2} \frac{L_\odot}{L} \mathrm{yr} \tag{5.11}$$

of Verbunt (1993), where we adopt the mass-luminosity relation for M-type stars of Neece (1984)

$$\frac{L_2}{L_\odot} = 0.231 \left(\frac{M_2}{M_\odot}\right)^{2.61} \tag{5.12}$$

and the mass-radius relation of Neece (1984) of eq. 5.10.

On the other hand, the mass transfer time-scale is given by:

$$\tau_{\dot{M}} = \frac{m_2}{\dot{m}} = \frac{G\, m_1 m_2}{L_X\, R_{NS}}, \tag{5.13}$$

where L_X is the bolometric source luminosity.
Imposing the similarity between τ_{KH} and $\tau_{\dot{M}}$ we obtain the maximum luminosity of the system in the hypothesis that the donor star is in thermal equilibrium in main sequence : $L_X \sim (10 \pm 2) \times 10^{36}\ erg\ s^{-1}$.
The distance to the source for XB 1254-690 can be obtained by the flux inferred by Iaria et al. (2001) in the band 0.1-100 keV and from the X-ray luminosity just obtained as

$$d = \sqrt{\frac{L_X}{4\pi\Phi}} = 7.6 \pm 0.8\ kpc. \tag{5.14}$$

Once we obtained the new value of the distance, we repeated the comparison between the mass accretion rate predicted by the theory of secular evolution and that observed by Iaria et al. (2001), rescaled for the updated distance.
In this case we observe that assuming β=1 (conservative mass transfer) there is no agreement between theory and observation adopting the parameter f=0.73 in eq. 5.8. Using f=1.78, however, the agreement is achieved for $n \sim 0.8$ (see Fig. 5.3, left lower panel). In this case, therefore, we find a solution that is consistent with our initial hypothesis of a donor star in thermal equilibrium. Again the magnetic braking term T_{MB} is necessary to explain the observed mass accretion rate, owing to the fact that otherwise for every n no accordance is found between the theoretical mass accretion rate and the observed one.
For completeness, we also explore the non-conservative mass transfer scenario for both the distances considered above, adopting the same f parameters used for the conservative case and assuming n=0.8. For a distance of 15.5±1.9 kpc the observation is in agreement with the theory for a value of $\beta \sim 0.9$, i.e. the 90% of the mass of the companion star is accreted onto the neutron star surface. On the other hand, adopting a distance of 7.6±0.8 kpc we find a lower limit for β of about 0.92. This actually means that most of the mass transferred by the donor star is accreted onto the neutron star.

In order to have a further confirmation of the scenario just depicted for XB 1254-690, and to understand the temporal evolution that the orbital separation of the system will undergo, we use the relation

$$\dot{m}_{-8} = 87.5\,(3n-1)^{-1} m_2 \left(\frac{\dot{P}_{-10}}{P_{2h}}\right), \tag{5.15}$$

of Burderi et al. (2010) to obtain a theoretical estimation of the orbital period derivative of the system. In the equation, $\dot{P}_{-10}$ is the orbital period derivative in units of 10^{-10} s/s, P_{2h} is the orbital period of the system in units of two hours and $\dot{m}_{-8}$ is the secondary mass derivative in units of 10^{-8} $M_\odot$ yr^{-1}. Adopting the value of $\dot{m}$ at n=0.8, the mass of the companion star inferred in our analysis and the orbital period obtained with the linear ephemeris, we predict a negative $\dot{P}$ of -5×10^{-13} s s^{-1}, meaning that the binary system is expected to shrink in agreement with the assumption of a companion star in thermal equilibrium and with the assumed mass-radius index

of 0.8.
The theoretical value of $\dot{P}$ we inferred for this system is indeed compatible with the upper limit of the orbital period derivative obtained through the quadratic ephemeris: $|\dot{P}| < 1.4 \times 10^{-10}$ s s^{-1}.

5.6 Conclusions

In this work we update the existent orbital ephemerides for XB 1254-690, taking the advantage of about 26 years of X-ray data and performing direct measurements of the dip arrival times on different pointed observations. We further increase the accuracy reached by Levine et al. (2011) by one order of magnitude.
The quadratic ephemeris, even though not statistically significant with respect to the linear ephemeris, allows to constrain the orbital period derivative of the system for the first time. Assuming that the companion star is in thermal equilibrium we infer a donor star mass of 0.42 ± 0.04 M$_\odot$, that is in agreement with the range of masses estimated by Cornelisse et al. (2013), assuming that the mass of the neutron star is 1.4 M$_\odot$.
In our analysis we propose a different estimate of the distance to the source with respect to those obtained by in't Zand et al. (2003) and Galloway et al. (2008). These authors provided an estimate of the distance to the source that, as they state, should be considered as upper limits to the distance to the source, owing to the relatively poor statistics of the data they analysed. We suggest a new distance of 7.6 ± 0.8 kpc that represents the distance for which the companion star has a Kelvin-Helmholtz time-scale that is similar to the mass transfer time-scale in this system. For larger distances, the inferred mass accretion rate would be higher, implying a mass transfer timescale shorter than the Kelvin-Helmholtz timescale of the donor, bringing the companion star out of thermal equilibrium.
These results, as well as the assumption of a neutron star of 1.4 M$_\odot$, allow us to state that the most probable scenario for this system is the one in which the companion star is in thermal equilibrium and that most of (if not all) the mass transferred by the companion is accreted onto the neutron star in a conservative way through the inner Lagrangian point, independently if we assume a distance of 15.5±1.9 kpc or of 7.6±0.8 kpc. Moreover, the analysis strongly supports the idea that the magnetic braking plays an important role in the the angular momentum loss in this binary system. In the hypothesis that the companion star is in thermal equilibrium with a mass-radius index of about 0.8, we also predict that the binary orbit is shrinking at a rate of about -5×10^{-13} s s^{-1}. This prediction can be easily tested with future observations, when the uncertainty on the orbital period derivative we have now will be greatly reduced.

CHAPTER 6

SIGNATURE OF THE PRESENCE OF A THIRD BODY ORBITING AROUND XB 1916-053

Iaria R., Di Salvo T., Gambino A. F., Del Santo M., Romano P., Matranga M., Galiano C. G., Scarano, F., Riggio A., Sanna A., Pintore F., Burderi L. (2015)
Published in Astronomy & Astrophysics,
Volume **582**, id.A32, 13 pp.

6.1 Abstract

Context: The ultra-compact dipping source XB 1916-053 has an orbital period of close to 50 min and a companion star with a very low mass (less than 0.1 $M_\odot$). The orbital period derivative of the source was estimated to be $1.5(3) \times 10^{-11}$ s/s through analysing the delays associated with the dip arrival times obtained from observations spanning 25 years, from 1978 to 2002.
Aims: The known orbital period derivative is extremely large and can be explained by invoking an extreme, non-conservative mass transfer rate that is not easily justifiable. We extended the analysed data from 1978 to 2014, by spanning 37 years, to verify whether a larger sample of data can be fitted with a quadratic term or a different scenario has to be considered.
Methods: We obtained 27 delays associated with the dip arrival times from data covering 37 years and used different models to fit the time delays with respect to a constant period model.
Results: We find that the quadratic form alone does not fit the data. The data are well fitted using a sinusoidal term plus a quadratic function or, alternatively, with a series of sinusoidal terms that can be associated with a modulation of the dip arrival times due to the presence of a third body that has an elliptical orbit. We infer that for a conservative mass transfer scenario the modulation of the delays can be explained by invoking the presence of a third body with mass

between 0.10–0.14 $M_\odot$, orbital period around the X-ray binary system of close to 51 yr and an eccentricity of 0.28 ± 0.15. In a non-conservative mass transfer scenario we estimate that the fraction of matter yielded by the degenerate companion star and accreted onto the neutron star is $\beta = 0.08$, the neutron star mass is ≥ 2.2 $M_\odot$, and the companion star mass is 0.028 $M_\odot$. In this case, we explain the sinusoidal modulation of the delays by invoking the presence of a third body with orbital period of 26 yr and mass of 0.055 $M_\odot$.
Conclusions: From the analysis of the delays associated with the dip arrival times, we find that both in a conservative and non-conservative mass transfer scenario we have to invoke the presence of a third body to explain the observed sinusoidal modulation. We propose that XB 1916-053 forms a hierarchical triple system.

6.2 Introduction

The X-ray source XB 1916-053 is a low-mass X-ray binary (LMXB) showing dips and type-I X-ray bursts in its light curves. Using *OSO 8* data, Becker et al. (1977) observed type-I X-ray bursts, implying that the compact source in XB 1916-053 is a neutron star. Assuming that the peak luminosity of the X-ray bursts in XB 1916-053 is at the Eddington limit, Smale et al. (1988) derived a distance to the source of 8.4 kpc or 10.8 kpc, respectively, depending on whether the accreting matter has cosmic abundances or is extremely hydrogen-deficient. Yoshida (1993) inferred a distance to the source of 9.3 kpc studying the photospheric radius expansion of the X-ray bursts in XB 1916-053 (see also Barret et al., 1996). XB 1916-053 was the first LMXB in which periodic absorption dips were detected (Walter et al., 1982; White and Swank, 1982). These dips represent a decrease in the count rate in the light curve caused by periodic absorption of the X-ray emission produced in the inner region of the system. The photoelectric absorption occurs in a bulge at the outer radius of the accretion disc where the matter streaming from a companion star impacts.

Accurate analysis of data sets from many X-ray satellites in the last 30 years have found different values for the X-ray period: Walter et al. (1982) found a period close to 2985 s, using *Einstein* data; White and Swank (1982) estimated a period of 3003.6 ± 1.8 s for the strongest dips, while Smale et al. (1989), analysing *GINGA* data, derived a period of 3005.0 ± 6.6 s. Church et al. (1997), analysing ASCA data, found an orbital period of 3005 ± 10 s. The X-ray light curve of XB 1916-053 also shows secondary dips occurring approximately half a cycle away from the primary dips with a certain variability in phase (see Grindlay, 1989). No eclipses were found; this constrains the orbital inclination of the system between 60° and 80°.

The optical counterpart of XB1916-053 was discovered by Grindlay et al. (1987), a star with a V magnitude of 21 already noted by Walter et al. (1982). Using thermonuclear flash models of X-ray bursts, Swank et al. (1984) argued that the companion star is not hydrogen exhausted and suggested a companion star mass of 0.1 $M_\odot$. Furthermore, Paczynski and Sienkiewicz (1981)

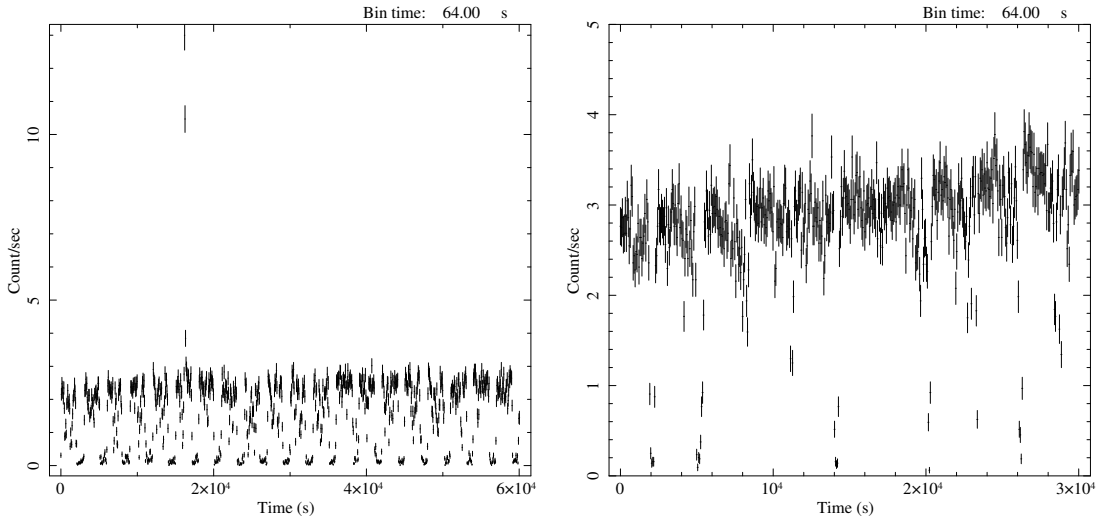

Figure 6.1: Chandra/LEG light curves of XB 1916-053 during the two observations performed in 2013, i.e. obsid. 15271 (left) and 15657 (right). The bin time is 64 s. A type-I X-ray burst that occurred during the obsid. 15271.

showed that X-ray binary systems with orbital periods shorter than 81 min cannot contain hydrogen-rich secondary stars.

A modulation in the optical light curve with a period of 3027.4 ± 0.4 s was discovered by Grindlay et al. (1988). The 1% discrepancy between the optical and X-ray period of XB 1916-053 was explained by Grindlay et al. (1988) invoking the presence of a third body with a period of 2.5 d and a retrograde orbit that influences the matter streaming from the companion star. The same authors also suggested the alternative scenario in which the disc bulge precesses around the disc with a prograde period equivalent to the beat period between the optical and X-ray period. White (1989) suggested the possibility that a precessing elliptical disc exists in XB 1916-053, and that the variation in the projected area of this disc causes optical modulation. Callanan et al. (1995) showed the stability of the optical period over seven years. Chou et al. (2001), analysing *Rossi X-ray Timing Explorer* (RXTE) data taken in 1996, found several periodicities including one at 3026.23 ± 3.23 s, which was similar to the optical modulation at 3027 s. The centroid of these peaks in the periodogram associated with the 3000 s period implies that there is a modulation with a fundamental period close to 3.9 d, as already noticed by Grindlay (1992) also in the optical band. The period of 3.9 d is interpreted as the beat period between the optical and X-ray periods. Furthermore, Chou et al. (2001), folding the RXTE light curves at the 3.9 d period, found changes in the dip shape following this modulation. Those authors also indicated that the dip-phase change, with a sinusoidal period of 6.5 ± 1.1 d from Ginga 1990 September observations (Yoshida, 1993; Yoshida et al., 1995), may be associated with the subharmonic of the 3.9 d period. Retter et al. (2002) detected a further independent X-ray period at 2979 s in the RXTE light curves of XB 1916-053, which was mistakenly identified by Chou et al. (2001) with a 3.9 d sideband of the

3000 s period. Retter et al. (2002) suggested that the period at 2979 s could be explained as a negative super-hump assuming the 3000 s period is the orbital period with a corresponding beat period of 4.8 d. The same authors suggested that the 3.9 and 4.8 d periods could be the apsidal and nodal precession of the accretion disc, respectively.

Finally, the source also showed a long-term 198.6 ± 1.72 d periodicity in X-rays (Priedhorsky and Terrell, 1984), which has not been confirmed by further observations (see Retter et al., 2002). To date the spin period of the neutron star in XB 1916-053 is not known. Galloway et al. (2001), analysing a Type-I X-ray burst, discovered a highly coherent oscillation drifting from 269.4 Hz up to 272 Hz. Interpreting the asymptotic frequency of the oscillation in terms of a decoupled surface burning layer, the neutron star could have a spin period around 3.7 ms.

Hu et al. (2008) inferred that $\dot{P}_{orb}/P_{orb} = (1.62 \pm 0.34) \times 10^{-7}$ yr^{-1} by analysing archival X-ray data from 1978 to 2002 and adopting a quadratic ephemeris to fit the dip arrival times.
In this work, we update the previously determined ephemeris using data from 1978 to 2014. We show that the quadratic ephemeris does not fit the dip arrival times and find that a sinusoidal component is necessary to fit the delays. We suggest the presence of a third body that influences the orbit of the X-ray binary system XB 1916-053.

Table 6.1: Observation Log.

Point	Satellite/Instrument	Observation	Start Time (UT)	Stop Time (UT)	T_{fold} (MJD,TDB)
1	OSO-8/GCXSE		1978 Apr 07 21:16:05	1978 Apr 14 22:20:37	43609.408575724435
2	Einstein/IPC		1979 Oct 22 04:52:01	1979 Oct 22 06:58:30	44168.24670380917
3	Einstein/IPC		1980 Oct 11 04:08:51	1980 Oct 11 09:07:19	44523.27644368849
4	EXOSAT/ME		1983 Sep 17 15:07:25	1983 Sep 17 21:29:49	45594.765324269885
5	EXOSAT/ME		1985 May 24 12:26:21	1985 May 24 21:30:23	46209.612747685185
6	EXOSAT/ME		1985 Oct 13 13:53:16	1985 Oct 13 22:34:04	46351.75944524423
7	Ginga/LAC		1988 Sep 09 15:47:56	1988 Sep 10 16:01:16	47414.165911835925
8	Ginga/LAC		1990 Sep 11 15:04:35	1990 Sep 13 09:18:11	48146.51075733274
9	ROSAT/PSPC	RP400274N00	1992 Oct 17 13:05:47	1992 Oct 19 15:24:20	48913.59379352164
10	ASCA/GIS3	40004000	1993 May 02 18:11:00	1993 May 03 09:46:17	49110.082393510115
11	RXTE/PCA	P10109-01-01-00, P10109-01-02-00, P10109-01-04-01, P10109-01-04-00, P10109-02-01-00, P10109-02-02-00, P10109-02-03-00, P10109-02-04-00, P10109-02-05-00, P10109-02-06-00, P10109-02-07-00, P10109-02-08-00, P10109-02-09-00, P10109-02-10-00, P10109-02-10-02	1996 Feb 02 00:14:56	1996 May 23 11:20:00	50174.74129123185
12	RXTE/PCA	P10109-01-05-00, P10109-01-06-00, P10109-01-07-00,	1996 Jun 01 17:38:40	1996 Oct 29 11:00:34	50310.596956288645

		P10109-01-08-00, P10109-01-09-00			
13	BeppoSAX/MECS	20106001	1997 Apr 27 21:00:06	1997 Apr 28 19:51:02	50566.35264963594
14	RXTE/PCA	P30066-01-01-04, P30066-01-01-00, P30066-01-01-01, P30066-01-01-02, P30066-01-01-03, P30066-01-02-00, P30066-01-02-01, P30066-01-02-02, P30066-01-02-03	1998 Jun 23 23:06:40	1998 Jul 20 15:35:55	51001.306447481845
15	RXTE/PCA	P30066-01-02-04, P30066-01-02-07, P30066-01-02-08, P30066-01-03-00, P30066-01-03-01, P30066-01-03-02, P30066-01-03-03, P30066-01-03-04, P30066-01-03-05, P30066-01-04-00	1998 Jul 21 07:11:44	1998 Sep 16 02:52:32	51043.70980975036
16	RXTE/PCA	P30066-01-05-01, P30066-01-05-00, P30066-01-06-00, P30066-01-06-01, P30066-01-07-00, P30066-01-07-01	2001 May 27 08:14:47	2001 Jul 01 19:15:33	52074.07302734295
17	BeppoSAX/MECS	21373002	2001 Oct 01 03:40:16	2001 Oct 02 07:01:06	52183.72270184033
18	RXTE/PCA	P50026-03-01-00, P50026-03-01-01	2001 Oct 01 10:35:44	2001 Oct 01 22:16:03	52183.684644754605
19	RXTE/PCA	P70034-02-02-01, P70034-02-02-00	2002 Sep 25 00:43:12	2002 Sep 25 09:31:12	52542.21332826887
20	XMM/Epic-pn	0085290301	2002 Sep 25 04:18:29	2002 Sep 25 08:28:27	52542.266295747205
21	INTEGRAL/JEM-X		2003 Nov 09 09:04:11	2003 Nov 20 12:18:01	52957.945226848465
22	Chandra/HETGS	4584	2004 Aug 07 02:34:45	2004 Aug 07 16:14:53	53224.59478392645
23	Suzaku/XIS0	401095010	2006 Nov 08 06:09:51	2006 Nov 09 02:42:02	54048.3655207864
24	RXTE/PCA	P95093-01-01-00, P95093-01-01-01	2010 Jun 19 13:41:52	2010 Jun 21 07:21:46	55367.43875650959
25	Chandra/LETGS	15271, 15657	2013 Jun 15 13:56:17	2013 Jun 18 05:13:17	56459.89915961875
26	Swift/XRT	00033336001	2014 Jul 15 08:04:57	2014 Jul 15 22:36:46	56853.63959388178
27	Suzaku/XIS0	409032010, 409032020	2014 Oct 14 16:49:56	2014 Oct 22 2:40:56	56949.56345974802

6.3 Observations and data reduction

We used all the available X-ray archival data of XB 1916-053 to study the long-term change of its orbital period. The last ephemeris of the source was reported by Hu et al. (2008) who used archival data from 1978 to 2002. We analysed more than 37 years of observational data from 1978 to 2014. The data have been obtained from the HEASARC (NASA's High Energy Astrophysics Science Archive Research Center) website and have been reduced using the standard procedures. In particular, we reanalysed the data used by Hu et al. (2008), collected from 1998 to 2002, and added new data spanning up to 2014 (see Tab. 6.1). We obtained 27 points from all the analysed observations. The data collected by RXTE, Ginga, EXOSAT, Einstein, and OSO-8 were downloaded from HEASARC in light-curve format. We used the standard-1 RXTE/PCA background-subtracted light curves, which include all the energy channels and have a time resolution of 0.125 s. All the pointing observations were used except for P70034-02-01-01, P70034-02-01-00, and P93447-01-01-00 due to the absence of dips in the corresponding light curves. The EXOSAT/ME light curves cover the energy range between 1 and 8 keV and have a time bin of 16 s. The Ginga/LAC light curves cover the 2-17 keV energy band. We only used the data from the top layer and the light curves binned at 16 s. We downloaded the ROSAT/PSPC events, and extracted the corresponding light curve using the FTOOLS `xselect`. The Medium Energy Concentrator Spectrometer (MECS) onboard the BeppoSAX satellite observed XB 1916-053 two times, in 1997 Apr 27-28 and 2001 Oct 01-02. Using `xselect`, we extracted the source light curves from a circular region centred on the source and with a radius of 4', no energy filter was applied to the data. The BeppoSAX/MECS light curves were obtained using a bin time of 2 sec. ASCA observed XB 1916-053 in 1993 May 02-03; we used the events collected by the GIS3 working in medium bit rate to extract the corresponding light curve. The OSO-8 light curve was obtained using the combined observation of the B and C detectors of the GSFC Cosmic X-ray Spectroscopy experiment (GCXSE). The light curve covers the 2-60 keV energy range. The Einstein light curve was obtained from events collected by the Image Proportional Counter (IPC) in the 0.2-3.5 keV energy range.

Table 6.2: Best-fit parameters obtained fitting the dips in the folded light curves.

Point	Phase Interval	C_1 count s^{-1}	C_2 count s^{-1}	C_3 count s^{-1}	ϕ_1	ϕ_2	ϕ_3	ϕ_4	$\chi^2_{red}(d.o.f.)$
1	0.7-1.7	7.23 ± 0.06	6.01 ± 0.09	7.59 ± 0.06	1.086 ± 0.012	1.113 ± 0.012	1.290 ± 0.016	1.388 ± 0.015	1.64(193)
2	0.7-1.7	5.74 ± 0.06	2.94 ± 0.13	5.75 ± 0.11	1.133 ± 0.004	1.170 ± 0.004	1.217 ± 0.005	1.263 ± 0.006	1.44(152)
3	0.1-1	11.24 ± 0.08	8.48 ± 0.12	11.14 ± 0.09	0.416 ± 0.006	0.450 ± 0.005	0.574 ± 0.006	0.603 ± 0.008	1.90(194)
4	0.8-1.8	23.02 ± 0.12	13.7 ± 0.4	23.73 ± 0.11	1.203 ± 0.003	1.239 ± 0.004	1.277 ± 0.003	1.321 ± 0.003	1.91(194)
5	0.095-0.8	14.6 ± 0.4	8.9 ± 0.3	17.7 ± 0.3	0.251 ± 0.015	0.329 ± 0.015	0.500 ± 0.008	0.576 ± 0.008	4.70(114)
6	0.1-0.8	25.6 ± 0.2	20.3 ± 0.4	27.1 ± 0.2	0.454 ± 0.007	0.487 ± 0.008	0.561 ± 0.007	0.605 ± 0.007	3.03(133)
7	0.5-1.1	72.9 ± 1.1	42.8 ± 1.0	75.6 ± 1.0	0.658 ± 0.004	0.680 ± 0.004	0.840 ± 0.009	0.940 ± 0.010	16.9(84)
8	0.5-1.2	107.1 ± 1.0	60.6 ± 1.3	106.3 ± 0.8	0.657 ± 0.007	0.805 ± 0.008	0.903 ± 0.004	0.954 ± 0.005	47.8(138)
9	0-1	6.05 ± 0.07	1.60 ± 0.06	6.15 ± 0.07	0.340 ± 0.008	0.535 ± 0.006	0.640 ± 0.004	0.752 ± 0.005	4.77(294)
10	0.6-1.4	9.3 ± 0.3	0.85 ± 0.05	9.3 ± 0.3	0.765 ± 0.004	0.809 ± 0.002	1.022 ± 0.003	1.100 ± 0.006	12.08(234)
11	0-1	41.00 ± 0.11	31.35 ± 0.11	45.06 ± 0.08	0.207 ± 0.004	0.323 ± 0.004	0.499 ± 0.002	0.611 ± 0.003	12.61(506)
12	0.1-1.1	36.60 ± 0.10	21.69 ± 0.13	37.45 ± 0.11	0.443 ± 0.003	0.569 ± 0.003	0.710 ± 0.002	0.808 ± 0.002	11.33(505)
13	0.95-1.95	0.986 ± 0.013	0.035 ± 0.003	0.982 ± 0.014	1.238 ± 0.004	1.340 ± 0.002	1.537 ± 0.002	1.647 ± 0.005	2.14(249)
14	0.24-0.75	27.6 ± 0.2	14.55 ± 0.10	27.7 ± 0.2	0.313 ± 0.003	0.433 ± 0.002	0.582 ± 0.002	0.705 ± 0.003	11.10(255)
15	0.15-1	36.51 ± 0.10	25.3 ± 0.2	38.31 ± 0.08	0.381 ± 0.004	0.566 ± 0.005	0.598 ± 0.003	0.738 ± 0.003	10.43(420)
16	0.35-0.9	25.4 ± 0.2	17.52 ± 0.10	26.9 ± 0.2	0.419 ± 0.004	0.489 ± 0.004	0.697 ± 0.003	0.763 ± 0.003	1.90(274)
17	0.9-1.9	1.030 ± 0.009	0.31 ± 0.02	1.016 ± 0.007	1.045 ± 0.004	1.160 ± 0.004	1.178 ± 0.004	1.272 ± 0.004	1.11(249)
18	0-1	23.75 ± 0.14	11.4 ± 0.3	24.40 ± 0.13	1.092 ± 0.002	1.113 ± 0.002	1.168 ± 0.005	1.281 ± 0.005	1.57(505)
19	0.6-1.6	28.8 ± 0.2	20.1 ± 0.2	29.8 ± 0.2	0.953 ± 0.004	0.985 ± 0.004	1.171 ± 0.006	1.249 ± 0.006	3.06(505)
20	0.1-1.1	69.9 ± 0.5	30.4 ± 0.5	72.4 ± 0.5	0.406 ± 0.004	0.506 ± 0.003	0.671 ± 0.003	0.730 ± 0.003	17.84(505)
21	0.2-1.2	0.0284 ± 0.0002	0.0256 ± 0.0004	0.0284 ± 0.0002	0.57 ± 0.02	0.63 ± 0.02	0.708 ± 0.014	0.733 ± 0.011	0.766(144)
22	0.3-1.3	9.92 ± 0.03	8.5 ± 0.2	10.04 ± 0.03	0.796 ± 0.005	0.835 ± 0.007	0.844 ± 0.013	0.923 ± 0.007	1.71(144)
23	0.9-1.9	15.10 ± 0.05	11.4 (fixed)	15.61 ± 0.05	1.263 ± 0.006	1.38 (fixed)	1.38 (fixed)	1.521 ± 0.006	2.41(505)
24	0.9-1.9	30.18 ± 0.13	23.1 ± 0.3	20.49 ± 0.15	1.322 ± 0.003	1.344 ± 0.003	1.499 ± 0.002	1.451 ± 0.002	1.22(505)
25	0.09-0.65	2.52 ± 0.03	0.759 ± 0.010	2.69 ± 0.04	0.194 ± 0.003	0.314 ± 0.002	0.525 ± 0.002	0.598 ± 0.003	2.39(567)
26	0.6-1.6	12.61 ± 0.11	4.4 ± 0.6	12.5 ± 0.2	1.025 ± 0.010	1.27 ± 0.02	1.295 ± 0.004	1.307 ± 0.004	4.08(171)
27	0.84-1.6	5.08 ± 0.04	1.607 ± 0.015	5.18 ± 0.02	0.909 ± 0.003	1.089 ± 0.002	1.2080 ± 0.0011	1.2904 ± 0.0014	3.29(382)

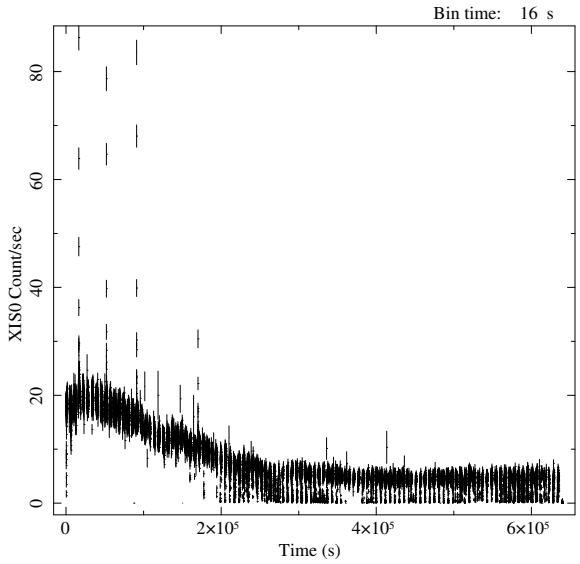

Figure 6.2: Suzaku/XIS0 light curve of XB 1916-053 during the long observation on 2014 Oct.

We applied barycentre corrections to the whole data set adopting the source position of XB 1916-053 shown by Iaria et al. (2006). For the RXTE/PCA light curves we used the ftools `faxbary`. The barycentre corrections for the ASCA and ROSAT data were obtained using the ftool `timeconv` and the tool `bct+abc`, respectively. All the other data sets were corrected using the ftool `earth2sun`. Finally, we excluded the time intervals containing X-ray bursts from each analysed light **curve**.

The Chandra satellite observed XB 1916-053 three times. The first time was on 2004 Aug 07 from 2:34:45 to 16:14:53 UT (obsid 4584). The observation had a total integration time of 50 ks and was performed in timed graded mode. The spectroscopic analysis of this data set was discussed by Iaria et al. (2006). We reprocessed the data and applied the barycentre corrections to the event-2 file using the Chandra Interactive Analysis of Observations (CIAO) tool `axbary`. In addition, we extracted the summed first-order medium energy grating (MEG) and high energy grating (HEG) light curves filtered in the 0.5-10 keV energy range using the CIAO tool `dmextract`. The last two Chandra observations of XB 1916-053 (obsid 15271 and 15657) were performed between 2013 June 15 13:56 and June 18 5:13 UT and have exposure times of 60 and 30 ks, respectively. We reprocessed the data and applied the barycentre corrections to the event-2 file using `axbary`. Moreover, we extracted the first-order low energy grating (LEG) light curve in the 0.5-5 keV energy range using `dmextract`. We show the Chandra/LEG light curve in Fig. 6.1. Very intense dipping activity is present during the two observations. A type-I burst occurred during the obsid. 15271.

The X-ray Multi-Mirror Mission-Newton (XMM-Newton) observed XB 1916-053 on 2002 Sep 25 from 3:55 to 8:31 UT and the European Photon Imaging Camera (EPIC-pn) collected data, in timing mode, over ~ 17 ks of exposure. An extensive study of this observation was performed by

Table 6.3: Journal of the X-ray dip arrival times of XB 1916-053.

Point	Dip Time (MJD;TDB)	Cycle	Delay (s)
1	43609.4168(12)	-187551	772 ± 74
2	44168.2535(5)	-171460	792 ± 28
3	44523.2941(5)	-161237	641 ± 42
4	45594.7744(3)	-130385	449 ± 18
5	46209.6271(13)	-112681	193 ± 112
6	46351.7778(9)	-108588	352 ± 52
7	47414.193(2)	-77997	162 ± 132
8	48146.539(3)	-56910	47 ± 182
9	48913.6127(10)	-34823	-140 ± 59
10	49109.1148(12)	-29165	-48 ± 76
11	50174.7555(5)	1490	-50 ± 46
12	50310.6187(4)	5402	-17 ± 37
13	50566.3680(4)	12766	-69 ± 39
14	51001.3241(5)	25290	-15 ± 40
15	51043.7292(5)	26511	-9 ± 45
16	52074.0935(3)	56179	151 ± 29
17	52183.7349(3)	59336	107 ± 28
18	52183.7008(2)	59335	162 ± 19
19	52542.2168(4)	69658	227 ± 39
20	52542.2860(11)	69660	202 ± 98
21	52957.9679(8)	81629	327 ± 69
22	53224.6246(4)	89307	467 ± 34
23	54048.3791(5)	113026	411 ± 39
24	55367.45218(15)	151007	593 ± 13
25	56459.9129(3)	182463	721 ± 20
26	56853.6454(8)	193800	821 ± 67
27	56949.84670(10)	196570	814 ± 8

NOTE — Epoch of reference 50123.00873 MJD, orbital period 3000.6511 s.

Boirin et al. (2004). We reprocessed the data, extracted the 0.5-10 keV light curve, and applied barycentre corrections to the times of the EPIC-pn events with the Science Analysis Software (SAS) tool `barycen`.

Suzaku observed XB 1916-053 twice, the first time on 2006 Nov 8 (obsid. 401095010) and the second time from 2014 Oct 14 to 22 (obsid. 409032010 and 409032020). The first observation has already been analysed by Zhang et al. (2014), while a study of the second observation has not been published yet. For both observations, we extracted the X-ray Imaging Spectrometer 0 (XIS0) events from a circular region centred on the source and with a radius of 130". We applied the barycentre corrections to the events with the Suzaku tool `aebarycen`. We do not show the light curve of the first Suzaku observation since it was already shown by Zhang et al. (2014) (Fig. 1 in their paper), however, we show in Fig. 6.2 the XIS0 light curve of the observation performed in 2014 Oct. The light curve indicates that a bursting activity is present in the first 200 ks of the observation and the persistent count rate decreases from 20 to 10 counts s^{-1}. In the second part of the observation, the persistent count rate is quite constant at 7 counts s^{-1} and an intense dipping activity is present. For the aim of this work, we selected and used the events from 250 ks

to the end of the observation.

Swift/XRT data were obtained as target of opportunity observations performed on 2014 Jul 15 from 07:55:53 to 22:27:58 UT (ObsID 00033336001) for a total on-source exposure of ~ 6.3 ks and on 2014 Jul 21 from 07:32:00 to 16:11:5 UT (ObsID 00033336002) for a total on-source exposure of ~ 9.0 ks. The count rate in the first observation reaches 15 counts s^{-1}, with a mean at about 10 counts s^{-1}, due to the dips seen down to 2 counts s^{-1}; the second observation shows no dips and has a mean count rate of 7 counts s^{-1}. Since the data from ObsID 00033336002 do not show dips we only used the first observation in our analysis. The XRT data were processed with standard procedures (`xrtpipeline` v0.13.1), and with standard filtering and screening criteria with FTOOLS (v6.16). Source events (selected in grades 0–2) were accumulated within a circular region with a radius of 20 pixels (1 pixel ~ 2.36"). For our timing analysis, we also converted the event arrival times to the solar system barycentre with `barycorr`.

We selected a public data set of *INTErnational Gamma-Ray Astrophysics Laboratory* (INTEGRAL Winkler et al., 2003) observations performed in staring mode on XB 1916-053. Then, we analysed the data collected by the X-ray telescope JEM-X2 (Lund et al., 2003b). A total amount of 87 pointings (the total observation elapsed time is ~ 310 ks) covered the INTEGRAL revolutions 131, 133, and 134, which were carried out on 2003 November 9-20. We performed the JEM-X2 data analysis using standard procedures within the Offline Science Analysis software (OSA10.0) distributed by the ISDC (Courvoisier et al., 2003). We extracted the light curves with a 16 seconds bin-size in the energy range 3-10 keV, and after that we applied the barycentre corrections to the events using the tool *barycent*.

6.4 Data analysis

We analysed 27 light curves and folded the barycentric-corrected light curves using a trial time of reference and orbital period, T_{fold} and P_0, respectively. For each light curve, the value of T_{fold} is defined as the average value between the corresponding start and stop time. We fitted the dips with a simple model consisting of a step-and-ramp function, where the count rates before, during, and after the dip are constant and the intensity changes linearly during the dip transitions. This model involves seven parameters: the count rate before, during, and after the dip, called C_1, C_2, and C_3, respectively; the phases of the start and stop time of the ingress (ϕ_1 and ϕ_2), and, finally, the phases of the start and stop time of the egress (ϕ_3 and ϕ_4). The phase corresponding to the dip arrival time ϕ_{dip} is estimated as $\phi_{dip} = (\phi_4 + \phi_1)/2$. The corresponding dip arrival time is given by $t_{dip} = T_{fold} + \phi_{dip} P_0$. To be more conservative, we scaled the error associated with ϕ_{dip} by the factor $\sqrt{\chi^2_{red}}$ to take a value of χ^2_{red} of the best-fit model larger than 1 into account. To obtain the delays with respect to a constant period reference, we used the values of the period $P_0 = 3\,000.6511$ s and reference epoch $T_0 = 50\,123.00873$ MJD reported in Hu et al. (2008). We show the values of T_{fold} in Tab. 6.1. The best-fit parameters of the step-and-ramp function and

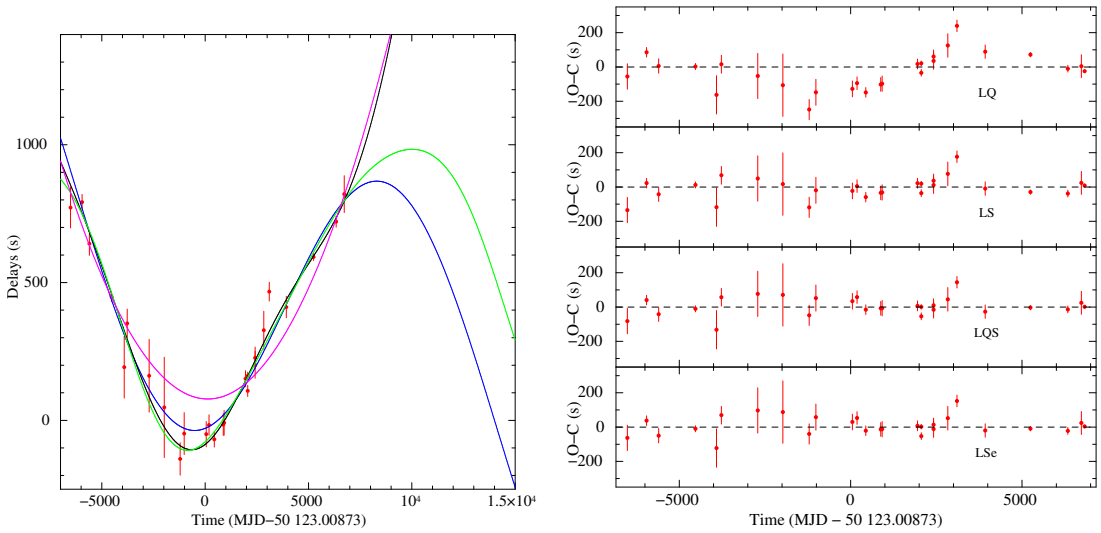

Figure 6.3: Left panel: dips's arrival time delays versus time. The magenta, blue, black , and green curves are the best-fit curves obtained using the linear+quadratic (LQ), linear+sinusoidal (LS), linear+quadratic+sinusoidal (LQS), and linear+sinusoidal function taking into account a possible eccentricity (LSe), respectively. Right panel: observed minus calculated delays in units of seconds. The residuals, from the top to the bottom, correspond to the LQC, LS, LQS, and LSe function, respectively.

the corresponding χ^2_{red} are shown in Tab. 6.2. The inferred delays, in units of seconds, of the dip arrival times with respect to a constant orbital period are reported in Tab. 6.3. For each point we computed the corresponding cycle and the dip arrival time in days with respect to the adopted T_0. We show the delays vs. time in Fig. 6.3 (left panel).

Initially we fitted the delays with a quadratic function

$$y(t) = a + bt + ct^2,$$

where t is the time in days with respect to T_0, $a = \Delta T_0$ is the correction to T_0 in units of seconds, $b = \Delta P/P_0$ in units of s d^{-1} with ΔP the correction to the orbital period, and finally, $c = 1/2\,\dot{P}/P_0$ in units of s d^{-2}, with $\dot{P}$, that is the orbital period derivative. The quadratic form does not fit the data, we obtained χ^2(d.o.f.) of 194.6(24). Here, and in the following, we scaled the uncertainties in the parameters by a factor $\sqrt{\chi^2_{red}}$ to take a value of χ^2_{red} of the best-fit model larger than 1 into account. The best-fit parameters are shown in the second column of Tab. 6.4. The corresponding quadratic ephemeris (hereafter LQ ephemeris) is

$$T_{dip}(N) = \text{MJD(TDB)}\,50\,123.0096(3) + \frac{3\,000.65094(14)}{86\,400}N + \\ +2.37(12)\times 10^{-13}N^2, \tag{6.1}$$

where N is the number of cycles, 50,123.0096(3) MJD is the new Epoch of reference, the revised orbital period is P = 3,000.65094(14) s, and the orbital period derivative obtained from the

Table 6.4: Best-fit values of the parameters of the functions used to fit the delays.

Parameters	LQ	LQC	LS	LQS		LSe	
a (s)	78 ± 23	$-2.7^{+2.1}_{-11.2}$	584 ± 157	16 ± 22	229 ± 336	56 ± 322	1.1 ± 299.2
b ($\times 10^{-3}$ s d^{-1})	-4 ± 4	37.1 ± 0.4	-43 ± 23	-4 ± 3	3 ± 20	3 ± 19	5 ± 22
c ($\times 10^{-5}$ s d^{-2})	1.70 ± 0.09	2.13 ± 0.03	–	1.79 ± 0.09	–	–	–
d ($\times 10^{-9}$ s d^{-3})	–	-1.35 ± 0.12	–	–	–	–	–
A (s)	–	–	658 ± 206	130 ± 15	519 ± 47	548 ± 43	577 ± 43
t_ϕ (d)	–	–	3897 ± 332	1356 ± 203	-3723 ± 1100	-3150 ± 1116	-2923 ± 1034
P_{mod} (d)	–	–	20409 ± 3381	9302 ± 752	17100 (fixed)	18600 (fixed)	20100 (fixed)
ϖ (deg)	–	–	–	–	195 ± 26	210 ± 28	217 ± 27
e	–	–	–	–	0.26 ± 0.20	0.28 ± 0.15	0.32 ± 0.13
χ^2(d.o.f.)	194.6(24)	92.4(23)	63.7(22)	39.4(21)	51.8(21)	48.2(21)	45.8(21)

NOTE — The reported errors are at 68% confidence level. The fit parameters of the delays are obtained using LQ (column 2), LQC (column 3), LS (column 4), LQS function (column 5), and LSe (columns 6, 7, and 8), respectively.

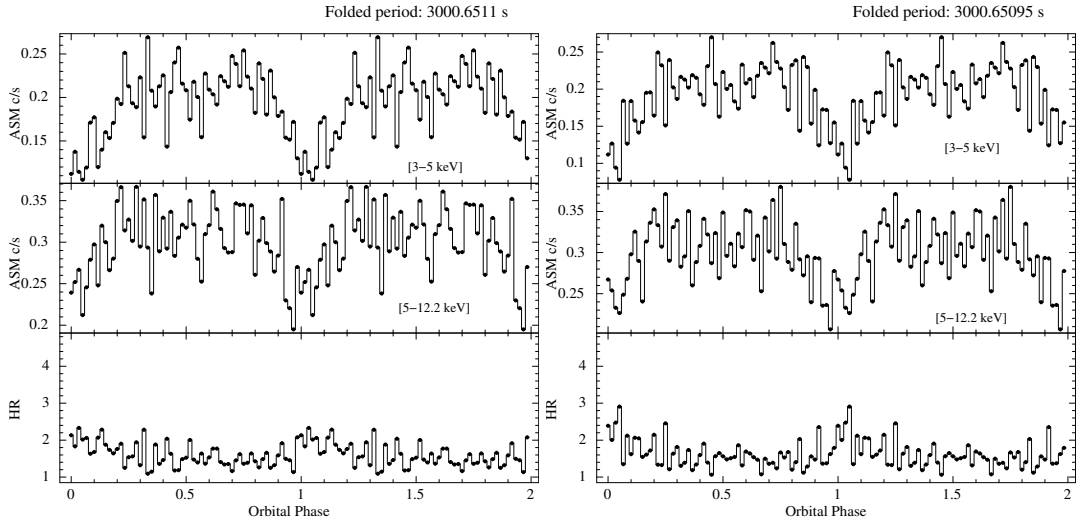

Figure 6.4: Folded RXTE/ASM light curve of XB 1916-053 in the 3-5 and 5-12.2 keV energy range (top and middle panels). The corresponding hardness ratios (HRs) are plotted in the bottom panels. The left and right plots show the folded RXTE/ASM light curve using the ephemeris discussed by Hu et al. (2008) and LQ ephemeris (eq. 6.1) shown in the Sect. 3, respectively. Each phase-bin is about 50 s.

quadratic term is $\dot{P} = 1.36(7) \times 10^{-11}$ s/s. The obtained quadratic ephemeris is compatible with that reported by Hu et al. (2008). We show the best-fit curve in Fig. 6.3 (left panel) and the corresponding residuals in units of seconds in Fig. 6.3 (right panel, upper plot).

As we obtained a large value of the χ^2, we fitted the delays vs. time adding a cubic term to the previous parabolic function, i.e.

$$y(t) = a + bt + ct^2 + dt^3,$$

where a, b and c are above defined whilst the cubic term, d, is defined as $\ddot{P}/(6P_0)$, and $\ddot{P}$ indicates the temporal derivative of the orbital period derivative. Fitting with a cubic function, we obtained

a χ^2(d.o.f.) of 92.4(23) with a $\Delta\chi^2$ of 101.2 and an F-test probability of chance improvement of 4.2×10^{-5} with respect to the quadratic form. The best-fit values are shown in the third column of Tab. 6.4. The corresponding ephemeris (hereafter LQC ephemeris) is

$$T_{dip}(N) = \mathrm{MJD(TDB)}\,50\,123.00870^{+0.00005}_{-0.00026} + \\ + \frac{3\,000.65239(3)}{86\,400}N + 2.97(12)\times10^{-13}N^2 - 2.2(4)\times10^{-22}N^3; \tag{6.2}$$

in this case we find an orbital period derivative of $1.71(7)\times10^{-11}$ s/s and its derivative is $\ddot{P} = -3.8(0.7)\times10^{-20}$ s/s^2.

We also fitted the delays using a linear plus a sinusoidal function having the following terms

$$y(t) = a + bt + A\sin\left[\frac{2\pi}{P_{mod}}(t - t_\phi)\right], \tag{6.3}$$

where a and b are defined as above, A is the amplitude of the sinusoidal function in seconds, P_{mod} is the period of the sine function in days, and, finally, t_ϕ is the time in days referred to T_0 at which the sinusoidal function is null. We obtained a value of χ^2(d.o.f.) of 63.7(22) with a $\Delta\chi^2$ of 131 with respect to the quadratic form. The best-fit parameters are shown in the fourth column of Tab. 6.4. The best-fit function is indicated with a blue curve in Fig. 6.3 (left panel) and the corresponding residuals are shown in Fig. 6.3 (right panel, the second plot from the top). The residuals are flatter than those obtained in the previous case. Using the sinusoidal function, the dip time obtained from the OSO-8 observation is distant ~200 s from the expected value. The corresponding ephemeris (hereafter LS ephemeris) is

$$T_{dip}(N) = \mathrm{MJD(TDB)}\,50\,123.01549(18) + \\ + \frac{3\,000.6496(8)}{86\,400}N + A\sin\left[\frac{2\pi}{N_{mod}}N - \phi\right], \tag{6.4}$$

where $N_{mod} = P_{mod}/P_0 = 587\,659.53 \pm 97\,351.67$ and $\phi = 2\pi t_\phi/P_{mod} =$ with $P_{mod} = 55.9 \pm 9.3$ yr. This functional form significantly improves the fit, even though it does not take the possible presence of an orbital period derivative into account.

We added a quadratic term to take the possible presence of an orbital period derivative and fitted the delays into account, using the function

$$y(t) = a + bt + ct^2 + A\sin\left[\frac{2\pi}{P_{mod}}(t - t_\phi)\right]. \tag{6.5}$$

We obtained a value of χ^2(d.o.f.) of 39.4(21) and a F-test probability of chance improvement with respect to the LS ephemeris of 1.7×10^{-3}. The best-fit parameters are shown in the fifth column of Tab. 6.4. The best-fit function is indicated with a black curve in Fig. 6.3 (left panel) and the corresponding residuals are shown in Fig. 6.3 (right panel, the third plot from the top). The corresponding linear+quadratic+sinusoidal ephemeris (hereafter LQS ephemeris) is

$$T_{dip}(N) = \mathrm{MJD(TDB)}\,50\,123.0089(3) + \frac{3\,000.65126(10)}{86\,400}N + \\ + 2.50(12)\times10^{-13}N^2 + A\sin\left[\frac{2\pi}{N_{mod}}N - \phi\right], \tag{6.6}$$

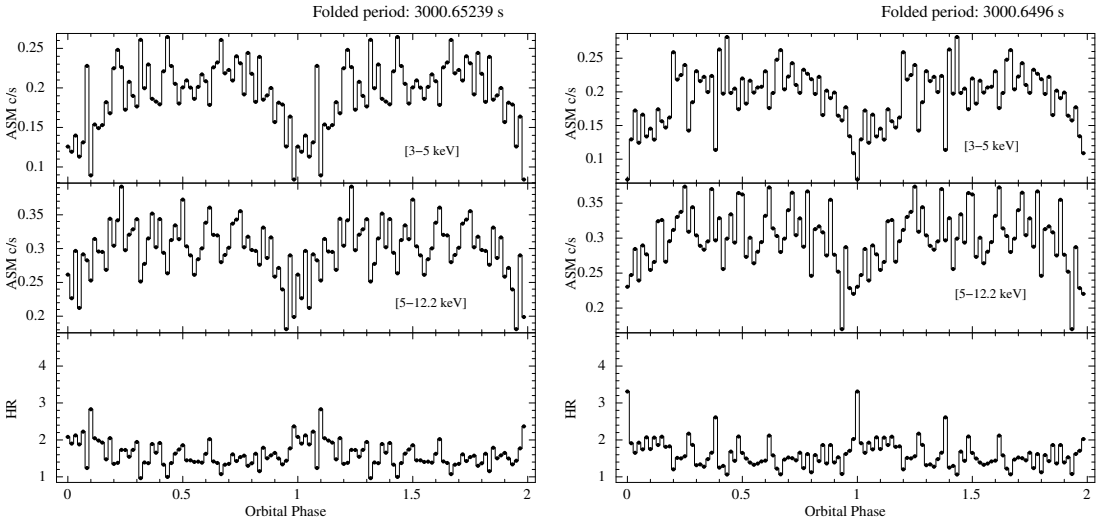

Figure 6.5: Left and right plots show the folded RXTE/ASM light curve using LQC ephemeris (eq. 6.2) and LS ephemeris (eq. 6.4), respectively. Each phase-bin is about 50 s.

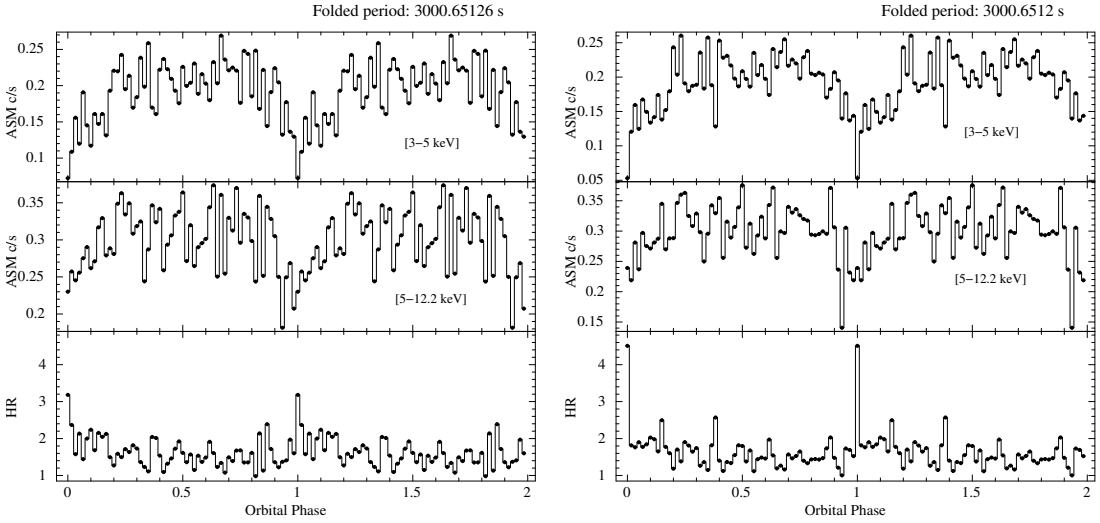

Figure 6.6: Left and right plots show the folded RXTE/ASM light curve using LQS ephemeris (eq. 6.6) and LSe ephemeris (eq. 6.8) with P_{mod} = 18600 d, respectively. Each phase-bin is about 50 s.

with $N_{mod} = 267\,837.87 \pm 21\,652.90$ and $\phi = 0.92 \pm 0.16$. The corresponding orbital period derivative is $\dot{P} = 1.44(7) \times 10^{-11}$ s/s and the period of the modulation is $P_{mod} = 25.5 \pm 2.1$ yr.

Our analysis of the delays suggests that a quadratic or a quadratic plus a cubic term do not fit the delays. A better fit is obtained using a sinusoidal function with a period close to 20 000 d and, finally, adopting a sinusoidal plus a quadratic term, we obtain the best fit of the delays. In this latter case, the sinusoidal function has a period of 9 300 d, about half of that obtained using only the sinusoidal function. Moreover, the orbital period derivative $\dot{P} = 1.44(7) \times 10^{-11}$ s/s (compatible with $\dot{P} = 1.5(3) \times 10^{-11}$ s/s obtained by Hu et al., 2008) is extremely high to be explained by a conservative mass transfer and loss of angular momentum from the binary system for gravitational radiation (see next section). This awkward result can be bypassed if the quadratic term is merely an approximation of a further sinusoidal function with a larger orbital period with respect to 9 300 d.

Under this assumption, the best fit obtained using the LQS ephemeris could be explained using a different scenario, where the quadratic term mimics the fundamental harmonic of a series expansion whilst the sinusoidal term is the first harmonic. This seems also suggested by the best fit obtained using the LS function (eq. 6.3), since we obtain a modulation period, which is almost twice that obtained using the LQS function (eq. 6.5).

If we assume that XB 1916-053 is part of a hierarchical triple system then the measured delays are also affected by the influence of a third body. If the orbits of the third body and of the X-ray binary system around the common centre of mass are slightly elliptical then the delay $\Delta_{DS}(t)$ associated with the Doppler shift can be expressed as

$$\begin{aligned} \Delta_{DS}(t) = A\Big\{ & \sin(m_t + \varpi) + \frac{e}{2}[\sin(2m_t + \varpi) - 3\sin(\varpi)] + \\ & + \frac{e^2}{4}[2\sin(3m_t + \varpi) - \sin(m_t + \varpi)\cos(2m_t + 1) + \\ & - 2\sin(m_t)\cos(\varpi)]\Big\}, \end{aligned} \tag{6.7}$$

where

$$m_t = \frac{2\pi}{P_{mod}}(t - t_\phi)$$

is the mean anomaly; e is the eccentricity of the orbit; P_{mod} is the orbital period of both the X-ray binary system and the third body around the common centre of mass; ϖ denotes the periastron angle; t_ϕ is the passage time at the periastron; and $A = a \sin i/c$ is the projected semi-major axis of the orbit, described by the centre of mass of the X-ray binary system around the centre of mass of the triple system. We neglect third and higher order terms in Eq. 6.7. Limiting Eq. 6.7 to the first-order terms, it becomes the expression shown by van der Klis and Bonnet-Bidaud (1984). Then, we fitted the delays using

$$y(t) = a + bt + \Delta_{DS}(t).$$

Because the 27 available points do not cover a whole period, we arbitrarily fixed the value of P_{mod} at 18 600, 17 100, and 20 100 d, which are the best, lower, and upper value of the period obtained

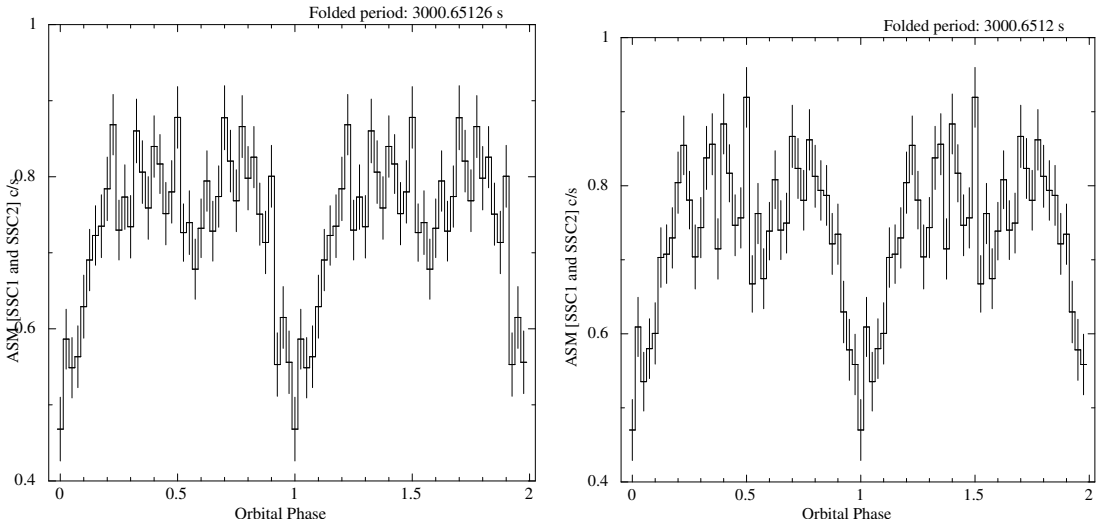

Figure 6.7: Folded RXTE/ASM light curve of XB 1916-053 selecting the events from SSC1 and SSC2. No energy filter is applied. Each phase-bin correspond to 75 s. Left panel: folded light curve using the LQS ephemeris (eq. 6.6). Right panel: folded light curve using the LSe ephemeris (eq. 6.8).

from the LQS ephemeris multiplied by a factor of two. The best-fit parameters are shown in Tab. 6.4 (columns 6, 7, and 8). The χ^2(d.o.f.) are similar for the three adopted periods and the F-test probability of chance improvement with respect to LS function is 4.1×10^{-2}, 1.7×10^{-2}, and 0.9×10^{-2} for a P_{mod} value of 17 100, 18 600, and 20 100 d, respectively. In the following, we discuss the case of $P_{mod} = 18\,600$ d. The best-fit function is indicated with a green curve in Fig. 6.3 (left panel). The corresponding residuals are shown in Fig. 6.3 (right panel, lower plot). The corresponding ephemeris (hereafter LSe ephemeris) is

$$T_{dip}(N) = \text{MJD(TDB)}\,50\,123.010(3) + \frac{3\,000.6512(6)}{86\,400}N + \\ + \Delta_{DS}(N). \tag{6.8}$$

To verify the robustness of our results, we produced the folded light curves in the 3-5 and 5-12.2 keV energy bands of XB 1916-053 obtained from the All Sky Monitor (ASM) on board RXTE using the ephemerides shown above. We inferred those ephemerides using only pointing observations from which we obtained 27 points spanning from 1978 to 2014, whilst the RXTE/ASM light curves cover from 1996 Sep 01 to 2011 Oct 31. We applied the barycentre corrections to the RXTE/ASM events. As a first step, we folded the RXTE/ASM light curves of XB 1916-053 using the LQ ephemeris reported by Hu et al. (2008) and by us (Eq. 6.1), adopting 60 phase-bins per period corresponding to ~50 s per bin. The folded light curves and the corresponding hardness ratios (HRs) are shown in Fig. 6.4. None of the HR show an evident increase at phase zero as we would expect if the ephemerides well define the dip arrival times. This implies that those ephemerides do not correctly predict the dip arrival times contained in the RXTE/ASM light

curve. Adopting the LQC ephemeris (eq. 6.2), the maximum value of HR (that is 2.8) is reached at phase 0.1 (see Fig. 6.5, left panels). Also in this case, the LQC ephemeris does not predict the dip arrival times in the ASM light curves of XB 1916-053. Using the LS ephemeris (Eq. 6.4) to fold the light curves, we obtained that the maximum value of HR is reached at phase zero and is close to 3.4 (see Fig. 6.5, right panels). In contrast, with the LQS ephemeris (Eq. 6.6) the maximum value of the HR falls in two phase-bins close to phase zero (see Fig. 6.6, left panels) and the maximum value of HR is 3.2, which is smaller than the value obtained with the LS ephemeris. Finally, we folded the RXTE/ASM light curves using the LSe ephemeris (eq. 6.8). We show the folded light curves and the corresponding HR in Fig. 6.6 (right panel). In this last case the maximum value of the HR falls in only one phase bin at phase zero and the maximum value of the HR is about 4.5.

We also folded the RXTE/ASM light curve (not filtered in energy) using the LQS and LSe ephemerides once we selected the events from the Scanning Shadow Cameras (SSCs) 1 and 2. Adopting 40 phase-bins per period (that is each bin is 75 s), the folded light curves are very similar (see Fig. 6.7), indicating that the two ephemerides are statistically equivalent. The dip is clearly observed at phase zero, the ASM count rate is reduced during the dip of 60% with respect to the persistent emission. Finally, the goodness of the two ephemerides allows us to observe the presence of a secondary dip at phase 0.55, which is typically observed in several dipping sources (see Grindlay, 1989, for XB 1916-053).

6.5 Discussion

From the study of the 27 dip arrival times obtained from the pointed observations of XB 1916-053 and of the RXTE/ASM light curves, we find that the quadratic and cubic ephemerides do not correctly predict the dip arrival times on a long time span; whilst to well fit the delays, we need to use a function that contains at least linear and sinusoidal terms (LS ephemeris, see Eq. 6.4). The addition of a quadratic term to the LS ephemeris (Eq. 6.6) gives a probability of chance improvement obtained with a F-test of 1.7×10^{-3} with respect to the LS ephemeris. Finally, using the ephemeris shown in Eq. 6.8, the probability of chance improvement, also with respect to the LS ephemeris, is 1.7×10^{-2}. The LQS and LSe ephemerides paint two different physical scenarios for XB 1916-053. In the first case the orbital period derivative of the X-ray binary system is $\dot{P} = 1.44(7) \times 10^{-11}$ s/s and the observed delays associated with the dip arrival times are affected by a relatively low-amplitude ($\sim$ 130 s) sinusoidal modulation with a period close to 26 yr. In the second case the orbital period derivative is fixed to zero and the modulation of the delays is solely sinusoidal with an amplitude of $\sim$ 550 s and an orbital period close to 51 yr. We explain in the following the sinusoidal modulation for both the scenarios, assuming the presence of a third body forming a hierarchical triple system with XB 1916-053, which alters the observed dip arrival times.

We start by discussing the plausible values of the companion star mass M_2. We know that the companion star is a degenerate star and its radius R_2 has to be equal to its Roche lobe radius R_{L2} since the binary system is in the Roche lobe overflow (RLOF) regime. Rearranging the Eq. 3.3.15 in Shapiro and Teukolsky (1983), the mass-radius relation for a degenerate star can be written as

$$\frac{R_2}{R_\odot} = 0.04 \left(\frac{Z}{A}\right)^{5/3} \left(\frac{M_2}{M_\odot}\right)^{-1/3} = 0.0126\,(1+X)^{5/3} m_2^{-1/3},$$

where Z and A are the atomic number and the atomic weight of the matter composing the star, and where we assumed that the matter is only composed of hydrogen and helium. The factor Z/A is the average of Z/A for matter composed of hydrogen and helium, X is the fraction of hydrogen in the star and, finally, m_2 is the companion star mass in units of solar mass. This equation has to be corrected for the thermal bloating factor f, which is the ratio of the companion star radius to the radius of a star with the same mass and composition, that is completely degenerate and supported only by the Fermi pressure of the electrons; then the factor f is > 1. The Roche lobe radius of the companion star can be written as

$$R_{L2} = 0.46224\, a \left(\frac{m_2}{m_1 + m_2}\right)^{1/3},$$

where a is the orbital separation of the binary system and m_1 is the neutron star (NS) mass in unit of solar mass. We can write a in terms of the orbital period P, m_1, and m_2, using Kepler's third law. Combining the last two equations and Kepler's third law, we obtain

$$m_2 = 0.0151\,(1+X)^{5/2} f^{3/2}. \tag{6.9}$$

Nelemans et al. (2006), analysing the optical spectrum with the European Southern Observatory Very Large Telescope, detected a He-dominated accretion disc spectrum and suggested direct evidence for a helium donor. The authors found a good match with an LTE model consisting of pure helium plus overabundant nitrogen. For this reason, we assume $X = 0$ in the rest of the discussion.

The bolometric X-ray flux of XB 1916-053 was estimated by several authors. Galloway et al. (2008), analysing a RXTE/PCA observation of XB 1916-053, determined a persistent flux in the 2.5-25 keV of $(3.82 \pm 0.04) \times 10^{-10}$ erg s^{-1} cm^{-2}. The authors corrected the flux for a bolometric factor $c_{bol} = 1.37 \pm 0.09$ to estimate the bolometric flux in the 0.1-200 keV energy range, obtaining a bolometric flux of $(5.2 \pm 0.3) \times 10^{-10}$ erg s^{-1} cm^{-2}. Recently, Zhang et al. (2014), analysing a Suzaku observation of XB 1916-053, found a value of F_{bol} in the 0.1-200 keV energy range between 5.5×10^{-10} and 6.1×10^{-10} erg s^{-1} cm^{-2}. Finally, analysing the persistent emission of the source during a BeppoSAX observation, Church et al. (1998) estimated a value of F_{bol} in the 0.5-200 keV energy range of 6.2×10^{-10} erg s^{-1} cm^{-2}. Since the RXTE/ASM light curve of XB 1916-053 shows that the count rate of the source is almost constant over more than ten years, we adopt a conservative value for the bolometric flux of $(5.5 \pm 0.5) \times 10^{-10}$ erg s^{-1} cm^{-2}.

The distance d to the source was estimated by Galloway et al. (2008) measuring the peak flux during the photospheric radius expansion (PRE) in type-I X-ray bursts. Equation 8 in Galloway et al. (2008) can be rewritten

$$d = 8.32 \left(\frac{F_{pk,PRE}}{3 \times 10^{-8}\, erg\, s^{-1}\, cm^{-2}} \right)^{-1/2} m_1^{1/2} \left(1 - 0.296 \frac{m_1}{r_{PRE}} \right)^{1/4} (1+X)^{-1/2} \text{ kpc}, \tag{6.10}$$

where r_{PRE} is the photospheric radius of the neutron star in units of 10 km and $F_{pk,PRE}$ is the flux at the peak of the type-I X-ray burst during the PRE. The authors measured $F_{pk,PRE} = (2.9 \pm 0.4) \times 10^{-8}\, erg\, s^{-1}\, cm^{-2}$ and $r_{PRE} \simeq 1.1$ for XB 1916-053 and concluded that the distance to the source is $d = 8.9 \pm 1.3$ kpc (adopting $X = 0$) for a NS mass of 1.4 $M_\odot$. The X-ray luminosity can be expressed as $L_x = 4\pi d^2 F_{bol}$, where we roughly assume that the emitted flux is isotropic. We obtain $L_x \simeq 5.2 \times 10^{36}$ erg s^{-1} for a NS mass of 1.4 $M_\odot$, whilst we find $L_x \simeq 6.6 \times 10^{36}$ erg s^{-1} for a massive NS of 2.2 $M_\odot$.

Rappaport et al. (1987) predicted the X-ray luminosity for highly compact binary systems under the reasonable hypothesis that the main mechanism to lose angular momentum is gravitational radiation. Combining the Eqs. 8 and 13 in their work, we obtain

$$L_x \simeq \frac{5.2 \times 10^{42}}{1 - 1.5\alpha(1-\beta)} m_1^{5/3} P_m^{-14/3} (1+X)^5 \beta \eta f^3 \text{ erg s}^{-1}, \tag{6.11}$$

where P_m is the orbital period in units of minutes, β is the fraction of matter yielded by the companion star and accreted onto the NS, η is the efficiency for converting gravitational potential energy into X-ray emission, and α is the specific angular momentum carried away by the mass lost from the system, in units of $2\pi a^2/P_{orb}$, where a is the orbital separation (see Rappaport et al., 1982). In Eq. 6.11 we assume that the NS radius is 10 km. Using the orbital period value of 3 000.65 s, assuming $\eta = 1$ and a conservative mass transfer scenario ($\beta = 1$), we find that $L_X \simeq 1.1 \times 10^{35} f^3$ erg s^{-1} and $L_X \simeq 2.3 \times 10^{35} f^3$ erg s^{-1} for a NS mass of 1.4 $M_\odot$ and 2.2 $M_\odot$, respectively. Comparing the observed luminosity and the predicted luminosity, we estimate that $f = 3.6 \pm 0.4$ and $f = 3.0 \pm 0.3$ for a NS mass of 1.4 $M_\odot$ and 2.2 $M_\odot$, respectively. Substituting the obtained values of f in eq. 6.9, we obtain that the companion star mass is $M_2 = 0.10 \pm 0.02$ $M_\odot$ and $M_2 = 0.078 \pm 0.012$ $M_\odot$ for a NS mass of 1.4 $M_\odot$ and 2.2 $M_\odot$, respectively. The mass ratio $q = M_2/M_1$ of XB 1916-053 is between 0.036 ± 0.009 and 0.071 ± 0.009.

Hu et al. (2008) inferred the mass ratio of XB 1916-053 from the negative super-hump period and found $q \simeq 0.045$, which is compatible with our estimated range of values of q. Chou et al. (2001) estimated a value of $q \simeq 0.022$ using the period of the apsidal precession of the accretion disc of $P_{prec} = 3.9087(8)$ d. The value of q obtained by Chou et al. (2001) is outside the range that we find.

To estimate the orbital period derivative we use the eq. 11 shown in Rappaport et al. (1987) that we rewrite as

$$\dot{P} \simeq \frac{1.54 \times 10^{-9}}{1 - 1.5\alpha(1-\beta)} m_1^{2/3} P_m^{-8/3} (1+X)^{5/2} f^{3/2} \text{ s s}^{-1}. \tag{6.12}$$

Using the value of $\dot{P} \sim 1.44 \times 10^{-11}$ s s^{-1} (LQS ephemeris) and the orbital period value of 3 000.65 s, we find that the thermal bloating factor f is 40 and 32 for a NS mass of 1.4 and 2.2 M$_\odot$. These values of f are not physically plausible and suggest that, in a conservative mass transfer scenario, the value of the orbital period derivative cannot be that obtained from the LQS ephemeris.

On the other hand, adopting an orbital period of 3 000.65 s and a factor f of 3.6 and 3.0 for a NS mass of 1.4 and 2.2 M$_\odot$ we find $\dot{P} = (3.9 \pm 0.2) \times 10^{-13}$ s s^{-1} and $\dot{P} = (3.98 \pm 0.15) \times 10^{-13}$ s s^{-1} for a NS mass of 1.4 M$_\odot$ and 2.2 M$_\odot$, respectively. The orbital period derivative normalised to the orbital period is $\dot{P}/P \simeq 4.2 \times 10^{-9}$ yr^{-1} and weakly depends on the NS mass. We conclude that the conservative mass transfer scenario with a thermal bloating factor of the companion star between three and four allows us to explain the discrepancy between the predicted and observed X-ray luminosity, but it does not solve the discrepancy between the predicted and measured orbital period derivative obtained from the LQS ephemeris. For this reason, we investigate the non-conservative mass transfer scenario.

Combining the eqs. 6.11 and 6.12, we obtain

$$\frac{L_x}{\dot{P}} \simeq 3.38 \times 10^{51} m_1 P_m^{-2} \beta f^{3/2} \eta \text{ erg s}^{-1}. \tag{6.13}$$

Adopting $L_x \simeq 5.2 \times 10^{36}$ erg s^{-1}, $\dot{P} = 1.44 \times 10^{-11}$ s s^{-1}, $P = 3\,000.65$ s and fixing $\eta = 1$, we find that $\beta f^{3/2} = 0.191$ for a NS mass of 1.4 M$_\odot$. Since $f > 1$, we expect that more than 81% of the mass yielded by the companion star leaves the system. Furthermore, since the measured values of L_x and $\dot{P}$ are positive, the term $1 - 1.5\alpha(1-\beta)$ in eqs. 6.11 and 6.12 should be positive. Solving for α while taking $\beta < 0.191$, we obtain that $\alpha < 0.823$. Because α is in unit of $2\pi a^2/P_{orb}$, we find that the matter should leave the binary system from a distance $\bar{d}$ from the neutron star of $\bar{d} < \alpha^{1/2} a$; the point of ejection in unit of orbital separation is $\bar{x} = \bar{d}/a < \alpha^{1/2}$. In the rest of the discussion, we assume that the matter is ejected at the inner Lagrangian point x_{L1} of the binary system. We rewrite the eq. 6.11 as function of f using the condition $\beta f^{3/2} = 0.191$. We find

$$L_x \simeq \frac{5.2 \times 10^{42}}{1 - 1.5\, \bar{x_{L1}}^2 (1 - 0.191\, f^{-3/2})} m_1^{5/3} P_m^{-14/3} 0.191 f^{3/2} \text{ erg s}^{-1}, \tag{6.14}$$

where $\bar{x_{L1}}$ is the position of the inner Lagrangian point in units of orbital separation. Using eq. 6.9 and a NS mass of 1.4 M$_\odot$, $\bar{x_{L1}}$ can be written as a cubic function of f for values of the thermal bloating factor between 1 and 10. We find

$$\bar{x_{L1}} = 0.915 - 6.87 \times 10^{-2} f + 6.61 \times 10^{-3} f^2 - 2.88 \times 10^{-4} f^3,$$

with an accuracy of 2×10^{-3}. Combining the last equation and eq. 6.14, we infer the luminosity as function of f. We show L_x in unit of 10^{36} erg s^{-1} versus f for a NS mass of 1.4 M$_\odot$ (purple colour) in Fig. 6.8. Since the observed luminosity for a NS mass of 1.4 M$_\odot$ is larger than the predicted one for each value of f, also taking the corresponding error into account, we conclude that this specific non-conservative mass transfer scenario fails for a NS mass of 1.4 M$_\odot$.

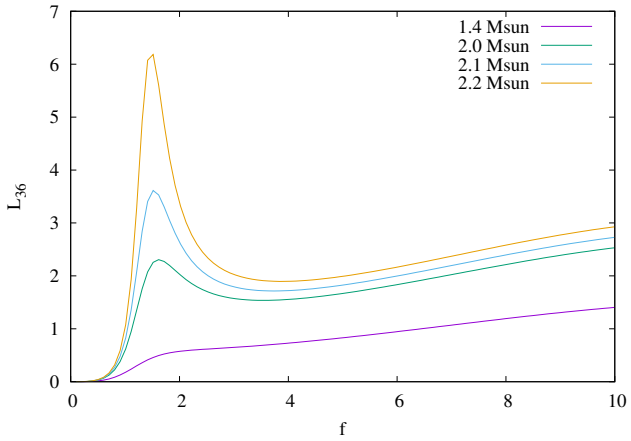

Figure 6.8: X-ray luminosity of XB 1916-053 in units of 10^{36} erg s^{-1} versus the thermal bloating factor f of the companion star. The four curves correspond to different values of the NS mass: purple, green, light blue, and gold colours correspond to a NS mass of 1.4, 2, 2.1, and 2.2 $M_\odot$, respectively. The peaks in the curves are at $f \simeq 1.5$.

We repeat the same procedure for NS masses of 2, 2.1 and 2.2 $M_\odot$, finding that the predicted and observed luminosities are only compatible in the case in which the NS mass is ≥ 2.2 $M_\odot$. In this case ,we find that $\beta f^{3/2} = 0.154$, $\alpha < 0.784$ and

$$x_{\bar{L}1} = 0.927 - 6.02 \times 10^{-2} f + 5.66 \times 10^{-3} f^2 - 2.88 \times 10^{-4} f^3$$

, with an accuracy of 2×10^{-3}. The luminosity for a NS mass of 2.2 $M_\odot$ (gold colour) is shown in Fig. 6.8. Furthermore, we plot the orbital period derivative as function of f for a NS mass of 2.1 $M_\odot$ (brown colour) and 2.2 $M_\odot$ (purple colour) in Fig. 6.9. We note that only for a NS mass of 2.2 $M_\odot$ the predicted and measured $\dot{P}$ are compatible for $f \simeq 1.5$. We conclude that this non-conservative mass transfer scenario predicts the observed values of luminosity and orbital period derivative only for NS masses larger than 2.2 $M_\odot$. For a NS mass of 2.2 $M_\odot$, the companion star has a mass of 0.028 $M_\odot$ and β is close to 0.084, which is more than 90% of the matter, yielded from the companion star, that leaves the binary system.

In this scenario, we suggest that XB 1916-053 could be considered as a possible progenitor of the ultra-compact "Black Widow" pulsars with very low-mass companions. Benvenuto et al. (2012) proposed that a binary system with an initial orbital period of 0.8 d, composed of a 1.4 $M_\odot$ NS and a companion star mass of 2 $M_\odot$, evolves in ~6.5 Gyr forming a binary system that well fits the known orbital parameters of the black widow millisecond pulsar PSR J1719-1438. We note that the same evolutive path fits the orbital parameters of XB 1916-053 at ~ 5 Gyr from the initial time. At 5 Gyr, the predicted orbital period is 0.035 d, the predicted companion star mass is 0.03 $M_\odot$, the NS mass is slightly larger than 2.2 $M_\odot$ (Benvenuto, private communication) and the companion star is helium dominated. These values are very similar to those of XB 1916-053 shown in this work for a non-conservative mass transfer scenario, although a discrepancy

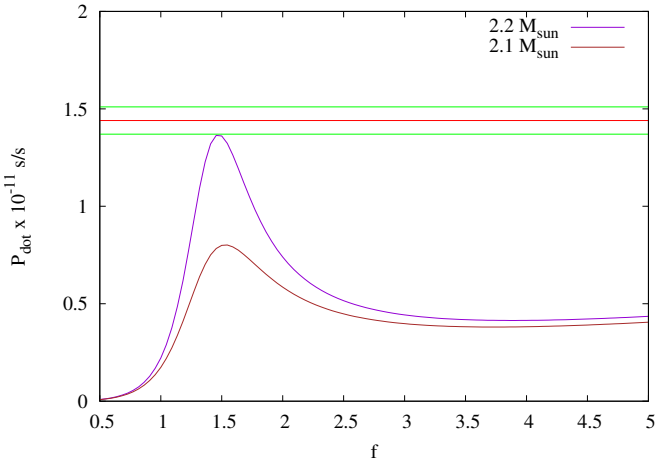

Figure 6.9: Orbital period derivative of XB 1916-053 in units of 10^{-11} s s^{-1} versus the thermal bloating factor f of the companion star. The brown and purple curves are obtained using a NS mass of 2.1 and 2.2 $M_\odot$. The red and green lines indicate the best-fit value and the values at 68% confidence level of the orbital period derivative obtained from the LQS ephemeris. The purple curve is compatible at 1 σ with the measured orbital period derivative for $f \simeq 1.5$.

between our estimation of $\dot{M}_2 \sim 4.1 \times 10^{-9}$ $M_\odot$ yr^{-1} and the value suggested by Benvenuto et al. (2012) at 5 Gyr ($\sim 10^{-10}$ $M_\odot$ yr^{-1}) is present. Furthermore, we note that as the spin period of PSR J1719-1438 is 5.7 ms (see Bailes et al., 2011, and references therein) the spin period of the NS in XB 1916-053 could also be extremely short. Indeed, Galloway et al. (2001) interpreted the asymptotic frequency of the coherent burst oscillations in terms of a decoupled surface burning layer and suggested that the NS could have a spin period around 3.7 ms.

Nevertheless, we note that our solution for a non-conservative mass transfer scenario is not supported by a robust physical mechanism to explain the large quantity of matter ejected from the inner Lagrangian point. To date, only two physical mechanisms are known to be able to eject the transferred matter partially (or totally) . The first mechanism predicts that when a super-Eddington mass transfer occurs, the X-ray luminosity has to be at the Eddington limit. Then, the radiation pressure from the compact object pushes away part of the transferred matter from the binary system. This mechanism was recently invoked to explain the large orbital period derivative measured in the accretion disc corona (ADC) source X1822-371 by Burderi et al. (2010), Iaria et al. (2013), and Iaria et al. (2015b). However, this mechanism cannot be applied in the case of XB 1916-053 because type-I X-ray bursts are observed in the light curve of the source (see e.g. Fig. 6.2), whilst the stable burning sets in at high accretion rate values that are comparable to the Eddington limit (see Bildsten, 2000, and references therein). Consequently, the mass transfer rate cannot be super-Eddington and this mechanism cannot justify a non-conservative mass transfer scenario. The second mechanism supposes that the X-ray binary system is a transient source and during the X-ray quiescence it is ejecting the transferred matter from the inner Lagrangian point due to the radiation pressure of the magneto-dipole rotator emission. This mechanism, which we

Table 6.5: Best-fit parameters of the delays assuming the presence of the third body in eccentric orbit and taking a quadratic term $c = 5 \times 10^{-7}$ s/d^{2}into account.

Parameters	P_{mod}=17 100 d	P_{mod}=18 600 d	P_{mod}=20 100 d
a (s)	180 ± 332	21 ± 307	-27 ± 285
b ($\times 10^{-3}$ s/d)	2 ± 20	2 ± 19	4 ± 21
A (s)	506 ± 46	534 ± 43	562 ± 43
e	0.26 ± 0.20	0.28 ± 0.15	0.32 ± 0.13
ϖ (deg)	198 ± 27	213 ± 28	219 ± 27
t_ϕ (d)	-3594 ± 1129	-3036 ± 1131	-2825 ± 1042
χ^2(d.o.f.)	51.3(21)	47.9(21)	45.5(21)
F-test prob.	3.5×10^{-2}	1.5×10^{-2}	0.8×10^{-2}

NOTE — The reported errors are at 68% confidence level. The F-test probability is estimated with respect to the χ^2 value of the LS ephemeris (the fourth column of Tab. 6.4).

call radio ejection after Burderi et al. (2001), was proposed by Di Salvo et al. (2008) to explain the large orbital period derivative measured in SAX J1808.4–3658. However, this mechanism also fails to explain our results because XB 1916-053 is a persistent X-ray source.

Finally, we discuss the sinusoidal modulation observed in the LQS and LSe ephemerides. If we assume a conservative mass transfer scenario, the predicted orbital period derivative is close to 4×10^{-13} s s^{-1} independent of the NS mass. Then we added a quadratic term to the LSe ephemeris to take the predicted value into account. We fitted again the delays using the relation

$$y(t) = a + bt + ct^2 + \Delta_{DS}(t),$$

where the term c is fixed to 5×10^{-7} s/d^2. The fit parameters are reported in Tab. 6.5. We note that the addition of the quadratic term does not significantly change the best-fit parameters.

An explanation of the sinusoidal modulation obtained from the LSe ephemeris could be the presence of a third body gravitationally bound to the X-ray binary system. Assuming the existence of a third body of mass M_3, the binary system XB 1916-053 orbits around the new centre of mass (CM) of the triple system. The distance of XB 1916-053 from the new CM is given by $a_x = a_{bin} \sin i = A\ c$, where i is the inclination angle of the orbit with respect to the line of sight, A is the amplitude of the sinusoidal function obtained from the ephemeris of eq. 6.8, and c is the light speed. We obtained $a_x = (1.60 \pm 0.13) \times 10^{13}$ cm for $P_{mod} = 18\,600$ d. We can write the mass function of the triple system as

$$\frac{M_3 \sin i}{(M_3 + M_{bin})^{2/3}} = \left(\frac{4\pi^2}{G}\right)^{1/3} \frac{a_x}{P_{mod}^{2/3}},$$

where M_3 is the third body mass, M_{bin} the binary system mass, and finally, P_{mod} is the orbital period of XB 1916-053 around the CM of the triple system. Substituting the values of M_{bin}, P_{mod}, a_x, and assuming an inclination angle for the source of 70°, we find that m_3 is ~ 0.10 M$_\odot$ and ~ 0.14 M$_\odot$ for a NS mass of 1.4 M$_\odot$ and 2.2 M$_\odot$, respectively. We used also P_{mod} of 17 100 and 20 100 d finding that the values of m_3 are substantially independent of the value of P_{mod}.

For a non-conservative mass transfer scenario, we discuss the sinusoidal modulation obtained from the LQS ephemeris assuming a NS mass of 2.2 $M_\odot$. In this case we find that $a_x = (3.9 \pm 0.5) \times 10^{12}$ cm and $m_3 \sim 0.055$ $M_\odot$ for an inclination angle of 70°.

6.6 Conclusions

We have systematically analysed all the historically reported X-ray light curves of XB 1916-053, which span 37 years. We find that the previously suggested quadratic ephemeris for this source no longer fits the dip arrival times.

We studied the conservative mass transfer scenario of the system, finding that the thermal bloating factor of the degenerate companion star is 3.6 and 3 for a NS mass of 1.4 and 2.2 $M_\odot$. In this scenario, the predicted and observed luminosity are compatible (~5-7 $\times 10^{36}$ erg s^{-1}), although the orbital period derivative is a factor of 40 smaller than the value of 1.44×10^{-11} s s^{-1} obtained fitting the delays with a quadratic plus a sinusoidal function (LQS ephemeris). If the conservative mass transfer scenario is correct, we conclude that the modulation of the delays associated with the dip arrivals time are solely due to a sinusoidal modulation caused by a third body orbiting around the binary system. In this case we estimate the third body mass is 0.10 and 0.14 $M_\odot$ for NS masses of 1.4 and 2.2 $M_\odot$, respectively. The orbital period of the third body around XB 1916-053 is close to 55 yr and the orbit shows an eccentricity $e = 0.28 \pm 0.15$.

In a non-conservative mass transfer scenario where the mass is ejected away from the inner Lagrangian point, we find that the observed luminosity and the orbital period derivative obtained from the LQS ephemeris are possible only from a NS mass ≥ 2.2 $M_\odot$. In this case we obtain that the thermal bloating factor of the degenerate companion star is $f \simeq 1.5$, the companion star mass is 0.028 $M_\odot$, and the fraction of matter yielded by the companion star and accreting onto the NS is $\beta = 0.084$. In this scenario, the sinusoidal modulation of the delays can be explained by the presence of a third body orbiting around XB 1916-053 with an period of 26 yr. We find that the third body mass is 0.055 $M_\odot$. Finally, if the non-conservative mass transfer scenario is valid, we suggest that XB 1916-053 and the ultra-compact black widow system PSR J1719-1438 could be two different stages of the same evolutive path discussed by Benvenuto et al. (2012). If it is true, then the age of XB 1916-053 is close to 5 Gyr, whilst PSR J1719-1438 is ~6.5 Gyr old.

CHAPTER 7

SPECTRAL ANALYSIS OF THE DIPPING SOURCE LMXB SYSTEM XB 1916-053

Gambino A. F. et al.

To be submitted

7.1 Abstract

Context: XB 1916-053 is a Low Mass X-ray binary system (LMXB) hosting a neutron star (NS) and showing periodic dips. The timing studies estimated an orbital period of approximately 50 min and recently also the possibility that this system should be a hierarchical triple system. The spectrum of the persistent emission has been modelled taking into account the contribution of a blackbody component having a temperature of 1.31 - 1.67 keV and a comptonization component having an electron temperature of 9.4 keV and a Γ of 2.5 - 2.9. In addition, the presence of several absorption features associated with the Kα transitions of Fe XXV, Fe XXVI, Mg XII, S XVI, Ne X and Si XIV, suggested the presence of relatively cold and partially ionized plasma in the system. The dip spectrum has been explained as a decrease of the ionization of the plasma along with a simultaneous increase of the equivalent hydrogen column density of a ionized absorber interposed between the observer and the central emitting source.

Aims: In this work we want to test the statistical significance of a model that describes the spectrum of the persistent emission of the source with the comptonization of both the photons emitted by the NS surface and those emitted by the accretion disk. In addition we want to compare this model with a model that considers the comptonisation of the only photons emitted by the NS surface.

Methods: We analyse three Suzaku observations of XB 1916-053: the first one performed on

November 2006 and the other two on October 2014. We extracted the persistent spectra from each observation. We combined the spectra of the two more recent observations, then obtaining a unique spectrum with a considerable statistic. In addition, we extracted and combined also the spectra of the dip taken during the same two most recent observations.
Results: Taking into account the comptonization process of the photons emitted by the disk in addition to those emitted by the NS surface does not represent a statistically significant improvement of the fit. We found that the source is in a soft spectral state in all the analysed observations and detect the Kα absorption lines of Fe XXV and Fe XXVI, and for the first time the Kβ absorption lines. Furthermore, we also detect an edge at 0.876 keV that is in agreement with the K absorption edge of O VIII. The dip spectrum is well described by a model that consists of a partially ionized material that covers the persistent spectrum and absorbs part of the rear radiation.

7.2 Introduction

XB 1916-053 is a dipping Low Mass X-ray binary system (LMXB) located at R.A: 19h 18m 47.871s, Dec.: -05°14' 17.09" (J2000), with a 90% uncertainty circle of the absolute position of 0.6" Iaria et al. (2006). The optical counterpart was associated to V1405 Aql that has a B-V magnitude of 0.4 and is located at 8.7" from the X-ray source (Liu et al., 2007). The X-ray light curves of the source show type I X-ray bursts that were observed for the first time by Becker et al. (1977) using *OSO 8* data. The presence of the type-I X-ray bursts, is a clear signal of the presence of a neutron star (NS) into the binary system. The distance to the source was evaluated by several authors taking into account the X-ray bursts as standard candles having a luminosity at the Eddington limit. Smale et al. (1988) evaluated a distance of 8.4 kpc for cosmic abundances of hydrogen, or of 10.8 kpc for a hydrogen-deficient accreted material. Galloway et al. (2008) suggested a distance of 7 kpc or 9 kpc, for a H-rich and He-rich plasma accreted onto the NS surface. In addition Yoshida (1993) suggested a distance of 9.3 kpc with an error of the 15% analysing the photospheric radius expansion (PRE) shown by a sample of analysed bursts.
The orbital period of the system was evaluated by Church et al. (1997) taking the advantage of the periodicity of the dips present in the *ASCA* data. The dips are an evident cause of the partial covering of the central emission region of the binary system by a bulge of cold and/or partially ionized material in the point at which the accretion flow hits the outer part of the accretion disk. They estimated an orbital period of $P = 3005 \pm 10$ s. The observation in the optical band, however, showed a modulation of the light curve having a period of 3027.4± 0.4 s (Grindlay et al., 1988). The successive extension of the orbital ephemeris made by Iaria et al. (2015a) revealed that this modulation is probably due to the presence of a third body in the system. The mass of this body and its orbital period is dependent on the mass transfer scenario adopted for XB 1916-053. The authors evaluated a mass for the third body of $M_3 = 0.10 - 0.0.14$ M$_\odot$ and an orbital period of 51

yr assuming a conservative mass transfer, or $M_3 = 0.055$ $M_\odot$ and an orbital period of 26 yr if the mass transfer is non-conservative. In the latter case, the analysis returned also an estimation of the companion star mass of $M_2 = 0.028$ $M_\odot$, that according to Nelemans et al. (2006) is a helium-rich star.

The presence of the dips in the light curve suggests that the system is seen with an high inclination angle, and in particular this constrains the inclination angle to be between 60°and 80°Frank et al. (1987).

The spectrum of XB 1916-053 has been widely studied both for the continuum and the dip contribution. Zhang et al. (2014) found the source in a high-soft spectral state and modelled the continuum spectrum of XB 1916-053 taking into account a unique corona that comptonizes both the photons emitted by the NS surface and those emitted by the innermost part of the accretion disk. Their model allowed them to constrain the spectral parameters of the accretion disk, as well as those related to the blackbody component associated to the emission of the NS surface. They constrained the equivalent column of hydrogen to the value of $N_H = 0.06 \pm 0.01 \times 10^{22}$ cm^{-2}, inferring spectral parameters that are typical of systems in a soft spectral state. They found a temperature of disk of $kT_{in} = 1.87 \pm 0.18$ keV and a temperature and a photon index of the electron cloud forming the corona of $kT_e = 3.7^{+1.8}_{-0.4}$ keV and $\Gamma = 2.65^{+1.28}_{-0.46}$, respectively.

The spectrum shows also some absorption lines superimposed to the continuum emission. The doublet of the Fe XXV and Fe XXVI Kα absorption lines was firstly detected by Boirin et al. (2004). The authors also found a weak evidence for the presence of the Mg XII, S XVI, Ni XXVII Kα absorption lines, as well as the possible presence of the Fe XXVI Kβ absorption line and an absorption edge at 0.98 keV. The authors proposed that the latter should be a K absorption edge from moderately ionized Ne ions, or an L absorption edge from moderately ionized Fe ions. They also proposed the possibility that this should be the result of a superimposition of the edges of both the kind of ions.

Iaria et al. (2006), using Chandra data, confirmed the presence of the Mg XII and S XVI Kα absorption lines, and furthermore detected the Kα absorption lines of Ne X and Si XIV. The diagnostic of the absorption lines with Chandra allowed the authors to obtain an estimation of the line widths of these narrow features, as well as an estimation of the emission region at which the lines originated: 4×10^{10} cm far away from the NS, that is almost at the accretion disk rim.

In Boirin et al. (2005) the transition from the persistent to the dip spectrum was explained as a decrease of the ionization parameter ξ of the plasma with a simultaneous increase of the equivalent hydrogen column density of a ionized absorber interposed between the observer and the central emitting source. Actually, the great variety of absorption features into the spectrum of XB 1916-053 suggests the presence of a partially ionized plasma into the system.

In this work we study the continuum and dip spectrum of XB 1916-053, taking the advantage of data provided by the *Suzaku* space mission. The aim of the work is to test the statistical significance of the model of Zhang et al. (2014), with respect to a simpler model in which the

Table 7.1: Results of the *1-seed* model. Errors on each parameter are quoted at the 90% confidence level. Model: CONSTANT*GABS*EDGE*PHABS*(GAUSSIAN + GAUSSIAN + GAUSSIAN + GAUSSIAN + DISKBB + NTHCOMP)

Model	Component	Spectrum 1	Spectrum 2
CONSTANT	factor	1 (frozen)	1 (frozen)
GABS	LineE(keV)		$4.5^{+0.2}_{-0.3}$
	Sigma(keV)		$1.12^{+0.3}_{-0.2}$
	Strength		$0.22^{+0.2}_{-0.10}$
EDGE	edgeE(keV)		$0.876^{+0.016}_{-0.013}$
	MaxTau		0.11 ± 0.02
PHABS	N_H (10^{22} cm^{-2})	$0.433^{+0.007}_{-0.012}$	0.479 ± 0.02
GAUSSIAN	LineE(keV)	$6.943^{+0.017}_{-0.013}$	$6.972^{+0.014}_{-0.010}$
	Sigma(keV)	0.02 (frozen)	0.02 (frozen)
	norm(10^{-5})	$-7.6^{+1.2}_{-1.2}$	-6.5 ± 0.7
GAUSSIAN	LineE(keV)	$6.65^{+0.03}_{-0.03}$	$6.69^{+0.03}_{-0.02}$
	Sigma(keV)	0.02 (frozen)	0.02 (frozen)
	norm(10^{-5})	$-3.3^{+1.2}_{-1.3}$	$-3.6^{+0.6}_{-0.7}$
GAUSSIAN	LineE(keV)	–	$8.19^{+0.07}_{-0.06}$
	Sigma(keV)	–	0.02 (frozen)
	norm(10^{-5})	–	$-1.7^{+0.6}_{-0.7}$
GAUSSIAN	LineE(keV)	–	$7.80^{+0.08}_{-0.07}$
	Sigma(keV)	–	0.02 (frozen)
	norm(10^{-5})	–	-1.3 ± 0.7
DISKBB	Tin(keV)	$0.68^{+0.03}_{-0.03}$	0.51 ± 0.05
	norm	44^{+7}_{-5}	80^{+36}_{-21}
NTHCOMP	Γ	$2.5^{+0.4}_{-0.3}$	$1.98^{+0.09}_{-0.08}$
	kT$_e$(keV)	>7	$6.5^{+3}_{-1.4}$
	kT$_{bb}$(keV)	$1.29^{+0.06}_{-0.13}$	0.81 ± 0.09
	inp_type(0/1)	0 (frozen)	0 (frozen)
	Redshift	0 (frozen)	0 (frozen)
	norm (10^{-3})	$5.1^{+0.9}_{-0.7}$	10^{+3}_{-2}
UNABS. FLUX [0.1 – 100 KEV]	erg cm^{-2} s^{-1}	5.9×10^{-10}	5.1×10^{-10}
	χ^2/dof	702.4/618	694.8/601

corona comptonizes only photons emitted by the NS surface.

The paper is structured as follows: in section 7.3 we report the data selection and reduction, in section 7.4 we report the spectral analysis performed on the persistent and dip spectra, whilst we discuss the obtained results in section 7.5. A conclusion has been reported in section 7.6.

7.3 Observation and data reduction

Suzaku (Mitsuda et al., 2007) observed XB 1916-053 three times. The first observation (ObsID 401095010) was performed from 8 November 2006 at 05:49:53 to 9 November 2006 at 02:41:15, for

Table 7.2: Results of the *2-seed* model. Errors on each parameter are quoted at the 90% confidence level. Model: CONSTANT*EDGE*GABS*PHABS(GAUSSIAN + GAUSSIAN + GAUSSIAN + GAUSSIAN + NTHCOMP + NTHCOMP)

Model	Component	Spectrum 1	Spectrum 2
CONSTANT	factor	1 (frozen)	1 (frozen)
EDGE	edgeE(keV)	–	$0.877^{+0.016}_{-0.014}$
	MaxTau	–	0.11 ± 0.02
GABS	LineE(keV)	–	4.6 ± 0.2
	Sigma(keV)	–	$0.9^{+0.4}_{-0.3}$
	Strength	–	$0.09^{+0.09}_{-0.06}$
PHABS	N_H (10^{22} cm^{-2})	$0.466^{+0.014}_{-0.013}$	$0.49^{+0.03}_{-0.02}$
GAUSSIAN	LineE(keV)	$6.65^{+0.04}_{-0.04}$	$6.69^{+0.03}_{-0.02}$
	Sigma(keV)	0.02 (frozen)	0.02 (frozen)
	norm(10^{-5})	$-2.9^{+1.2}_{-1.3}$	$-3.4^{+0.3}_{-0.7}$
GAUSSIAN	LineE(keV)	$6.943^{+0.02}_{-0.013}$	$6.972^{+0.014}_{-0.010}$
	Sigma(keV)	0.02 (frozen)	0.02 (frozen)
	norm(10^{-5})	$-7.4^{+1.2}_{-1.2}$	$-6.3^{+0.8}_{-0.7}$
GAUSSIAN	LineE(keV)	–	$7.80^{+0.08}_{-0.07}$
	Sigma(keV)	–	0.02 (frozen)
	norm(10^{-5})	–	-1.3 ± 0.7
GAUSSIAN	LineE(keV)	–	$8.19^{+0.07}_{-0.06}$
	Sigma(keV)	–	0.02 (frozen)
	norm(10^{-5})	–	-1.8 ± 0.7
NTHCOMP	Γ	$2.89^{+0.14}_{-0.2}$	$2.11^{+0.2}_{-0.12}$
	kT_e(keV)	>4	7^{+11}_{-2}
	kT_{bb}(keV)	$1.64^{+0.05}_{-0.04}$	1.4 ± 0.2
	inp_type(0/1)	0 (frozen)	0 (frozen)
	Redshift	0 (frozen)	0 (frozen)
	norm(10^{-3})	$2.2^{+0.2}_{-0.2}$	$1.6^{+0.8}_{-0.5}$
NTHCOMP	Γ	$2.89^{+0.14}_{-0.2}$	$2.11^{+0.2}_{-0.12}$
	kT_e(keV)	>4	7^{+11}_{-2}
	kT_{bb}(keV)	$0.54^{+0.02}_{-0.03}$	0.43 ± 0.06
	inp_type (0/1)	1 (frozen)	1 (frozen)
	Redshift	0 (frozen)	0 (frozen)
	norm (10^{-3})	$60.8^{+1.3}_{-1.2}$	45 ± 2
UNABS. FLUX [0.1 – 100 KEV]	erg cm^{-2} s^{-1}	6×10^{-10}	5.1×10^{-10}
	χ^2/dof	702.2/618	698.5/601

a net exposure of about 39 ks. The other two observations were acquired in 2014 and in particular the first observation (ObsID 409032010) has been performed from 14 October at 16:20:52 to 18 October at 12:20:16, for a total exposure of 155.9 k. The second observation (ObsID 409032020) has been performed from 18 October at 12:20:17 to 22 October at 02:40:09, for a net exposure of 140.5 ks. For simplicity, hereafter we will attribute the names Obs1, Obs2 and Obs3 to ObsID 401095010, ObsID 409032010 and ObsID 409032020, respectively.

During all the observations both the X-ray Imaging Spectrometers (XIS; Koyama et al., 2007) and the Hard X-ray Detector (HXD; Takahashi et al., 2007) were operative. The XIS detectors consist of four chips generally numbered as 0 to 3 that are sensible to the energy band between 0.2 and 12 keV. The XIS0, XIS2 and XIS3 chips have a similar response to the incoming radiation, consisting of the same kind of front-illuminated CCD. On the other hand, the XIS1 chip uses a back-illuminated CCD. However, in the observations of 2014 only the the XIS0, XIS1 and XIS3 were operative, owing to the fact that the XIS2 chip broke down just during the observation of 2006 that we analyse in this work (ObsID 401095010). The HXD assembly, on the other hand, consists of two non imaging detectors: the PIN diodes (10–70 keV) and GSO scintillators (30–600 keV).
In Obs1 the XIS chips operated in full window mode and collected data edited both in 3x3 and 5x5 pixel mode for a net exposure of 40 ks, while the HXD-PIN detector was exposed for 37 ks. On the other hand, In Obs2, the XIS0, XIS1 and XIS3 detectors operated in full window mode and collected data edited both in 3x3 and 5x5 pixel mode for a net exposure of 155.9 ks, while the HXD-PIN detector was exposed for 8.8 ks. In Obs3, instead, all the XIS detectors operated using the 1/4 window option and collected data edited both in 3x3 and 5x5 pixel mode for a net exposure of 140.5 ks, whilst the HXD-PIN for 6.9 ks.
The source is not detected in the GSO, and for this reason we limit our analysis only to the spectra collected from the XIS and PIN detectors for all the observations. The data have been analysed inside the HEASoft v. 6.19 environment. Additionally, for Obs1 we used the calibration files v. 20070731 and v. 20070710 for XIS and HXD/PIN, respectively. Similarly, for Obs2 and Obs3 we used the XIS calibration files v. 20160607 and the HXD-PIN calibration files v. 20110913.
All the data have been processed with the `aepipeline` routine provided with the Heasoft FTOOLS. For each XIS chip we co-added the data edited in 3x3 and 5x5 pixel format and performed a better estimation of the attitude using the `aeattcor.sl` tool distributed and created by J. E. Davis. The attitude correction to the XIS data has been applied with the supplementary tool `xiscoord`.

The light curve of Obs1 shows a slightly increasing trend in the count-rate that starts from about 5 c/s and that arrives up to 11 c/s. The observation shows periodic dips and one type I X-ray burst, as already observed by Zhang et al. (2014).
Obs2 starts with a count-rate of about 18 c/s that decreases reaching a final value of about 5 c/s at the end of the observation. Four type I X-ray bursts occur during the observation as well as several periodic dips. The hardness ratio of the source during the observation, however,

does not show significant variations. On the other hand, during Obs3 the source maintains an approximately constant count-rate of about 5 c/s and several periodic dips occur. However, the hardness ratio does not show any important variations.
In this work we are not interested in the analysis of the type I X-ray bursts, then we removed the time segments starting 5 s before the rise time of each burst and ending 100 s after the peak time. Furthermore, we distinguished between the dip and the persistent emission events, performing a time selection on the data of all the observations.
To estimate if the XIS data are affected by pile up, we used the tool `pile-estimate.sl` created by M. A. Novak. For Obs1 we obtain a pile-up fraction between the 9% and the 13 % for all the XIS chips considering the events in a circular region centered at the coordinates of XB 1916-053 and with radius 114". Then, in order to reduce the pile-up fraction under the 4% we considered only the events included in a annular regions centered onto the source and having an outer radius of 114" and an inner radius of 31". On the other hand, for Obs2 and Obs3 a circular region centered at the coordinates of the source and having a radius of 114" is sufficient to obtain an estimation of the pile-up fraction of the 4% at most for Obs2 and of about 2% for Obs3. The XIS spectra of the source for each observation, have been obtained considering events falling inside these extraction regions. The corresponding background spectra have been extracted considering events localized far away from the source and inside a circular region covering the same area of the corresponding source extraction region. For Obs1 we extracted the spectra of the persistent emission and of the dips taking into account the data collected by each XIS chip. For the only XIS2 data, we excluded the last 6 ks of observation during which the XIS2 did not acquired data anymore, owing to the damage it undergone. As a consequence of this, we took into account the only spectra extracted from the XIS0, XIS1 and XIS3 data for Obs2 and Obs3.
The response of each XIS chip has been obtained using the tool `xisrmfgen`, whilst the ancillary response files (ARFs) have been obtained using the tool `xissimarfgen`, setting as input coordinates for the source R. A.=289.699462°Dec.=-5.238081°(Iaria et al., 2006).
The HXD-PIN spectrum has been extracted using the tool `hxdpinxbpi`. For Obs1 we selected the response file `ae_hxd_pinxinome3_20080129.rsp` provided by the HXD team, whilst we selected the response file `ae_hxd_pinxinome11_20110601.rsp` for Obs2 and Obs3.
The background file of Obs1 has been regularly produced by the HXD team and then used in the analysis, whilst the background files for the Obs2 and Obs3 of 2014 were not available. Starting from that year, indeed, normal operation of the HXD was very rare due to the power consumption of the spacecraft. In order to estimate the background generated by the NXB+CXB events, the HXD team suggested us to use the spectrum of the source RXJ 1856.5-3754, that is a neutron star with a very soft X-ray emission, and thus the PIN data are almost attributed to the CXB + NXB contribution. Since our source is very bright with respect to RXJ 1856.5-3754, the background systematic error is not so significant below 30 keV, whilst the NXB systematics above 30 keV may be around the 10-20% in Obs2 and Obs3.

Then, as suggested by the HXD team, we processed the ObsID 109008010 data of RXJ 1856.5-3754 of 2014 April with the `aepipeline` routine. This observation has an exposure of 35 ks that has been considered in its entirety in order to extract the HXD/PIN spectrum of the source through the `hxdpinxbpi` tool. To take into account a systematic error of the 20% above 30 keV, we used the ftool `grppha`. Hereafter, this spectrum represents the HXD/PIN CXB + NXB background spectrum for both Obs2 and Obs3.
The products of this first processing step for the Obs1 are spectra of the persistent emission of XB 1916-053 for a net exposure of 33 ks for the XIS0 and XIS3 chips, and 30 ks for the XIS2. Furthermore, the corresponding HXD/PIN spectrum has an exposure of 30 ks.
From Obs2 we extracted XIS persistent spectra of 120 ks of exposure for each considered chip respectively and a HXD/PIN persistent spectrum of 8 ks of exposure. In addition, from this observation we also extracted XIS spectra of the dips for an amount of 13 ks of exposure for each XIS chip, as well as a HXD/PIN spectrum of the dips of 502 s of exposure. On the other hands, for the Obs3 we extracted XIS spectra of the persistent emission for an amount of 83 ks of exposure for each of the considered chips, and of 1.5 ks of exposure from the HXD/PIN data. As far as concerns the dip part, we extrapolated spectra of 23 ks from the XIS data of each considered chip, as well as a HXD/PIN spectrum of 5 ks of exposure.
Considering the similar spectral response of the XIS0, XIS2 and XIS3 chips, in order to increase the statistics, we choose to combine the spectra extracted from these devices as well as their spectral responses using the `addascaspec` routine. We did this for all the observations and both for the persistent and the dip spectra (we remark here that during the Obs2 and Obs3 only the XIS0 and XIS3 chips were active).

Furthermore, we noticed that the spectral shape of the persistent emission of XB 1916-053 was the same in Obs2 and Obs3. Then, also supported by the fact that these observations are extremely close in time, in order to further increase the statistic of the observations, we combined the XIS03 spectra as well as the HXD/PIN spectra of the two observations, obtaining a broad band spectrum with a considerably high statistics: the resulting exposure times for the XIS03 and PIN total combined spectra are of 400 ks and 9.3 ks, respectively.

7.4 Data analysis

The broad band spectrum obtained from Obs1, that will be hereafter named *Spectrum 1*, covers the energy range between 0.8 and 40 keV. Similarly, the spectrum obtained from the combination of data of Obs 2 and Obs 3 will be named *Spectrum 2* and covers the energy range between 0.8 and 30 keV, respectively. In these two spectra, however, the XIS data cover the energy range between 0.8 and 10 keV, whereas the data of the HXD/PIN cover the energy range between 15 and 40 keV in Spectrum 1 and between 15 and 30 keV in Spectrum 2, respectively. In all the spectra we ignored the energy ranges 1.7–1.9 keV and 2.2–2.4 keV in the XIS spectra, owing to

the presence of calibration systematic features in those energy ranges due to the neutral silicon and gold. In order to avoid an oversampling of the energy resolution of the XIS, we applied a grouping of a factor 4 to the data. Furthermore, we grouped all the spectra in order to have al least 25 photons per energy channel, with the only exception for the HXD/PIN data of Spectrum 1, where due to the lower statistics we grouped the spectrum to have al least 100 photons per energy channel.
In the subsequent part of this work we want to test if the model used by Zhang et al. (2014) to describe the persistent spectrum of XB 1916-053 acquired in Obs1 actually fits the spectrum of this source that has a higher statistic. To complete this task, as a first step we will test our persistent spectra with a simple model consisting in only one source of seed photons for the comptonization, represented by the blackbody emission from the NS surface. Successively, we will compare the obtained results with respect to the case in which we use the model of Zhang et al. (2014) to fit the spectra and a conclusion will be reported.

For the spectral analysis we use Xspec v. 12.9.0 as well as the cross section table of Verner et al. (1996) and the chemical abundances reported by Wilms et al. (2000).
We first fit Spectrum 1 with a spectral model that is usually suitable for atoll class LMXB systems (see e.g. Di Salvo et al., 2009; Piraino et al., 2007). This model consists in a soft blackbody component plus a hard component represented by the Comptonization. Furthermore, in this model we take into account the photoelectric absorption by the neutral matter in the interstellar medium (ISM).
More precisely, we used a multicolor-disk blackbody component (`diskbb` - see Mitsuda et al. (1984)) that consists of two parameters: the temperature at the inner disk radius and a normalisation parameter N linked to the value of the inner radius through the relation $N = (R_{in}/D_{10})^2\, cos(\theta)$, where R_{in} is an apparent inner disk radius in km and θ is the inclination angle of the disk with respect to the line of sight ($\theta = 0$ is the face-on case). As comptonization component we used `nthcomp` (Życki et al., 1999), that is a thermally comptonized continuum model that is defined by an asymptotic power-law photon index Γ, the electron temperature KT_e, and the seed photon temperature KT_{bb}. This model takes also into account a $redshift$ parameter as well as a supplementary parameter named inp_type that can be set to 0 or 1 depending if we want to consider seed photons distributed according to a blackbody or disk-blackbody distribution, respectively. On the other hand, to take into account the photoelectric absorption by the neutral matter in the ISM, we use the multiplicative spectral component `phabs`, that takes into account the cosmic abundances and the defined cross sections. This spectral component is defined through the parameter N_H that is the equivalent hydrogen column (in units of 10^{22} atoms cm^{-2}). To take into account the different instrumental responses of the XIS and HXD/PIN detectors we also introduced an inter-calibration constant into the model.

The application of this model (hereafter *1-seed Model*) to Spectrum 1 returns a $\chi^2(d.o.f.)$ of 817.61(622) and evident residuals in absorption at about 7 keV, as observed by Zhang et al. (2014).

We modelled these residuals with the two absorption lines already found by Boirin et al. (2004) using the additive spectral component gauss in Xspec. We fixed the value of the line widths to σ=20 eV due to the discrete energetic resolution of the Suzaku/XIS instrument. This quantity is actually compatible with the line width of the Fe XXVI Kα absorption line evaluated by Iaria et al. (2006) using data of the Chandra observatory, and will be used for all the subsequent analysis.
The fit returns a value of $\chi^2(d.o.f.)$ of 702.4(618) and an f-test probability of chance improvement of 1.8×10^{-19} with respect to the previous fit. The lines we obtain from the fit are centred at 6.65 and 6.943 keV, and are actually compatible with the Kα absorption lines of Fe XXV and Fe XXVI. The detection of these two absorption lines has been obtained with a confidence level of 4σ and 10σ, respectively. This level of statistical confidence has been inferred taking into account the magnitude of the normalization parameter of each line with respect to its associated error evaluated with a level of confidence of 1 σ. The obtained fit parameters are reported in Tab. 7.1, whilst the best-fit model and the residuals are shown in the left panel of Fig. 7.2.
From this best fit model we extrapolate an unabsorbed flux of 6×10^{-10} erg cm^{-2} s^{-1} in the energy band between 0.1 and 100 keV, where about the 33% of the contribution is given by the diskbb component and more that the 63% by nthcomp.

In order to understand if substantial changes in the spectral shape of the source occurred, we fitted Spectrum 2 with the same model. The fit returns a value of $\chi^2(d.o.f.)$ of 933(610) and evident residuals in absorption at about 8 keV, probably due to the combination of more than one absorption line. The residuals also show a bump at about 4.5 keV and the clear presence of an edge at about 0.8 keV, that is the energy at which the K absorption edge of O VIII (E~ 0.871 keV) is expected.
We modelled this last feature with an absorption edge at 0.871 keV, while the absorption feature at about 8 keV has been modelled with two gaussian absorption lines whose width has been fixed to σ=20 eV. On the other hand, the bump in the residuals at 4.5 keV is often observed in the high statistics Suzaku/XIS spectra and is probably of systematic and non-physical nature. Here we model this feature with the gabs spectral component.
The addition of these spectral components actually improves the fit that returns us a value of $\chi^2(d.o.f.)$ of 694.8(601) and an f-test probability of chance improvement of 1.2×10^{-33} with respect to the previous fit.
The detection of the two Kα lines remains confirmed with respect to the Spectrum 1 and here is stronger owing to the high statistics of Spectrum 2. The spectral model returns a detection of the Fe XXV and Fe XXVI Kα lines with a level of confidence of 8σ and 16σ, respectively. In addition, the two supplementary absorption lines we added to fit the residuals at 8 keV actually returned energies that are consistent with those we expect for the Kβ absorption lines of Fe XXV and Fe XXVI. Our fit allows us to detect these lines with a level of confidence of 3σ and of 4σ, respectively.
The model allows to obtain a value of unabsorbed flux between 0.1 and 100 keV of 5.1×10^{-10} erg

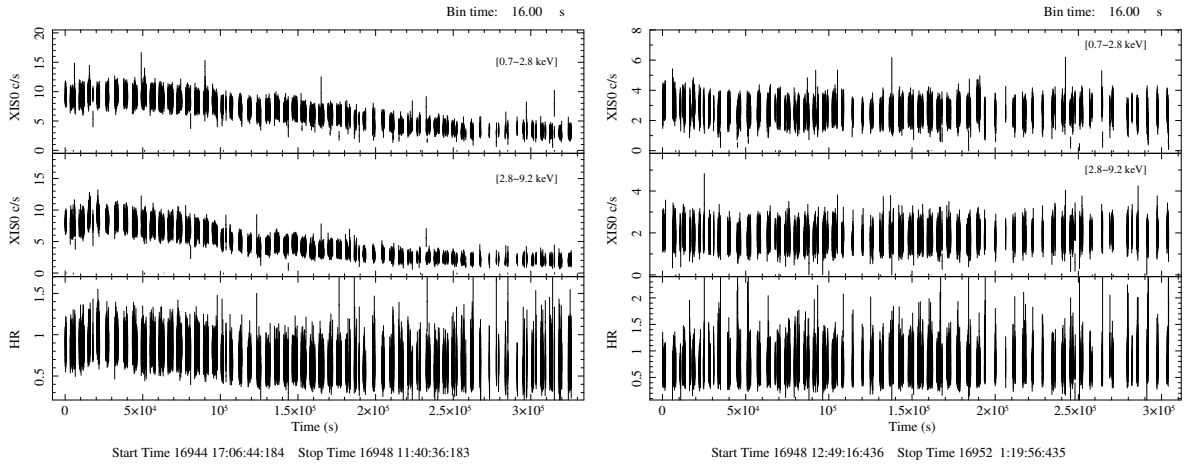

Figure 7.1: XIS0 light curves in the energy bands 0.7-2.8 keV (top panels) and 2.8-9.2 keV (middle panels) for ObsID 401095010 (left) and ObsID 401095020 (right), respectively. The corresponding hardness ratios are reported in the bottom panels.

cm^{-2} s^{-1}, where the `diskbb` and `nthcomp` components contribute with about the 23% and 79% of the total flux, respectively.

The results we obtain from the application of this simple model both to Spectrum 1 and Spectrum 2 are typical of sources that are in a soft state. Adopting a distance to the source of 9.3 kpc, we obtain that the luminosity of XB 1916-053 is of about the 2% with respect to the Eddington luminosity. According to this, taking into account a correction factor of ψ= 1.7 (Shimura and Takahara, 1995) for the apparent inner radius that can be evaluated from the normalization of the `diskbb` component, we obtain that the inner radii of the accretion disk are considerably close to the compact object, and of the order of 32±14 km and 40^{+17}_{-14} km for the spectra 1 and 2 respectively.

These values of the inner radius of the accretion disk are in agreement with those estimated by Zhang et al. (2014). As suggested by these authors, for disks so close to the NS surface it is possible that the electron corona Compton-scatters a fraction of the photons emitted by the innermost part of the accretion disk in addition to the photons emitted by the NS surface. For this reason Zhang et al. (2014) took into account this hypothesis adopting a double comptonization model to fit the persistent spectrum of XB 1916-053. This model will be statistically tested on the available persistent spectra of the source.

The model consists of two thermal comptonization components having the same photon index Γ and electron temperature, owing to the fact that we are considering a unique electron cloud. While the first comptonization component scatters photons emitted by the neutron star surface and that are distributed following a blackbody law, on the other hand the second component scatters photons that are emitted by the accretion disk and that are distributed following a multicolor-disk blackbody law. In the model we also include all the absorption lines we detected using the *1-seed* model, leaving the associated energies free to vary and fixing their width to the

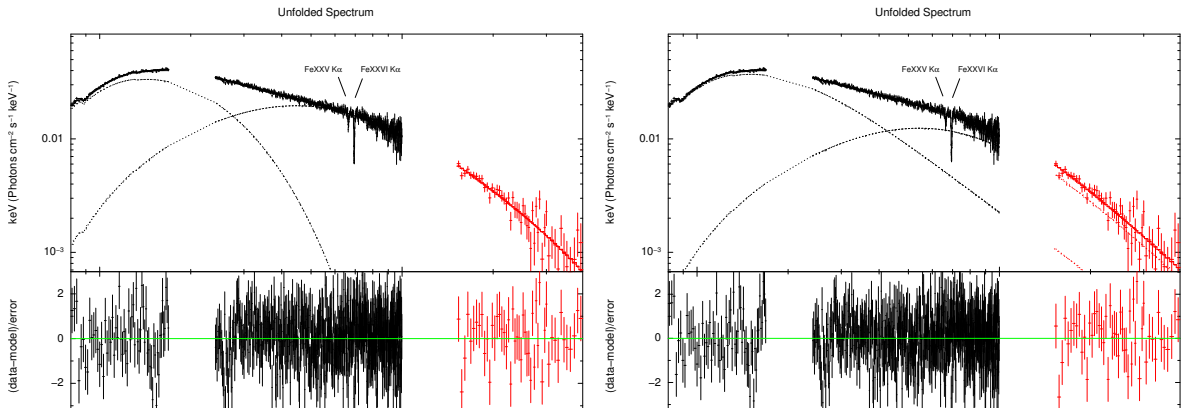

Figure 7.2: spectral fits performed on data of ObsID 401095010 (Spectrum 1). Left: *1-seed* model. Right: *2-seed* model. In each plot the black data represent the XIS03 spectrum, whilst the red data represent the PIN spectrum. The bottom panel of each plot represents the residuals with respect to the adopted model. The plots show also the Fe XXV and Fe XXVI Kα absorption lines detected in the analysis.

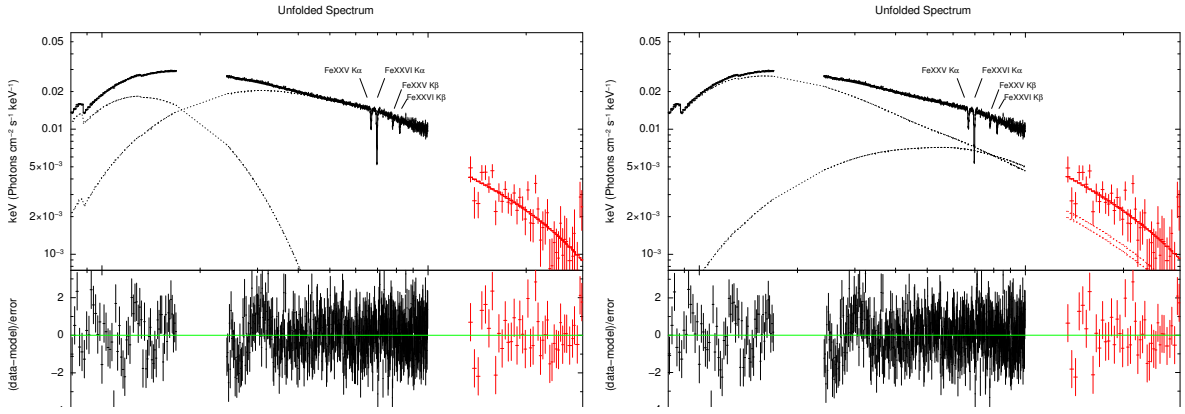

Figure 7.3: Spectral fits performed on data of ObsID 401095010 + 401095020 (Spectrum 2). Left: *1-seed* model. Right: *2-seed* model. In each plot the black data represent the composite XIS03 spectra of the two observations, whilst the red data represent the composite PIN spectra of the two observations. The bottom panel of each plot represents the residuals with respect to the adopted model. The plots show also the Fe XXV and Fe XXVI Kα and Kβ absorption lines detected in the analysis.

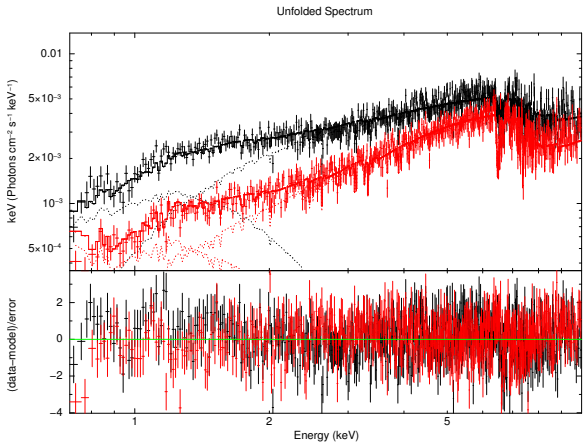

Figure 7.4: Best-fit model of the dip spectrum (top panel) using Suzaku/XIS03 data of ObsID 401095010 (black) and ObsID 401095020 (red). In the bottom panel the residuals with respect to the adopted model are show.

same value adopted in the first part of the data analysis, that is σ=20 eV.
Fitting this model (hereafter *2-seed Model*) on Spectrum 1 we obtain a good accordance of the results with those obtained with the fit of the *1-seed* model on the same spectrum. We report the best-fit parameters in Table 7.2 and the unfolded spectrum with the residuals with respect to the used model in Figure 7.3. We confirm the detection of the Kα absorption lines of Fe XXV and Fe XXVI with a level of statistical confidence of 4σ and 10σ, respectively.
The temperature of the seed photons emitted from the accretion disk kT_{bb}=0.54 keV, as well as the values of the index Γ=2.89 and the lower limit on the temperature of the electron cloud $kT_e > 4$ keV are all in agreement with the same parameters found using the *1-seed* model to fit the spectrum and could make stronger the hypothesis that the source could be in a soft spectral state, as already suggested by Zhang et al. (2014). The fit, however, returns a value of the $\chi^2(d.o.f.)$ of 702.2(618) that does not represent a statistically significant variation in the χ^2 with respect to the *1-seed* model.
We also considered the case in which the corona that envelopes the NS has a different optical depth (and then a different Γ index) with respect to the corona that envelopes the accretion disc. However, we imposed that these coronae have the same electron temperature (kT_e). The fit returns spectral parameters that are fully in agreement with those obtained with the previous fit and a $\chi^2(d.o.f.)$ of 699.8(617) with an f-test probability of chance improvement of 0.148. This indicates that assuming different $Gamma$ indexes for the coronae does not imply a statistical improvement of the fit in which we consider a unique corona that scatters photons emitted by the NS and the disc.

Applying the *2-seed* model also to the higher statistic Spectrum 2, we obtain results that are consistent with those obtained fitting this model onto the Spectrum 1, suggesting that the continuum emission of XB 1916-053 has not substantially changed during the 8 years that

separate the two observations.
Moreover, we observe that the *2-seed* model allows to constrain spectral parameters that are consistent with those obtained with the *1-seed* model applied to the same spectrum.
We detect also this time the Kα absorption lines of Fe XXV and Fe XXVI with a level of statistical confidence of 7 and 15σ, respectively. The Kβ absorption lines of Fe XXV and Fe XXVI, on the other hand, are detected with a level of confidence of 3σ and 4σ, respectively.
Similarly to the case in which we fitted the *1-seed* model to Spectrum 2, here we detect an edge at 0.877 keV that is compatible with a O VIII K absorption edge. The fit, however, returns a value of $\chi^2(d.o.f.)$ of 698.5(601) that actually does not represent a significant improvement of the fit performed on the Spectrum 1 with the same model.
As already considered for the Spctrum 1, we tried to take into account different values of the index $Gamma$ for the two comptonization components, assuming the same electron temperature. Also in this case the fit is not sensitive to the change produced into the spectral model and returns a $\chi^2(d.o.f.)$ of 698.3(600) with an f-test probability of chance improvement of 0.679 with respect to the previous fit.

Then, comparing the *1-seed* and *2-seed* models we notice that, even though these models describe with the same goodness and with an equivalent number of degrees of freedom the observed spectrum ($\Delta\chi^2$=3.7), however the *2-seed* model can be considered over-parameterized with respect to the *1-seed* model, that in any case returns a lower value of the χ^2, even if compatible with that obtained with the *2-seed* model.
For this reason, even if we are not able to distinguish which model better describes the observed spectrum, all the parameters we will use in the following discussion are those obtained by fitting the *1-seed* model on Spectrum 2.

While the persistent emission of the spectrum of XB 1916-053 does not show a spectral change between the Obs2 and Obs3, on the other hand, the spectrum of the dip appears to be non consistent between these two observations, in particular at the low energies. As a consequence of this, we performed an individual analysis to the dip spectra of these two observations.
Being the dip caused by a gradual covering of the central emitting area of the binary system that results in a progressive photoelectric absorption of the incoming flux, here we use only the spectra extracted from the XIS data between 0.7 and 9 keV where the dip is more evident.
According to the nature of the dipping phenomenon, we modelled the two spectra using a simple model consisting of a `diskbb` and `nthcomp` spectral components over which we apply a partial covering absorption component by partially ionized material (`zxipcf` in Xspec). Furthermore, we take into account the photoelectric absorption by the neutral matter in the interstellar medium applying the model `phabs` to all the previous spectral components.
`zxipcf` is a multiplicative model that uses a grid of XSTAR photoionized absorption models to describe the absorption of the incoming radiation by the plasma, taking into account a micro-

Table 7.3: Best-fit model for the dip spectra. Errors on each parameter are quoted at the 90% confidence level. Model: CONSTANT*PHABS*ZXIPCF*(DISKBB + NTHCOMP)

Model	Component	Obs2	Obs3
CONSTANT	factor	1 (frozen)	$0.68^{+0.11}_{-0.19}$
PHABS	N_H (10^{22} cm^{-2})	0.479 (frozen)	0.479 (frozen)
ZXIPCF	N_H (10^{22} cm^{-2})	103^{+25}_{-39}	62 ± 4
	$log(xi)$	$2.89^{+0.05}_{-0.07}$	$2.89^{+0.05}_{-0.07}$
	CvrFract	$0.66^{+0.09}_{-0.16}$	$0.88^{+0.06}_{-0.04}$
	Redshift	0 (frozen)	0 (frozen)
DISKBB	Tin(keV)	$0.44^{+0.05}_{-0.04}$	$0.44^{+0.05}_{-0.04}$
	norm	19^{+11}_{-8}	19^{+11}_{-8}
NTHCOMP	Gamma	$1.55^{+0.16}_{-0.20}$	$1.55^{+0.16}_{-0.20}$
	kT_e(keV)	>6	
	kT_{bb}(keV)	$1.04^{+0.18}_{-0.14}$	$1.04^{+0.18}_{-0.14}$
	inp_type(0/1)	0 (frozen)	0 (frozen)
	Redshift	0 (frozen)	0 (frozen)
	norm(10^{-3})	2.3 ± 0.6	2.3 ± 0.6
	χ^2/dof	1234.2/1072	

turbulent velocity of the plasma of 200 km/s. The model assumes that the absorbing plasma covers only a fraction of the source, whilst the remaining part of the spectrum is seen directly (see Reeves et al., 2008; Miller et al., 2007). Moreover, this model takes into account the column density of absorbing material N_H, the ionization state of the plasma $log(\xi)$ as well as the covering fraction and the redshift. The value of the equivalent column of absorbing hydrogen in the `phabs` component has been fixed to the value of N_H evaluated in the best-fit model for the persistent emission, that is N_H=4.79×10^{21} cm^{-2}. In addition, considering that the persistent continuum emission did not change during the Obs2 and Obs3, we assumed that the `diskbb` and `nthcomp` components have the same spectral parameters in the two observations.

As far as concerns the absorption from the ionized material, we assume that the ionization state and the redshift of the absorbing plasma is the same for the two spectra, keeping free to vary the covering fraction and the equivalent hydrogen column. The fit of this model onto the dip spectra results in a value of the $\chi^2(d.o.f.)$ of 1234.20(1072). The spectral parameters related to the blackbody and comptonization components are in agreement with those obtained with the fit of the persistent spectrum. For the warm absorber we observe that $log(\xi)$=$2.89^{+0.05}_{-0.07}$ and that the equivalent column density of hydrogen N_H slightly variates between $(103^{+25}_{-39}) \times 10^{22}$ cm^{-2} and $(62 \pm 4) \times 10^{22}$ cm^{-2} in Obs2 and Obs3, respectively. Furthermore, we observe a variation of the covering fraction from $0.66^{+0.09}_{-0.16}$ in Obs2 to $0.88^{+0.06}_{-0.04}$ in Obs3. We show the best-fit model parameters in Tab. 7.3 and the unfolded spectrum with the best-fit residuals in Fig. 7.4.

7.5 Discussion

We analysed and modelled the continuum and dip spectrum of the LMXB source XB 1916-053, using high statistic observations collected by the Suzaku space mission at different times.
As far as concerns the persistent emission, we analysed the spectrum of ObsID 401095010 (renamed Spectrum 1) taken in November of 2006 as well as the spectrum obtained from a combination of ObsID 409032010 and 409032020 (renamed Spectrum 2). The Spectrum 2 has a considerably high exposure of 400 ks and 9.3 ks for the XIS and PIN data, respectively.
Fitting the *1-seed* model onto the Spectrum 1, we obtained spectral parameters that are well in agreement with the results that Zhang et al. (2014) obtained in their work.
The fit returns a value of the photon index of Γ=$2.5^{+0.4}_{-0.3}$ and only a lower limit on the temperature of the comptonizing cloud of kT_e>7 keV. Moreover, the normalization parameter of the `diskbb` component, allowed us to obtain an estimation of the apparent inner radius of the accretion disk, that can be evaluated as $R_{in} = \sqrt{N/cos(\theta)}$, were θ is the angle of inclination of the system with respect to the line of sight, D_{10} is the distance to the source in units of 10 kpc and N is the normalization of the `diskbb` spectral component. An estimation of the real inner radius can be obtained using a correction factor ψ, that according to Shimura and Takahara (1995) is equal to 1.7 for sources having a luminosity of about the 10% of the Eddington luminosity. Assuming an inclination angle of $i = 70 \pm 10$ deg (van Paradijs et al., 1988; Frank et al., 1987), together with the distance of $D = 9.3$ kpc evaluated by Yoshida (1993) to which we assume an associated error of the 20% (Zhang et al., 2014), we infer a radius of $R_{in} = 32 \pm 14$ km. Such value of the inner radius is in agreement with other radii measurements performed in other atoll sources (Di Salvo et al., 2015) and suggests that the accretion disk extends close to the NS surface as observed by Zhang et al. (2014) that analysed the same observation.

On the other hand, the application of the same model to the Spectrum 2 returns similar results, even though the parameters here are more constrained owing to the higher statistic of the spectrum. The values of the photon index and of the temperature of the electron cloud ($\Gamma = 1.98^{+0.09}_{-0.08}$ and $KT_e = 6.5^{+3}_{-1.4}$ keV) are compatible with those obtained from the previous fit, suggesting that no evident changes in the corona have been observed during the 8 years that separate the observations. In this case we infer an inner radius for the accretion disk of 40^{+17}_{-14} km that is in agreement with the previous estimation.
We extracted the unabsorbed bolometric flux between 0.1 and 100 keV for each of the spectra modelled with the *1-seed* model, obtaining $\Phi = 5.9 \times 10^{-10}$ erg cm^{-2} s^{-1} and $\Phi = 5.1 \times 10^{-10}$ erg cm^{-2} s^{-1} for the Spectrum 1 and Spectrum 2, respectively. Assuming a distance to the source of $d = 9.3 \pm 1.4$ kpc (Yoshida, 1993), we obtain an unabsorbed bolometric luminosity in the 0.1–100 keV energy band of $L = (6 \pm 2) \times 10^{36}$ erg s^{-1} and $L = (5 \pm 2) \times 10^{36}$ erg s^{-1} for the Spectrum 1 and Spectrum 2, respectively. This is indicative of the fact that XB 1916-053 is a persistent source that does not show important changes of flux as also shown by the X-ray monitors.

Using the relation of Zdziarski et al. (1996)

$$\Gamma = \left[\frac{9}{4} + \frac{1}{\tau\left(1+\frac{\tau}{3}\right)\left(\frac{kT_e}{m_e c^2}\right)} \right]^{1/2} - \frac{1}{2}, \tag{7.1}$$

we evaluated the optical depth of the comptonizing electron cloud for the Spectrum 1 and Spectrum 2, according to the spectral parameters obtained by fitting the *1-seed* model to the data. We infer an optical depth of $\tau \leq 4.5$ for Spectrum 1 and $\tau = 6.1$ for Spectrum 2, respectively.
An estimation of the radius of the seed photons that are scattered by the corona, can be obtained using the relation of in 't Zand et al. (1999) assuming a spherical photon emission from the corona:

$$R_0 = 3 \times 10^4 \, d \left(\frac{f_{bol}}{1+y} \right)^{1/2} (kT_{bb})^{-2}, \tag{7.2}$$

where d is the distance to the source in kpc, f_{bol} is the unabsorbed bolometric flux extrapolated from the comptonization component in erg cm^{-2} s^{-1}, kT_{bb} is the temperature of the seed photons in keV, and $y = 4kT_e max[\tau, \tau^2]/(m_e c^2)$ is the compton parameter, in which kT_e is the electron temperature in keV.
On the basis of the results we obtained fitting the *1-seed* model onto the data, we obtain a Comptonization parameter $y < 1.1$ and $y = 1.9^{+0.9}_{-0.4}$ for Spectrum 1 and Spectrum 2 and a radius for the seed photons of $R_0 > 2$ km and $R_0 = 5 \pm 1$ km, respectively.
The obtained optical depth, if considered together with the values found for the temperature of the electron cloud, seem to suggest that the corona is hotter and optically thin in Spectrum 1, while it is colder and optically thick in Spectrum 2. On the other hand, we observe that the inner radius we obtain for the two observations is compatible even though it extends closer to the NS surface in the case of Spectrum 1. This is actually in agreement with the fact that the electron cloud forming the corona is optically thin in Spectrum 1 and then we can observe also the spectral contribution of the innermost part of the accretion disk. In Spectrum 2, on the other hand, the corona is optically thick and the spectral contribution of the innermost part of the accretion disk is shielded by the colder corona.
However, the unabsorbed luminosity of the source between 0.1 and 100 keV is almost the same and the spectral parameters of the the source do not considerably change in the two spectra. This suggests that the physical properties of the corona have not changed substantially in the two observations, and that the source persisted in a soft spectral state.

Zhang et al. (2014) in their work suggest that the use of the *2-seed* model better describe the comptonization process that contributes into the observed spectrum of the source. In addition,

in Zhang et al. (2016) the persistent spectrum of the dipping and eclipsing LMXB source EXO 0748-676 is modelled with a *2-seed* model on the basis of the fact that the authors obtain a radius of the seed photons that is larger with respect to the radius of the NS, and then a larger contribution of photons is required for the comptonization.
The use of the model of Zhang et al. (2014) in our spectra, however suggested that considering the comptonization process both for the photons emitted by the neutron star surface and those emitted by the innermost part of the disk is statistically irrelevant, although the radius of the accretion disk extends relatively close to the NS surface, and although we obtain a radius of the seed photons of $R_0 = 5 \pm 1$ km fitting the higher statistic Spectrum 2 with the *1-seed* model.
The *2-seed* model applied to the Spectrum 1 and 2 returns similar values of the spectral parameters with respect to those obtained with the *1-seed* model. However, for each of the two persistent spectra, the fit of the *2-seed* model returns a value of the χ^2 that at parity of degrees of freedom is compatible with respect to the value returned by the *1-seed* model. For this reason we are not able to distinguish which one of the two model better describe the observed spectra, even with the analysis of a spectrum with a higher statistic.

Using Equation 7.1, we obtain optical depths of $\tau < 5$ and $\tau = 6.1$ for Spectrum 1 and Spectrum 2, respectively. Using these optical depths and the electron temperature kT_e of the corona obtained with the *2-seed* model (see Table 7.2) we found comptonization parameters of $y < 0.8$ and $y = 1.7^{+3}_{-0.5}$, for Spectrum 1 and Spectrum 2, respectively.
As far as concerns the estimation of the radius of the seed photons, here we distinguished between the componization component arising from the scattering of photons spherically emitted from the NS surface, and the component ascribed for the scattering of photons emitted by the accretion disk, that are emitted following a plane geometry. In the first case, the radius of the seed photons is given by Equation 7.2. In the latter case, considering the emission of photons from an annulus in which the inner radius is R_{in} and the outer radius is R_0, the in 't Zand et al. (1999) relation has to be modified in

$$R_p = \left(R_{in}^2 + 4R^2 R_0\right)^{1/2}, \tag{7.3}$$

where R_p is the outer radius of the emitting annulus and R_0 is the radius of the seed photons spherically emitted of Equation 7.2.
Considering a non-truncated disc that extends up to the NS surface, we used $R_{in} = 10$ km. With these assumpions, for Spectrum 1 we estimate $R_0 < 1$ km and $R_p < 22$ km. For Spectrum 2 we obtain $R_0 < 1.1^{+0.6}_{-0.2}$ km and $R_p = 36^{+18}_{-7}$ km.
These values suggest that in the case of the Spectrum 1, the photons emitted by the disc and afterwards scattered by the corona come from an annulus that extends from the NS surface up to a distance that could be lower than 22 km. The smaller extension of the radius of the seed photons that are sperically emitted, on the other hand could be explained with the probable

contribution of a region that is compatible with the boundary layer, where the accretion flow hits the NS surface.
For the Spectrum 2, we infer compatible values for these radii, that however are more constrained due to the higher statistic of the data.
On the basis of the fact that it is not possible to distinguish which one of the two model better describe the observed spectra, in the subsequent discussion we will adopt the less parameterized *1-seed* model for the description of the spectrum of XB 1916-053.

In the modelling of Spectrum 1 and Spectrum 2, regardless of the model we used, we needed to add the two absorbing Kα lines of Fe XXV and Fe XXVI in order to improve the fit. These lines are quite strong and have been detected with a level of statistical confidence of 8σ and 16σ, for the Fe XXV and Fe XXVI Kα lines, respectively in the case of the *1-seed* model, or alternatively with a level of confidence of 7σ and 15σ for the *2-seed* model, respectively. As reported in Iaria et al. (2006), these features originate at the disk rim where the plasma forming the disk is colder but also partially ionized. The strength of the lines, and in particular the difference in the line depth, could be explained as a difference of the number of population of the Fe XXV ions with respect to Fe XXVI, for the Kα transitions. To explain the larger depth of the Fe XXVI absorption line, one should expect a prevalence of this kind of ions with respect to the Fe XXV ions. To estimate the difference of the population for the two ions, we used the relation of Spitzer (1978):

$$\frac{W_\lambda}{\lambda} = \frac{\pi e^2}{m_e c^2} N_j \lambda f_{ij}, \tag{7.4}$$

where N_j is the column density for the relevant species, f_{ij} is the oscillator strength, W_λ is the equivalent width of the line, and λ is the wavelength expressed in centimeters.

The values of the oscillator strength are tabulated in Verner and Yakovlev (1995) and are equal to $f_{ij} = 0.798$ and $f_{ij} = 0.416$ for the Fe XXV and Fe XXVI Kα transitions, respectively. From the *1-seed* model applied on Spectrum 2 we find an equivalent width of $W_\lambda = -0.0150$ cm and $W_\lambda = -0.0344$ cm for the Fe XXV and Fe XXVI Kα absorption lines, respectively. Then, using Equation 7.4 we obtain $N_{Fe25,k\alpha} = 6.21 \times 10^{25}$ cm^{-2} and $N_{Fe26,k\alpha} = 2.95 \times 10^{26}$ cm^{-2}, whose ratio suggest a predominance of Fe XXVI ions with respect to the Fe XXV by a factor of 5, and probably the difference in the two lines' depth. These strong absorption lines, were already noticed by Zhang et al. (2014), Boirin et al. (2004) and Iaria et al. (2006), where a full diagnostic of the absorption lines has been performed using Chandra data.
The Spectrum 2, however, has a higher statistic with respect to the Spectrum 1 and in addition to the Kα absorption lines it showed also residuals that we found to be consistent with the Kβ absorption lines of Fe XXV and Fe XXVI, respectively.
Due to the discrete energy resolution of Suzaku, these two absorption lines have been modelled keeping their widths fixed to the same value of the Kα lines, that is 20 eV. The inclusion of these

two lines in both the *1-seed* and *2-seed* models, actually improve the fits on the Spectrum 2. The probability for such improvement to occur by chance is of 6×10^{-4} in the case of the single-seed model and of 3×10^{-4} in the case of the *2-seed* model.

The presence of the Fe XXV Kβ line has been faintly induced by Boirin et al. (2004) with XMM-Newton data, and here is confirmed taking the advantage of the statistic of Spectrum 2. We detected the line with a level of confidence of 3σ, independently of the model adopted. In addition, we also detected a line that is consistent with a Fe XXVI Kβ absorption line with a level of confidence of 4σ. Actually, this line is located in the energy range in which Boirin et al. (2004) saw some weak residuals that though to be caused by the presence of Ni XXVII. Here we introduce the further possibility that this feature is due to the presence of Fe XXVI ions making Kβ transitions.
Taking into account Equation 7.4, we can estimate the number of population of the two species of ions. From the *1-seed* model performed on Spectrum 2 we obtain an equivalent width of $W_\lambda = -0.0089$ cm and $W_\lambda = -0.0119$ cm for the Fe XXV and Fe XXVI Kβ transitions respectively, using the equivalent oscillator strengths $f_{ij} = 0.156$ and $f_{ij} = 0.079$, respectively tabulated in (Verner and Yakovlev, 1995). We obtain $N_{Fe25,k\beta} = 2.56 \times 10^{26}$ cm^{-2} and $N_{Fe26,k\beta} = 7.46 \times 10^{26}$ cm^{-2}, with a ratio that suggests a predominance of Fe XXVI ions making kβ transitions by a factor of 3 with respect to the Fe XXV.

In addition to these discrete features, we also detected an absorption edge in the Spectrum 2 at 0.87 keV. This edge is compatible with a O VIII absorption edge that has been already observed in several LMXB systems (see e.g. Iaria et al., 2016; Cottam et al., 2001). This absorption feature is indicative of the presence of a warm absorber along the line of sight to the observer and this theory is actually reflected by the evidence of the many absorption features superimposed on the persistent spectrum of XB 1916-053.

The dip spectrum, on the other hand, has been studied considering the combined XIS data of the ObsID 409032010 (Obs2) and 409032020 (Obs3). The resulting spectrum has a net exposure of 36 ks.
This spectrum has been fitted with the model `zxipcf` that takes into account a partial covering absorption induced by a partially ionized material. In addition to this component, the model contains also the same spectral components that have been already used to model the persistent spectrum with the *1-seed* model, that is the multi-disk blackbody component `diskbb` and the comptonization component `nthComp`.
In the fit we fixed the equivalent column of hydrogen to the same value found for the persistent Spectrum 2, that is N_H=4.79$\times$ 10^{21} cm^{-2}. Considering that the persistent continuum emission did not change during the Obs2 and Obs3, we assumed that the `diskbb` and `nthcomp` components have the same spectral parameters in the two observations.
In addition, being the two observations extremely close in time we assume also the same spectral

parameters for the warm absorber, leaving free to vary its covering fraction between the observations.
The result of the fit, shows that the value of the temperature of the disk, as well as the parameters of the comptonization component are in agreement with the spectral parameters obtained for the persistent spectrum. This is a clear indication that along with the dip emission, we are also observing a fraction of the persistent emission that is probably scattered by the corona. This contamination should be visible in the dip spectrum probably due to the extreme inhomogeneity of the bulge of opaque matter that is the effective cause of the dip phenomenon. Actually, the spectral component `zxipcf` associated with the warm absorber, suggests a discrete ionization parameter $log(\xi)$=$2.89^{+0.05}_{-0.07}$ and an equivalent column density of hydrogen that slightly variates between $N_H = (103^{+25}_{-39}) \times 10^{22}$ cm^{-2} and $N_H = (62 \pm 4) \times 10^{22}$ cm^{-2} in Obs2 and Obs3, respectively. This change in the column density of the absorber is combined with a variation of the covering fraction from $0.66^{+0.09}_{-0.16}$ in Obs2 to $0.88^{+0.06}_{-0.04}$ for Obs3.
These considerations suggest that the bulge should change its morphology and density in time scales of the order of some orbital periods.
The parameter ξ determines the ionization state of the material of the warm absorber and according to Tarter et al. (1969) is defined as:

$$\xi = \frac{L}{nr^2}, \tag{7.5}$$

where L is the unabsorbed luminosity of the source in erg s^{-1}, n is the gas density in cm^{-3} and r is the distance of the absorber from the centre of the system in cm.
A roughly estimation of the density of the warm absorber could be evaluated assuming a distance of the warm absorber of r=4 × 10^{10} cm. This value is reported in Iaria et al. (2006) as the distance at which the absorption lines that are detected in the persistent spectrum form and can be considered as a good estimation of the distance of the disk rim from the centre of the system. Using the value of the unabsorbed luminosity L=5 × 10^{36} erg s^{-1} obtained between 0.1 and 100 keV fitting the *1-seed* model on Spectrum 2, and the value of the $log(\xi)$ returned by the fit of the dip spectrum, we obtain a density of the gas that is of n=4 × 10^{12} cm^{-3}.

7.6 Conclusions

In this work we showed a spectral study performed on both the persistent as well as the dip spectra of the LMXB system XB 1916-053, using Suzaku data.
Even though the statistic of the spectrum obtained from the most recent observations is considerable, this is not sufficient to discriminate if a model that considers the double-comptonization of photons emitted by the NS surface and by the innermost part of the accretion disk is statistically relevant with respect to a model in which only the photons emitted by the NS surface are

scattered. Furthermore, the analysis showed that the radius associated to the seed photons does not represent an absolute discriminant of the importance of the comptonisation of the photons emitted by the accretion disk. Indeed, even though with the fit of the 2-seed model on Spectrum 2 we obtain a radius of $R_0 = 5 \pm 1$ km for the seed photons, we are not able to statistically constrain which one of the two models we tried better describes the observed spectra.

The source has been found in a soft state independently of the model adopted to fit the continuum spectrum. The achievement of a greater statistic, on the other hands, brought to discriminate various discrete absorption features, and in particular the Kβ absorption lines of Fe XXV and Fe XXVI, in addition to the Kα transition lines of the same ions, already detected in literature. The equivalent widths of these absorption lines seem to be consistent with a higher number of Fe XXVI ions with respect to the Fe XXV. Moreover, the detection of a O VIII K absorption edge, highlights the high possibility that these features originate at great radial distances from the NS and possibly in the outer parts of the accretion disk, where the relatively cold and more opaque plasma is partially ionized.

According to this fact, the analysis of the dip spectrum highlighted how the dip itself could be explained as a gradual covering of the persistent spectrum by a cold and partially ionized bulk of matter in which the morphology continually changes in considerably short time scales of the order of some orbital periods.

In order to better constrain the persistent absorption features and their relative widths we encourage high exposure observations to be performed by space missions provided of a high energy resolution.

CHAPTER 8

A POSSIBLE SOLUTION OF THE PUZZLING VARIATION OF THE ORBITAL PERIOD OF MXB 1659-298

Iaria R., Gambino A. F., Di Salvo T., Burderi L., Matranga M., Riggio A., Sanna A., Scarano F., D'Aì A. (2018)
Published in Monthly Notices of the Royal Astronomical Society,
Volume **473**, Issue 3, p.3490-3499

8.1 Abstract

MXB 1659-298 is a transient neutron star Low-Mass X-ray binary system that shows eclipses with a periodicity of 7.1 hr. MXB 1659-298 went to outburst in August 2015 after 14 years of quiescence. We investigate the orbital properties of this source with a baseline of 40 years obtained combining the eight eclipse arrival times present in literature with 51 eclipse arrival times collected during the last two outbursts. A quadratic ephemeris does not fit the delays associated with the eclipse arrival times and the addition of a sinusoidal term with a period of 2.31 ± 0.02 yr is required. We infer a binary orbital period of P = 7.1161099(3) hr and an orbital period derivative of $\dot{P}$ = -8.5(1.2) × 10^{-12} s s^{-1}. We show that the large orbital period derivative can be explained with a highly non conservative mass transfer scenario in which more than 98% of the mass provided by the companion star leaves the binary system. We predict an orbital period derivative value of $\dot{P}$ = -6(3) × 10^{-12} s s^{-1} and constrain the companion star mass between ~ 0.3 and 0.9 ± 0.3 $M_\odot$. Assuming that the companion star is in thermal equilibrium the periodic modulation can be due to either a gravitational quadrupole coupling due to variations of the oblateness of the companion star or with the presence of a third body of mass M3 > 21 Jovian masses.

8.2 Introduction

One of the most direct evidence for binary orbital motion is the presence of eclipse of the central source by a companion star. For Low Mass X-ray Binaries (LMXBs) with inclination angles between 75° and 80° the X-ray emission may be totally shielded by the companion star. As the companion transits between the X-ray central source and the observer the light curves show total eclipses. For inclination angles between 80° and 90° the LMXB is observed as an Accretion Disc Corona (ADC) source. In this case the observed X-ray emission comes from an extended corona that can reach the outer region of the accretion disc. The light curves of the ADC sources show an almost sinusoidal modulation and partial eclipses. The modulation of the light curve is generally explained with the presence of a geometrically thick disc whose height varies depending on the azimuthal angle and occults part of the X-ray emission. Since the companion star does not shield the whole extended corona the observed eclipses are partial; the prototype of the ADC sources is X1822-371 (see e.g. Iaria et al., 2011, 2013, 2015a, and references therein).

Total eclipses represent a good time reference, which is ideal to perform timing analysis of the binary orbital period, e.g. the O-C method is usually applied to refine the orbital period or trace orbital period changes (see Chou, 2014, for a recent review). To date, 12 LMXBs show total eclipses in their light curve. One of the best studied eclipsing X-ray source is EXO 0748-676, as it was active for more than 20 years (see Wolff et al., 2009, and references therein).

The eclipsing LMXB MXB 1659-298 was discovered by Lewin et al. (1976b) in 1976. The light curve showed type-I X-ray bursts, thus revealing that the compact object was an accreting neutron star. The source was observed in outburst up to 1978 with *SAS3* and *HEAO* (Cominsky et al., 1983; Cominsky and Wood, 1984, 1989). Eclipses were firstly reported by by Cominsky and Wood (1984), which estimated a periodicity of 7.1 hr. Cominsky and Wood (1989) analysed two whole eclipses estimating two eclipse arrival times. From 1978 up to 1999 the region containing MXB 1659-298 was monitored by the X-ray observatories onboard *Hakucho*, *EXOSAT* and *ROSAT*, but the source was never detected (see Cominsky and Wood, 1989; Verbunt, 2001). On April 1999 the Wide Field Cameras onboard *BeppoSAX* observed the source in outburst again (in 't Zand et al., 1999). This new outburst continued up to September 2001. During the outburst MXB 1659-298 was observed with the Proportional Counter Array (PCA) onboard *Rossi X-ray Timing Explorer* (*RXTE*, see e.g. Wachter et al., 2000), with the Narrow Field Instruments (NFI) onboard *BeppoSAX* (Oosterbroek et al., 2001) and with *XMM-Newton*. From the analysis of the RXTE light curves of the source, Wachter et al. (2000) obtained four eclipse arrival times and found an orbital period derivative of $(-7.2 \pm 1.8) \times 10^{-11}$ s s^{-1} suggesting that the orbit of the binary system is shrinking. Oosterbroek et al. (2001) obtained two eclipse arrival times from a *BeppoSAX*/NFI observation and combining their data with those present in literature found that the orbital period derivative, $\dot{P}_{orb}$, is positive with a value of $(7.4 \pm 2.0) \times 10^{-12}$ s/s. MXB 1659-298 turned again on outburst on 2015 August 21 (Negoro et al., 2015) and up to 2017 March is still X-ray bright. Using data of the X-ray Telescope (XRT) onboard *Swift*, Bahramian et al. (2016)

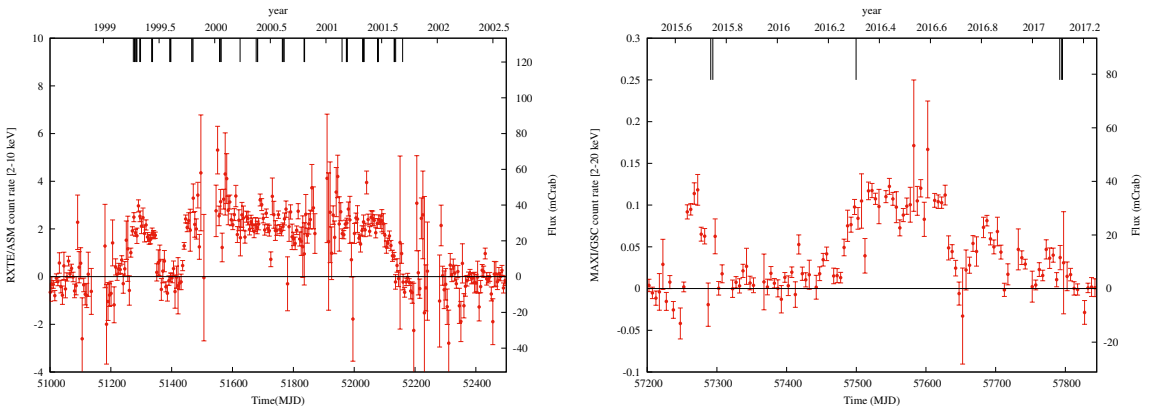

Figure 8.1: Light curve of MXB 1659-298 during the outburst occurred between 1999 and 2001 (left panel) and the latest started 2015 (right panel). The left panel shows the RXTE/ASM light curve in the 2-10 keV, the right panel shows the MAXI/GSC light curve in the 2-20 keV energy range; the bin time is **five days** for both the light curves. The eclipse arrival times are also indicated.

observed that the unabsorbed flux in the 0.5-10 keV energy range was 1.5×10^{-10}, 4.6×10^{-10} and 2.2×10^{-10} erg cm^{-2} s^{-1} on 2016 January 28, February 2 and 11, respectively.

Cominsky and Wood (1989) measured an eclipse duration, ΔT_{ecl}, of 932 ± 13 s and an ingress/egress duration of $\Delta T_{ing} = 41 \pm 13$ s and $\Delta T_{egr} = 19 \pm 13$ s, respectively. They showed that, if the companion star is a main-sequence star of 0.9 $M_\odot$ with a temperature close to 5000 K, the scale height of the stellar atmosphere should be around 200 km, corresponding to an ingress/egress duration close to 0.5 s. The authors concluded that the small value of the scale height cannot justify the large value of the measured ingress/egress durations. Furthermore, Cominsky and Wood (1989) suggested that the observed asymmetry between the ingress and egress duration could be caused by a one-sided extended corona of size 5×10^5 km.

From the analysis of four eclipses obtained with *RXTE*/PCA, Wachter et al. (2000) estimated an average eclipse duration of 901.9 ± 0.8 s and average values of ingress/egress durations of $\Delta T_{ing} = 9.1 \pm 3.0$ s and $\Delta T_{egr} = 9.5 \pm 3.3$ s. The authors proposed that the large spread of values associated with the ingress/egress times could be caused either by flaring activity of the companion star or by the presence of an evaporating wind from the surface of the companion star created by irradiation from the X-ray source.

Cominsky and Wood (1984) discussed the nature of the optical counterpart of MXB 1659-298, named V2134 Oph, assuming an orbital period of 7.1 hr and an eclipse duration of 900 s. They constrained the mass of the companion star to be between 0.3 $M_\odot$ and 0.9 $M_\odot$ for an inclination angle of the binary system of 90° and 71°.5, respectively. Warner (1995) inferred that the companion star mass is between 0.75 and 0.78 $M_\odot$ if the companion fills its Roche lobe. This range of masses suggests that the companion is a K0 main-sequence star. During the quiescence of MXB 1659-298, Wachter et al. (2000) measured a magnitude in the I-band of 22.1 ± 0.3 mag

and Filippenko et al. (1999) measured a magnitude in the R-band of 23.6 ± 0.4 mag. Wachter et al. (2000) found that the value of $(R-I)_0$ is compatible with an early K spectral type. Moreover, they suggested that, for a companion star belonging to the K0 class, the visual magnitude should be $V = 23.6$ mag, value that is compatible with the measured lower limit of $V > 23$ mag.

Galloway et al. (2008), analysing the type-I X-ray bursts observed with *RXTE*/PCA, inferred a distance to the source of 9 ± 2 and 12 ± 3 kpc for a hydrogen-rich and helium-rich companion star, respectively. Furthermore, Wijnands et al. (2001) detected nearly coherent oscillations with a frequency around 567 Hz during type-I X-ray bursts suggesting that the neutron star could be an X-ray millisecond pulsar with a spin period of 1.8 ms.

The interstellar hydrogen column density, N_H, was estimated by Cackett et al. (2008b) during the X-ray quiescence of MXB 1659-298. Combining *Chandra* and *XMM-Newton* observations collected between 2001 and 2008 they fitted the X-ray spectrum obtaining $N_H = (2.0 \pm 0.1) \times 10^{21}$ cm^{-2}. Two more recents *Chandra* observations of the source, taken in 2012 Cackett et al. (2013), seem to suggest an increase of the interstellar hydrogen column density at the value of $(4.7 \pm 1.3) \times 10^{21}$ cm^{-2}. The authors proposed three different scenarios to explain the increase of N_H: a) material is building up in the outer region of the accretion disc, b) the presence of a precessing accretion disc, and c) sporadic variability during quiescence due to low-level accretion.

Studying the *XMM*-Newton spectrum of MXB 1659-298, Sidoli et al. (2001) detected two absorption lines at 6.64 and 6.90 keV associated with the presence of highly ionised iron (Fe XXV and Fe XXVI ions) as well as absorption lines associated with highly ionised oxygen and neon (O VIII 1s-2p, O VIII 1s-3p, O VIII 1s-4p and Ne IX 1s-2p transition) at 0.65, 0.77, 0.81 and 1.0 keV.

In this paper we report the updated ephemeris of MXB 1659-298 combining 45 eclipse arrival times obtained with *XMM-Newton* and *RXTE* during the outburst between 1999 and 2001 and six eclipse arrival times obtained with *XMM-Newton*, *NuSTAR* and *Swift*/*XRT* during the outburst started in 2015. The available temporal baseline allows to partially constrain the bizarre behaviour of the eclipse arrival times.

8.3 Observations

During the outburst occurred from 1999 to 2001, MXB 1659-298 was observed with *XMM-Newton* (Jansen et al., 2001) two times: on March 22 2000 and on Feb. 20 2001. The latter observation (obsid. 0008620701) was analysed by Sidoli et al. (2001) and Díaz Trigo et al. (2006), which studied the spectral properties of the source during the persistent emission, the dip and the eclipse, while the former observation (obsid. 0008620601) was never analysed. During the 2015 outburst, MXB 1659-298 was observed with *XMM-Newton* on September 26, 2015.

The European Photon Imaging Camera (Epic-pn, Strüder et al., 2001) onboard *XMM-Newton* collected data from the source in timing mode, with exposure times of 10, 32 and 34 ks, respectively. The Epic-pn light curve of the observation taken in 2001 shows two eclipses in the light curve

(see Fig. 1 in Sidoli et al., 2001). To verify the presence of eclipses in the Epic-pn light curves of the observations taken in 2000 and 2015 we filtered the source events with the Science Analysis System (SAS) ver. 15.0.0. We reprocessed the Epic-pn events and applied the solar-system barycentre corrections adopting as coordinates RA= 255°.527250 and Dec= −29°.945583 (see Wijnands et al., 2003). During the observation taken in 2000, the light curve of MXB 1659-298 shows an eclipse with a duration of 900 s approximately 1400 s after the start time. The count rate is 32 c s^{-1} and 1.4 c s^{-1} outside and during the eclipse, respectively. During the observation taken in 2015, the light curve shows the presence of a type-I X-ray burst at 12 ks after the start of the observation. The count rate varies from 32 c s^{-1} at the beginning of the burst up to 320 c s^{-1} at the peak. An intense dipping activity is present at about 20 ks from the beginning of the observation, a complete eclipse is observed at 26 ks from the start time and an eclipse without the ingress is observed at beginning of the observation. The count rate out and during the eclipse is 32 and 1.4 c s^{-1}, respectively.

The PCA instrument onboard *RXTE* (Jahoda et al., 1996) observed several times the source from 1999 to 2001. In our analysis we selected 43 *RXTE*/PCA observations showing the eclipse and for which it is possible to estimate the ingress and egress time accurately. To estimate the eclipse arrival times from the *RXTE*/PCA observations we analysed the standard product background-subtracted light curves with a bin time of 0.125 s and we applied the solar-system barycentric correction to the events using the ftool `faxbary`.

NuSTAR (Harrison et al., 2013) observed MXB 1659-298 two times in 2015 and 2016 with both the independent solid state photon counting detector modules (FPMA and FPMB), with elapsed times of 96 ks and 50 ks, respectively. We processed the raw (Level 1) data with the ftool `nupipeline` (Heasoft ver. 6.19), obtaining cleaned and calibrated event data (Level 2). The solar-system barycentric corrected events of the FPMA and FPMB telescopes have been obtained applying the tool `nuproducts` on the Level 2 data. The corresponding light curves were created selecting a circular extraction region for the source events with a radius of 49″ and using the 1.6-20 keV energy range. The persistent emission has a count rate of 2 c s^{-1}. A complete eclipse and an eclipse without the ingress are observed at 24 and 76 ks from the start time. The count rate during the eclipse is 0.02 c s^{-1}. It is also evident the presence of the ingress to the eclipse at 49.7 ks from the start time. During the second observation MXB 1659-298 is brighter, with a persistent count rate of 20 c s^{-1}, a whole eclipse is observed 30 ks after the start time of the observation. To increase the statistics of the *NuSTAR* light curve we summed the FPMA and FPMB light curve using the ftool `lcmath`.

During the 2015 outburst, MXB 1659-298 was observed several times with *Swift*/XRT (Gehrels et al., 2004; Burrows et al., 2005), although only three observations show a complete eclipse. We obtained further *Swift*/XRT data as target of opportunity observations performed on February 8, 10 and 11, 2017 (obsid 0003400266, 0003400267 and 0003400268). All of the three observations cover the whole eclipse. The XRT data were processed with standard procedures (xrtpipeline

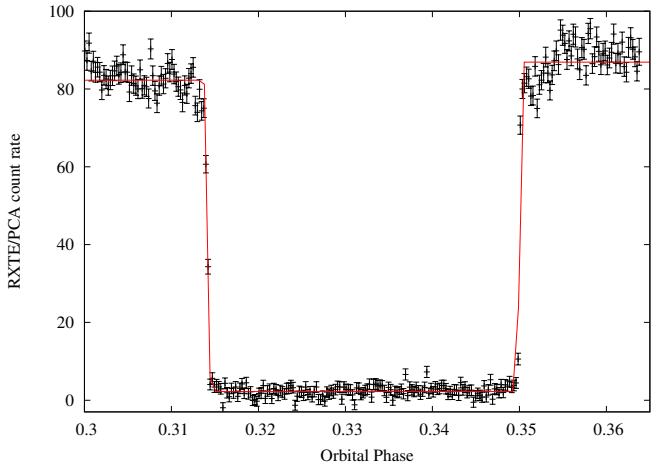

Figure 8.2: Eclipse of MXB 1659-628 observed by the RXTE/PCA instrument (observation P40050-04-16-00). The superimposed red function is the step-and-ramp function adopted to estimate the eclipse arrival time.

v0.13.1), and with standard filtering and screening criteria with ftools. For our timing analysis, we also converted the event arrival times to the solar-system barycentre with the tool `barycorr` and subtracted the background using the ftool `lcmath`.

The All Sky monitor (ASM, Levine et al., 1996) onboard *RXTE* monitored the 1999-2001 outburst (Fig. 8.1, left panel). The two *XMM-Newton* observations were performed at a similar ASM count rate of 2.5 c s^{-1} (about 30 mCrab in flux), corresponding to the source maximum flux. The outburst showed a sort of precursor lasting 100 d, afterwards the flux decreased up to a value compatible with zero for 86 d, and finally increased again rapidly reaching a constant flux of 30 mCrab for 700 d.

The Gas Slit Camera (GSC, Mihara et al., 2011) onboard the Monitor of All-sky X-ray Image (MAXI, Matsuoka et al., 2009) observed the recent outburst (see Fig. 8.1, right panel). The morphology of the outburst is similar to the previous one with a sort of precursor lasting 50 d, a new quiescent stage lasting 150 d and, after that, an increase of the flux at 30 mCrab lasting 150 d. The maximum GSC count rate is 0.12 c s^{-1}. *XMM-Newton* and *NuSTAR* (obsid. 90101013002) observed the source when the GSC count rate was 0.05 c s^{-1}; *NuSTAR* observed the source a second time when MXB 1659-298 was brighter with a corresponding GSC count rate of 0.1 c s^{-1}.

8.4 Method and Analysis

To estimate the eclipse arrival times, we folded the solar-system barycentric corrected light curves using a trial time of reference and orbital period, T_{fold} and P_0, respectively. The value of the adopted T_{fold} corresponds to a time close to the start time of the corresponding observation. The adopted value of P_0 is 7.11610872 hr corresponds to the value of the orbital period at

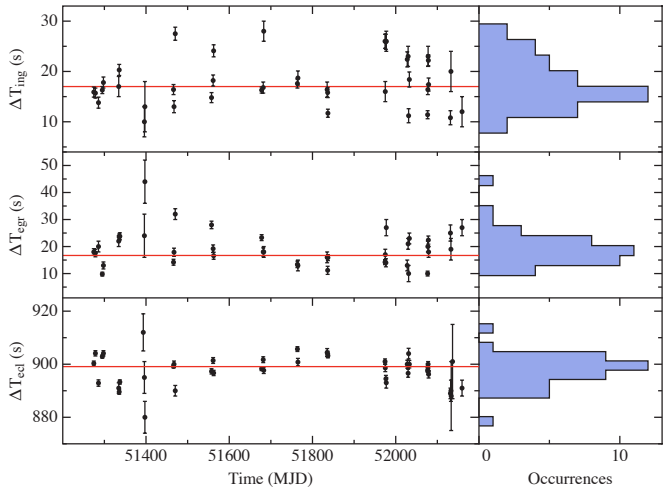

Figure 8.3: From the top-left to the bottom-left the ingress, egress and eclipse duration, respectively, as function of time. The values are obtained from the RXTE/PCA eclipses analysed in this work. The red lines indicate the average values for each duration. From the top-right to the bottom-right we show the histograms of the occurrences of the ingress, egress and eclipse duration.

Table 8.1: Journal of the X-ray eclipse arrival times of MXB 1659-298

Point	Eclipse Time (MJD;TDB)	Cycle	Delay (s)	Ref.	Point	Eclipse Time (MJD;TDB)	Cycle	Delay (s)	Ref.
1	43 058.7260(2)	0	0(13)	[1],[2]	31	51 769.43726(2)	29378	107.0(1.3)	[4]
2	43 574.6441(2)	1740	26(13)	[1],[2]	32	51 835.261275(9)	29600	106.9(7)	[3]
3	51 273.978079(2)	27707	96.46(13)	[2]	33	51 836.447292(6)	29604	106.8(5)	[3]
4	51 274.571102(8)	27709	97.7(7)	[3]	34	51 837.040274(5)	29606	104.4(4)	[3]
5	51 277.832626(4)	27720	95.4(3)	[2]	35	51 960.08961(2)	30021	101(2)	[3]
6	51 278.425648(10)	27722	96.5(9)	[3]	36	51 974.321836(6)	30069	101.4(5)	[3]
7	51 281.687174(4)	27733	94.5(3)	[2]	37	51 974.914836(8)	30071	100.6(7)	[3]
8	51 283.762726(3)	27740	96.2(3)	[2]	38	51 976.397381(8)	30076	102.5(6)	[3]
9	51 285.838220(11)	27747	93.0(9)	[3]	39	51 977.286855(12)	30079	99.1(1.0)	[3]
10	51 295.029855(5)	27778	92.5(4)	[3]	40	52 027.692627(9)	30249	99.2(7)	[3]
11	51 297.698476(8)	27787	99.4(7)	[3]	41	52 029.768118(8)	30256	95.8(7)	[3]
12	51 334.464970(12)	27911	93.6(1.1)	[3]	42	52 030.954185(12)	30260	100.0(1.1)	[3]
13	51 335.650973(6)	27915	92.2(5)	[3]	43	52 032.733167(8)	30266	96.1(7)	[3]
14	51 337.133479(6)	27920	90.8(5)	[3]	44	52 076.615786(4)	30414	91.7(3)	[3]
15	51 393.46935(4)	28110	92(4)	[3]	45	52 077.208801(7)	30416	92.2(6)	[3]
16	51 396.13784(4)	28119	87(3)	[3]	46	52 077.801847(6)	30418	95.3(5)	[3]
17	51 397.32378(3)	28123	81(3)	[3]	47	52 078.394837(7)	30420	93.7(6)	[3]
18	51 466.112958(9)	28355	91.5(8)	[3]	48	52 078.987831(8)	30422	92.4(7)	[3]
19	51 467.29898(12)	28359	92.2(1.0)	[3]	49	52 131.469068(10)	30599	86.8(9)	[3]
20	51 470.264016(9)	28369	91.1(8)	[3]	50	52 132.65509(2)	30603	87(2)	[3]
21	51 557.436333(6)	28663	89.8(5)	[3]	51	52 133.24811(8)	30605	88(7)	[3]
22	51 561.290937(6)	28676	93.7(5)	[3]	52	52 136.50958(8)	30616	81(7)	[3]
23	51 562.477008(6)	28680	98.3(5)	[3]	53	52 159.34046(2)	30693	83.9(1.4)	[3]
24	51 625.03951(2)	28891	104(2)	[3]	54	57 291.24010(2)	48001	17(2)	[3]
25	51 677.817305(4)	29069	101.3(4)	[3]	55	57 294.20513(2)	48011	16(2)	[3]
26	51 681.671901(6)	29082	104.5(5)	[3]	56	57 499.682737(14)	48704	13.7(1.2)	[3]
27	51 682.857903(7)	29086	103.2(6)	[3]	57	57 792.03631(3)	49690	23(3)	[3]
28	51 763.803676(5)	29359	106.3(4)	[3]	58	57 794.70484(5)	49699	22(4)	[3]
29	51 764.989711(8)	29363	107.7(7)	[3]	59	57 795.89087 (5)	49703	23(4)	[3]
30	51 768.84426(2)	29376	106.0(1.4)	[4]					

NOTE — Epoch of reference 43 058.72595 MJD, orbital period 7.11610872 hr, the associated errors are at 68% confidence levels; [1] Cominsky and Wood (1989), [2] Wachter et al. (2000), [3] this work, [4] Oosterbroek et al. (2001) .

$T_0 = 43\,058.72609$ MJD obtained by Oosterbroek et al. (2001) adopting quadratic ephemeris.

We fitted the eclipse profiles with a simple model consisting of a step-and-ramp function, where the count rates before, during, and after the eclipse are constant and the intensity changes linearly during the eclipse transitions. This model involves seven parameters: the count rate before, during, and after the eclipse, called C_1, C_2, and C_3, respectively; the phases of the start and stop times of the ingress (ϕ_1 and ϕ_2), and, finally, the phases of the start and stop times of the egress (ϕ_3 and ϕ_4). We show a typical eclipse of MXB 1659-298 in Fig. 8.2. The eclipse was observed during the RXTE/PCA observation P40050-04-16-00, the superimposed red function is the step-and-ramp best-fitting function. The phase corresponding to the eclipse arrival time ϕ_{ecl} is estimated as $\phi_{ecl} = (\phi_2 + \phi_3)/2$. The corresponding eclipse arrival time is given by $T_{ecl} = T_{fold} + \phi_{ecl} P_0$. To be more conservative, we scaled the error associated with ϕ_{ecl} by the factor $\sqrt{\chi^2_{red}}$ to take into account values of χ^2_{red} of the best-fit model larger than one. We show the obtained eclipse arrival times in Barycentric Dynamical Time (TDB), in units of MJD, in Tab. 8.1.

We used the 43 RXTE/PCA observations to estimate the average duration, ΔT_{ecl}, ΔT_{ing} and ΔT_{egr} of the eclipse, the ingress and the egress, respectively. The values of ΔT_{ecl}, ΔT_{ing} and ΔT_{egr} for each eclipse are shown as function of the eclipse arrival times in Fig. 8.3. We found that ΔT_{ecl} is scattered between 890 and 910 s. Fitting the values of eclipse duration with a constant we obtained a $\chi^2(d.o.f.)$ of 561(42) and a best-fit value of $\Delta T_{ecl} = 899.1 \pm 0.6$ s at 68% confidence level (c.l.). The ingress duration is scattered between 10 and 30 s while the egress duration is scattered between 10 and 35 s. Fitting the ingress duration values with a constant we obtained a $\chi^2(d.o.f.)$ of 457 (38) and a best-fit value of $\Delta T_{ing} = 17.0 \pm 0.7$ s at 68% c. l., while, fitting the egress duration values we obtained a $\chi^2(d.o.f.)$ of 560 (39) and a best-fit value of $\Delta T_{egr} = 16.7 \pm 0.9$ s at 68% c. l.. The associated errors were scaled by the factor $\sqrt{\chi^2_{red}}$ to take a value of χ^2_{red} of the best-fit model larger than one into account. We find that the average duration of the ingress and egress are similar. We also show in Fig. 8.3 the occurrences of the measured ingress, egress and duration using a bin of 3.1, 3.7 and 3.5 s, respectively.

We calculated the delays with respect to $P_0 = 7.11610872$ hr and to a reference epoch of $T_0 = 43\,058.72595$ MJD, corresponding to the first eclipse arrival time obtained by Cominsky and Wood (1989). The inferred delays, in units of seconds, of the eclipse arrival times with respect to a constant orbital period are reported in Tab. 8.1. For each point we computed the corresponding cycle and the eclipse arrival time in days with respect to the adopted T_0. We show the delays vs. time in Fig. 8.4 (top panel).

Initially we fitted the delays with a quadratic function

$$y(t) = a + bt + ct^2, \tag{8.1}$$

where t is the time in days (MJD-43 058.72595), $a = \Delta T_0$ is the correction to T_0 in units of seconds, $b = \Delta P/P_0$ in units of s d^{-1} with ΔP the correction to the orbital period, and finally, $c = 1/2\,\dot{P}/P_0$ in units of s d^{-2}, with $\dot{P}$ representing the orbital period derivative. The corresponding best-fitting

Table 8.2: Best-fit values

Parameter	LQ	LQS	LQCS
a (s)	-109 ± 38	65 ± 20	9 ± 29
b (s d^{-1})	0.046 ± 0.007	0.015 ± 0.004	0.037 ± 0.009
c ($\times 10^{-6}$ s d^{-2})	-2.6 ± 0.3	-1.2 ± 0.2	-4.0 ± 1.1
d ($\times 10^{-10}$ s d^{-3})	-	-	1.0 ± 0.4
A (s)	-	9.6 ± 0.6	10.2 ± 0.7
P_{mod} (d)	-	843 ± 7	855 ± 8
t_ϕ (d)	-	137 ± 75	-7 ± 82
χ^2(d.o.f.)	4083(56)	512(53)	455(52)

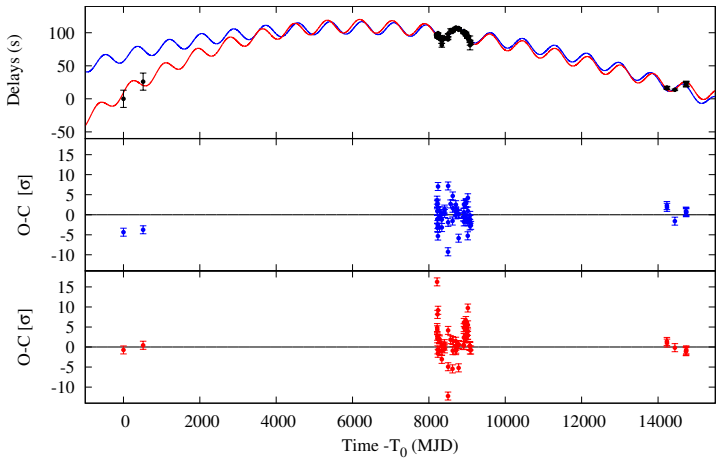

Figure 8.4: Top panel: delays with respect to the predicted eclipse arrival times, assuming as epoch of reference T_0 = 43 058.72595 MJD and as orbital period P_0 = 7.11610872 hr, plotted versus time. The blue and red curves indicate the best-fit functions corresponding to eqs. 8.2 and 8.4, respectively. Middle panel: residuals in units of σ with respect to the blue curve. Bottom panel: residuals in units of σ with respect to the red curve.

parameters are shown in the LQ column of Tab. 8.2. With a χ^2 of 4083 for 56 d.o.f., we note that the quadratic function does not acceptably fit the data. Since the delays seem to show a periodic modulation we fitted them using the function

$$y(t) = a + bt + ct^2 + A \sin\left[\frac{2\pi}{P_{mod}}(t - t_\phi)\right], \tag{8.2}$$

where A is the amplitude in seconds of the sinusoidal function, P_{mod} is the period of the sine function in days, and, finally, t_ϕ represents the time in days at which the sinusoidal function is null. A clear improvement is obtained with a value of $\chi^2(d.o.f.)$ of 512 (53) that translates to a F-test probability chance improvement of 7×10^{-24}. The best-fit function, indicated with a blue curve, and the corresponding residuals are shown in the top and middle panels of Fig. 8.4. The best-fit values are shown in the third column of Tab. 8.2. The corresponding ephemeris (hereafter

LQS) is

$$T_{ecl}(N) = MJD(TDB)\,43\,058.7267(2) + 0.296504580(13)N - 1.3(2)\times10^{-12}N^2 + A\sin\left[\frac{2\pi}{N_{mod}}N - \phi\right], \tag{8.3}$$

where N indicates the number of cycles, $N_{mod} = P_{mod}/P_0$ and $\phi = 2\pi t_\phi/P_{mod}$. We obtained an orbital period derivative $\dot{P} = -8.5(1.2)\times10^{-12}$ s s^{-1}, a sinusoidal modulation characterised by a periodicity $P_{mod} = 2.31\pm0.02$ yr and a semiamplitude $A = 9.6\pm0.6$ s.

It is evident that the LQS ephemeris does not predict the first two eclipse arrival times. A possible explanation is that the orbital period derivative is changing from 1976 up to now. To take into account this fact, we added a cubic term to eq. 8.2, defining the new function

$$y(t) = a + bt + ct^2 + dt^3 + A\sin\left[\frac{2\pi}{P_{mod}}(t - t_\phi)\right], \tag{8.4}$$

where d includes the presence of a derivative of $\dot{P}$ with $d \simeq \ddot{P}/(6P)$. With the latter model we obtain a value of $\chi^2(d.o.f.)$ of 455 (52). By adding the cubic term we find a F-test probability chance improvement of 0.014 indicating that the improvement of the fit is between two and three σ of confidence level. The best-fit function, indicated with a red curve, and the corresponding residuals are shown in the top and bottom panel of Fig. 8.4. The best-fit parameters are shown in the fourth column of Tab. 8.2. The corresponding ephemeris (hereafter LQCS) is

$$T_{ecl}(N) = MJD(TDB)\,43\,058.7261(3) + 0.296504566(3)N - 4.0(1.1)\times10^{-12}N^2 + 3.0(1.2)\times10^{-17}N^3 + A\sin\left[\frac{2\pi}{N_{mod}}N - \phi\right], \tag{8.5}$$

from which we inferred the orbital period derivative at time $T_0 = 43\,058.7261$ MJD to be $\dot{P} = -2.7(7)\times10^{-11}$ s s^{-1} and the orbital period second derivative $\ddot{P} = 2.4(9)\times10^{-20}$ s s^{-2}. The sinusoidal modulation has a period of $P_{mod} = 2.34\pm0.02$ yr and a semiamplitude of $A = 10.2\pm0.7$ s.

8.5 Discussion

We analysed the eclipse arrival times of MXB 1659-298 with the main aim to estimate its ephemeris. Our baseline spans 40 years and covers the three outbursts of the source observed from 1976. We combined 51 eclipse arrival times, corresponding to the outbursts occurred in 1999-2001 and in 2015-2017, with the data already reported in literature. The campaign of observations made with *Rossi-XTE*/PCA during the 1999-2001 outburst seems to indicate a possible periodic modulation of 2.3 years; the delays associated with the six eclipse arrival times obtained during the most recent outburst agree with that periodic modulation. We find that the LQS ephemeris accounts for the eclipse arrival times except for the two eclipses observed

in 1976-1978. The addiction of a cubic term (LQCS ephemeris) allows to account for all the available data, however the statistical improvement is less than three sigma, suggesting that a larger baseline is needed to confirm the more complex ephemerides. In both cases, a sinusoidal modulation with a period between 840 and 860 days is needed to obtain an acceptable fit of the eclipse arrival times. In the following we restrict our discussion to the LSQ ephemeris.

To estimate the eclipse arrival times we fitted the shape of the eclipse using a step-and-ramp function. We used the *RXTE*/PCA observations, covering 2.4 years during the second outburst of MXB 1659-298, to estimate the ingress/egress and eclipse durations. The obtained values are scattered, the mean values associated with the eclipse, ingress and egress are $\Delta T_{ecl} = 899.1 \pm 0.6$ s, $\Delta T_{ing} = 17.0 \pm 0.7$ s and $\Delta T_{egr} = 16.7 \pm 0.9$ s, respectively. We find that the ingress and egress durations are similar contrarily to what reported by Cominsky and Wood (1989), that obtained an ingress and egress duration of 41 ± 13 s and 19 ± 13 s, respectively. Our different results can be explained by the larger sample and the higher quality of our dataset.

The ingress, egress, and eclipse durations show a jittered behaviour of the order of 15 s similarly to what observed in EXO 0748-676 (Wolff et al., 2002). Wolff et al. (2007) discussed the possibility that magnetic activity of the companion star generates extended coronal loops above the photosphere that could explain the amplitude of the observed jitter. This scenario may be plausible given the late K or early M type nature of the 0.3-0.4 $M_\odot$ companion star in EXO 0748-676. Such stars can have magnetic activity if they rotate and if they have significant convective envelopes (see Wolff et al., 2007). The companion star in MXB 1659-298 is an early K type main-sequence star (see below), and hence it likely has similar magnetic activity. Ponti et al. (2017) showed that AX J1745.6-2901 has a different phenomenology. Although jitters are observed in the ingress and egress, the eclipse duration is nearly constant. The authors suggested that the matter ejected from the accretion disc could reach the companion star with a ram pressure comparable to the pressure in the upper layers of the companion star (that is a K type main-sequence star). This interaction could displace the atmosphere of the companion star delaying both the ingress and the egress times.

8.5.1 The masses of the binary system

We can estimate the companion star radius from the size of its Roche lobe, that can be expressed by using the formula of Paczyński (1971)

$$R_{L_2} = 0.462 a \left(\frac{m_2}{m_1 + m_2} \right)^{1/3}, \tag{8.6}$$

where a is the orbital separation of the binary system and m_1 is the neutron star mass in units of solar masses. Combining the previous equation with the third Kepler's law we find that

$$R_{L_2} = 0.233\, m_2^{1/3} P_h^{2/3} R_\odot. \tag{8.7}$$

Assuming that the companion star fills its Roche lobe then the radius of the companion star R_2 coincides with R_{L_2}. To estimate the mass of the companion star we adopted the mass-radius

relation for a companion star in thermal equilibrium obtained by studying the cataclysmic variable systems (eq. 16 in Knigge et al., 2011) although LMXBs lie in a somewhat different region of parameter space. We adopted the relation valid for large orbital periods that is

$$R_2 = 0.293 \pm 0.010 \left(\frac{M_2}{M_{conv}} \right)^{0.69 \pm 0.03} R_\odot, \tag{8.8}$$

where M_{conv} has a value of 0.20 ± 0.02 $M_\odot$ and it is the mass of the convective region of the companion star. Combining the eqs. 8.7 and 8.8 and taking into account that the accuracy associated with the Roche lobe radius is 2% we find that the companion star has a mass of 0.9 ± 0.3 $M_\odot$ and a radius of 0.84 ± 0.10 $R_\odot$. Hereafter we will assume a neutron star mass of 1.48 ± 0.22 $M_\odot$, this mass value was estimated by Özel et al. (2012) analysing the mass distribution of neutron stars that have been recycled; the best value is the mean of the distribution and the associated error is the corresponding dispersion.

8.5.2 The mass accretion rate and the mass transfer rate

Using RXTE/PCA data taken during the outburst in 1999, Galloway et al. (2008) observed that the flux of MXB 1659-298 peaked at $\sim 1.0 \times 10^{-9}$ erg s^{-1} cm^{-2} in the 2-25 keV energy range during April 1999 , but it was between 4×10^{-10} and 6×10^{-10} erg s^{-1} cm^{-2} throughout the remainder of the outburst. To infer a good estimation of the flux in the 0.1-100 keV energy band, we adopted the broadband best-fit model of the persistent spectrum obtained by Oosterbroek et al. 2001, from which we extrapolate an unabsorbed flux of 1.0×10^{-9} erg s^{-1} cm^{-2}.

From the analysis of the type-I X-ray bursts the distance to MXB 1659-298 was estimated to be 9 ± 2 and 12 ± 3 kpc for a hydrogen-rich and helium-rich companion star, respectively (see Galloway et al., 2008). We assume the average of the two values, $d = 11 \pm 4$ kpc, considering that the source is accreting mixed H/He (Galloway et al., 2008).

To convert the X-ray luminosity in mass accretion rate we used the relation $L_x = \gamma \dot{M}_{acc} c^2$, where γ is the efficiency of the accretion and c is the speed of the light. We take into account that the neutron star is rapidly spinning with a frequency of 567 Hz (Wijnands et al., 2001) adopting the relation proposed by Sibgatullin and Sunyaev (2000)

$$\gamma = 0.213 - 0.153 f_{kHz} + 0.02 f_{kHz}^2, \tag{8.9}$$

where f_{kHz} is the spin frequency of the neutron star in units of kHz. The latter relation is valid assuming a gravitational mass of the neutron star of 1.4 $M_\odot$ and the commonly adopted FPS equation of state for a neutron star. Using a spin frequency of 567 Hz we find that $\gamma \simeq 0.132$. Our assumption implies that all of the released gravitational energy is converted to X-ray emission and that negligible amount of energy is carried away by bulk outflows. This is confirmed by the spectral studies of the source; in fact, the absorption lines associated with the presence of Fe XXV and Fe XXVI ions are narrow suggesting that it is not possible to associate to the source a

superluminal jet (see Sidoli et al., 2001). Furthermore Díaz Trigo and Boirin (2016) suggested that MXB 1659-298 could have a mild thermal wind but only static atmospheres have been reported.

Using $\gamma \simeq 0.132$ we find $\dot{M}_{acc} = (2.0 \pm 1.5) \times 10^{-9}$ M$_\odot$ yr^{-1}. Considering a quiescence duration of almost 14.5 yr and a mean outburst duration of 1.5 yr we find that the average value of the observed mass accretion rate is $|\langle \dot{M}_{acc} \rangle| \simeq \dot{M}_{acc} 1.5/16 = (1.9 \pm 1.4) \times 10^{-10}$ M$_\odot$ yr^{-1}.

On the other hand, from theoretical considerations, we can estimate the rate of mass that has to be transferred from the companion star in order to explain the quadratic term of the LQS ephemeris interpreted as the orbital period derivative of the system. From the long-term orbital evolution we can estimate the mass transfer rate $\dot{M}_2$ using the eq. 4 in Burderi et al. (2010)

$$\dot{m}_{-8} = 35(3n-1)^{-1} m_2 \left(\frac{\dot{P}_{-10}}{P_{5h}} \right), \tag{8.10}$$

where $\dot{m}_{-8}$ is the mass transfer rate $\dot{M}_2$ in units of 10^{-8} M$_\odot$ yr^{-1}, n is the mass-radius index of the companion star, m_2 is the companion star mass in units of solar masses, $\dot{P}_{-10}$ is the orbital period derivative in units of 10^{-10} s s^{-1} and P_{5h} is the orbital period in units of 5 hr. This is derived combining the third Kepler law with the contact condition, that is $\dot{R}_{L2}/R_{L2} = \dot{R}_2/R_2$ (where $\dot{R}_{L2}$ is the Roche Lobe radius of the secondary and R_2 is the radius of the secondary). Adopting $n = 0.69 \pm 0.03$, $m_2 = 0.9 \pm 0.3$, $\dot{P} = -8.5(1.2) \times 10^{-12}$ s s^{-1} and $P = 7.1161099(3)$ hr, we find that the mass transfer rate implied by the observed orbital period derivative is $\dot{M}_2 = -(1.8 \pm 0.7) \times 10^{-8}$ M$_\odot$ yr^{-1}, that is almost two orders of magnitude higher that the observed averaged mass accretion rate. This means that in order to explain the observed orbital period change rate we have to invoke a highly not conservative mass transfer for this system.

The above described scenario assumes a mass transfer rate of $\dot{M}_2 = -(1.8 \pm 0.7) \times 10^{-8}$ M$_\odot$ yr^{-1} and a companion star mass of 0.9 ± 0.3 M$_\odot$ in thermal equilibrium. The time scale associated with the mass transfer rate, $\tau_{\dot{M}} = M_2/|\dot{M}_2|$, is $(5 \pm 3) \times 10^7$ yr. The companion star is in thermal equilibrium if $\tau_{\dot{M}}$ is longer than the thermal time scale $\tau_{KH} = GM_2^2/(R_2 L_2)$ of the companion star (Paczyński, 1971). To estimate the thermal timescale we need to infer the luminosity L_2 of the companion star. For a star close to the lower main sequence it holds the relation $L_2/L_\odot = (M_2/M_\odot)^4$ (see Salaris and Cassisi, 2005). For a companion star mass of 0.9 ± 0.3 M$_\odot$ we obtain that $\tau_{KH} = (5 \pm 3) \times 10^7$ yr which is comparable with $\tau_{\dot{M}}$, for this reason we cannot exclude the the companion star is less massive of 0.9 ± 0.3 M$_\odot$.

8.5.3 The prediction of the orbital period derivative for a highly non conservative mass transfer

We can define a parameter β in the following way, $-\dot{M}_1 = \beta \dot{M}_2$, where $\dot{M}_1 = |\langle \dot{M}_{acc} \rangle|$ is the mass accretion rate. Hence $\beta = 1$ in a conservative mass transfer scenario and $\beta < 1$ in a non conservative mass transfer scenario. Comparing the observed averaged mass accretion rate with the mass transfer rate implied by the observed orbital period derivative, we obtain

$\beta = 0.011 \pm 0.009$, suggesting that only $\sim 1\%$ of the mass transferred from the companion star is indeed accreted onto the neutron star.

According to the orbital evolution theory, orbital period changes are expected to be driven by mass transfer from the companion to the compact object, by emission of gravitational waves (GR) and/or by magnetic braking (MB). For orbital periods larger than two hours the effects of MB dominate the orbital evolution of the binary system. Following Verbunt and Zwaan (1981), Verbunt (1993) and Tauris (2001) the torque associated with MB can be parametrised as

$$T_{MB} = 8.4(k^2)_{0.1} f^{-2} m_1^{-1} P_{2h}^2 q^{1/3} (1+q)^{2/3}, \tag{8.11}$$

where f is a dimensionless parameter for which a value of either 0.79 (Skumanich, 1972) or 1.78 (Smith, 1979) has been assumed, $k = 0.323$ is the gyration radius for a star with mass of 0.8 $M_\odot$ (Claret and Gimenez, 1990), P_{2h} is the orbital period in units of two hours, q is the mass ratio M_2/M_1 and, finally, m_1 is the mass of the compact object in units of solar masses. Because T_{MB} depends on f^{-2} the effects of the MB on the derivative of the angular momentum of the binary system will be larger for $f = 0.79$ than for $f = 1.78$.

We can calculate the secular orbital period derivative expected from the non-conservative secular evolution of the system using the relation

$$\dot{P}_{-12} = 1.37 q (1+q)^{-1/3} m_1^{5/3} P_{2h}^{-5/3} \left[\frac{1/3 - n}{2g(\alpha,\beta,q) - 1/3 + n} \right] \times [1 + T_{MB}], \tag{8.12}$$

where

$$g(\alpha,\beta,q) = 1 - \beta q - \frac{1-\beta}{1+q}\left(\frac{q}{3} + \alpha\right) \tag{8.13}$$

(see Di Salvo et al., 2008; Burderi et al., 2009, 2010), where $\dot{P}_{-12}$ is the orbital period derivative in units of 10^{-12} s s^{-1} and α is a dimensionless parameter that quantifies the specific angular momentum of the ejected matter in the case of a non-conservative mass transfer scenario. The specific angular momentum, l_{ej}, with which the transferred mass is lost from the system can be written in units of the specific angular momentum of the secondary, that is $\alpha = l_{ej}/(\Omega_{orb} r_2^2) = l_{ej} P (M_1 + M_2)^2/(2\pi a^2 M_1^2)$, where r_2 is the distance of the secondary star from the centre of mass of the system, a is the orbital separation and P is the orbital period of the binary system. For a neutron star mass of 1.48 ± 0.22 $M_\odot$ we obtain an orbital period derivative of $-(6 \pm 3) \times 10^{-12}$ s s^{-1}, which is compatible within one σ with the value $\dot{P} = -(8.5 \pm 1.2) \times 10^{-12}$ s s^{-1} inferred from the eclipse arrival times.

A highly non-conservative mass transfer in this source may be justified by the fact that MXB 1659-298 is a fast spinning neutron star (Wijnands et al., 2001). During the quiescent periods, if the region around the neutron star is free from matter up to the light cylinder radius, the radiation pressure of the rotating magnetic dipole, given by the Larmor formula, may be able

to eject from the system the matter transferred by the companion star at the inner Lagrangian point, according to the mechanism termed *radio ejection* and described in detail in Burderi et al. (2001). Once significant temporary reduction of the mass accretion rate occurs, the neutron star can emit as a magnetic-dipole rotator and the radiation pressure from the pulsar may be able to eject the matter transferred from the companion out of the system. We note that the disc instability model (see the review of Lasota, 2001) may have a role in triggering the *radio ejection* and starting a non conservative mass transfer. The *radio ejection* has been invoked to explain the high orbital period derivative observed in the accreting millisecond pulsar (AMSP) SAX J1808.4-3658 (see Di Salvo et al., 2008; Burderi et al., 2009), and, more recently, for the AMSP SAX J1748.9-2021 for which a high orbital period derivative is also observed (Sanna et al., 2016). We therefore suggest that a similar mechanism could be also at work for MXB 1659-298.

The above described scenario assumes a mass transfer rate of $\dot{M}_2 = -(1.8 \pm 0.7) \times 10^{-8}$ M$_\odot$ yr^{-1} and a companion star mass of 0.9 ± 0.3 M$_\odot$. The time scale associated with the mass transfer rate, $\tau_{\dot{M}} = M_2/|\dot{M}_2|$, is $(5.1 \pm 2.7) \times 10^7$ yr. The companion star is in thermal equilibrium if $\tau_{\dot{M}}$ is longer than the thermal time scale $\tau_{KH} = GM_2^2/(R_2 L_2)$ of the companion star (Paczyński, 1971). To estimate the thermal timescale we need to infer the luminosity L_2 of the companion star. For a star close to the lower main sequence it holds the relation $L_2/L_\odot = (M_2/M_\odot)^4$ (see Salaris and Cassisi, 2005). Since the companion star mass is 0.9 ± 0.3 M$_\odot$ we obtain that $\tau_{KH} = (5 \pm 3) \times 10^7$ yr which is comparable with $\tau_{\dot{M}}$. Since the two timescales are comparable we cannot exclude that the companion star is out of the thermal-equilibrium; hence, the value of 0.9 ± 0.3 M$_\odot$ has to be considered an upper limit to the companion star mass.

We note that for a mass of the companion star lower than $0.9 M_\odot$ the mass transfer rate would be also lower, because of the linear dependence of $\dot{M}_2$ on m_2 in eq. 8.10. Therefore, the minimum mass transfer rate is reached for a $m_2 = 0.35$ M$_\odot$. This has to be considered as a lower limit to the mass of the companion since below this mass the companion star is expected to become fully convective and the magnetic braking switches off (Rappaport et al., 1983). For this limiting mass, the mass transfer rate is $(7 \pm 3) \times 10^{-9}$ M$_\odot$ yr^{-1}. However, a detailed study of the evolution of this system is beyond the aims of this paper and will be reported elsewhere. Here we note that the results presented in this paper do not change significantly adopting a lower mass for the companion star. Therefore, we will continue our discussion assuming a companion star mass of 0.9 ± 0.3 M$_\odot$, keeping in mind that lower masses for the companion star are also possible.

8.5.3.1 The changes of the equivalent hydrogen column density N_H during the X-ray quiescence

The mass ejected from the system can explain the variable equivalent hydrogen column density N_H measured during the X-ray quiescence of the source. Cackett et al. (2008b, 2013) measured two different N_H values of $(2.0 \pm 0.1) \times 10^{21}$ cm^{-2} and $(4.7 \pm 1.3) \times 10^{21}$ cm^{-2}, respectively, at different times, while the estimation of N_H obtained by Dickey and Lockman (1990) is 1.8×10^{21} cm^{-2}. Here

we suggest that the matter ejected from the system can account for the additional absorption. Most of the matter provided by the companion is ejected from the inner Lagrangian point forming a circumbinary ring of matter around MXB 1659-298. Because of the large inclination angle of the system it is possible that the ejected matter interposes between the source and the observer. Local density inhomogeneities and/or changes in the mass transfer rate could produce changes in the equivalent hydrogen column as observed by Cackett et al. (2008b, 2013) during quiescence.

We use the eq. 4 of Iaria et al. (2013) to estimate the density of the ejected matter

$$n(r) \simeq 6.9 \times 10^{11} (1-\beta) \zeta^{-1} \eta^{-1} \dot{m}_E (m_1 + m_2)^{-1} P_h^{-1} \left(\frac{r}{a}\right)^{-3/2}, \tag{8.14}$$

where $n(r)$ is the density in units of cm^{-3}, r is the distance from the inner Lagrangian point, ζ is a parameter that takes into account a non-spherical distribution of matter, η a parameter larger than 1, $\dot{m}_E$ is the mass transfer rate in units of Eddington mass accretion rate and a is the orbital separation of the binary system. Adopting a mass transfer rate of $|\dot{M}_2| = (1.8 \pm 0.7) \times 10^{-8}$ M$_\odot$ yr^{-1}, an orbital period of 7.116 hr, a companion star mass and a neutron star mass of 0.9 ± 0.3 M$_\odot$ and 1.48 ± 0.22 M$_\odot$, respectively, we obtain $n(a) = (5 \pm 2) \times 10^{10} (\zeta\eta)^{-1}$ cm^{-3}. Supposing a constant particle density along the line of sight, we can determine the equivalent hydrogen column density N_H associated with the neutral matter using $N_H = n(a) \times a$, where $a = (1.74 \pm 0.10) \times 10^{11}$ cm. We find $N_H = (8 \pm 4) \times 10^{21} (\zeta\eta)^{-1}$ cm^{-2}. Since the quantity $\zeta\eta$ is close to unity (see Iaria et al., 2013) we find that the equivalent hydrogen column of the cold matter is $N_H = (8 \pm 4) \times 10^{21}$ cm^{-2}, that is of the same order of magnitude of the changes observed during quiescence of the source and, furthermore, it explains the discrepancy by a factor of two between the N_H values measured by Cackett et al. (2013) and Dickey and Lockman (1990).

8.5.3.2 The inclination angle of the source

From our estimate of the duration of the eclipse ingress, that is $\Delta T_{ing} \simeq 17$ s, we can estimate the size of the corona, R_c, surrounding the central source using the relation

$$\frac{2\pi}{P} a = \frac{2R_c}{\Delta T_{ing}}, \tag{8.15}$$

we find $R_c = (3.6 \pm 0.3) \times 10^8$ cm. Assuming a neutron star mass of 1.48 ± 0.22 M$_\odot$ and a companion star mass of 0.9 ± 0.3 M$_\odot$ we infer that the Roche lobe radius, R_{L_1} of the compact object is 5.8×10^{10} cm. The radius of the accretion disc, R_d, corresponds to the tidal radius $R_T \simeq 0.9 R_{L_1}$ (see Frank et al., 2002, eq. 5.122), hence the accretion disc radius is $R_d \simeq 5.3 \times 10^{10}$ cm. This result suggests that the corona is much smaller than the accretion disk, and therefore it is a relatively compact corona around the neutron star.

Using our estimate of the eclipse duration we can also estimate the inclination angle, $i = 90^\circ - \theta$, of the system finding the angle θ represented in Fig. 8.5. Knowing that the eclipse duration is $\Delta T_{ecl} \simeq 899.1$ s we can estimate the size of the occulted region x as before using

$$\frac{2\pi}{P} a = \frac{2x}{\Delta T_{ecl}}. \tag{8.16}$$

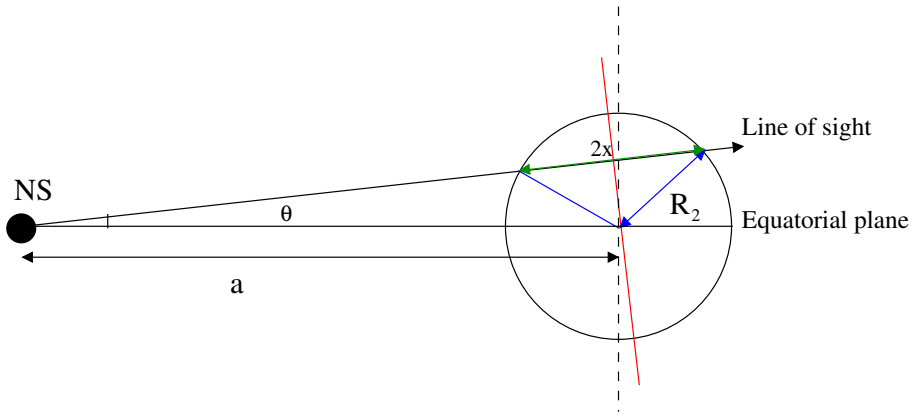

Figure 8.5: Schematic geometry of MXB 1659-298 not in scale.

We obtain $x = (1.92 \pm 0.11) \times 10^{10}$ cm, where $2x$ is the green segment shown in Fig. 8.5. The angle θ, representing the angle between the line of sight and the equatorial plane of MXB 1659-298, is obtained from

$$\tan\theta = \left[\frac{R_2^2 - x^2}{a^2 - (R_2^2 - x^2)} \right]^{1/2} .$$

We infer $i = 72 \pm 3$ degrees. Our result is compatible with the presence in the light curve of the source of dips and total eclipses that can be observed for inclination angles in the approximate range 75°–80° (see Fig. 5.10 in Frank et al., 2002). We note that for a companion star mass of 0.35 $M_\odot$ the inclination angle of the system is 76.0 ± 0.7 degree, that is marginally compatible with the value obtained for a companion star mass of 0.9 ± 0.3 $M_\odot$.

Sidoli et al. (2001) detected absorption lines associated with the presence of O VIII, Ne IX, Fe XXV and Fe XXVI ions in the XMM spectrum of MXB 1659-298. The authors, assuming an inclination angle of 80° inferred the distance of the absorbing plasma from the central source, finding $r_{Fe} \lesssim 2.4 \times 10^8$ cm, $r_O \gtrsim 3 \times 10^8$ cm and $r_{Ne} \gtrsim 9 \times 10^7$ cm, respectively. Revisiting the results obtained by Sidoli et al. (2001) for an inclination angle of 72° we find $r_{Fe} \lesssim 8 \times 10^8$ cm, $r_O \gtrsim 1 \times 10^9$ cm and $r_{Ne} \gtrsim 3 \times 10^8$. Since we have estimated a size of the corona of $R_c \simeq 3.6 \times 10^8$ cm, we suggest that the absorbing plasma is located in the outer regions of the corona.

8.5.4 The 2.31-yr periodic modulation: possible explanations

Our ephemeris of MXB 1659-298 also includes a sinusoidal modulation with a period of 2.31 ± 0.02 yr. One possibility is that this periodic modulation observed in the delays may be produced by the gravitational coupling of the orbit with changes in the shape of the magnetically active companion star. These changes are thought to be the consequence of the torque applied by the magnetic activity of a sub-surface magnetic field in the companion star with the convective envelope. The convective envelope induces a cyclic exchange of angular momentum between the inner and outer regions of the companion star causing a change in the gravitational quadrupole moment (see

Applegate, 1992; Applegate and Shaham, 1994). A similar mechanism has been proposed for the eclipsing LMXBs EXO 0748-676 (Wolff et al., 2009) and AX J1745.6-2901 (Ponti et al., 2017).

The inferred periodicity of 843 d and the amplitude of 9.6 s correspond in this case to an orbital period variation of $\Delta P/P = (8.3 \pm 0.5) \times 10^{-7}$. We estimate that the transfer of angular momentum needed to produce an orbital period change ΔP is $\Delta J \simeq 3.8 \times 10^{46}$ g cm^2 s^{-1} (see Applegate, 1992, eq. 27). The asynchronism of the companion, quantified through the quantity $\Delta\Omega/\Omega$, is 3.7×10^{-4}, where Ω is the orbital angular velocity of the binary system and $\Delta\Omega$ is the variation of the orbital angular velocity needed to produce ΔP (see Applegate and Shaham, 1994, eq. 3). The variable part of the luminosity of the companion star required to power the gravitational quadrupole changes is $\Delta L \simeq 1.5 \times 10^{32}$ erg s^{-1}. Considering that $L_2/L_\odot = (M_2/M_\odot)^4$ we obtain $\Delta L/L_2 = 0.06 \pm 0.10$, in agreement with the prediction of $\Delta L \simeq 0.1 L$ obtained for magnetic active stars (see Applegate, 1992, and references therein). Our results suggest that a change in the magnetic quadrupole of the companion star can produce the observed sinusoidal modulation. The energy required to transfer the angular momentum from the interior of the companion star to a thin shell, with a mass of 10% of M_2, at the surface (and viceversa) is furnished by ten percentage of the thermonuclear energy produced by the companion star. Furthermore, we obtain that the mean sub-surface magnetic field B of the companion star is close to 1×10^5 G (see Applegate, 1992, eq. 23).

The origin of the sinusoidal modulation could also be explained by the presence of a third body orbiting around the binary system, similarly to what is found for the LMXB XB 1916-053 (Iaria et al., 2015b). Adopting the inclination angle of 72°.1 we find that the orbital separation between the centre of mass of MXB 1659-298 and the centre of mass of the triple system is $a_x \sin i = A\, c$, where c is the speed of light. Using the values in the third column of Tab. 8.2 we obtain that $a_x \sin i = (2.9 \pm 0.2) \times 10^{11}$ cm. Assuming a non-eccentric and coplanar orbit of the third body and that the companion star is in thermal equilibrium, the mass M_3 of the third body is obtained from

$$\frac{M_3 \sin i}{(M_3 + M_{bin})^{2/3}} = \left(\frac{4\pi^2}{G}\right)^{1/3} \frac{A c}{P_{mod}^{2/3}}, \tag{8.17}$$

where M_{bin} is the mass of the binary system and P_{mod} is the revolution period of the third body around the binary system (see e.g. Bozzo et al., 2007). We obtain that the mass of the third body is 22 ± 3 M_J, where M_J indicates the Jovian mass; the distance of the third body from the centre of mass of the triple system is 2.3 ± 0.3 AU. Releasing the constrain of a co-planar orbit the mass of the third body is larger than 21 M_J. We have checked that the derived orbit of the third body is stable in the formalism by Kiseleva et al. (1994). If this result will be confirmed, this will be the first circumbinary Jovian planet spotted around a LMXB. In the case of a no-coplanar orbit we find that the mass of the third body should be larger than 21 M_J.

8.6 Conclusions

We have estimated 51 eclipse arrival times for MXB 1659-298 when the source was in outburst in 2000, 2001 and 2015 using *Rossi-XTE*, *XMM-Newton*, *NuSTAR* and *Swift*/*XRT* data. Combining these times to the previous ones reported in literature we obtain a baseline of 40 years, from 1976 to 2017, to constrain the ephemeris of the source. The data are clustered in three temporal intervals covering six years corresponding to the periods when the source was in outburst. In the hypothesis that the companion star is in thermal equilibrium and fills its Roche Lobe, we estimate that the companion star mass is 0.9 ± 0.3 $M_\odot$, in agreement with the possibility that the companion is an early K-type main-sequence star as reported in literature.

Using RXTE/PCA data we have studied the profile of the total eclipse observing jitters in the ingress/egress duration and eclipse duration of about 10-15 s. The average values of the ingress, egress and eclipse durations are 17.0 ± 0.7 s, 16.7 ± 0.9 s and 899.1 ± 0.6 s, respectively. Using the average ingress and eclipse duration values we find that the size of the corona surrounding the neutron star is $R_c = (3.6 \pm 0.3) \times 10^8$ cm and the inclination angle of the binary system is 72 ± 3 degree assuming a companion star in thermal equilibrium.

We find that the eclipse arrival times are well described by ephemeris composed of a linear, a quadratic and a sinusoidal term. We find an orbital period derivative of $\dot{P} = -8.5(1.2) \times 10^{-12}$ s s^{-1}. We are able to explain the value of $\dot{P}$ assuming a highly non conservative mass transfer scenario. We find that the mass transfer rate is $\dot{M}_2 = -(1.8 \pm 0.7) \times 10^{-8}$ $M_\odot$ yr^{-1}, and only 1% of this mass is observed to accrete onto the neutron star. We also suggest that the ejected matter produces a local absorber with an equivalent hydrogen column density of $(8 \pm 4) \times 10^{21}$ cm^{-2}.

The sinusoidal modulation has a period of 2.31 ± 0.02 yr and an amplitude of 9.6 ± 0.6 s. The 2.3-yr periodic modulation of the orbital period can be explained either with the presence of a gravitational quadrupole coupling of the orbit to a variable deformation of the magnetically active companion star or with the presence of a third body orbiting around the binary system. In the second scenario we find that the mass of the third body is larger than 21 M_J.

Finally, we note that the first two eclipse arrival times, measured during the outburst occurred in 1976-1978, are marginally accounted for the quadratic ephemeris. To fit them we adopted a more complex ephemeris taking into account the second derivative of the orbital period. However, the statistical improvement is smaller than three σ. A larger baseline is needed to confirm or discard more complex ephemerides.

CHAPTER 9

PROBING A SAMPLE OF GAMMA-RAY PULSARS WITH FERMI-LAT: SEARCHING FOR A SPECTRAL HARD TAIL COMPONENT.

9.1 Introduction

In this chapter I will report the preliminary results of a work I performed in 6 months of research activity in Barcelona (Spain) with the High Energy Astrophysics group of the Institut de Ciencies de l'Espai (ICE). Here the discussion is limited to a brief report on the main problem that stands at the basis of the work and some preliminary results will be shown.
The aim of the work is the search for spectral marks to attribute to the emission of pulsar wind nebulae in proximity of pulsars in the gamma-ray band between 20 MeV and 300 GeV. The pulsar wind nebulae (PWNe) are created entirely by a confined magnetic wind produced by a pulsar that is composed essentially by electrons and positrons accelerated at relativistic velocities. The wind is confined by the ejecta in the supernova remnant (SNR) at the beginning and by the interstellar medium (ISM) once the wind has crossed the SNR, gradually forming an expanding magnetic bubble of relativistic particles that forms the PWN and that are gradually decelerated from the material they sweep (Slane, 2017).
The relativistic particles forming the PWN produce Synchrotron radiation that extends from the radio band up to the X-rays, as well as up-scattered photons that emit in the gamma-rays after being reprocessed via Inverse Compton scattering. In addition, for young PWNe with high magnetic fields, the up-scattering of the Synchrotron high energy spectrum can produce gamma-ray photons through the so-called synchrotron self-Compton emission. Then the final spectrum is strongly dependent on the age, magnetic field and pulsar spin-down power (Torres et al., 2013).

Table 9.1: Sources selected for the analysis.

Source	Flux (ph cm^{-2} s^{-1})	E_{cut} (MeV)	Fermi-LAT catalogue
J0357+3205	9.04×10^{-8}	817	2PC
J1057-5226	3.22×10^{-7}	1362	2PC
J1741-2054	1.66×10^{-7}	918	2PC
J1836+5925	6.3×10^{-7}	2043	3FHL
J0633+1746 (Geminga)	4.2×10^{-6}	2221	3FHL
J1732-3131	1.7×10^{-7}	1879	3FHL

9.2 Observation and data reduction

Whereas a pulsar hosts a PWN, according to the processes that determine the formation of the nebula, we expect to detect a non thermal component in the broad band gamma-ray spectra of these pulsars.
In order to probe the detection of this component above the high energy cut off of these sources we took the advantage of the data acquired by the Fermi-LAT instrument on board the Fermi space observatory (Atwood et al., 2009).
The pulsar we selected for the analysis have been chosen from both the 2PC and 3FHL Fermi-LAT catalogues: the first contains sources detected above 0.1 GeV during 3 years of LAT observations, whilst the latter contains sources detected above 10 GeV during 7 years of LAT observations of the gamma-ray sky. The selection criterion of the sources is finalised to increase the statistic of the spectral energy distribution (SED) that we want to obtain, especially at energies above the cut off energy of each source. For this reason, we selected a sample of six sources (three for each of the two Fermi-LAT catalogues) showing a flux that is larger than 5×10^{-8} ph cm^{-2} s^{-1} in the energy band between 0.1 and 100 MeV and with cut off energies between 1 GeV and 2 GeV (see Tab. 9.1).

We selected all the available data for each source inside a region of interest (ROI) of 10°and in the energy range between 100 MeV and 300 GeV. The data cover a time span of 8 years (from 5 Aug 2008 to 30 Nov 2016) and have been first processed with the Fermi Science Tools v10r0p5, using the `P8R2 V6 Clean` instrument response functions (IRFs) for the analysis. In addition, to reject contaminating gamma-rays from the Earth's limb, we selected events with a zenith angle < 90°. In order to take into account only events that are associated to each pulsar, we selected only events that according to the gamma ephemerides for these sources have an associated orbital phase included inside the pulse profile of each source. Then, we extended the orbital ephemerides of each source using *Tempo2* (Hobbs et al., 2006) along with the Fermi plug-in (Ray et al., 2011). The main task to accomplish, here, was to minimize as much as possible the rms associated to the distribution of the time of arrival of the gamma-ray photons. These times have been calculated with respect to the existing gamma-ray ephemerides. The result of the extension of the pulsar ephemerides is shown in Figure 9.1.
Having better estimations of the gamma-ray ephemerides implies increasing the S/N ratio of

the pulse profile, or equivalently the test statistic (TS) on the pulsation peak. The test statistic is defined as $TS = -2\,ln(L_{max,0}/L_{max,1})$, where $L_{max,0}$ is the maximum likelihood value for a model without an additional source (that is called "null hypothesis") and $L_{max,1}$ is the maximum likelihood value for a model with an additional source at a certain specified location. The detection of a gamma-ray excess in a certain probed position occurs when the null hypothesis is less important with respect to the case in which an additional source is taken into account, that is when the TS value is maximized. In particular, the square root of the TS can be approximated the detection significance of the source.
Then, once the timing ephemerides have been extended up to be valid for all the selected time span, we determined the on-peak phase interval for each source performing a Bayesian block analysis extending the data over three orbital periods, then covering the phase range between -1 and 2. For this analysis has been used the same algorithm already used by Scargle et al. (2013). The results of the Bayesian analysis is reported in Figure 9.2 and according to these, we selected only photons in the on-peak part of the pulse profile.

In the subsequent part of the work we performed the spectral analysis aimed to understand if the addition of a supplementary power law component determines a detection of this same component, with respect to the case in which the SEDs of each source are modelled according to the best fit models already catalogued in literature for each source. In this work we performed a spectral analysis using binned maximum likelihood fits, using 37 bins in the energy range between 0.1 and 300 GeV with the Science Tool gtlike. The spectral-spatial model constructed to perform the likelihood analysis includes the Galactic and isotropic diffuse emission components `gll_iem_v06.fits` (Acero et al., 2016) and `iso_P8R2_CLEAN_V6_v06.txt`, respectively. We fixed the position and the spectral parameters of each source to the values reported in the catalogue, with the exception for the sources falling inside a ROI of 3°from each selected source. For these latter sources the normalization and prefactor parameters were rescaled for the relative width of the selected phase interval (see Li et al., 2016, e.g.). The significance of the flux detection for the sources is evaluated with the estimation of test statistic (TS).
In literature the SED of each of the selected pulsar has been modelled with a power law with a super exponential cut-off, that has the functional form:

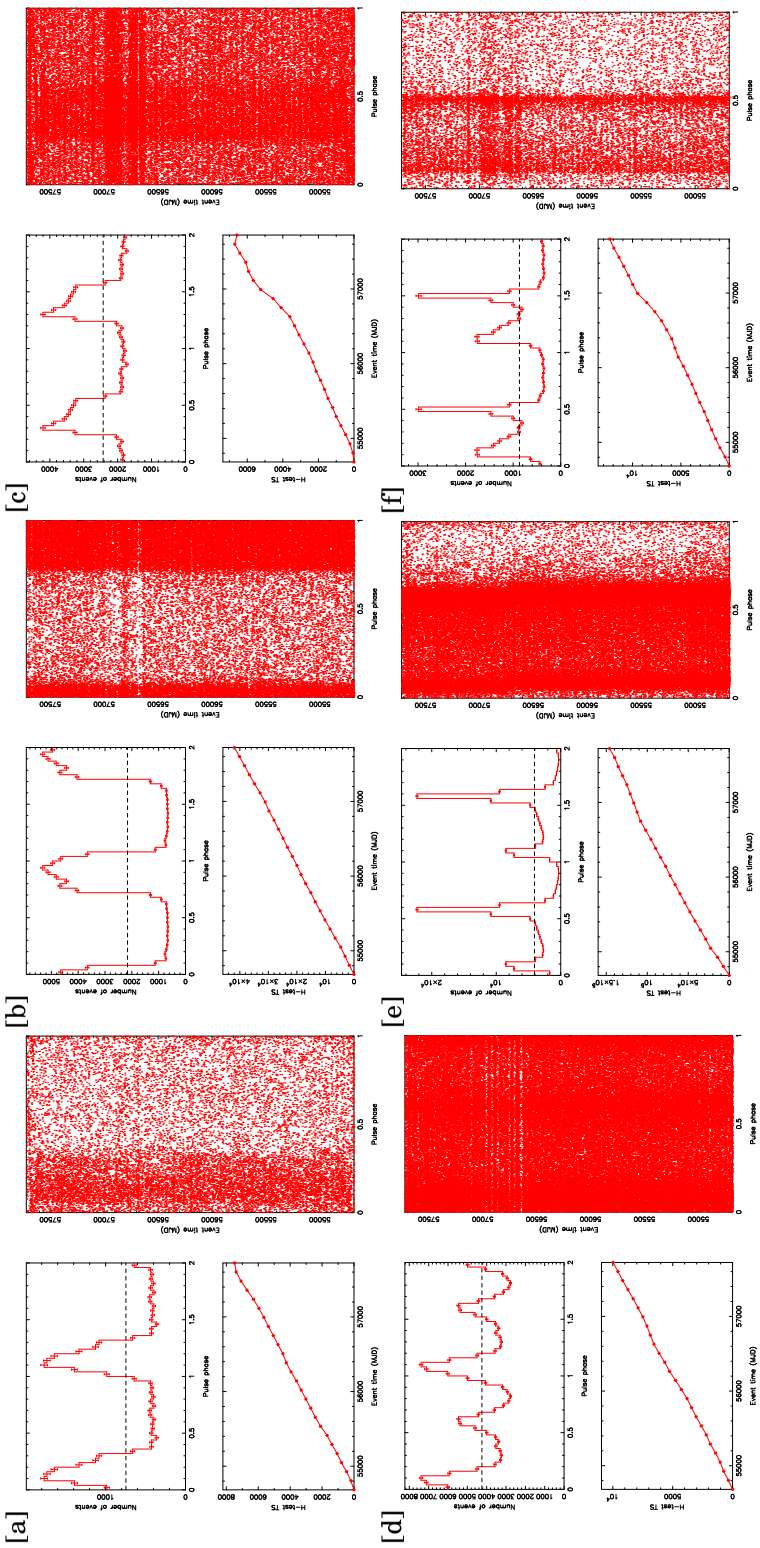

Figure 9.1: Timing results from Tempo2 with the Fermi plug-in for each analysed source (a- PSR J0357+3205, b- PSR J1057-5226, c- PSR J1741-2054, d- PSR J1836+5925, e- PSR J0633+1746, f- PSR J1732-3131). For each box we show: Top-left panel: phase histogram of the data we analysed in which two full periods are shown for clarity. Bottom-left panel: H-test significance (TS) as a function of time. Right panel: pulse phase for each gamma-ray event versus time.

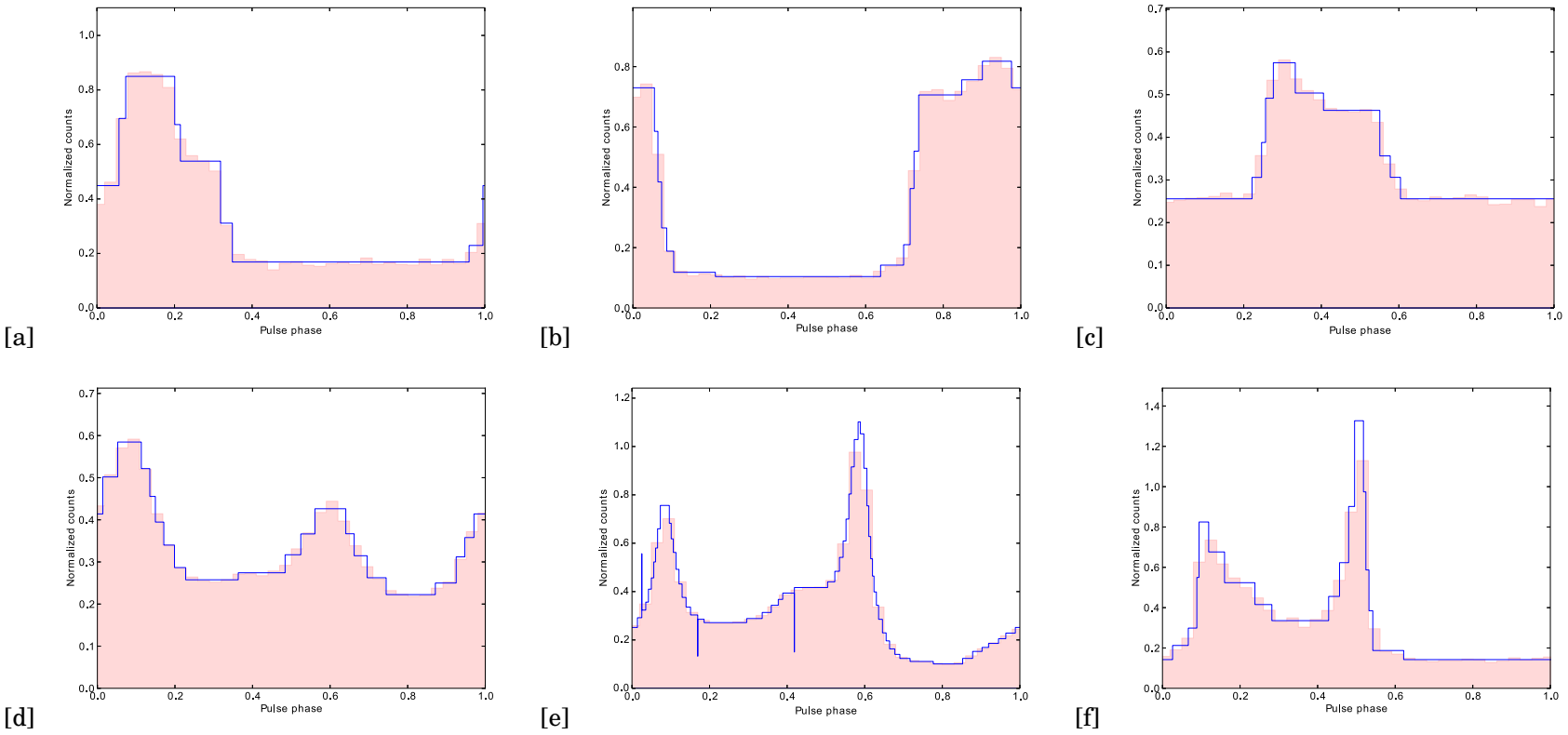

Figure 9.2: Bayesian block analysis output over three orbital periods (a- PSR J0357+3205, b- PSR J1057-5226, c- PSR J1741-2054, d- PSR J1836+5925, e- PSR J0633+1746, f- PSR J1732-3131).

$$\frac{dN}{dE} = N_0 \left(\frac{E}{E_0}\right)^{\gamma_1} exp\left(-\frac{E}{E_{cut}}\right)^{\gamma_2} \tag{9.1}$$

As a first step, the γ_2 index has been fixed to 1 for all the analysed sources. The fits performed on the data returns values of the spectral parameters that are in agreement with respect to those obtained in literature and reported in the Fermi LAT catalogues. However, the addition of a supplementary power law component having an index γ to the model of Equation 9.1 does not allow to obtain a detection of the latter component, with the exception of the two sources of the 3FHL Fermi-LAT catalogue PSR J1836+5925 and PSR J0633+1746 (Geminga) for which we found a detection level of confidence of about 5σ and of 8 σ respectively. For PSR J1836+5925 the gtlike fit allowed to evaluate $\gamma_1 = -1.207 \pm 0.010$, $E_{cut} = 2066 \pm 35$ MeV, and in addition a photon index for the supplementary power law component of $\gamma = -1.87 \pm 0.09$.
However, at least in the case of Geminga, keeping the index γ_2 free to vary gives a value for this parameter whose significance is at a level of confidence of about 20σ with respect to the case in which it was kept freed at $\gamma_2 = 1$. In this case from the fit of the SED of Geminga we obtain $\gamma_2 = 0.69 \pm 0.03$, $\gamma_1 = -1.02 \pm 0.04$ and $E_{cut} = 996 \pm 136$ MeV. The supplementary power law component, on the other hand, shows a photon index of $\gamma = -2.64 \pm 0.11$ and is detected with a level of confidence of about 4.4 σ. In Figure 9.3 we report the SED of these two candidate pulsars extrapolated from the on-peak pulse phase range. We also show the two spectral components with which we modelled the spectra.

9.3 Conclusions

As it can be observed in Figure 9.3, above the cut off energy of each of the two best candidates sources the SED shows upper limits that could be important to establish if the detected power law component is actually an extension of the pulsar spectrum or if it is due to instrumental causes. In order to solve this issue we need further checks on the obtained results, possibly comparing these results with those that could be obtained extending the same analysis also to the off-peak phase range.
For this reason the present work is only a brief report of the results obtained so far and is still in progress in order to shed full light on this issue.
Future facilities as the CTA (Cherenkov Telescope Array) could represent further opportunities to search for these spectral high energy components even in a wider energy range (from 20 GeV to more than 300 TeV) and with a higher angular resolution and sensitivity in comparison to any existing gamma-ray detector.

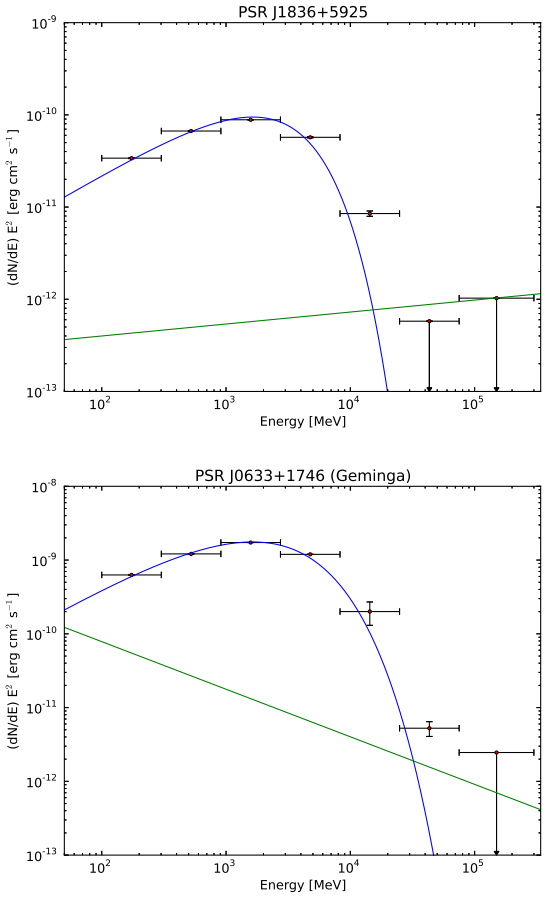

Figure 9.3: SED of the on-peak pulse phase range emission for the sources PSR J1836+5925 (upper panel) and PSR J0633+1746 (bottom panel). The blue curves represent the resulting best fit functions of Equation 9.1 that model the main gamma-ray emission of the pulsars, as seen in literature. The green lines represent the supplementary power law components we want to detect.

CHAPTER 10

GENERAL CONCLUSIONS

The aim of this thesis has been the study of the Low Mass X-ray Binary systems (LMXB) that host neutron stars and that show periodic dips or eclipses. We studied both the temporal and spectral properties of these systems obtaining a clearer view of the general properties of the studied sources, that also allowed us to discover new pieces of information that are fundamental for the future studies of these systems.
The sources I treated in this thesis are the dipping sources 4U 1323-619, 4U1254-690, XB 1916-053 and the eclipsing source MXB 1659-298.

The study of the timing properties of the dipping source 4U 1323-619 allowed to extend the orbital ephemeris of this source to the whole temporal span covered by the X-ray archival data, that is of 26 years. Taking the advantage of the periodical dips, we extrapolated an orbital period of the source of P=10590.896(2) s compatible with the estimations that are present in the literature, but with an accuracy ten times higher. We also obtained a constraint on the orbital period derivative for the first time, obtaining that $\dot{P}$= (8 ± 13)× 10^{-12} s s^{-1}. The use of the 3D extinction map of the K_s radiation in the Galaxy of Marshall et al. (2006) allowed to rescale the existing estimations of the distance to the source to the value of 4.2 $^{+0.8}_{-0.7}$ kpc. The comparison between the theory of secular evolution and the observations allowed to understand that the companion star is in main sequence and has a mass of 0.28±0.03 $M_\odot$ and that the mass transfer onto the NS surface is conservative.

A similar scenario has been found for the dipping source 4U 1254-690. The study of the distribution of the dip arrival times with respect to the existing orbital ephemeris, allowed to better constrain the orbital period of the source to P=14160.004(6) s, with an accuracy improved of one order of magnitude with respect to the previous estimations. Furthermore, the analysis

provided an estimation of the orbital period derivative of $|\dot{P}| < 1.4 \times 10^{-10}$ s s^{-1}. This value, even though represents a weak constrain to the real orbital period derivative, is the first estimation of the orbital period derivative for this source in literature and could be further constrained by future observations.
We estimated a mass for the companion star of M_2=(0.42 $\pm$ 0.04) $M_\odot$ on the basis of a comparison between the observational data and the predictions of the theory of secular evolution and we inferred that the companion star is in main sequence. We rescaled the distance to the source to 7.6$\pm$ 0.8 kpc and inferred that the magnetic braking has a fundamental role in the balance of the angular momentum losses from the system. These results allowed us to predict a conservative mass transfer onto the neutron star surface.

The timing properties of the dipping source XB 1916-053 have been analysed on the basis of 37 years of data. We observed that the distribution of the delays of the dip arrival times obtained adopting the ephemeris for the source in literature is equally fitted by two functional forms. In both the cases, however, a modulation of the distribution has been observed. For the first possible scenario we infer an orbital period of the system of P=3000.6512(6) s. This scenario considers a conservative mass transfer in which the modulation of the delays is explained invoking the presence of a third body orbiting around the system. In this case, we evaluated that the third body should have a mass between 0.10 $M_\odot$ and 0.14 $M_\odot$, an orbital period of about 51 years and an orbit with an eccentricity of $e = 0.28 \pm 0.15$.
For the alternative scenario, on the other hand, we evaluate an orbital period of P=3000.65126(10) s and an orbital period derivative of $\dot{P}$= 1.44(7)$\times$ 10^{-11} s s^{-1}. The scenario is consistent with a highly non conservative mass transfer, where more than the 92% of the mass of the companion star of M_2=0.028 $M_\odot$ is lost from the system during the accretion. In this case, we explained the modulation of the delays invoking the presence of a third body having a mass of 0.055 $M_\odot$ and an orbital period of about 26 years.

On the other hand, the spectral study performed on the source suggests that the continuum contribution to the persistent spectrum can be modelled invoking a thermal comptonization component that scatters photons that are emitted by the neutron star surface, plus a multi-disk blackbody component that models the emission of the accretion disk. The analysis suggests that the XB 1916-053 was in a soft spectral state in all the observations we analysed with a unabsorbed flux of 5.14$\times$ 10^{-10} erg cm^{-2} s^{-1} between 0.1 and 100 keV. We find that the accretion disk extends up to 40^{+17}_{-14} km from the neutron star and has a temperature of kT_{in}=0.51$\pm$0.05 keV. Furthermore, we find the corona with a temperature of kT_e=$6.5^{+3}_{-1.4}$ keV, a photon index Γ=$1.98^{+0.09}_{-0.08}$ and an optical depth of τ=6. We detect the Kα absorption lines of Fe XXV and Fe XXVI with a level of confidence of 8σ and 16σ respectively, and the Kβ absorption lines of the same ions with a level of confidence of 3σ and of 4σ, respectively. Moreover, the analysis returned the detection of the K absorption edge of O VIII.

Finally, we find that the dip spectrum can be described as a gradual covering of the persistent spectrum by a cold and partially ionized bulk of matter. For this warm absorber we find a ionization parameter $log(\xi) = 2.89^{+0.05}_{-0.07}$ and an equivalent column density N_H that slightly variates in the analysed observations between $(103^{+25}_{-39}) \times 10^{22}$ cm^{-2} and $(62 \pm 4) \times 10^{22}$ cm^{-2}. This change in the column density is combined with a variation of the covering fraction from $0.66^{+0.09}_{-0.16}$ to $0.88^{+0.06}_{-0.04}$ in the same observations, suggesting that the warm absorber has a morphology and a density that continually change in time scales of the order of some orbital periods.

The timing analysis performed on the eclipsing source MXB 1659-298 when the source was in outburst, allowed to constrain the ephemeris of the source with a baseline of data that span 40 years. We infer an orbital period of P=25617.9956(11) s. In the hypothesis that the companion star is in thermal equilibrium and fills its Roche Lobe, we estimate that the companion star mass is M_2=0.9± 0.3 $M_\odot$. From the average duration of the eclipses we found that the size of the corona surrounding the neutron star is R_c= (3.6 ± 0.3)× 10^8 cm and that the inclination angle of the binary system is 72±3 degree. We infer an orbital period derivative of $\dot{P} = (-8.5 \pm 1.2) \times 10^{-12}$ s s^{-1}. We are able to explain the value of $\dot{P}$ assuming a highly non conservative mass transfer scenario in which only 1% of this mass is observed to accrete onto the neutron star. We also suggest that the ejected matter produces a local absorber with an equivalent hydrogen column density of $(8 \pm 4) \times 10^{21}$ cm^{-2}. The sinusoidal modulation has a period of 2.31 ± 0.02 yr and can be explained either with the presence of a gravitational quadrupole coupling of the orbit to a variable deformation of the magnetically active companion star or with the presence of a third body orbiting around the binary system. In the second scenario we find that the mass of the third body is equal to 22 ± 3 M_J in the case we consider an orbit for the third body that is co-planar to the orbital plane of the binary system, or larger than 21 M_J otherwise.
If confirmed by future observations, this should be the first evidence of a super-Jovian planet orbiting around a LMXB system.

Finally, I presented the preliminary results obtained from a phase-resolved spectral analysis performed on a sample of gamma-ray pulsars observed with the Fermi space mission. This work has been performed during a research period in Barcelona (Spain) at the Institut de Ciencies de l'Espai (ICE). The analysis, at the moment, seems to reveal a weak detection of a hard spectral component that extends beyond the cut-off energy of the sources PSR J0633+1746 and PSR J1836+5925. This spectral component could be associated to the presence of a pulsar wind nebulae emitting in the gamma-rays close to these systems. Currently, I am investigating on the reliability of this detection performing some checks on the results in collaboration with the High Energy Astrophysics group of the ICE of Barcelona.

In conclusion, the orbital timing techniques we used allowed us to obtain estimations of

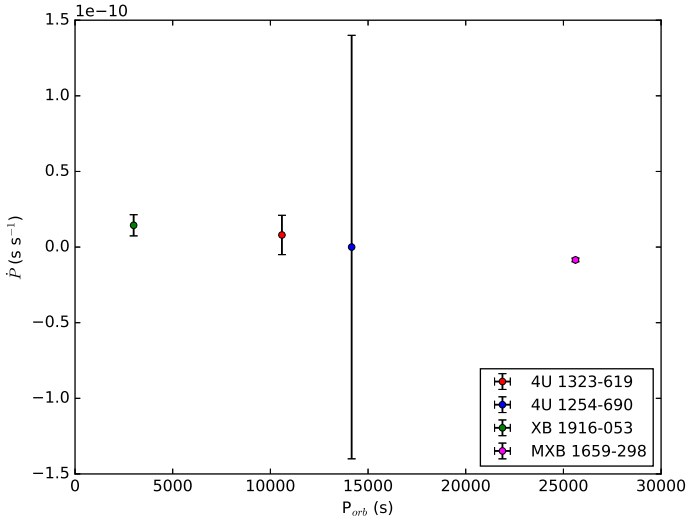

Figure 10.1: Orbital period derivative as a function of the orbital period for each of the analysed sources in this thesis.

the orbital periods of the systems we studied with high accuracy. Taking the advantage of the periodic dips or eclipses shown in the light curves of the sources, we improved the accuracy of the available ephemerides in literature also of one order of magnitude, measuring in some cases the orbital period derivatives of the systems for the first time.

On the basis of the only results obtained from the analysis of the LMXB systems we took into account in this thesis, we conclude that it is not possible to find out a clear correlation between the orbital periods and the corresponding time derivative for these systems, as it is possible to notice looking at Figure 10.1. Indeed, even if the data used in our work span temporal baselines that include all the available X-ray data in the archives for each source, the estimations of the orbital period derivatives actually represent upper limits that can be further constrained with the additional observations provided by the current or future space missions.

On the basis of the available data, we evaluated a plausible evolutive scenario for each examined source according to the theory of secular evolution for the binary systems. We observed that for a part of LMXB systems the analysis suggests a conservative mass transfer, while for a sample of sources the evolutive scenario could be equally described both with a conservative or with a non conservative mass transfer in which also more than the 90% of the mass left from the companion star is lost from the system.

Furthermore, we observed that the timing solutions for some systems show sinusoidal components that fit the modulations in the distribution of the delays of the dip arrival times evaluated with respect to the available ephemeris in literature. These modulations have been interpreted as marks of the presence of third bodies around LMXB systems. The mass of these bodies can vary from few tens of Jovian masses up to some tenths of solar masses. If confirmed by other

future observations, the detection of super Jovian planets orbiting around LMXB systems should be a new scientific topic that could link different branches of astrophysics between each other.

APPENDIX A

LOGARITHMIC DERIVATIVE

If $u(t)$ is a function of the variable t, then the logarithmic differentiation rule is:

$$\frac{d}{dt}\,u(t) = \frac{1}{u}\,\frac{d}{dt}\,u = \frac{\dot{u}}{u}$$

If $u(t) = a^{\alpha}\, b^{\beta}\, c^{\gamma}$, then the logarithm of this quantity can be written as:

$$log(u(t)) = log(a^{\alpha}\, b^{\beta}\, c^{\gamma}) = \alpha\, log(a) + \beta\, log(b) + \gamma\, log(c)$$

Then, differentiating the function $log(u(t))$ we obtain:

$$\frac{d}{dt} log(u(t)) = \frac{d}{dt}\left(\alpha\, log(a) + \beta\, log(b) + \gamma\, log(c)\right)$$

from which evaluate the general rule:

$$\frac{\dot{u}}{u} = \alpha\,\frac{\dot{a}}{a} + \beta\,\frac{\dot{b}}{b} + \gamma\,\frac{\dot{c}}{c}$$

BIBLIOGRAPHY

Abbassi, S., Ghanbari, J., and Najjar, S. (2008). The effects of thermal conduction on the ADAF with a toroidal magnetic field. *MNRAS*, 388:663–668. 33

Abbott, B. P., Abbott, R., Abbott, T. D., Acernese, F., Ackley, K., Adams, C., Adams, T., Addesso, P., Adhikari, R. X., Adya, V. B., and et al. (2017a). Gravitational Waves and Gamma-Rays from a Binary Neutron Star Merger: GW170817 and GRB 170817A. *ApJ*, 848:L13. 7

Abbott, B. P., Abbott, R., Abbott, T. D., Acernese, F., Ackley, K., Adams, C., Adams, T., Addesso, P., Adhikari, R. X., Adya, V. B., and et al. (2017b). Multi-messenger Observations of a Binary Neutron Star Merger. *ApJ*, 848:L12. 7

Abramowicz, M. A., Chen, X., Kato, S., Lasota, J.-P., and Regev, O. (1995). Thermal equilibria of accretion disks. *ApJ*, 438:L37–L39. 33

Abramowicz, M. A., Igumenshchev, I. V., and Lasota, J.-P. (1998). A note on the conditions for SSD-ADAF transitions. *MNRAS*, 293:443. 33

Acero, F., Ackermann, M., Ajello, M., Albert, A., Baldini, L., Ballet, J., Barbiellini, G., Bastieri, D., Bellazzini, R., Bissaldi, E., Bloom, E. D., Bonino, R., Bottacini, E., Brandt, T. J., Bregeon, J., Bruel, P., Buehler, R., Buson, S., Caliandro, G. A., Cameron, R. A., Caragiulo, M., Caraveo, P. A., Casandjian, J. M., Cavazzuti, E., Cecchi, C., Charles, E., Chekhtman, A., Chiang, J., Chiaro, G., Ciprini, S., Claus, R., Cohen-Tanugi, J., Conrad, J., Cuoco, A., Cutini, S., D'Ammando, F., de Angelis, A., de Palma, F., Desiante, R., Digel, S. W., Di Venere, L., Drell, P. S., Favuzzi, C., Fegan, S. J., Ferrara, E. C., Focke, W. B., Franckowiak, A., Funk, S., Fusco, P., Gargano, F., Gasparrini, D., Giglietto, N., Giordano, F., Giroletti, M., Glanzman, T., Godfrey, G., Grenier, I. A., Guiriec, S., Hadasch, D., Harding, A. K., Hayashi, K., Hays, E., Hewitt, J. W., Hill, A. B., Horan, D., Hou, X., Jogler, T., Jóhannesson, G., Kamae, T., Kuss, M., Landriu, D., Larsson, S., Latronico, L., Li, J., Li, L., Longo, F., Loparco, F., Lovellette, M. N., Lubrano, P., Maldera, S., Malyshev, D., Manfreda, A., Martin, P., Mayer, M., Mazziotta, M. N., McEnery, J. E., Michelson, P. F., Mirabal, N., Mizuno, T., Monzani, M. E., Morselli, A., Nuss, E., Ohsugi, T., Omodei, N., Orienti, M., Orlando, E., Ormes, J. F., Paneque, D., Pesce-Rollins, M., Piron, F., Pivato, G., Rainò, S., Rando, R., Razzano, M., Razzaque, S., Reimer, A., Reimer, O., Remy, Q., Renault, N., Sánchez-Conde, M., Schaal, M., Schulz, A.,

Sgrò, C., Siskind, E. J., Spada, F., Spandre, G., Spinelli, P., Strong, A. W., Suson, D. J., Tajima, H., Takahashi, H., Thayer, J. B., Thompson, D. J., Tibaldo, L., Tinivella, M., Torres, D. F., Tosti, G., Troja, E., Vianello, G., Werner, M., Wood, K. S., Wood, M., Zaharijas, G., and Zimmer, S. (2016). Development of the Model of Galactic Interstellar Emission for Standard Point-source Analysis of Fermi Large Area Telescope Data. *ApJS*, 223:26. 151

Applegate, J. H. (1992). A mechanism for orbital period modulation in close binaries. *ApJ*, 385:621–629. 146

Applegate, J. H. and Shaham, J. (1994). Orbital period variability in the eclipsing pulsar binary PSR B1957+20: Evidence for a tidally powered star. *ApJ*, 436:312–318. 146

Arnaud, K. A. (1996). XSPEC: The First Ten Years. In Jacoby, G. H. and Barnes, J., editors, *Astronomical Data Analysis Software and Systems V*, volume 101 of *Astronomical Society of the Pacific Conference Series*, page 17. 59

Asplund, M., Grevesse, N., Sauval, A. J., and Scott, P. (2009). The Chemical Composition of the Sun. *ARA&A*, 47:481–522. 59

Atwood, W. B., Abdo, A. A., Ackermann, M., Althouse, W., Anderson, B., Axelsson, M., Baldini, L., Ballet, J., Band, D. L., Barbiellini, G., and et al. (2009). The Large Area Telescope on the Fermi Gamma-Ray Space Telescope Mission. *ApJ*, 697:1071–1102. 150

Bahramian, A., Heinke, C. O., Wijnands, R., and Degenaar, N. (2016). Continuing outburst from H 1658-298. *The Astronomer's Telegram*, 8699. 130

Bailes, M., Bates, S. D., Bhalerao, V., Bhat, N. D. R., Burgay, M., Burke-Spolaor, S., D'Amico, N., Johnston, S., Keith, M. J., Kramer, M., Kulkarni, S. R., Levin, L., Lyne, A. G., Milia, S., Possenti, A., Spitler, L., Stappers, B., and van Straten, W. (2011). Transformation of a Star into a Planet in a Millisecond Pulsar Binary. *Science*, 333:1717. 104

Balbus, S. A. and Hawley, J. F. (1998). Instability, turbulence, and enhanced transport in accretion disks. *Reviews of Modern Physics*, 70:1–53. 33

Bałucińska-Church, M., Church, M. J., Oosterbroek, T., Segreto, A., Morley, R., and Parmar, A. N. (1999). An X-ray study of the dipping low mass X-ray binary XV 1323-619. *A&A*, 349:495–504. 50, 51, 62, 64

Bałucińska-Church, M., Dotani, T., Hirotsu, T., and Church, M. J. (2009). Neutral absorber dips in the periodic burster LMXB XB 1323-619 from Suzaku. *A&A*, 500:873–882. 50, 51, 62, 64, 65

Barret, D., Grindlay, J. E., Strickman, M., and Vedrenne, G. (1996). CGRO/OSSE observations of the X-ray burster 4U 1915-05 (XB 1916-053). *A&AS*, 120:269–273. 84

Becker, R. H., Smith, B. W., Swank, J. H., Boldt, E. A., Holt, S. S., Serlemitsos, P. J., and Pravdo, S. H. (1977). Spectral characteristics of 3U 1915-05, a burst source candidate. *ApJ*, 216:L101–L104. 84, 108

Benvenuto, O. G., De Vito, M. A., and Horvath, J. E. (2012). Evolutionary Trajectories of Ultracompact "Black Widow" Pulsars with Very Low Mass Companions. *ApJ*, 753:L33. 103, 104, 106

Bhattacharyya, S. (2007). Timing properties of XB 1254-690. *MNRAS*, 377:198–202. 68

Bildsten, L. (2000). Theory and observations of Type I X-Ray bursts from neutron stars. In Holt, S. S. and Zhang, W. W., editors, *American Institute of Physics Conference Series*, volume 522 of *American Institute of Physics Conference Series*, pages 359–369. 104

Boirin, L., Méndez, M., Díaz Trigo, M., Parmar, A. N., and Kaastra, J. S. (2005). A highly-ionized absorber in the X-ray binary 4U 1323-62: A new explanation for the dipping phenomenon. *A&A*, 436:195–208. 50, 51, 109

Boirin, L. and Parmar, A. N. (2003). Discovery of narrow X-ray absorption features from the low-mass X-ray binary X 1254-690 with XMM-Newton. *A&A*, 407:1079–1084. 69

Boirin, L., Parmar, A. N., Barret, D., Paltani, S., and Grindlay, J. E. (2004). Discovery of X-ray absorption features from the dipping low-mass X-ray binary XB 1916-053 with XMM-Newton. *A&A*, 418:1061–1072. 91, 109, 116, 125, 126

Bozzo, E., Falanga, M., Papitto, A., Stella, L., Perna, R., Lazzati, D., Israel, G., Campana, S., Mangano, V., Di Salvo, T., and Burderi, L. (2007). X-ray eclipse time delays in <ASTROBJ>4U 2129+47</ASTROBJ>. *A&A*, 476:301–306. 146

Bradt, H. (2014). *Astrophysics Processes*. 14

Bradt, H. V. D. and McClintock, J. E. (1983). The optical counterparts of compact galactic X-ray sources. *ARA&A*, 21:13–66. 7

Burderi, L., Di Salvo, T., Riggio, A., Papitto, A., Iaria, R., D'Aì, A., and Menna, M. T. (2010). New ephemeris of the ADC source 2A 1822-371: a stable orbital-period derivative over 30 years. *A&A*, 515:A44. 20, 61, 65, 78, 79, 81, 104, 141, 142

Burderi, L., Di Salvo, T., Robba, N. R., Del Sordo, S., Santangelo, A., and Segreto, A. (1998). Temporal Analysis of EXO 0531-66 in Outburst. *ApJ*, 498:831–836. 6

Burderi, L., Di Salvo, T., Robba, N. R., La Barbera, A., and Guainazzi, M. (2000). The 0.1-100 KEV Spectrum of Centaurus X-3: Pulse Phase Spectroscopy of the Cyclotron Line and Magnetic Field Structure. *ApJ*, 530:429–440. 6

Burderi, L., Possenti, A., D'Antona, F., Di Salvo, T., Burgay, M., Stella, L., Menna, M. T., Iaria, R., Campana, S., and d'Amico, N. (2001). Where May Ultrafast Rotating Neutron Stars Be Hidden? *ApJ*, 560:L71–L74. 105, 143

Burderi, L., Riggio, A., Di Salvo, T., Papitto, A., Menna, M. T., D'Aì, A., and Iaria, R. (2009). Timing of the 2008 outburst of SAX J1808.4-3658 with XMM-Newton: a stable orbital-period derivative over ten years. *A&A*, 496:L17–L20. 142, 143

Burrows, D. N., Hill, J. E., Nousek, J. A., Kennea, J. A., Wells, A., Osborne, J. P., Abbey, A. F., Beardmore, A., Mukerjee, K., Short, A. D. T., Chincarini, G., Campana, S., Citterio, O., Moretti, A., Pagani, C., Tagliaferri, G., Giommi, P., Capalbi, M., Tamburelli, F., Angelini, L., Cusumano, G., Bräuninger, H. W., Burkert, W., and Hartner, G. D. (2005). The Swift X-Ray Telescope. *Space Sci. Rev.*, 120:165–195. 133

Cackett, E. M., Brown, E. F., Cumming, A., Degenaar, N., Fridriksson, J. K., Homan, J., Miller, J. M., and Wijnands, R. (2013). A Change in the Quiescent X-Ray Spectrum of the Neutron Star Low-mass X-Ray Binary MXB 1659-29. *ApJ*, 774:131. 132, 143, 144

Cackett, E. M., Miller, J. M., Bhattacharyya, S., Grindlay, J. E., Homan, J., van der Klis, M., Miller, M. C., Strohmayer, T. E., and Wijnands, R. (2008a). Relativistic Iron Emission Lines in Neutron Star Low-Mass X-Ray Binaries as Probes of Neutron Star Radii. *ApJ*, 674:415–420. 43

Cackett, E. M., Wijnands, R., Miller, J. M., Brown, E. F., and Degenaar, N. (2008b). Cooling of the Crust in the Neutron Star Low-Mass X-Ray Binary MXB 1659-29. *ApJ*, 687:L87. 132, 143, 144

Callanan, P. J., Grindlay, J. E., and Cool, A. M. (1995). Optical Observations of 4U 1915-05, and the Stability of the Long Term Ephemeris. *PASJ*, 47:153–162. 85

Chou, Y. (2014). Measuring the orbital periods of low mass X-ray binaries in the X-ray band. *Research in Astronomy and Astrophysics*, 14:1367–1382. 130

Chou, Y., Grindlay, J. E., and Bloser, P. F. (2001). Timing Analysis of the Light Curve of the Dipping-Bursting X-Ray Binary X1916-053. *ApJ*, 549:1135–1144. 85, 101

Church, M. J., Dotani, T., BałuciŃska-Church, M., Mitsuda, K., Takahashi, T., Inoue, H., and Yoshida, K. (1997). Simple Photoelectric Absorption during Dipping in the ASCA Observation of XB 1916-053. *ApJ*, 491:388–394. 84, 108

Church, M. J., Parmar, A. N., Balucinska-Church, M., Oosterbroek, T., dal Fiume, D., and Orlandini, M. (1998). Progressive covering in dipping and Comptonization in the spectrum of XB 1916-053 from the BeppoSAX observation. *A&A*, 338:556–562. 100

Claret, A. and Gimenez, A. (1990). The moment of inertia of low mass stars. *Ap&SS*, 169:215–217. 79, 142

Cominsky, L., Ossmann, W., and Lewin, W. H. G. (1983). Irregular X-ray variability in the transient X-ray burst source MXB 1659-29. *ApJ*, 270:226–232. 130

Cominsky, L. R. and Wood, K. S. (1984). Discovery of a 7.1 hour period and eclipses from MXB 1659-29. *ApJ*, 283:765–773. 130, 131

Cominsky, L. R. and Wood, K. S. (1989). Further observations of the eclipsing X-ray burst source MXB 1659-29. *ApJ*, 337:485–493. 130, 131, 135, 136, 139

Cornelisse, R., Kotze, M. M., Casares, J., Charles, P. A., and Hakala, P. J. (2013). The origin of the tilted disc in the low-mass X-ray binary GR Mus (XB 1254-690). *MNRAS*, 436:910–920. 69, 79, 80, 82

Cottam, J., Kahn, S. M., Brinkman, A. C., den Herder, J. W., and Erd, C. (2001). High-resolution spectroscopy of the low-mass X-ray binary <ASTROBJ>EXO 0748-67</ASTROBJ>. *A&A*, 365:L277–L281. 126

Courvoisier, T. J.-L., Parmar, A. N., Peacock, A., and Pakull, M. (1986). The discovery of 39 hour periodic dips in the X-ray intensity of XB 1254 - 690. *ApJ*, 309:265–274. 68, 69

Courvoisier, T. J.-L., Walter, R., Beckmann, V., Dean, A. J., Dubath, P., Hudec, R., Kretschmar, P., Mereghetti, S., Montmerle, T., Mowlavi, N., Paltani, S., Preite Martinez, A., Produit, N., Staubert, R., Strong, A. W., Swings, J.-P., Westergaard, N. J., White, N., Winkler, C., and Zdziarski, A. A. (2003). The INTEGRAL Science Data Centre (ISDC). *A&A*, 411:L53–L57. 59, 92

D'Aì, A., Iaria, R., Di Salvo, T., Matt, G., and Robba, N. R. (2009). Disk Reflection Signatures in the Spectrum of the Bright Z-Source GX 340+0. *ApJ*, 693:L1–L5. 43

Di Salvo, T., Burderi, L., Riggio, A., Papitto, A., and Menna, M. T. (2008). Orbital evolution of an accreting millisecond pulsar: witnessing the banquet of a hidden black widow? *MNRAS*, 389:1851–1857. 78, 105, 142, 143

Di Salvo, T., D'Aí, A., Iaria, R., Burderi, L., Dovčiak, M., Karas, V., Matt, G., Papitto, A., Piraino, S., Riggio, A., Robba, N. R., and Santangelo, A. (2009). A relativistically smeared spectrum in the neutron star X-ray binary 4U 1705-44: looking at the inner accretion disc with X-ray spectroscopy. *MNRAS*, 398:2022–2027. 43, 115

Di Salvo, T., Iaria, R., Matranga, M., Burderi, L., D'Aí, A., Egron, E., Papitto, A., Riggio, A., Robba, N. R., and Ueda, Y. (2015). Suzaku broad-band spectrum of 4U 1705-44: probing the reflection component in the hard state. *MNRAS*, 449:2794–2802. 122

Di Salvo, T., Iaria, R., Méndez, M., Burderi, L., Lavagetto, G., Robba, N. R., Stella, L., and van der Klis, M. (2005). A Broad Iron Line in the Chandra High Energy Transmission Grating Spectrum of 4U 1705-44. *ApJ*, 623:L121–L124. 43

Díaz Trigo, M. and Boirin, L. (2016). Accretion disc atmospheres and winds in low-mass X-ray binaries. *Astronomische Nachrichten*, 337:368. 141

Díaz Trigo, M., Parmar, A. N., Boirin, L., Méndez, M., and Kaastra, J. S. (2006). Spectral changes during dipping in low-mass X-ray binaries due to highly-ionized absorbers. *A&A*, 445:179–195. 132

Díaz Trigo, M., Parmar, A. N., Boirin, L., Motch, C., Talavera, A., and Balman, S. (2009). Variations in the dip properties of the low-mass X-ray binary XB 1254-690 observed with XMM-Newton and INTEGRAL. *A&A*, 493:145–157. 68, 69, 77

Dickey, J. M. and Lockman, F. J. (1990). H I in the Galaxy. *ARA&A*, 28:215–261. 143, 144

Done, C., Gierliński, M., and Kubota, A. (2007). Modelling the behaviour of accretion flows in X-ray binaries. Everything you always wanted to know about accretion but were afraid to ask. *A&A Rev.*, 15:1–66. 46

Esin, A. A., Narayan, R., Ostriker, E., and Yi, I. (1996). Hot One-Temperature Accretion Flows around Black Holes. *ApJ*, 465:312. 33

Fabian, A. C., Iwasawa, K., Reynolds, C. S., and Young, A. J. (2000). Broad Iron Lines in Active Galactic Nuclei. *PASP*, 112:1145–1161. 44

Fabian, A. C., Pringle, J. E., and Rees, M. J. (1975). Tidal capture formation of binary systems and X-ray sources in globular clusters. *MNRAS*, 172:15p–18p. 10

Fabian, A. C., Rees, M. J., Stella, L., and White, N. E. (1989). X-ray fluorescence from the inner disc in Cygnus X-1. *MNRAS*, 238:729–736. 42, 44

Feynman, R. P. (1965). *Feynman lectures on physics. Volume 3: Quantum mechancis*. 31

Filippenko, A. V., Leonard, D. C., Matheson, T., Li, W., Moran, E. C., and Riess, A. G. (1999). A Black Hole in the X-Ray Nova Velorum 1993. *PASP*, 111:969–979. 132

Forman, W., Jones, C., Cominsky, L., Julien, P., Murray, S., Peters, G., Tananbaum, H., and Giacconi, R. (1978). The fourth Uhuru catalog of X-ray sources. *ApJS*, 38:357–412. 50

Frank, J., King, A., and Raine, D. (1992). *Accretion power in astrophysics*. 7, 9, 31, 32

Frank, J., King, A., and Raine, D. J. (2002). *Accretion Power in Astrophysics: Third Edition*. 144, 145

Frank, J., King, A. R., and Lasota, J.-P. (1987). The light curves of low-mass X-ray binaries. *A&A*, 178:137–142. 9, 10, 50, 68, 109, 122

Galeev, A. A., Rosner, R., and Vaiana, G. S. (1979). Structured coronae of accretion disks. *ApJ*, 229:318–326. 33

Galloway, D. K., Chakrabarty, D., Muno, M. P., and Savov, P. (2001). Discovery of a 270 Hertz X-Ray Burst Oscillation in the X-Ray Dipper 4U 1916-053. *ApJ*, 549:L85–L88. 86, 104

Galloway, D. K., Muno, M. P., Hartman, J. M., Psaltis, D., and Chakrabarty, D. (2008). Thermonuclear (Type I) X-Ray Bursts Observed by the Rossi X-Ray Timing Explorer. *ApJS*, 179:360–422. 51, 62, 69, 77, 79, 82, 100, 101, 108, 132, 140

Gambino, A. F., Iaria, R., Di Salvo, T., Del Santo, M., Burderi, L., Matranga, M., Pintore, F., Riggio, A., and Sanna, A. (2016). New orbital ephemerides for the dipping source 4U 1323-619: constraining the distance to the source. *A&A*, 589:A34. 71, 72

Gehrels, N., Chincarini, G., Giommi, P., Mason, K. O., Nousek, J. A., Wells, A. A., White, N. E., Barthelmy, S. D., Burrows, D. N., Cominsky, L. R., Hurley, K. C., Marshall, F. E., Mészáros, P., Roming, P. W. A., Angelini, L., Barbier, L. M., Belloni, T., Campana, S., Caraveo, P. A., Chester, M. M., Citterio, O., Cline, T. L., Cropper, M. S., Cummings, J. R., Dean, A. J., Feigelson, E. D., Fenimore, E. E., Frail, D. A., Fruchter, A. S., Garmire, G. P., Gendreau, K., Ghisellini, G., Greiner, J., Hill, J. E., Hunsberger, S. D., Krimm, H. A., Kulkarni, S. R., Kumar, P., Lebrun, F., Lloyd-Ronning, N. M., Markwardt, C. B., Mattson, B. J., Mushotzky, R. F., Norris, J. P., Osborne, J., Paczynski, B., Palmer, D. M., Park, H.-S., Parsons, A. M., Paul, J., Rees, M. J., Reynolds, C. S., Rhoads, J. E., Sasseen, T. P., Schaefer, B. E., Short, A. T., Smale, A. P., Smith, I. A., Stella, L., Tagliaferri, G., Takahashi, T., Tashiro, M., Townsley, L. K., Tueller, J., Turner, M. J. L., Vietri, M., Voges, W., Ward, M. J., Willingale, R., Zerbi, F. M., and Zhang, W. W. (2004). The Swift Gamma-Ray Burst Mission. *ApJ*, 611:1005–1020. 133

Ghisellini, G., editor (2013). *Radiative Processes in High Energy Astrophysics*, volume 873 of *Lecture Notes in Physics, Berlin Springer Verlag*. 40

Ghosh, P. and Lamb, F. K. (1979). Accretion by rotating magnetic neutron stars. III - Accretion torques and period changes in pulsating X-ray sources. *ApJ*, 234:296–316. 6

Gierliński, M. and Done, C. (2002). A comment on the colour-colour diagrams of low-mass X-ray binaries. *MNRAS*, 331:L47–L50. 47

Gilfanov, M. (2010). X-Ray Emission from Black-Hole Binaries. In Belloni, T., editor, *Lecture Notes in Physics, Berlin Springer Verlag*, volume 794 of *Lecture Notes in Physics, Berlin Springer Verlag*, page 17. 30

Golub, L. and Pasachoff, J. M. (2009). *The Solar Corona*. 33

Griffiths, R. E., Gursky, H., Schwartz, D. A., Schwarz, J., Bradt, H., Doxsey, R. E., Charles, P. A., and Thorstensen, J. R. (1978). Positions and identifications for galactic X-ray sources 2A1822-371 and 2S1254-690. *Nature*, 276:247–249. 68

Grindlay, J. E. (1989). Studies of the possible X ray triple 4U1915-05. In Hunt, J. and Battrick, B., editors, *Two Topics in X-Ray Astronomy, Volume 1: X Ray Binaries. Volume 2: AGN and the X Ray Background*, volume 296 of *ESA Special Publication*. 84, 99

Grindlay, J. E. (1992). The Bursting, Dipping, Precessing Ultra-Compact X-Ray Binary X1916-05. In Tanaka, Y. and Koyama, K., editors, *Frontiers Science Series*, page 69. 85

Grindlay, J. E., Bailyn, C. D., Cohn, H., Lugger, P. M., Thorstensen, J. R., and Wegner, G. (1988). Discovery of a possible X-ray triple - 4U 1915-05. *ApJ*, 334:L25–L29. 85, 108

Grindlay, J. E., Cohn, H., and Schmidtke, P. (1987). Optical Counterpart of 4U 1915-05. *IAU Circ.*, 4393. 84

Güver, T. and Özel, F. (2009). The relation between optical extinction and hydrogen column density in the Galaxy. *MNRAS*, 400:2050–2053. 64

Hanke, M. (2011). *Probing the Environment of Accreting Compact Objects*. PhD thesis. 32

Harrison, F. A., Craig, W. W., Christensen, F. E., Hailey, C. J., Zhang, W. W., Boggs, S. E., Stern, D., Cook, W. R., Forster, K., Giommi, P., Grefenstette, B. W., Kim, Y., Kitaguchi, T., Koglin, J. E., Madsen, K. K., Mao, P. H., Miyasaka, H., Mori, K., Perri, M., Pivovaroff, M. J., Puccetti, S., Rana, V. R., Westergaard, N. J., Willis, J., Zoglauer, A., An, H., Bachetti, M., Barrière, N. M., Bellm, E. C., Bhalerao, V., Brejnholt, N. F., Fuerst, F., Liebe, C. C., Markwardt, C. B., Nynka, M., Vogel, J. K., Walton, D. J., Wik, D. R., Alexander, D. M., Cominsky, L. R., Hornschemeier, A. E., Hornstrup, A., Kaspi, V. M., Madejski, G. M., Matt, G., Molendi, S., Smith, D. M., Tomsick, J. A., Ajello, M., Ballantyne, D. R., Baloković, M., Barret, D., Bauer, F. E., Blandford, R. D., Brandt, W. N., Brenneman, L. W., Chiang, J., Chakrabarty, D., Chenevez, J., Comastri, A., Dufour, F., Elvis, M., Fabian, A. C., Farrah, D., Fryer, C. L., Gotthelf, E. V., Grindlay, J. E., Helfand, D. J., Krivonos, R., Meier, D. L., Miller, J. M., Natalucci, L., Ogle, P., Ofek, E. O., Ptak, A., Reynolds, S. P., Rigby, J. R., Tagliaferri, G., Thorsett, S. E., Treister, E., and Urry, C. M. (2013). The Nuclear Spectroscopic Telescope Array (NuSTAR) High-energy X-Ray Mission. *ApJ*, 770:103. 133

Hasinger, G. and van der Klis, M. (1989). Two patterns of correlated X-ray timing and spectral behaviour in low-mass X-ray binaries. *A&A*, 225:79–96. 46

Heitler, W. (1954). *Quantum theory of radiation*. 41

Hewish, A., Bell, S. J., Pilkington, J. D. H., Scott, P. F., and Collins, R. A. (1968). Observation of a Rapidly Pulsating Radio Source. *Nature*, 217:709–713. 7

Hobbs, G., Edwards, R., and Manchester, R. (2006). TEMPO2: a New Pulsar Timing Package. *Chinese Journal of Astronomy and Astrophysics Supplement*, 6(2):189–192. 150

Hu, C.-P., Chou, Y., and Chung, Y.-Y. (2008). A Parameterization Study of the Properties of the X-Ray Dips in the Low-Mass X-Ray Binary X1916-053. *ApJ*, 680:1405–1411. 71, 72, 74, 86, 88, 92, 94, 97, 98, 101

Iaria, R., D'Aí, A., Di Salvo, T., Robba, N. R., Riggio, A., Papitto, A., and Burderi, L. (2009). A ionized reflecting skin above the accretion disk of GX 349+2. *A&A*, 505:1143–1151. 43

Iaria, R., Di Salvo, T., Burderi, L., D'Aí, A., Papitto, A., Riggio, A., and Robba, N. R. (2011). Detailed study of the X-ray and optical/UV orbital ephemeris of X1822-371. *A&A*, 534:A85. 130

Iaria, R., Di Salvo, T., Burderi, L., Riggio, A., D'Aì, A., and Robba, N. R. (2014). Discovery of periodic dips in the light curve of GX 13+1: the X-ray orbital ephemeris of the source. *A&A*, 561:A99. 57

Iaria, R., Di Salvo, T., Burderi, L., and Robba, N. R. (2001). A Hard Tail in the Broadband Spectrum of the Dipper XB 1254-690. *ApJ*, 548:883–888. 77, 79, 81

Iaria, R., Di Salvo, T., D'Aì, A., Burderi, L., Mineo, T., Riggio, A., Papitto, A., and Robba, N. R. (2013). X-ray spectroscopy of the ADC source X1822-371 with Chandra and XMM-Newton. *A&A*, 549:A33. 104, 130, 144

Iaria, R., Di Salvo, T., Del Santo, M., Pintore, F., Sanna, A., Papitto, A., Burderi, L., Riggio, A., Gambino, A. F., and Matranga, M. (2016). Study of the reflection spectrum of the LMXB 4U 1702-429. *A&A*, 596:A21. 126

Iaria, R., Di Salvo, T., Gambino, A. F., Del Santo, M., Romano, P., Matranga, M., Galiano, C. G., Scarano, F., Riggio, A., Sanna, A., Pintore, F., and Burderi, L. (2015a). Signature of the presence of a third body orbiting around XB 1916-053. *A&A*, 582:A32. 56, 72, 108, 130

Iaria, R., Di Salvo, T., Lavagetto, G., D'Aí, A., and Robba, N. R. (2007). Chandra observation of the dipping source XB 1254-690. *A&A*, 464:291–297. 68, 69, 70

Iaria, R., Di Salvo, T., Lavagetto, G., Robba, N. R., and Burderi, L. (2006). Chandra Observation of the Persistent Emission from the Dipping Source XB 1916-053. *ApJ*, 647:1341–1348. 90, 108, 109, 113, 116, 125, 127

Iaria, R., Di Salvo, T., Matranga, M., Galiano, C. G., D'Aí, A., Riggio, A., Burderi, L., Sanna, A., Ferrigno, C., Del Santo, M., Pintore, F., and Robba, N. R. (2015b). A possible cyclotron resonance scattering feature near 0.7 keV in X1822-371. *A&A*, 577:A63. 104, 146

Iaria, R., Gambino, A. F., Di Salvo, T., Burderi, L., Matranga, M., Riggio, A., Sanna, A., Scarano, F., and D'Aì, A. (2017). A possible solution of the puzzling variation of the orbital period of MXB 1659-298. *ArXiv e-prints*. 71

Ichimaru, S. (1977). Bimodal behavior of accretion disks - Theory and application to Cygnus X-1 transitions. *ApJ*, 214:840–855. 33

in 't Zand, J., Heise, J., Smith, M. J. S., Cocchi, M., Natalucci, L., Celidonio, G., Augusteijn, T., and Freyhammer, L. (1999). V2134 Ophiuchi = MXB 1659-29. *IAU Circ.*, 7138. 123, 124, 130

in't Zand, J. J. M., Kuulkers, E., Verbunt, F., Heise, J., and Cornelisse, R. (2003). A superburst from 4U 1254-69. *A&A*, 411:L487–L491. 69, 79, 82

Jahoda, K., Swank, J. H., Giles, A. B., Stark, M. J., Strohmayer, T., Zhang, W., and Morgan, E. H. (1996). In-orbit performance and calibration of the Rossi X-ray Timing Explorer (RXTE) Proportional Counter Array (PCA). In Siegmund, O. H. and Gummin, M. A., editors, *EUV, X-Ray, and Gamma-Ray Instrumentation for Astronomy VII*, volume 2808 of *Proc. SPIE*, pages 59–70. 133

Jansen, F., Lumb, D., Altieri, B., Clavel, J., Ehle, M., Erd, C., Gabriel, C., Guainazzi, M., Gondoin, P., Much, R., Munoz, R., Santos, M., Schartel, N., Texier, D., and Vacanti, G. (2001). XMM-Newton observatory. I. The spacecraft and operations. *A&A*, 365:L1–L6. 132

Kaastra, J. S. and Mewe, R. (1993). Multiple Auger ionisation and fluorescence processes for Be to Zn. In Silver, E. H. and Kahn, S. M., editors, *UV and X-ray Spectroscopy of Laboratory and Astrophysical Plasmas*. 43

Kalogera, V. and Webbink, R. F. (1998). Formation of Low-Mass X-Ray Binaries. II. Common Envelope Evolution of Primordial Binaries with Extreme Mass Ratios. *ApJ*, 493:351–367. 12

King, A. R. (1988). The evolution of compact binaries. *QJRAS*, 29:1–25. 51, 62

Kiseleva, L. G., Eggleton, P. P., and Orlov, V. V. (1994). Instability of Close Triple Systems with Coplanar Initial Doubly Circular Motion. *MNRAS*, 270:936. 146

Klein, O. and Nishina, Y. (1929). Über die streuung von strahlung durch freie elektronen nach der neuen relativistischen quantendynamik von dirac. *Zeitschrift für Physik*, 52(11):853–868. 36

Knigge, C., Baraffe, I., and Patterson, J. (2011). The Evolution of Cataclysmic Variables as Revealed by Their Donor Stars. *ApJS*, 194:28. 140

Koyama, K., Tsunemi, H., Dotani, T., Bautz, M. W., Hayashida, K., Tsuru, T. G., Matsumoto, H., Ogawara, Y., Ricker, G. R., Doty, J., Kissel, S. E., Foster, R., Nakajima, H., Yamaguchi, H., Mori, H., Sakano, M., Hamaguchi, K., Nishiuchi, M., Miyata, E., Torii, K., Namiki, M., Katsuda, S., Matsuura, D., Miyauchi, T., Anabuki, N., Tawa, N., Ozaki, M., Murakami, H., Maeda, Y., Ichikawa, Y., Prigozhin, G. Y., Boughan, E. A., Lamarr, B., Miller, E. D., Burke, B. E., Gregory, J. A., Pillsbury, A., Bamba, A., Hiraga, J. S., Senda, A., Katayama, H., Kitamoto, S., Tsujimoto, M., Kohmura, T., Tsuboi, Y., and Awaki, H. (2007). X-Ray Imaging Spectrometer (XIS) on Board Suzaku. *PASJ*, 59:23–33. 112

Landau, L. D. and Lifshitz, E. M. (1975). *The classical theory of fields*. 22, 31

Lasota, J.-P. (2001). The disc instability model of dwarf novae and low-mass X-ray binary transients. *New A Rev.*, 45:449–508. 143

Lebrun, F., Leray, J. P., Lavocat, P., Crétolle, J., Arquès, M., Blondel, C., Bonnin, C., Bouère, A., Cara, C., Chaleil, T., Daly, F., Desages, F., Dzitko, H., Horeau, B., Laurent, P., Limousin, O., Mathy, F., Mauguen, V., Meignier, F., Molinié, F., Poindron, E., Rouger, M., Sauvageon, A., and Tourrette, T. (2003). ISGRI: The INTEGRAL Soft Gamma-Ray Imager. *A&A*, 411:L141–L148. 59

Levine, A. M., Bradt, H., Cui, W., Jernigan, J. G., Morgan, E. H., Remillard, R., Shirey, R. E., and Smith, D. A. (1996). First Results from the All-Sky Monitor on the Rossi X-Ray Timing Explorer. *ApJ*, 469:L33. 134

Levine, A. M., Bradt, H. V., Chakrabarty, D., Corbet, R. H. D., and Harris, R. J. (2011). An Extended and More Sensitive Search for Periodicities in Rossi X-Ray Timing Explorer/All-Sky Monitor X-Ray Light Curves. *ApJS*, 196:6. 50, 56, 57, 59, 60, 66, 68, 72, 77, 82

Lewin, W. H. G., Doty, J., Clark, G. W., Rappaport, S. A., Bradt, H. V. D., Doxsey, R., Hearn, D. R., Hoffman, J. A., Jernigan, J. G., Li, F. K., Mayer, W., McClintock, J., Primini, F., and Richardson, J. (1976a). The discovery of rapidly repetitive X-ray bursts from a new source in Scorpius. *ApJ*, 207:L95–L99. 9

Lewin, W. H. G., Hoffman, J. A., Doty, J., and Liller, W. (1976b). X-Ray Bursts. *IAU Circ.*, 2994. 130

Lewin, W. H. G., van Paradijs, J., and Taam, R. E. (1995). X-ray bursts. *X-ray Binaries*, pages 175–232. 9

Li, J., Torres, D. F., de Oña Wilhelmi, E., Rea, N., and Martin, J. (2016). Gamma-ray Emission from PSR J0007+7303 Using Seven Years of Fermi Large Area Telescope Observations. *ApJ*, 831:19. 151

Liang, E. P. T. and Price, R. H. (1977). Accretion disk coronae and Cygnus X-1. *ApJ*, 218:247–252. 33

Lin, D. N. C. and Papaloizou, J. (1979). On the structure of circumbinary accretion disks and the tidal evolution of commensurable satellites. *MNRAS*, 188:191–201. 4

Liu, Q. Z., van Paradijs, J., and van den Heuvel, E. P. J. (2007). A catalogue of low-mass X-ray binaries in the Galaxy, LMC, and SMC (Fourth edition). *A&A*, 469:807–810. 108

Longair, M. S. (2011). *High energy astrophysics*. Cambridge University Press, 3rd ed edition. 14, 31

Lund, N., Budtz-Jørgensen, C., Westergaard, N. J., Brandt, S., Rasmussen, I. L., Hornstrup, A., Oxborrow, C. A., Chenevez, J., Jensen, P. A., Laursen, S., Andersen, K. H., Mogensen, P. B., Rasmussen, I., Omø, K., Pedersen, S. M., Polny, J., Andersson, H., Andersson, T., Kämäräinen, V., Vilhu, O., Huovelin, J., Maisala, S., Morawski, M., Juchnikowski, G., Costa, E., Feroci, M., Rubini, A., Rapisarda, M., Morelli, E., Carassiti, V., Frontera, F., Pelliciari, C., Loffredo, G., Martínez Núñez, S., Reglero, V., Velasco, T., Larsson, S., Svensson, R., Zdziarski, A. A., Castro-Tirado, A., Attina, P., Goria, M., Giulianelli, G., Cordero, F., Rezazad, M., Schmidt, M., Carli, R., Gomez, C., Jensen, P. L., Sarri, G., Tiemon, A., Orr, A., Much, R., Kretschmar, P., and Schnopper, H. W. (2003a). JEM-X: The X-ray monitor aboard INTEGRAL. *A&A*, 411:L231–L238. 59

Lund, N., Budtz-Jørgensen, C., Westergaard, N. J., Brandt, S., Rasmussen, I. L., Hornstrup, A., Oxborrow, C. A., Chenevez, J., Jensen, P. A., Laursen, S., Andersen, K. H., Mogensen, P. B., Rasmussen, I., Omø, K., Pedersen, S. M., Polny, J., Andersson, H., Andersson, T., Kämäräinen, V., Vilhu, O., Huovelin, J., Maisala, S., Morawski, M., Juchnikowski, G., Costa, E., Feroci, M., Rubini, A., Rapisarda, M., Morelli, E., Carassiti, V., Frontera, F., Pelliciari, C., Loffredo, G., Martínez Núñez, S., Reglero, V., Velasco, T., Larsson, S., Svensson, R., Zdziarski, A. A., Castro-Tirado, A., Attina, P., Goria, M., Giulianelli, G., Cordero, F., Rezazad, M., Schmidt, M., Carli, R., Gomez, C., Jensen, P. L., Sarri, G., Tiemon, A., Orr, A., Much, R., Kretschmar, P., and Schnopper, H. W. (2003b). JEM-X: The X-ray monitor aboard INTEGRAL. *A&A*, 411:L231–L238. 92

Malzac, J. (1999). *Modelisation de l'emission X et gamma des objets compacts par des methodes Monte-Carlo*. PhD thesis. 40

Marino, A., Di Salvo, T., Gambino, A. F., Iaria, R., Burderi, L., Matranga, M., Sanna, A., and Riggio, A. (2017). Evidence of a non-conservative mass transfer for XTE J0929-314. *Astron. Astrophys.*, 603:A137. 20

Marshall, D. J., Robin, A. C., Reylé, C., Schultheis, M., and Picaud, S. (2006). Modelling the Galactic interstellar extinction distribution in three dimensions. *A&A*, 453:635–651. 62, 64, 157

Mason, K. O., Seitzer, P., Tuohy, I. R., Hunt, L. K., Middleditch, J., Nelson, J. E., and White, N. E. (1980). A 5.57 HR modulation in the optical counterpart of 2S 1822-371. *ApJ*, 242:L109–L113. 68

Matranga, M., Papitto, A., Di Salvo, T., Bozzo, E., Torres, D. F., Iaria, R., Burderi, L., Rea, N., de Martino, D., Sanchez-Fernandez, C., Gambino, A. F., Ferrigno, C., and Stella, L. (2017). XMM-Newton and INTEGRAL view of the hard state of EXO 1745-248 during its 2015 outburst. *A&A*, 603:A39. 43

Matsuoka, M., Kawasaki, K., Ueno, S., Tomida, H., Kohama, M., Suzuki, M., Adachi, Y., Ishikawa, M., Mihara, T., Sugizaki, M., Isobe, N., Nakagawa, Y., Tsunemi, H., Miyata, E., Kawai, N., Kataoka, J., Morii, M., Yoshida, A., Negoro, H., Nakajima, M., Ueda, Y., Chujo, H., Yamaoka, K., Yamazaki, O., Nakahira, S., You, T., Ishiwata, R., Miyoshi, S., Eguchi, S., Hiroi, K., Katayama, H., and Ebisawa, K. (2009). The MAXI Mission on the ISS: Science and Instruments for Monitoring All-Sky X-Ray Images. *PASJ*, 61:999–1010. 134

Mayer, M. and Pringle, J. E. (2007). Time-dependent models of two-phase accretion discs around black holes. *MNRAS*, 376:435–456. 46

Meyer, F., Liu, B. F., and Meyer-Hofmeister, E. (2000). Evaporation: The change from accretion via a thin disk to a coronal flow. *A&A*, 361:175–188. 46

Michaely, E. and Perets, H. B. (2016). Tidal capture formation of low-mass X-ray binaries from wide binaries in the field. *MNRAS*, 458:4188–4197. 10

Migliari, S. and Fender, R. P. (2006). Jets in neutron star X-ray binaries: a comparison with black holes. *MNRAS*, 366:79–91. 47

Mihara, T., Nakajima, M., Sugizaki, M., Serino, M., Matsuoka, M., Kohama, M., Kawasaki, K., Tomida, H., Ueno, S., Kawai, N., Kataoka, J., Morii, M., Yoshida, A., Yamaoka, K., Nakahira, S., Negoro, H., Isobe, N., Yamauchi, M., and Sakurai, I. (2011). Gas Slit Camera (GSC) onboard MAXI on ISS. *PASJ*, 63:S623–S634. 134

Miller, L., Turner, T. J., Reeves, J. N., George, I. M., Kraemer, S. B., and Wingert, B. (2007). The variable X-ray spectrum of Markarian 766. I. Principal components analysis. *A&A*, 463:131–143. 121

Mitsuda, K., Bautz, M., Inoue, H., Kelley, R. L., Koyama, K., Kunieda, H., Makishima, K., Ogawara, Y., Petre, R., Takahashi, T., Tsunemi, H., White, N. E., Anabuki, N., Angelini, L.,

Arnaud, K., Awaki, H., Bamba, A., Boyce, K., Brown, G. V., Chan, K.-W., Cottam, J., Dotani, T., Doty, J., Ebisawa, K., Ezoe, Y., Fabian, A. C., Figueroa, E., Fujimoto, R., Fukazawa, Y., Furusho, T., Furuzawa, A., Gendreau, K., Griffiths, R. E., Haba, Y., Hamaguchi, K., Harrus, I., Hasinger, G., Hatsukade, I., Hayashida, K., Henry, P. J., Hiraga, J. S., Holt, S. S., Hornschemeier, A., Hughes, J. P., Hwang, U., Ishida, M., Ishisaki, Y., Isobe, N., Itoh, M., Iyomoto, N., Kahn, S. M., Kamae, T., Katagiri, H., Kataoka, J., Katayama, H., Kawai, N., Kilbourne, C., Kinugasa, K., Kissel, S., Kitamoto, S., Kohama, M., Kohmura, T., Kokubun, M., Kotani, T., Kotoku, J., Kubota, A., Madejski, G. M., Maeda, Y., Makino, F., Markowitz, A., Matsumoto, C., Matsumoto, H., Matsuoka, M., Matsushita, K., McCammon, D., Mihara, T., Misaki, K., Miyata, E., Mizuno, T., Mori, K., Mori, H., Morii, M., Moseley, H., Mukai, K., Murakami, H., Murakami, T., Mushotzky, R., Nagase, F., Namiki, M., Negoro, H., Nakazawa, K., Nousek, J. A., Okajima, T., Ogasaka, Y., Ohashi, T., Oshima, T., Ota, N., Ozaki, M., Ozawa, H., Parmar, A. N., Pence, W. D., Porter, F. S., Reeves, J. N., Ricker, G. R., Sakurai, I., Sanders, W. T., Senda, A., Serlemitsos, P., Shibata, R., Soong, Y., Smith, R., Suzuki, M., Szymkowiak, A. E., Takahashi, H., Tamagawa, T., Tamura, K., Tamura, T., Tanaka, Y., Tashiro, M., Tawara, Y., Terada, Y., Terashima, Y., Tomida, H., Torii, K., Tsuboi, Y., Tsujimoto, M., Tsuru, T. G., Turner, M. J. L. ., Ueda, Y., Ueno, S., Ueno, M., Uno, S., Urata, Y., Watanabe, S., Yamamoto, N., Yamaoka, K., Yamasaki, N. Y., Yamashita, K., Yamauchi, M., Yamauchi, S., Yaqoob, T., Yonetoku, D., and Yoshida, A. (2007). The X-Ray Observatory Suzaku. *PASJ*, 59:S1–S7. 110

Mitsuda, K., Inoue, H., Koyama, K., Makishima, K., Matsuoka, M., Ogawara, Y., Suzuki, K., Tanaka, Y., Shibazaki, N., and Hirano, T. (1984). Energy spectra of low-mass binary X-ray sources observed from TENMA. *PASJ*, 36:741–759. 115

Morton, D. C. (1960). Evolutionary Mass Exchange in Close Binary Systems. *ApJ*, 132:146. 14

Motch, C., Pedersen, H., Courvoisier, T. J.-L., Beuermann, K., and Pakull, M. W. (1987). The optical light curve of the low-mass X-ray binary XB 1254-690. *ApJ*, 313:792–800. 68, 69

Narayan, R. (1996). Advection-dominated Models of Luminous Accreting Black Holes. *ApJ*, 462:136. 33

Narayan, R. and Yi, I. (1994). Advection-dominated accretion: A self-similar solution. *ApJ*, 428:L13–L16. 33

Neece, G. D. (1984). Models of lower-main-sequence stars. *ApJ*, 277:738–743. 26, 61, 65, 79, 80

Negoro, H., Furuya, K., Ueno, S., Tomida, H., Nakahira, S., Kimura, M., Ishikawa, M., Nakagawa, Y. E., Mihara, T., Sugizaki, M., Serino, M., Shidatsu, M., Sugimoto, J., Takagi, T., Matsuoka, M., Kawai, N., Tachibana, Y., Yoshii, T., Yoshida, A., Sakamoto, T., Kawakubo, Y., Ohtsuki, H., Tsunemi, H., Imatani, R., Nakajima, M., Masumitsu, T., Tanaka, K., Ueda, Y., Kawamuro, T., Hori, T., Tsuboi, Y., Kanetou, S., Yamauchi, M., Itoh, D., Yamaoka, K., and Morii, M. (2015).

MAXI/GSC detection of renewed X-ray activities of SAX J1324.5-6313/MAXI J1327-627 and H 1658-298/MAXI J1702-301. *The Astronomer's Telegram*, 7943. 130

Nelemans, G., Jonker, P. G., and Steeghs, D. (2006). Optical spectroscopy of (candidate) ultracompact X-ray binaries: constraints on the composition of the donor stars. *MNRAS*, 370:255–262. 100, 109

Nelson, L. A. and Rappaport, S. (2003). Theoretical Considerations on the Properties of Accreting Millisecond Pulsars. *ApJ*, 598:431–445. 61, 78

Nishiyama, S., Nagata, T., Tamura, M., Kandori, R., Hatano, H., Sato, S., and Sugitani, K. (2008). The Interstellar Extinction Law toward the Galactic Center. II. V, J, H, and K_s Bands. *ApJ*, 680:1174–1179. 64

Oosterbroek, T., Parmar, A. N., Sidoli, L., in't Zand, J. J. M., and Heise, J. (2001). BeppoSAX observation of the eclipsing dipping X-ray binary X 1658-298. *A&A*, 376:532–542. 130, 135, 136, 140

Özel, F., Psaltis, D., Narayan, R., and Santos Villarreal, A. (2012). On the Mass Distribution and Birth Masses of Neutron Stars. *ApJ*, 757:55. 140

Paczyński, B. (1971). Evolutionary Processes in Close Binary Systems. *ARA&A*, 9:183. 3, 18, 25, 61, 80, 139, 141, 143

Paczynski, B. and Sienkiewicz, R. (1981). Gravitational radiation and the evolution of cataclysmic binaries. *ApJ*, 248:L27–L30. 84

Papaloizou, J. and Pringle, J. E. (1977). Tidal torques on accretion discs in close binary systems. *MNRAS*, 181:441–454. 4

Parmar, A. N., Gottwald, M., van der Klis, M., and van Paradijs, J. (1989). The discovery of 2.93 hour periodic intensity dips from X1323-619. *ApJ*, 338:1024–1032. 50, 51, 59, 62

Piraino, S., Santangelo, A., Di Salvo, T., Kaaret, P., Horns, D., Iaria, R., and Burderi, L. (2007). BeppoSAX observation of 4U 1705-44: detection of hard X-ray emission in the soft state. *A&A*, 471:L17–L20. 115

Ponti, G., De, K., Muñoz-Darias, T., Stella, L., and Nandra, K. (2017). The puzzling orbital period evolution of the LMXB AX J1745.6-2901. *MNRAS*, 464:840–849. 139, 146

Predehl, P. and Schmitt, J. H. M. M. (1995). X-raying the interstellar medium: ROSAT observations of dust scattering halos. *A&A*, 293:889–905. 51

Priedhorsky, W. C. and Terrell, J. (1984). Long-term observations of X-ray sources - The Aquila-Serpens-Scutum region. *ApJ*, 280:661–670. 86

Pringle, J. E. and Rees, M. J. (1972). Accretion Disc Models for Compact X-Ray Sources. *A&A*, 21:1. 30

Rappaport, S., Joss, P. C., and Webbink, R. F. (1982). The evolution of highly compact binary stellar systems. *ApJ*, 254:616–640. 101

Rappaport, S., Ma, C. P., Joss, P. C., and Nelson, L. A. (1987). The evolutionary status of 4U 1820-30. *ApJ*, 322:842–851. 101

Rappaport, S., Verbunt, F., and Joss, P. C. (1983). A new technique for calculations of binary stellar evolution, with application to magnetic braking. *ApJ*, 275:713–731. 143

Ray, P. S., Kerr, M., Parent, D., Abdo, A. A., Guillemot, L., Ransom, S. M., Rea, N., Wolff, M. T., Makeev, A., Roberts, M. S. E., Camilo, F., Dormody, M., Freire, P. C. C., Grove, J. E., Gwon, C., Harding, A. K., Johnston, S., Keith, M., Kramer, M., Michelson, P. F., Romani, R. W., Saz Parkinson, P. M., Thompson, D. J., Weltevrede, P., Wood, K. S., and Ziegler, M. (2011). Precise γ-ray Timing and Radio Observations of 17 Fermi γ-ray Pulsars. *ApJS*, 194:17. 150

Reale, F. (2010). Coronal Loops: Observations and Modeling of Confined Plasma. *Living Reviews in Solar Physics*, 7:5. 33

Reeves, J., Done, C., Pounds, K., Terashima, Y., Hayashida, K., Anabuki, N., Uchino, M., and Turner, M. (2008). On why the iron K-shell absorption in AGN is not a signature of the local warm/hot intergalactic medium. *MNRAS*, 385:L108–L112. 121

Retter, A., Chou, Y., Bedding, T. R., and Naylor, T. (2002). Detection of negative superhumps in a low-mass X-ray binary - an end to the long debate on the nature of V1405 Aql (X1916-053). *MNRAS*, 330:L37–L42. 85, 86

Reynolds, C. S. (1999). Compton Reflection and Iron Fluorescence in Active Galactic Nuclei and Galactic Black Hole Candidates. In Poutanen, J. and Svensson, R., editors, *High Energy Processes in Accreting Black Holes*, volume 161 of *Astronomical Society of the Pacific Conference Series*, page 178. 42

Rybicki, G. B. and Lightman, A. P. (1979). *Radiative processes in astrophysics*. 37

Salaris, M. and Cassisi, S. (2005). *Evolution of Stars and Stellar Populations*. 141, 143

Sanna, A., Burderi, L., Riggio, A., Pintore, F., Di Salvo, T., Gambino, A. F., Iaria, R., Matranga, M., and Scarano, F. (2016). Timing of the accreting millisecond pulsar SAX J1748.9-2021 during its 2015 outburst. *MNRAS*, 459:1340–1349. 143

Scargle, J. D., Norris, J. P., Jackson, B., and Chiang, J. (2013). Studies in Astronomical Time Series Analysis. VI. Bayesian Block Representations. *ApJ*, 764:167. 151

Shadmehri, M. and Khajenabi, F. (2005). Self-similar structure of magnetized radiation-dominated accretion discs. *MNRAS*, 361:719–724. 33

Shakura, N. I. (1973). Disk Model of Gas Accretion on a Relativistic Star in a Close Binary System. *Soviet Ast.*, 16:756. 30, 31

Shakura, N. I. and Sunyaev, R. A. (1973). Black holes in binary systems. Observational appearance. *A&A*, 24:337–355. 33

Shapiro, S. L. and Teukolsky, S. A. (1983). *Black holes, white dwarfs, and neutron stars: The physics of compact objects*. 100

Shimura, T. and Takahara, F. (1995). On the spectral hardening factor of the X-ray emission from accretion disks in black hole candidates. *ApJ*, 445:780–788. 117, 122

Sibgatullin, N. R. and Sunyaev, R. A. (2000). Energy Release During Disk Accretion onto a Rapidly Rotating Neutron Star. *Astronomy Letters*, 26:699–724. 140

Sidoli, L., Oosterbroek, T., Parmar, A. N., Lumb, D., and Erd, C. (2001). An XMM-Newton study of the X-ray binary MXB 1659-298 and the discovery of narrow X-ray absorption lines. *A&A*, 379:540–550. 132, 133, 141, 145

Skumanich, A. (1972). Time Scales for CA II Emission Decay, Rotational Braking, and Lithium Depletion. *ApJ*, 171:565. 23, 79, 142

Slane, P. (2017). Pulsar Wind Nebulae. *ArXiv e-prints*. 149

Smale, A. P. (1995). The Infrared Counterpart of X1323-619. *AJ*, 110:1292. 50

Smale, A. P., Mason, K. O., White, N. E., and Gottwald, M. (1988). X-ray observations of the 50-min dipping source XB1916-053. *MNRAS*, 232:647–660. 84, 108

Smale, A. P., Mason, K. O., Williams, O. R., and Watson, M. G. (1989). GINGA observations of the dipping X-ray binary XB 1916-053. *PASJ*, 41:607–615. 84

Smith, M. A. (1979). Rotational studies of lower main-sequence stars. *PASP*, 91:737–745. 142

Smith, S. E., Noah, P. V., and Cottrell, M. J. (1979). The spectral development of Nova Cygni 1978. *PASP*, 91:775–780. 23, 79

Spitzer, L. (1978). *Physical processes in the interstellar medium*. 125

Strüder, L., Briel, U., Dennerl, K., Hartmann, R., Kendziorra, E., Meidinger, N., Pfeffermann, E., Reppin, C., Aschenbach, B., Bornemann, W., Bräuninger, H., Burkert, W., Elender, M., Freyberg, M., Haberl, F., Hartner, G., Heuschmann, F., Hippmann, H., Kastelic, E., Kemmer,

S., Kettenring, G., Kink, W., Krause, N., Müller, S., Oppitz, A., Pietsch, W., Popp, M., Predehl, P., Read, A., Stephan, K. H., Stötter, D., Trümper, J., Holl, P., Kemmer, J., Soltau, H., Stötter, R., Weber, U., Weichert, U., von Zanthier, C., Carathanassis, D., Lutz, G., Richter, R. H., Solc, P., Böttcher, H., Kuster, M., Staubert, R., Abbey, A., Holland, A., Turner, M., Balasini, M., Bignami, G. F., La Palombara, N., Villa, G., Buttler, W., Gianini, F., Lainé, R., Lumb, D., and Dhez, P. (2001). The European Photon Imaging Camera on XMM-Newton: The pn-CCD camera. *A&A*, 365:L18–L26. 132

Swank, J. H., Taam, R. E., and White, N. E. (1984). MXB 1916-053/4U 1915-05 - Burst properties and constraints on a 50 minute binary secondary. *ApJ*, 277:274–285. 84

Takahashi, T., Abe, K., Endo, M., Endo, Y., Ezoe, Y., Fukazawa, Y., Hamaya, M., Hirakuri, S., Hong, S., Horii, M., Inoue, H., Isobe, N., Itoh, T., Iyomoto, N., Kamae, T., Kasama, D., Kataoka, J., Kato, H., Kawaharada, M., Kawano, N., Kawashima, K., Kawasoe, S., Kishishita, T., Kitaguchi, T., Kobayashi, Y., Kokubun, M., Kotoku, J., Kouda, M., Kubota, A., Kuroda, Y., Madejski, G., Makishima, K., Masukawa, K., Matsumoto, Y., Mitani, T., Miyawaki, R., Mizuno, T., Mori, K., Mori, M., Murashima, M., Murakami, T., Nakazawa, K., Niko, H., Nomachi, M., Okada, Y., Ohno, M., Oonuki, K., Ota, N., Ozawa, H., Sato, G., Shinoda, S., Sugiho, M., Suzuki, M., Taguchi, K., Takahashi, H., Takahashi, I., Takeda, S., Tamura, K.-I., Tamura, T., Tanaka, T., Tanihata, C., Tashiro, M., Terada, Y., Tominaga, S., Uchiyama, Y., Watanabe, S., Yamaoka, K., Yanagida, T., and Yonetoku, D. (2007). Hard X-Ray Detector (HXD) on Board Suzaku. *PASJ*, 59:35–51. 112

Tarter, C. B., Tucker, W. H., and Salpeter, E. E. (1969). The Interaction of X-Ray Sources with Optically Thin Environments. *ApJ*, 156:943. 127

Tauris, T. M. (2001). On the Pre-RLO Spin-Orbit Couplings in LMXBs. In Podsiadlowski, P., Rappaport, S., King, A. R., D'Antona, F., and Burderi, L., editors, *Evolution of Binary and Multiple Star Systems*, volume 229 of *Astronomical Society of the Pacific Conference Series*, page 145. 142

Tauris, T. M. and van den Heuvel, E. P. J. (2006). *Formation and evolution of compact stellar X-ray sources*, pages 623–665. 10, 11

Torres, D. F., Martín, J., de Oña Wilhelmi, E., and Cillis, A. (2013). The effects of magnetic field, age and intrinsic luminosity on Crab-like pulsar wind nebulae. *MNRAS*, 436:3112–3127. 149

Troja, E., Piro, L., van Eerten, H., Wollaeger, R. T., Im, M., Fox, O. D., Butler, N. R., Cenko, S. B., Sakamoto, T., Fryer, C. L., Ricci, R., Lien, A., Ryan Jr, R. E., Korobkin, O., Lee, S. K., Burgess, J. M., Lee, W. H., Watson, A. M., Choi, C., Covino, S., D'Avanzo, P., Fontes, C. J., González, J. B., Khandrika, H. G., Kim, J., Kim, S. L., Lee, C. U., Lee, H. M., Kutyrev, A.,

Lim, G., Sánchez-Ramírez, R., Veilleux, S., Wieringa, M. H., and Yoon, Y. (2017). The x-ray counterpart to the gravitational-wave event gw170817. *Nature*, advance online publication:–. 7

van der Klis, M. and Bonnet-Bidaud, J. M. (1984). The orbital parameters and the X-ray pulsation of VELA X-1 (4U 0900 - 40). *A&A*, 135:155–170. 97

van der Klis, M., Jansen, F., van Paradijs, J., and Stollman, G. (1985). First detection of an X-ray burst and a one hour intensity dip in 4U1323-62. *Space Sci. Rev.*, 40:287–291. 50

van Paradijs, J., van der Klis, M., and Pedersen, H. (1988). Optical photometry of the X-ray source EXO 0748-676/UY Volantis. *A&AS*, 76:185–188. 122

Verbunt, F. (1993). Origin and evolution of X-ray binaries and binary radio pulsars. *ARA&A*, 31:93–127. 7, 12, 51, 65, 78, 79, 80, 142

Verbunt, F. (2001). A census with ROSAT of low-luminosity X-ray sources in globular clusters. *A&A*, 368:137–159. 130

Verbunt, F. and Zwaan, C. (1981). Magnetic braking in low-mass X-ray binaries. *A&A*, 100:L7–L9. 23, 142

Verner, D. A., Ferland, G. J., Korista, K. T., and Yakovlev, D. G. (1996). Atomic Data for Astrophysics. II. New Analytic FITS for Photoionization Cross Sections of Atoms and Ions. *ApJ*, 465:487. 59, 115

Verner, D. A. and Yakovlev, D. G. (1995). Analytic FITS for partial photoionization cross sections. *A&AS*, 109:125–133. 125, 126

Wachter, S., Smale, A. P., and Bailyn, C. (2000). The Reappearance of the Transient Low-Mass X-Ray Binary X1658-298. *ApJ*, 534:367–372. 130, 131, 132, 135

Walter, F. M., Mason, K. O., Clarke, J. T., Halpern, J., Grindlay, J. E., Bowyer, S., and Henry, J. P. (1982). Discovery of a 50 minute binary period and a likely 22 magnitude optical counterpart for the X-ray burster 4U 1915-05. *ApJ*, 253:L67–L71. 84

Warner, B. (1995). Cataclysmic variable stars. *Cambridge Astrophysics Series*, 28. 131

Warwick, R. S., Marshall, N., Fraser, G. W., Watson, M. G., Lawrence, A., Page, C. G., Pounds, K. A., Ricketts, M. J., Sims, M. R., and Smith, A. (1981). The Ariel V /3 A/ catalogue of X-ray sources. I - Sources at low galactic latitude /absolute value of B less than 10 deg/. *MNRAS*, 197:865–891. 50

Whelan, J. and Iben, Jr., I. (1973). Binaries and Supernovae of Type I. *ApJ*, 186:1007–1014. 12

White, N. E. (1989). X-ray binaries. *A&A Rev.*, 1:85–110. 85

White, N. E. and Swank, J. H. (1982). The discovery of 50 minute periodic absorption events from 4U 1915-05. *ApJ*, 253:L61–L66. 68, 84

Wijnands, R., Nowak, M., Miller, J. M., Homan, J., Wachter, S., and Lewin, W. H. G. (2003). A Chandra Observation of the Neutron Star X-Ray Transient and Eclipsing Binary MXB 1659-29 in Quiescence. *ApJ*, 594:952–960. 133

Wijnands, R., Strohmayer, T., and Franco, L. M. (2001). Discovery of Nearly Coherent Oscillations with a Frequency of ˜567 HZ during Type I X-Ray Bursts of the X-Ray Transient and Eclipsing Binary X1658-298. *ApJ*, 549:L71–L75. 132, 140, 142

Wijnands, R. and van der Klis, M. (1998). A millisecond pulsar in an X-ray binary system. *Nature*, 394:344–346. 6

Wilms, J., Nowak, M. A., Boyd, P., Pottschmidt, K., Heindl, W. A., and Begelman, M. C. (2000). Soft-to-Hard State Transitions in LMC X-3. In *AAS/High Energy Astrophysics Division #5*, volume 32 of *Bulletin of the American Astronomical Society*, page 1247. 115

Winkler, C., Courvoisier, T. J.-L., Di Cocco, G., Gehrels, N., Giménez, A., Grebenev, S., Hermsen, W., Mas-Hesse, J. M., Lebrun, F., Lund, N., Palumbo, G. G. C., Paul, J., Roques, J.-P., Schnopper, H., Schönfelder, V., Sunyaev, R., Teegarden, B., Ubertini, P., Vedrenne, G., and Dean, A. J. (2003). The INTEGRAL mission. *A&A*, 411:L1–L6. 92

Wolff, M. T., Hertz, P., Wood, K. S., Ray, P. S., and Bandyopadhyay, R. M. (2002). Eclipse Timings of the Low-Mass X-Ray Binary EXO 0748-676. III. Orbital Period Jitter Observed with the Unconventional Stellar Aspect Experiment and the Rossi X-Ray Timing Explorer. *ApJ*, 575:384–396. 139

Wolff, M. T., Ray, P. S., Wood, K. S., and Hertz, P. L. (2009). Eclipse Timings of the Transient Low-Mass X-ray Binary EXO 0748-676. IV. The Rossi X-ray Timing Explorer Eclipses. *ApJS*, 183:156–170. 130, 146

Wolff, M. T., Wood, K. S., and Ray, P. S. (2007). Possible Magnetic Activity in the Low-Mass X-Ray Binary EXO 0748-676. *ApJ*, 668:L151–L154. 139

Yoshida, K. (1993). PhD thesis, Thesis, Tokyo University, (1993). 84, 85, 108, 122

Yoshida, K., Inoue, H., Mitsuda, K., Dotani, T., and Makino, F. (1995). The Dipping Low-Mass X-Ray Binary X1916-05 Observed with GINGA. *PASJ*, 47:141–152. 85

Zdziarski, A. A., Johnson, W. N., and Magdziarz, P. (1996). Broad-band γ-ray and X-ray spectra of NGC 4151 and their implications for physical processes and geometry. *MNRAS*, 283:193–206. 123

Zhang, Z., Makishima, K., Sakurai, S., Sasano, M., and Ono, K. (2014). Probing the accretion scheme of the dipping X-ray binary 4U 1915-05 with Suzaku. *PASJ*, 66:120. 91, 100, 109, 112, 115, 117, 119, 122, 123, 124, 125

Zhang, Z., Sakurai, S., Makishima, K., Nakazawa, K., Ono, K., Yamada, S., and Xu, H. (2016). Suzaku Observation of the High-inclination Binary EXO 0748-676 in the Hard State. *ApJ*, 823:131. 124

Zolotukhin, I. Y., Revnivtsev, M. G., and Shakura, N. I. (2010). Infrared identification of 4U1323-619 revisited. *MNRAS*, 401:L1–L4. 50, 51, 52, 53, 61, 64, 66

Życki, P. T., Done, C., and Smith, D. A. (1999). The 1989 May outburst of the soft X-ray transient GS 2023+338 (V404 Cyg). *MNRAS*, 309:561–575. 115

Acknowledgements

Primo tra tutti vorrei ringraziare Rosario, che oltre a rivestire il difficile compito di tutor, è riuscito a farmi sentire a mio agio sin dal primo giorno di lavoro. Lo ringrazio per essersi rivelato, con la sua precisione, un punto di riferimento saldo per la mia crescita scientifica e per avermi aiutato a gestire al meglio le difficoltà che si sono presentate nel corso del lavoro di ricerca.

Un ringraziamento lo devo anche a Tiziana, che si è dimostrata un forte modello di concretezza e rigore scientifico a cui spero di potermi avvicinare in futuro il più possibile. La ringrazio per avermi trasmesso molte delle sue innumerevoli conoscenze scientifiche e per avermi dato coraggio quando se ne è presentata l'occasione.

Ringrazio Luciano per avermi reso partecipe dei progetti scientifici e delle mille idee su cui ha lavorato. Grazie a lui ho capito che anche le cose più semplici e scontate a volte possono contenere aspetti ancora irrisoluti che bisogna affrontare con impegno, rigore scientifico e con il massimo dell'eleganza che la formulazione matematica e fisica è in grado di fornirci.

Un ringraziamento particolare lo devo a Marco che mi ha trasmesso parte delle sue conoscenze, soprattutto nella prima fase del mio lavoro di ricerca. Con lui ho costantemente interagito e mi sono confrontato su temi scientifici e non. Amico fedele e compagno di mille avventure mi ha sostenuto fino alla fine del mio lavoro con la sua tranquillità, pacatezza d'animo e soprattutto con la sua ironia. Di questo gliene sarò sempre grato.

Ringrazio Simona, Alessio, Roberta e Tiziana (Tizianina) per l'amicizia e la collaborazione negli ultimi mesi di lavoro. E' anche grazie a loro che l'ultimo periodo di ricerca è stato svolto in maniera piacevole e con un continuo e costruttivo confronto di idee.

Ringrazio i ragazzi del gruppo di ricerca di Cagliari (Alessandro e Andrea) e Fabio per il loro importante contributo alla nostra collaborazione e per avermi trasmesso molte conoscenze scientifiche riguardo l'oggetto delle nostre ricerche.

Ringrazio il Prof. Gian Luca Israel e il Dr. Paolo D'Avanzo per il gran lavoro nel revisionare questa Tesi e per aver contribuito a migliorarne il contenuto.

Ringrazio Nanda, Diego e Jian per avermi accolto a Barcellona a braccia aperte e per avermi fatto integrare perfettamente all'interno dell'Institut de Ciencies de l'Espai, dove ho imparato molto sull'analisi dati fatta nella banda Gamma. A questo proposito ringrazio tutto il gruppo dei "PhD students", ovvero Marius, Laura, Núria, Ramon, Anna, Marina, Nacho, Carles, Clara, Linda e Mariona per avermi accolto in Istituto con spontaneità e per avermi fatto integrare subito nel

loro gruppo.
Ringrazio Ciccio per la compagnia in ufficio e anche per l'amicizia al di fuori del lavoro. Non lo ringrazierò mai abbastanza per avermi insegnato a sciare durante una delle scorribande di gruppo sui Pirenei Catalani.
Un grandissimo ringraziamento lo devo ai miei coinquilini Barcellonesi Dennis, Matthieu, Marcello, Joseph e il quasi coinquilino Ilael per la loro amicizia e per i mille momenti belli passati assieme. A loro devo molto, soprattutto per avermi fatto sopportare meglio la lontananza da casa.
Ringrazio Salvo e Joseph (a.k.a. Magia) che mi hanno introdotto pian piano nel mondo della Capoeira. A loro va una "volta ao mundo" e un ringraziamento speciale per avermi insegnato in tempo record molte delle tecniche utilizzate in quest'arte marziale a dir poco affascinante.
Ringrazio la Mallorquina Caterina per il sostegno "a distanza" e per l'amicizia pura e onesta che non mi ha mai fatto mancare. Giuro che tornerò a trovarla presto per perderci nuovamente in macchina per le strade di Mallorca.
Un ringraziamento particolare va ad Angela che ha sempre saputo sostenermi e starmi vicino soprattutto nei momenti più difficili. La ringrazio per la pazienza e per aver assecondato ogni mia pazzia, compresa quella di farmi da assistente durante le nottate di osservazione astronomica passate al freddo e al gelo nelle Madonie.
Ringrazio il gruppo delle Archirafine di "casa Amato" (Mariella, Aurora e Miriana) per avermi sempre accolto nella loro casa e per le belle serate passate in compagnia a parlare di calendari e serie TV.
Per ultimi, ma certamente non per importanza, ringrazio mio padre, mia madre e mio fratello per la loro costante vicinanza e per i loro sacrifici che mi hanno permesso di arrivare fin qui.
A tutti, grazie di cuore!

Angelo
Palermo, Febbraio 2018